

Adaptive deformable mirror based on electromagnetic actuators

This research was partially funded by TNO Science and Industry and the IOP Precision Technology program of the Dutch Ministry of Economic Affairs.
A catalogue record is available from the Eindhoven University of Technology Library
Adaptive deformable mirror, based on electromagnetic actuators / by Roger Hamelinck – Eindhoven : Technische Universiteit Eindhoven, 2010, Proefschrift ISBN 978-90-386-2278-1
Copyright © 2010 by R.F.M.M. Hamelinck.
This thesis was prepared with the LaTeX $2_{\mathcal{E}}$ documentation system. Reproduction by ORO Grafisch Project Management, Koekange, The Netherlands.

Cover design by Hans Timmer, Oosterhout, The Netherlands.

Adaptive deformable mirror based on electromagnetic actuators

Proefontwerp

ter verkrijging van de graad van doctor aan de Technische Universiteit Eindhoven, op gezag van de rector magnificus, prof.dr.ir. C.J. van Duijn, voor een commissie aangewezen door het College voor Promoties in het openbaar te verdedigen op dinsdag 22 juni 2010 om 16.00 uur

door

Roger Francisus Mattheus Maria Hamelinck

geboren te Dongen

De documentatie van het proefontwerp is goedgekeurd door de promotor:

prof.dr.ir. M. Steinbuch

Copromotor:

dr.ir. P.C.J.N. Rosielle

Contents

St	ımma	ry		ix
N	omen	clature		xi
A	crony	ms		xix
1	Intr	oductio	on	1
	1.1	Imagii	ng through atmospheric turbulence	2
	1.2	The ac	daptive optics system	4
		1.2.1	Atmospheric turbulence	4
		1.2.2	Wavefront sensing	5
		1.2.3	Wavefront correction	5
		1.2.4	Wavefront control	9
	1.3	Challe	enges	10
		1.3.1	Challenges for the wavefront corrector	11
		1.3.2	Challenges for the control system	12
	1.4	Proble	em formulation and outline	13
2	Desi	gn requ	uirements and design concept	15
	2.1	Requi	rements	16
		2.1.1	Atmospheric turbulence	16
		2.1.2	The Kolmogorov turbulence model	16
	2.2	Error l	budget	20
		2.2.1	The fitting error	21
		2.2.2	The temporal error	21
		2.2.3	Error budget division	22
	2.3	Actuat	tor requirements	23
	2.4		ol system and electronics requirements	25
	2.5	The de	esign concept	27
		2.5.1	The mirror facesheet	28
		2.5.2	The actuator modules	29
		2.5.3	The control system and electronics	30
		2.5.4	The base frame	30
3	The	mirror	facesheet	31
	3.1	Overv	iew of thin mirrors	32
		3.1.1	Thin and ultra thin glass mirrors	32
		3.1.2	Beryllium X-ray windows	34
		3.1.3	Existing membrane deformable mirrors	35

vi Contents

		3.1.4	Thin and ultra thin wafers	36
		3.1.5	Thin Carbon Fiber Reinforced Plastic (CFRP) mirrors	37
		3.1.6	Nanolaminate deformable mirrors	37
		3.1.7	Epoxy Replicated Aluminum Foil (ERAF)	38
		3.1.8	Space membrane mirror technologies	38
	3.2	Design	n of the mirror facesheet	40
		3.2.1	The facesheet thickness	40
		3.2.2	Actuator forces for mirror deformation	42
		3.2.3	Power dissipation	42
		3.2.4	Mirror facesheet material comparison	45
	3.3	Constr	raining the mirror facesheet	47
		3.3.1	The facesheet's out-of-plane Degrees Of Freedoms (DOFs)	47
		3.3.2	The mirror's in-plane DOF	50
		3.3.3	Wrinkling and pretension in the membrane	52
	3.4	The in	fluence function	54
	3.5	The co	onnection struts	55
	3.6	Assem	bly of the connection struts	57
	3.7		8	70
	3.8	Conclu	usions and recommendations	71
4	Mod	lulan aa	tuoton avid	73
+	4.1		tuator grid or requirements	74
	4.1	4.1.1	The actuator force	75
	4.2		omagnetic actuators	75
	4.2	4.2.1	The Lorentz actuator	75 75
		4.2.1		75 76
	4.3		Reluctance actuators	80
	4.3	4.3.1	riable reluctance actuator	82
		4.3.1	The actuator membrane suspension	85
		4.3.3	A static actuator model	89
		4.3.4		92
		4.3.4	A dynamic actuator model	92 97
		4.3.6		97 100
		4.3.7		100 104
	4.4			104 106
	4.4			
		4.4.1		106
		4.4.2	8	109
		4.4.3		113
	4.5	4.4.4		115
	4.5			116
	4.6	Recom	nmendations	117

5	Elec	tronics	119
	5.1	Introduction	120
	5.2	Driver electronics	120
		5.2.1 Requirements	120
		5.2.2 Concepts	121
	5.3	Communication electronics	124
	5.4	Implementation and realization	125
		5.4.1 Pulse Width Modulation (PWM) implementation	125
		5.4.2 Field Programmable Gate Array (FPGA) implementation	128
		5.4.3 The ethernet to Low Voltage Differential Signalling (LVDS) bridge	130
	5.5	Modeling	130
	5.6	Testing and validation	133
		5.6.1 Communications tests	133
		5.6.2 Parasitic resistance measurements	134
		5.6.3 Actuator system validation	134
		5.6.4 Nonlinear behavior	139
	5.7	Power dissipation	140
	5.7	5.7.1 Optimizing the FPGA power efficiency	141
		5.7.2 Cooling	143
	5.8	Conclusions	144
	5.0	Conclusions	1
6	-	em modeling and characterization	147
	6.1	Introduction	148
	6.2	Deformable Mirror (DM) integration	149
		6.2.1 Integration of the 61 actuator mirror	149
		6.2.2 Integration of the 427 actuator mirror	150
	6.3	Static system validation	153
		6.3.1 Modeling	154
		6.3.2 Measurements and results	157
		6.3.3 Power dissipation	166
	6.4	Dynamic system validation	169
		6.4.1 Dynamic modeling	169
		6.4.2 System identification	173
		6.4.3 Modal analysis	175
	6.5	Conclusions	179
7	Con	clusions	181
	7.1	Conclusions	182
	7.2	Recommendations	186
Δn	pend	ices	187
τ×Γ	А	Measurement of the magnetic properties of Permanent Magnets (PMs)	189
	В	Setup to measure the nonlinear stiffness of the membrane suspensions	193
	C	Fourier series of a PWM signal	193
	D	The LVDS protocol	199
	E	The UDP protocol	203

viii	Contents
V111	Contents

F G	Spatial variation of actuator properties	
Bibliog	raphy	209
Sameny	ratting	223
Dankw	oord	225
Curricu	ılum Vitae	227

Adaptive deformable mirror based on electromagnetic actuators

Refractive index variations in the earth's atmosphere cause wavefront aberrations and limit thereby the resolution in ground-based telescopes. With Adaptive Optics (AO) the temporally and spatially varying wavefront distortions can be corrected in real time. Most implementations in a ground based telescope include a WaveFront Sensor, a Deformable Mirror and a real time wavefront control system. The largest optical telescopes built today have a $\approx\!10\text{m}$ primary mirror. Telescopes with more collecting area and higher resolution are desired. ELTs are currently designed with apertures up to 42m. For these telescopes serious challenges for all parts of the AO system exist. This thesis addresses the challenges for the DM. An 8m class telescope on a representative astronomical site is the starting point.

The atmosphere is characterized by the spatial and temporal spectra of Kolmogorov turbulence and the frozen flow assumption. The wavefront fitting error, caused by a limited number of actuators and the temporal error, caused by a limited control bandwidth, are the most important for the DM design. It is shown that $\approx\!5000$ actuators and 200Hz closed loop bandwidth form a balanced choice between the errors and correct an 8m wavefront in the visible to nearly diffraction limited. An actuator stroke of $\approx\!5.6\mu m$ and $\approx\!0.36\mu m$ inter actuator stroke is thereby needed. Together with the nm's resolution, low power dissipation, no hysteresis and drift, these form the main DM requirements.

The design, realization and tests of a new DM that meets these requirements and is extendable and scalable in mechanics, electronics and control to suit further ELTs is presented. In the DM a few layers are distinguished: a continuous mirror facesheet, the actuator grid and the base frame. Below the facesheet, in the actuator grid, the low voltage electromagnetic push-pull actuators are located. Identical actuator modules, each with 61 actuators, hexagonally arranged on a 6mm pitch can be placed adjacent to form large grids. The base frame provides a stable and stiff reference.

A thin facesheet is needed for low actuator forces and power dissipation, whereby its lower limit is set by the facesheets inter actuator deflection determined by gravity or wind pressure. For both scaling laws for force and dissipation are derived. Minimum power dissipation is achieved when beryllium is used for the mirror facesheet. Pyrex facesheets with $100\mu m$ thickness are chosen as a good practical, alternative in the prototype development. Struts ($\emptyset 0.1 \times 8 mm$) connect the facesheet to the actuators and ensure a smooth surface over the imposed heights and allow relative lateral movement of the facesheet and the actuator grid. Measurements show 3 nm RMS surface unflattness from the glued attachment.

The stiffness of the actuators form the out-of-plane constraints for the mirror facesheet and determine the mirrors first resonance frequency. The stiffness is chosen such that the resonance frequency is high enough to allow the high control bandwidth but not higher that needed to avoid excessive power dissipation and fix points in the surface in case of failure.

x Summary

The electromagnetic variable reluctance actuators designed, are efficient, have low moving mass and have suitable stiffness. Other advantages are the low costs, low driving voltages and negligible hysteresis and drift. The actuators consist of a closed magnetic circuit in which a PM provides static magnetic force on a ferromagnetic core that is suspended in a membrane. This attraction force is increased of decreased by a current through a coil. The actuators are free from mechanical hysteresis, friction and play and therefore have a high positioning resolution with high reproducibility. The actuator modules are build in layers to reduces the number of parts and the complexity of assembly and to improve the uniformity in properties.

Dedicated communication and driver electronics are designed. FPGA implemented PWM based voltage drivers are chosen because of their high efficiency and capability to be implemented in large numbers with only a few electronic components. A multidrop LVDS based serial communication is chosen for its low power consumption, high bandwidth and consequently low latency, low communication overhead and extensive possibilities for customization. A flat-cable connects up to 32 electronics modules, each suited to drive 61 actuators in an actuator module, to a custom communications bridge, which translates the Ethernet packages from the control PC into LVDS.

Two DMs prototypes were successfully assembled: a \(\preceq 50 \text{mm DM with 61 actuators and } \) a Ø150mm DM with 427 actuators. In the second prototype modularity is shown by the assembly of seven identical grids on a common base. The dynamic performance of each actuator is measured, including its dedicated driver and communication. All actuators were found to be functional, indicating that the manufacturing and assembly process is reliable. A nonlinear mathematical model of the actuator was derived describing both its static and dynamic behavior based on equations from the magnetic, mechanic and electric domains. The actuator model was linearized, leading to expressions for the actuator transfer function and properties such as motor constant, coil inductance, actuator stiffness and resonance frequency. From frequency response function measurements these properties showed slight deviations from the values derived from the model, but the statistical spread for the properties was small, stressing the reliability of the manufacturing and assembly process. The mean actuator stiffness and resonance frequency were 0.47kN/m and 1.8kHz respectively, which is close to their design values of 500N/m and 1.9kHz. The time domain response of an actuator to a 4Hz sine voltage was used to determine hysteresis and semi-static nonlinear response of the actuator. This showed the first to be negligible and the second to remain below 5% for $\pm 10 \mu m$ stroke. Measurements showed that in the expected operating range, the total power dissipation is dominated by indirect losses in FPGAs.

The static DM performance is validated using interferometric measurements. The measured influence matrix is used to shape the mirror facesheet into the first 28 Zernike modes, which includes the piston term that represents the best flat mirror. The total RMS error is $\approx 25 \, \mathrm{nm}$ for all modes. The dynamic behavior of the DM is validated by measurements. A laser vibrometer is used to measure the displacement of the mirror facesheet, while the actuators are driven by zero-mean, bandlimited, white noise voltage sequence. Using the MOESP system identification algorithm, high-order black-box models are identified with VAF values around 95%. The first resonance frequency identified is 725Hz, and lower than the 974Hz expected from the analytical model. This is attributed to the variations in actuator properties, such as actuator stiffness. The power dissipation in each actuator of the $\varnothing 50 \, \mathrm{mm}$ mirror to correct a typical Von Karmann turbulence spectrum is $\approx 1.5 \, \mathrm{mW}$.

Nomenclature

Symbols

Symbol	Description	Unit
0	vector or matrix whose elements are all zero	
1	vector or matrix whose elements are all unity	
A_{g_a}	cross section of the axial airgap	$[m^2]$
A_{g_r}	cross section of the radial airgap	$[m^2]$
A_m	cross section of the actuator membrane suspension	$[m^2]$
A_w	cross section of the coil winding	$[m^2]$
B	magnetic field density	[T]
B_s	magnetic saturation	[T]
$\mathbf{B}_{ ho}$	influence matrix that links the PWM voltages to the facesheet	[m/V]
,	deflection at the actuator locations	
$\mathbf{B_{f,w}}$	influence matrix that links the PWM voltages to the facesheet	[m/V]
	deflection on the measurement grid of the Wyko interferometer	
$\tilde{\mathbf{B}}_{f,w}$	measured, zero piston, influence matrix that links the PWM	[m/V]
J,-	voltages to the facesheet deflection on the measurement grid	
	of the Wyko interferometer	
$\mathbf{B_f}$	influence matrix that links the PWM voltages to the facesheet	[m/V]
_	deflections at an arbitrary grid of points on the facesheet	
C(s)	continuous time controller	
C(z)	discrete time controller	
$\widehat{C_1}$	linear stiffness coefficient	[-]
C_2	nonlinear stiffness coefficient	[-]
\mathbf{C}_a	diagonal matrix whose i^{th} diagonal element is the stiffness c_a	[N/m]
	of actuator i	
\mathbf{C}_{af}	stiffness matrix comprehending both the facesheet and actuator	[N/m]
-	stiffnesses	
C_{FPGA}	capacitance of the FPGA	[F]
C_l	capacitance used in the analog low pass filter	[F]
C_N^2	Atmospheric turbulence strength	$[m^{\frac{-2}{3}}]$
D	diameter	[m]
D_f	flexural rigidity	[Nm]
D_n	index of refraction structure function	[-]
D_s	diameter of the connection struts	[m]
D_t	diameter of the telescopes primary mirror	[m]
D_{DM}	diameter of the DM	[m]
D_{ϕ}	phase structure function	[-]
E	Young's modulus or elastic modulus	$[N/m^2]$

xii Nomenclature

Symbol	Description	Unit
E_f	Young's modulus of the mirror facesheet	$[N/m^2]$
E_g	Young's modulus of the glue	$[N/m^2]$
E_m	Young's modulus of the actuator membrane suspension	$[N/m^2]$
E_s	Young's modulus of the connection strut	$[N/m^2]$
F_a	actuator force	[N]
\mathbf{F}_a	vector of actuator forces	[N]
F_{ρ}	net force acting on the facesheet at the actuator location	[N]
$\dot{F_b}$	buckling force	[N]
F_L	Lorentz force	[N]
F_m	magnetic force	[N]
F_{res}	actuator force resolution	[N]
F_s	spring force	[N]
$\mathbf{F}_{ ho}$	vector of net forces acting on the facesheet at the actuator loca-	[N]
P	tions	
\mathfrak{F}_i	magnetomotive force in the flux path with index i	[A]
H(s)	transfer function from voltage to position	[m/V]
$H_I(s)$	transfer function from current to position	[m/A]
$H_{m}(s)$	transfer function from force to position	[m/N]
$H_{p,Ts}^*(z,\theta)$	discretized transfer function from voltage to position	[m/V]
$H_{v,Ts}^*(z,\theta)$	discretized transfer function from voltage to position	[m/sV]
$\hat{H}_{v,Ts}(z,\theta)$ $\hat{H}_{p,Ts}(z,\theta)$	estimated transfer function from voltage to speed	
		[m/V]
$\hat{H}_{v,Ts}(z,\theta)$	estimated transfer function from voltage to speed	[m/sV]
$\hat{H}_{p,Ts}^*(z,\theta)$	estimated and discretized transfer function from voltage to po- sition	[m/V]
$\hat{H}_{v,Ts}^*(z,\theta)$	estimated and discretized transfer function from voltage to speed	[m/sV]
$H_{ au_c}$	Transfer function for the communication latency	[-]
$H_{ZOH}(s)$	Transfer function of the zero order hold operation	[-]
H_{bc}	magnetic field intensity in the coil core	[A/m]
H_{c_m}	coercivity of the PM	[A/m]
H_{g_a}	magnetic field intensity in the axial airgap	[A/m]
$H_{g_r}^{ga}$	magnetic field intensity in the radial airgap	[A/m]
H_m	magnetic field intensity in the PM	[A/m]
H_r	magnetic field intensity in the core and baseplate	[A/m]
, I	current	[A]
I	identity matrix	
I_s	second moment of inertia of the connection strut	$[m^4]$
I_a	current through the actuator coil	[A]
I_{C_1}	current through the capacitance C_l	[A]
I_f	current through the fictitious winding	[A]
I_{R_l}	current through the resistance R_l	[A]
$J_1(\cdot)$	Bessel function of the first kind	[A] [-]
J_a	current density in the actuator coil	$[A/m^2]$
J_a $J_ heta$	moment of inertia around the z-axis	[kgm ²]
K_a	motor constant	[N/A]
	motor constant diagonal matrix, whose i^{th} diagonal element is the motor con-	
\mathbf{K}_a		[N/A]
T/	stant k_a of actuator i	DAT/ 3
\mathbf{K}_m	facesheet stiffness matrix	[N/m]
L	length	[m]

Symbol	Description	Unit
L_0	atmospheric outer scale	[m]
L_{11}, L_{22}	self inductance	[H]
L_{12}, L_{21}	mutual inductance	[H]
L_a	actuator inductance	[H]
L_l	inductance of the low pass filter	[H]
L_s	length of the connection strut	[m]
L_w	length of coil wire	[m]
M	moment	[Nm]
\mathbf{M}_{af}	diagonal matrix whose ith diagonal element is the sum of the	[kg]
3	moving actuator mass and the lumped facesheet mass at its lo-	. 03
	cation	
	magnetization	[A/m]
M_{φ}	moment around the x-axis	[Nm]
N^{φ}	number of windings	[-]
N_a	number of actuators	[-]
N_{av}	number of actuators	[-]
N_b	number of counter bits	[-]
N_d	demagnetization factor	[-]
N_f	number of fictitious windings	[-]
N_m	number of actuator modules	[-]
N_s	number of WaveFront Sensor (WFS) lenselets	[-]
N_w	number of waver fold Sensor (WTS) lenseleds	[-]
\mathcal{P}	plant to be controlled	ſ J
$\stackrel{\prime}{P}$	pressure	$[N/m^2]$
1	temporal power spectrum	[J/Hz]
	Power dissipation	[W]
P	projection matrix to remove the 'piston' term	[-]
P_0	light intensity	[lm/m ²]
P_a	power dissipation in the actuator	[W]
$P_{dyn}(f_{clk})$	dynamic power dissipation in an FPGA as function of the clock	[W]
$I_{dyn}(J_{clk})$	frequency	[W]
P_e	electrical power dissipation	[337]
P_{load}		[W]
P_{sc}	power dissipation due to the load	[W]
P_{tot}	short circuit power dissipation	[W]
_	total power dissipation	[W]
\mathbf{Q}_n	Hadamard matrix of size nxn	[-]
R_a	electrical resistance of the actuator coil	$[\Omega]$
R_c	electrical resistance applied for the fine PWM signal	$[\Omega]$
R_l	electrical resistance of the analog low pass filter	$[\Omega]$
\Re_{bc}	magnetic reluctance of the part of the baseplate that forms the core of the actuator coil	[1/H]
\Re_c	magnetic reluctance of the actuator moving core	[1/H]
\Re_{flc}	magnetic reluctance of leakage flux path of the coil	[1/H]
\Re_{flm}	magnetic reluctance of leakage flux path of the PM	[1/H]
\Re_{g_a}	magnetic reluctance of the actuator axial airgap	[1/H]
\Re_{g_r}	magnetic reluctance of the actuator radial airgap	[1/H]
\Re_m	magnetic reluctance of the PM	[1/H]
* * * * * * * * * * * * * * * * * * * *	Strehl ratio	
S	SUCIII IAUO	1-1
$S \\ S(s)$	transfer function from disturbance to residual error	[-] [-]

xiv Nomenclature

Symbol	Description	Unit
T	temperature	[K]
T_e	control loop delay	[s]
T_s	sampling time	[s]
T_{PWM}	time periode for the PWM base frequency	[s]
\mathbf{U}_r	three-column matrix containing piston, tip and tilt modes eval-	[-]
	uated on an arbitrary grid	
$\mathbf{U}_{ ho}$	three-column matrix containing piston, tip and tilt modes eval-	[-]
	uated on the actuator grid	
V	voltage	[V]
\mathbf{V}	matrix of actuator command voltage vectors for identification	[V]
V_a	voltage over the actuator coil	[V]
V_{cc}	supply voltage	[V]
V_{C_l}	voltage over the capacitor C_l	[V]
\mathbf{v}_i	actuator command voltage vector with index i for identification	[V]
V_m	volume of the PM	[m ³]
V_w	coil volume	[m ³]
V_{R_a}	voltage over the resistance R_a	[V]
W	magnetic coenergy	[J]
b_a	mechanical damping in the actuator	[Ns/m]
c	speed of light in vacuum	[m/s]
c_D	compression factor $(=D_t/D_{DM})$	[-]
c_a	actuator stiffness	[N/m]
c_f	out-of-plane stiffness of the mirror facesheet	[N/m]
c_s	axial stiffness of the connection strut	[N/m]
$c_{x,y,z}$	stiffness in direction x, y and z	[N/m]
d	inter actuator spacing	[m]
d_t	inter actuator spacing projected on the telescope aperture	[m]
f	frequency of light	[Hz]
f_c	control bandwidth	[Hz]
f_{clk}	FPGA clock frequency	[Hz]
$f_{e_x,y,z}$	resonance frequency in x, y and z	[Hz]
f_{e_s}	resonance frequency of the actuator strut	[Hz]
f_e	undamped mechanical actuator resonance frequency	[Hz]
f_{FPGA}	FPGA clock frequency	[Hz]
f_G	Greenwood frequency	[Hz]
f_{PWM}	PWM base frequency	[Hz]
f_N	Nyquist frequency	[Hz]
f_s	sampling frequency	[Hz]
g	gravitation acceleration	$[m/s^2]$
h	distance between the core in the undeflected membrane suspen-	[m]
h	sion core and the PM	[m]
	height heat transfer coefficient	[m] [W/m ²]
h_n		[W/m ⁻] [Nm/rad]
$k_{\phi,arphi, heta}$	rotational stiffness around the x, y and z axis	[Mm/rad] [m]
k_H	Helmholtz coil constant	
l_0	atmospheric inner scale	[m]
l_b	magnetic flux path length through the baseplate	[m]
l_c	magnetic flux path length through the moving core	[m]

Symbol	Description	Unit
l_{g_a}	magnetic flux path length through the axial air gap	[m]
l_{gr}	magnetic flux path length through the radial air gap	[m]
l_m	magnetic flux path length through the PM	[m]
m	mass	[kg]
m_{a_c}	mass of the moving core in the actuator	[kg]
m_{a_f}	mass of the mirror facesheet per actuator	[kg]
m_f	mass of the mirror facesheet	[kg]
m_s	mass of the actuator strut	[kg]
m_z	magnetic dipole moment	$[m^2A]$
n	white noise vector	' '
n	index of refraction	[-]
n_{air}	index of refraction of air	[-]
p_w	wind pressure	$[N/m^2]$
r	spatial coordinate	[m]
	Fried parameter	[m]
r_0	normalized spatial coordinate with index i in the complex plane	[-]
r_i	vector of normalized coordinates in the complex plane	[-]
r	mirror facesheet radius	
r_f		[m]
r_m	actuator membrane suspension radius	[m]
s	Laplacian variable ($s=j\omega$)	[rad/s]
	the number of block-rows used in the Multivariable Output-	[-]
	Error State-sPace (MOESP) algorithm	
t	time	[s]
t	thickness	[m]
t_m	actuator membrane suspension thickness	[m]
t_f	mirror facesheet thickness	[m]
v(h)	wind speed at altitude h	[m/s]
v	speed of light	[m/s]
v_w	wind speed	[m/s]
w_x	rigid body rotation around the x-axis (tip)	[m]
w_p	rigid body displacement in z-direction (piston)	[m]
w_y	rigid body rotation around the y-axis (tilt)	[m]
z_a	actuator displacement	[m]
\dot{z}_a	actuator velocity	[m/s]
\ddot{z}_a	actuator acceleration	$[m/s^2]$
z_f	facesheet deflection	[m]
$z_{f,0}$	unactuated facesheet deflection	[m]
\hat{z}_f	measured facesheet deflection	[m]
z_{ia}	inter actuator stroke	[m]
z_0	initial axial air gap height	[m]
z_s	suspension membrane deflection	[m]
α	linear coefficient of expansion	[m/m/K]
	switching activity in an FPGA	[-]
	integrator gain	[-]
β	Catalan Beta function	[-]
γ	contact angle	[rad]
,	command vector scaling constant	[m]
$rac{\gamma_w}{\Gamma_v}$	diagonal scaling matrix on command voltages	
1 v	diagonal scaring matrix on confinanti voltages	[-]

xvi Nomenclature

Symbol	Description	Unit
Γ_z	diagonal scaling matrix on measured displacements	[-]
ζ	Riemann Zeta function	
÷	telescope angle w.r.t. Zenith	[°]
7	actuator coupling	[-]
7	actuator efficiency	[-]
,)	rotation around the z-axis	[rad]
)	angular coordinate	[-]
O_a	angular distance between object and reference star	[rad]
Э	angle of the chief ray w.r.t. the optical axis	[rad]
ડ ૧	spatial frequency	[1/m]
	spatial frequency in x direction	[1/m]
κ_x	spatial frequency in x direction	[1/m]
\mathfrak{c}_y		
\mathfrak{c}_z	spatial frequency in z direction	[1/m]
\mathfrak{c}_f	fitting error coefficient	[-]
\	wavelength of light	[m]
	thermal conductivity	[W/mK]
	flux linkage	[Wb]
1	diagonal scaling matrix on command voltages	[-]
ι_0	magnetic permeability of vacuum	$[N/A^2]$
ι_r	relative magnetic permeability	[-]
ι_{r_m}	relative magnetic permeability of the PM	[-]
ι_{r_b}	relative magnetic permeability of the baseplate	[-]
,	Poisson ratio	[-]
$'_m$	Poisson ratio of the actuator membrane suspension material	[-]
'f	Poisson ratio of the mirror facesheet material	[-]
)	material density	[kg/m ³]
o_m	density of the actuator membrane suspension material	[kg/m ³]
O_a	density of air	[kg/m ³]
Df	density of the mirror facesheet material	[kg/m ³]
j_i	complex coordinate with index i	[m]+j[n
O_S	density of the connection strut material	[kg/m ³]
νs 7 ₁₁	principle stress	$[N/m^2]$
$ au_{22}$	principle stress	$[N/m^2]$
2	wavefront variance due to off axis observation angle	[nm ²]
σ_{angle}^2 σ_{cal}^2 σ_{ctrl}^2	wavefront variance due to oil axis observation angle wavefront variance due to calibration errors	[nm ²]
cal_2	wavefront variance due to cambration error	[nm ²]
2^{ctrl}		
σ_{delay}^2	wavefront variance due to a delay	$[nm^2]$
σ_{fit}^2	wavefront variance due to limited number of actuators	[nm ²]
τ_g	gravitational sag	[m]
σ_{meas}^2	wavefront variance due to measurement errors	[nm ²]
σ_n^2	wavefront variance due to measurement noise	[nm ²]
σ_{temp}^2	wavefront variance due to limited bandwidth	[nm ²]
σ_{total}^2	total wavefront variance	$[nm^2]$
$\sigma(v,i)$	expected Root Mean Square (RMS) actuator voltage based on a	[V]
	Von Karmann spatial power spectrum	
σ_w	deflection by wind	[m]
σ_{wf}^{2}	wavefront variance	[nm ²]
г <i>w</i> ј	delay	[s]

Symbol	Description	Unit
$ au_c$	communication latency	[s]
$ au_{UDP}$	delay caused by the User Datagram Protocol (UDP) packet	[s]
	transfer	
$ au_{LVDS}$	delay caused by the LVDS packet transfer	[s]
ϕ	optical phase	[rad]
	rotation around the x-axis	[rad]
ϕ_i	magnetic flux in a circuit with index i	[Wb]
Φ	spatial PSD	[rad ²]
	magnetic flux	[Vs]
ψ	rotation around the y-axis	[rad]
$oldsymbol{\Omega}_{ ho ho}$	facesheet compliance matrix w.r.t. the actuator grid	[m/N]
$oldsymbol{\Omega}_{r ho}$	facesheet compliance matrix mapping forces at the actuator lo-	[m/N]
	cations $ ho$ to displacements at an arbitrary grid ${f r}$	

Operators and sets

Symbol	Description
∇	Laplacian operator (partial derivative)
$\operatorname{Tr}(\cdot)$	Trace of the dotted matrix
$\langle \cdot \rangle$	expected value of the dotted expression
$\mathcal{N}_n(\mathbf{m}, \mathbf{C})$	set of ergodic white noise signals $\mathbf{s}(t) \in \mathbb{R}^n$ with mean \mathbf{m} and covariance
	(matrix) C
$\ \cdot\ _F$	Frobenius norm of the dotted expression

Acronyms

ADC	Analog to Digital Convertor	FPGA	Field Programmable Gate
AFRL	Air Force Research Laboratory		Array
AO	Adaptive Optics	FRF	Frequency Response Function
ASIC	Application-Specific Integrated	FWHM	Full Width Half Maximum
	Circuit	GMT	Giant Magellan Telescope
ASM	Adaptive Secondary Mirror	HST	Hubble Space Telescope
CAN	Controller Area Network	IC	Integrated Circuit
CCD	Charge Coupled Device	IP	Internet Protocol
CFHT	Canada France Hawaii	IR	Infra Red
	Telescope	JWST	James Webb Space Telescope
CFRP	Carbon Fiber Reinforced	LBT	Large Binocular Telescope
	Plastic	LLNL	Lawrence Livermore National
CPU	Central Processing Unit		Laboratory
$_{\mathrm{CME}}$	Coefficient of Moisture	CAD	Computer Aided Design
	Expansion	LTI	Linear Time-Invariant
CMOS	Complementary Metal Oxide	LVDS	Low Voltage Differential
	Semiconductor		Signalling
CNC	Computer Numerical Control	LSB	Least Significant Bit
CS	Curvature Sensor	MAC	Media Access Control
CTE	Coefficient of Thermal	MOESP	Multivariable Output-Error
	Expansion		State-sPace
DAC	Digital to Analog Convertor	MEMS	Micro-Electro-Mechanical
DM	Deformable Mirror		Systems
DOF	Degrees Of Freedom	MIMO	Multi-Input Multi-Output
DC	Direct Current	MIT	Massachusetts Institute of
EDM	Electrical Discharge Machining		Technology
E- ELT	European Extremely Large	MMT	Multiple Mirror Telescope
	Telescope	MTBF	Mean Time Before Failure
ELT	Extremely Large Telescope	MSB	Most Significant Bit
ERAF	Epoxy Replicated Aluminum	NCPA	Non Common Path Aberration
	Foil	NGST	Next Generation Space
ERA	Eigensystem Realization		Telescopes
	Algorithm	NMSD	NGST Mirror System
FEM	Finite Element Model		Demonstrator
FET	Field Effect Transistor	OPD	Optical Path Difference
FOV	Field Of View	OWL	Overwhelmingly Large
FPD	Flat Panel Display		Telescope

xx Acronyms

IDentification TF Transfer Function PCB Printed Circuit Board TMT Thirty Meter Telescope
PCB Printed Circuit Board TMT Thirty Meter Telescope
PHY PHYsical layer (ethernet) UDP User Datagram Protocol
PMN Lead Manganese Niobate ULE Ultra Low Expansion
PM Permanent Magnet USB Universal Serial Bus
PSD Power Spectral Density UV Ultra Violet
PSF Point Spread Function VAF Variance Accounted For
PS Pyramid Sensor VLT Very Large Telescope
PTV Peak To Valley WFS WaveFront Sensor
PWM Pulse Width Modulation WHT William Herschel Telescope
RAM Random Access Memory ZOH Zero Order Hold
RMS Root Mean Square NASA National Aeronautics and
SCIDAR SCIntillation Detection and Space Administration
Ranging SMEC Stretched Membrane with
SHS Shack Hartmann sensor Electrostatic Curvature
SISO Single-Input Single-Output XUP Xylinx University Program
SVD Singular Value Decomposition

Chapter one

Introduction

Atmospheric turbulence is introduced as the cause of wavefront aberrations. This limits the resolution in ground-based telescope systems. The image quality can be improved with an Adaptive Optics system. In an AO system the wavefront aberration is measured with a wavefront sensor and in realtime corrected by a wavefront corrector and control system. The wavefront corrector is usually a Deformable Mirror, where the reflective surface takes the opposite shape of the disturbed wavefront. An overview is given of current available wavefront correctors and the main challenges for the wavefront corrector and control system for future AO systems are addressed. A problem formulation and outline of this thesis is given at the end of this chapter.

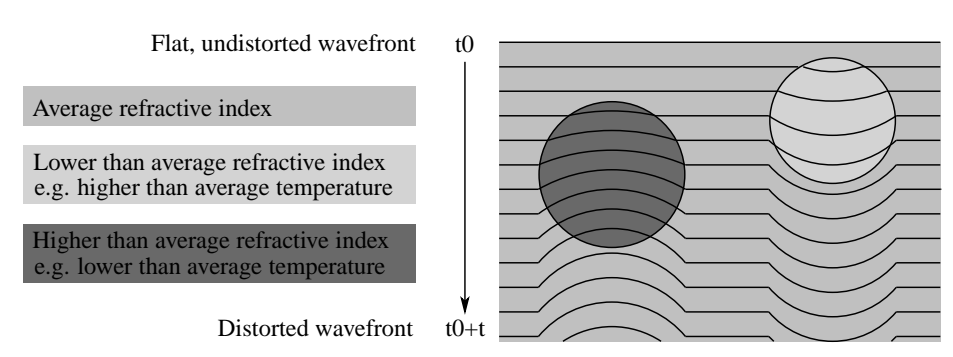


Figure 1.1: The atmosphere, represented by a set of air bubbles with higher- and lower-than-average refractive index. The refractive index variations change the wavelength of the wavefront and the speed by which the light travels through the atmosphere such that the initially flat wavefront distorts.

1.1 Imaging through atmospheric turbulence

After the invention of the telescope in 1608 astronomers realized that for higher resolution of the observed images larger telescope apertures are required. This does not bring a full solution. Christian Huygens proposed around 1656 that the atmosphere was to blame. Light emitted by a distant star is undistorted as it enters the earth's atmosphere. The atmosphere can be seen as a set of air bubbles with slightly different physical properties, e.g. temperature and pressure. The initially flat wavefront distorts when passing through these air bubbles due to refractive index variations caused by the temperature, pressure, humidity and CO₂-concentration variations [57].

The index of refraction is defined as the ratio between the speed of light in vacuum (c) and the speed of light in the medium (v): $n=\frac{c}{v}$ [100]. With the variation of the refractive index, the speed of light at which the wavefront travels through the atmosphere will vary. Since the frequency of the light (f) does not change, the change of speed of light will lead to a change of its wavelength: $\lambda=\frac{v}{f}$ [100]. In Chapter 2, Equation (2.1), it will be shown that parts of the atmosphere that are hotter-than-average have a lower-than-average refractive index and vice versa. Parts of the wavefront that pass through air with lower-than-average refractive index are advanced and parts that pass through air with higher refractive index are retarded. As a result, the initially flat wavefront is distorted. This is shown schematically in Figure 1.1. Optical distortions caused by the earth's atmosphere are always present. Even Newton did not see a solution. In his 'Opticks' in 1730 he stated that it was impossible to overcome the optical degradation caused by the earth's atmosphere [139]:

"If the Theory of making Telescopes could at length be fully brought into Practice, yet there would be certain Bounds beyond which Telescopes could not perform. For the Air Through which we look upon the Stars, is in perpetual Tremor; as may be seen by the tremulous Motion of Shadows cast from high Towers, and by the twinkling of the fix'd Stars. But these Stars do not twinkle

when viewed through Telescopes which have large apertures. For the Rays of Light which pass through divers parts of the aperture, tremble each of them apart, and by means of their various and sometimes contrary Tremors, fall at one and the same time upon different points in the bottom of the Eye, and their trembling Motions are too quick and confused to be perceived severally. And all these illuminated Points constitute one broad lucid Point, composed of those many trembling Points confusedly and insensibly mixed with one another by very short and swift Tremors, and thereby cause Star to appear broader than it is, and without any trembling brighter and larger than short ones can do, but they cannot be so formed as to take away that confusion of the Rays which arises from the Tremors of the Atmosphere. The only Remedy is a most serene and quiet Air, such as may perhaps be found on the tops of the highest Mountains above the grosser Clouds."

With an ideal telescope and without the presence of the atmosphere a point source is shaped by diffraction and is described by the Airy function [100]:

$$P_0(\vec{\theta}) = \frac{\pi D_t^2}{4\lambda^2} \left[\frac{2J_1\left(\frac{\pi D_t|\vec{\theta}|}{\lambda}\right)}{\left(\frac{\pi D_t|\vec{\theta}|}{\lambda}\right)} \right]^2 \tag{1.1}$$

where P_0 is the light intensity as function of the angular coordinate $\vec{\theta}$, λ the wavelength, D_t the telescope diameter and J_1 the Bessel function. The first dark ring (Figure 1.3) is at an angular distance of $1.22\frac{\lambda}{D_t}$ and is called the resolution of the ideal telescope. An astronomical object can be seen as an number of point sources. Each point spreads according to the Airy function. The convolution of these functions forms the object's image. This forms the image with the least degradation possible and is called diffraction limited.

In practice the image quality is not diffraction limited, but further degraded. Imperfect optical components and misalignment and atmospheric turbulence are a few causes. The function Equation (1.1) is then referred to as the Point Spread Function (PSF). From this, multiple measures of the optical quality are defined:

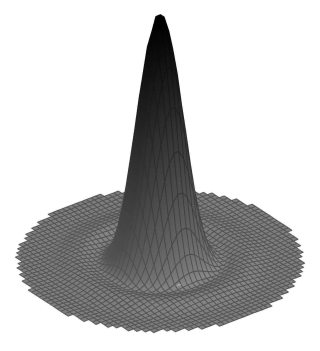


Figure 1.2: The diffraction limited Airy function of a point source.



Figure 1.3: Top view of the Airy function.

• Strehl ratio (S) = $\frac{P_0(\vec{\theta})}{P(\vec{\theta})}$. This is the theoretical central peak intensity $(P_0(\vec{\theta}))$ compared to the central peak intensity of the Point Spread Function (PSF) $(P(\vec{\theta}))$.

- The Full Width Half Maximum (FWHM) of the PSF.
- Encircled energy. This is a measure for the energy concentration in the optical image. It gives the distribution of energy in the PSF. The PSF integral over the disc of radius r is called the encircled energy.

For long time no solution to the natural degradation of the optical quality was seen. This changed in 1953 when Horace Babcock proposed to use a deformable optical element and a wavefront sensor to compensate for the 'Tremors of the Atmosphere' [8]. This is regarded as the start of the field of adaptive optics as defined today [187]. Adaptive optics is a technique for removing temporally and spatially varying optical wavefront aberrations in real time. Its applications are broad and include optics, lasers and medicine, but one of the most challenging is correcting blurred images in large ground-based astronomical telescopes. In the next section the standard implementation of the adaptive optics system and its components in ground based telescopes is described.

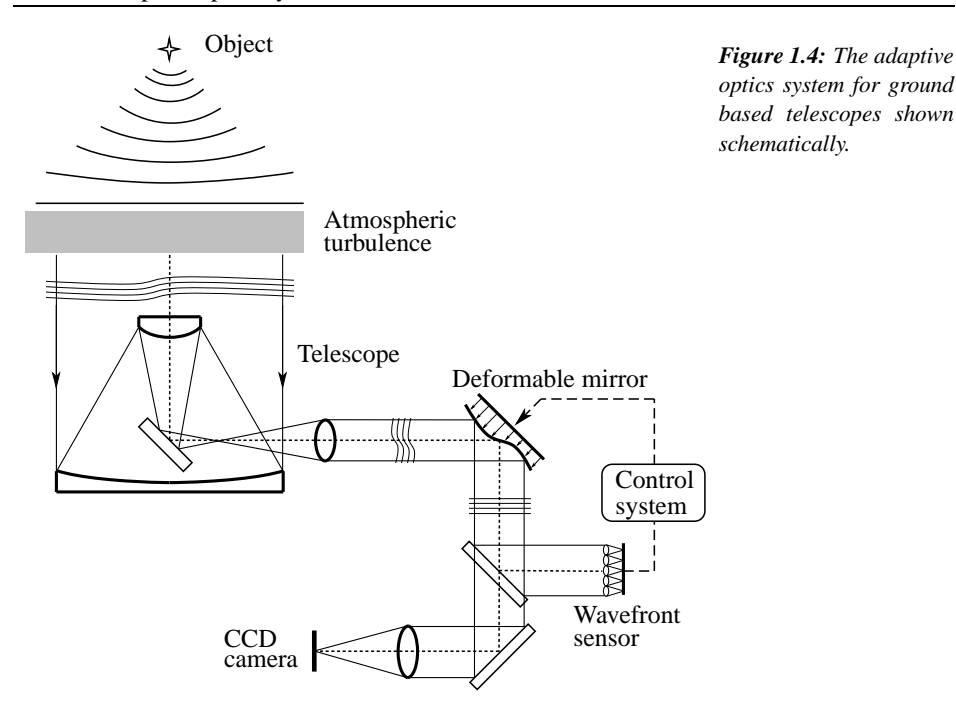
1.2 The adaptive optics system

An Adaptive Optics system for astronomy consists of a WaveFront Sensor, a wavefront corrector and a real time wavefront control system. A schematic of the AO system is shown in Figure 1.4. After a few reflections in the telescope, the wavefront reflects on the wavefront corrector, usually a Deformable Mirror, after which a dichroic beamsplitter splits the wavefront: partially to the WaveFront Sensor and partially to the science camera. The controller calculates the new actuator signals for the DM based on information from the WFS. In the next sections atmospheric turbulence and the main components of the AO system will be discussed.

1.2.1 Atmospheric turbulence

The atmosphere is often represented as a set of different size air bubbles, each with their own physical properties as temperature, pressure and humidity, and therefore with their own refractive index n. The wind carries these air bubbles over the telescope aperture without significant change in properties. The latter is called the frozen flow assumption or Taylor hypothesis. At most telescope sites a large part of the turbulence is at the lower altitude, where a temperature gradient between air and ground exists [186].

In 1941 Kolmogorov laid the foundation for the currently used atmospheric turbulence models [117]. Kolmogorov concluded that in a turbulent flow the kinetic energy decreases with the $\frac{-5}{3}$ power of the spatial frequency. From this, Tatarski [182] and Fried [65] developed the standard model for astronomical seeing. In Chapter 2 a more detailed description of atmospheric turbulence and its consequences on the deformable mirror design is given.



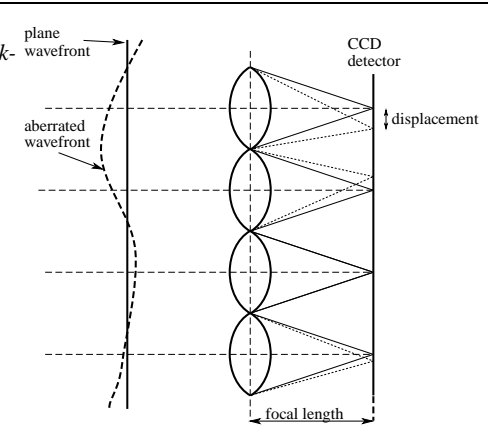
1.2.2 Wavefront sensing

For the correction, measurement of the wavefront is needed. Direct phase measurement is difficult and often replaced by slope measurements with a Shack Hartmann sensor (SHS) [169]. This sensor is shown schematically in Figure 1.5. The wavefront is focused through a lensslet array on a Charge Coupled Device (CCD) camera. Local slopes result in a translation of the foci on the CCD, which is a measure of slope. The wavefront shape can be reconstructed by the integration of these slopes. Besides the widely used SHS other sensors such as the Curvature Sensor (CS) [155] and the Pyramid Sensor (PS) [150] exist. As in the SHS, the CS uses an array of lenses to focus the wavefront, but a sensor measures the intensity before and after the focal plane. If there's a local curvature in the wavefront, the position of the focal spot is changed. By measuring the different relative spot intensities the curvature can be deduced. In the PS the wavefront falls on the top of many small pyramids. The facets of each pyramid split the light into a number of beams, which then are imaged onto a detector. If the wavefront is flat the result is an equal amount of light in all beams. If wavefront aberrations are present this distribution changes. By additional movement of the pyramids extra resolution is gained [150].

1.2.3 Wavefront correction

The wavefront corrector performs the physical correction of the wavefront. A wide variety of wavefront correctors exists. Not all types will be covered in this section. The objective here is to display the diversity and to point out the main properties of the different correc-

Figure 1.5: Wavefront sensing with the Shack-Hartmann sensor



tors.

Probably the oldest wavefront corrector is the segmented mirror. This mirror is made up from a number of small closely packed mirror segments that can move in one or three Degrees Of Freedom. In the first case the individual mirror elements can only move up and down (piston) along the optical axis, in the second case each mirror segment can rotate over two orthogonal axes of tilt as well. Piezoelectric actuators and strain gauges are most commonly used to move the segments and to provide position feedback. One example is the segmented mirror from ThermoTrex Corporation used on the 4.2 meter William Herschel Telescope (WHT) [138, 210]. This mirror has 76 mirror segments, each of which have tip/tilt and piston actuation giving a total of 228 DOFs. Other examples can be found in [45], [108], [97] and [75]. By having separated segments there is no cross coupling and mirror parts can be relatively easily replaced, this at the cost of having small gaps that act as a grating and cause diffraction.

Another type of wavefront corrector is the Deformable Mirror. Most DMs have continuous facesheets and have a stack of piezoelectric actuators placed under the reflective surface. They are placed perpendicular to the mirror surface and impose out-of-plane displacements on the facesheet. This type of DM is under development since 1974 and was first built for high energy laser systems [187]. At the end of the '70s these mirrors were developed for infrared systems [54, 55]. Current development on this type of mirror is driven by miniaturization [171], increasing actuator linearity, stroke [161] and position accuracy and decreasing operating voltages, drift [33, 161] and hysteresis [172]. Piezo stacked deformable mirrors are made by e.g. Xinetics, CILAS and OKO Technologies. A large AO-system with a piezo stacked mirror is on the 10-meter Keck telescope. Here a 349-channel piezoelectric mirror from Xinetics is implemented [203]. Besides piezoelectric materials also Lead Manganese Niobate (PMN) or magnetostrictive actuators are used. Recently a 3368 channel, PMN DM from Xinetics on a 66×66 grid with 1.8mm pitch, with $\approx 1.2 \mu m$ actuator stroke, is developed for the 5.1 meter Hale Telescope at Palomar Observatory as a high-order upgrade to the Palomar Adaptive Optics System [16]. The high voltage drivers dissipate about 4kW and need liquid cooling since cable constraints force the drivers to be placed near the Cassegrain focus. The system is planned to operate in 2011.

A separate class of continuous facesheet DMs are the bimorph mirrors. Unlike the DMs with stacked piezo actuators, bimorph mirrors have actuators placed parallel to the reflec-

tive surface. A bimorph mirror usually consists of a glass or metal facesheet that is bonded to a sheet of piezoelectric ceramic. There is a conductive electrode in the bond between the piezoelectric material and the facesheet. On the backside of the ceramic a series of electrodes is attached. When a voltage is applied between the front and back electrode the dimensions of the piezoelectric material change and a local radius of curvature is forced into the mirror. Bimorph mirror were first used in astronomy in the beginning of the '90s on the Canada France Hawaii Telescope (CFHT) [156]. One of the largest bimorph mirrors is a 188-element bimorph mirror, developed by CILAS, and currently used in the AO-system for the 8.2-meter SUBARU telescope. This mirror is \emptyset 130mm, but only the inner \emptyset 90mm is illuminated [179]. The remaining 40 electrodes outside this diameter are needed to enforce the proper boundary conditions [143].

In bimorph mirrors the local curvature is proportional with the voltage and the coefficient of the dielectric tensor and inversely proportional with the square of the thickness. The maximum voltage is given by the breakdown voltage. This also determines the gap between the electrodes and thereby sets a limit for the actuator density. Since the mechanical resonance frequency is mainly determined by the diameter-thickness ratio it is clear that a trade-off between mirror size, resonance frequency and stroke (curvature) is to be made. Critical in the design are the bonds between the different layers. Bimorph mirrors suitable for high power lasers with integrated cooling have also been developed [6, 164, 197]. Bimorph mirrors are used in combination with a CS because the reconstruction step can then be avoided ([118, 187]).

Besides piezo stacked and bimorph mirrors a few implementations exist with actuators that impart bending moments at the edge of the mirror [69].

To reduce the background emissivity from surfaces added by the AO system the number of reflective surfaces in astronomical telescopes should be kept to a minimum. This is especially the case for Infra Red (IR) observations. From this thought the idea for an Adaptive Secondary Mirror (ASM) was born in the '90s [162]. In contrast with the previously discussed correctors, secondary mirrors in a telescope are usually strongly curved, giving additional challenges in making them adaptive. The first ASM is build for the 6.5m Multiple Mirror Telescope (MMT) in Arizona in the mid '90s and has 336 actuators [123]. The static secondary mirror is replaced by a thin deformable zerodur shell with a radius of curvature of 1795mm. The shell is 1.9mm thick and 640mm in diameter [129]. In the center of the shell a membrane suppresses the lateral DOFs. A number of 336 small radially magnetized permanent magnets are glued at the backside of the zerodur shell and form together with the voice coils that are fixed in a reference plate the actuators that push and pull at the shell. Capacitive sensors are placed concentric with the actuators in between the Ultra Low Expansion (ULE) glass reference structure and the backside of the thin shell. They provide distance measurements for the local feedback loops. A 30mm thick aluminium plate with cooling channels is used to remove the heat produced [18, 20, 105, 189, 190]. The schematic of the ASM unit and photo can be seen in Figure 1.6 and Figure 1.7. After the conversion at the MMT two ASMs were made for the Large Binocular Telescope (LBT). Both the ASMs have a radius of curvature of 1974.2mm and measure 911mm across. To reduce the deformation forces and resulting power dissipation, a 1.6mm thick zerodur shell is chosen. Each of the shells have 672 electromagnetic actuators [70]. One of the Very Large Telescopes (VLTs) will be equipped with an ASM as well. First light is foreseen in 2015. This one has a radius of curvature of 4553mm and is 1120mm across and equipped

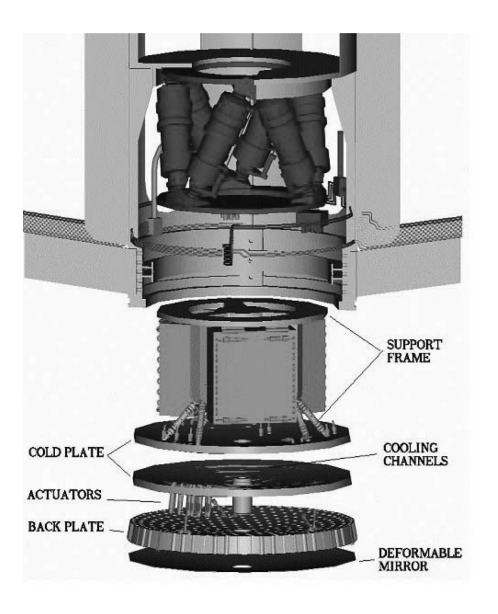




Figure 1.6: The ASM unit at the MMT shown in schematic. Figure taken from [200]

Figure 1.7: Photo of the adaptive secondary mirror unit at the MMT. Photo taken from [200].

with 1170 actuators [7].

The ASMs exhibit a few drawbacks. One of them is the high complexity. Due to the lack of mechanical stiffness in the thin shell, literary hundreds of eigenmodes need to be suppressed by the control system. To be able to control the mirror each actuator is equipped with a capacitive sensor and associated conditioning electronics and needs a significant amount of computational power for closed-loop control [199]. Research on controlling this thin shell is still ongoing [159]. Since the power consumption is high (MMT:2kW [123], LBT:2.665kW [12], VLT:1.47kW [7]), active fluidic cooling is needed. Leakage is known to occur in such systems [70]. Furthermore it is difficult to keep the dust out of the 50µm thin gap between the shell and reference structure [70]. The assembly has a high mass (MMT:130kg, LBT:250kg, VLT:180kg) which results in low mechanical resonances: the assembly hub starts to resonate in its metering structure. At the MMT, the wind causes the hub to rotate both perpendicular as well as along its optical axis. The resonance frequencies are 14 and 19 Hz respectively. Extra measures have been taken to reduce the optical degradation mentioned [174].

The last type of continuous facesheet deformable mirror discussed here is the membrane mirror. A very thin membrane ($<1\mu m$) usually not bigger than 15mm across is deformed by electrostatic forces. The membrane is usually stretched and placed in a silicon housing. Electrodes exist at the backside of the membrane and the housing. By applying a voltage to the electrostatic electrode actuators it is possible to deform the membrane. In most cases a bias voltage is applied to all the electrodes, to make the membrane initially spherical. In this way the membrane can be moved in both directions. Probably the most wide spread example is the 37 actuator electrostatic deformable mirror from OKO Technologies [125, 188].

Due to the thickness of the membrane the mirrors are very fragile. Critical in the design is to avoid possible snap down and avoid dust in the very narrow gaps. Another actuation method on membrane mirrors can be found in [46, 47]. Here a small magnet is suspended to the membrane and coils are used to deform the membrane. Since no mechanical stiffness exists, scaling to large diameters is not possible while retaining inter actuator stroke and density as well as dynamic properties.

Other small DMss are the Micro-Electro-Mechanical Systems (MEMS) devices. With the potential to be fabricated in large quantities and with large numbers of actuators this seems a promising technique. Most MEMS suffer from limited (inter)actuator stroke and poor surface quality. MEMS DMs are manufactured by Boston Micromachines [149] and Iris AO [102].

Not all wavefront correctors are based on reflection, high-order transmission based correctors are also available [124]. Most of them are based on liquid crystals and are limited in stroke and dynamic behavior.

It is clear that, since the first wavefront corrector, many different types have been developed. Constant development of the DM has led to large, meter scale mirrors with ≈ 1000 actuators with several tens of Hz control bandwidth and smaller DMs with several hundred actuators. Mirrors with more actuators and a higher control bandwidth are needed for existing large and future European Extremely Large Telescopes (E-ELTs) telescopes. Section 1.3.1 will address the main challenges for these wavefront correctors. Issues as extendability, scalability, low power dissipation, low failure probability, and a low price per channel still needs to be solved.

1.2.4 Wavefront control

The goal of the control system is to compensate the atmospheric wavefront distortion. The quality of this compensation can be measured using the Strehl ratio. According to the Maréchal approximation [187], this ratio is inversely related to the variance of the wavefront aberration. Therefore, the goal for the control system reflected in the mathematical formulae is to minimize this variance.

Based on mathematical formulae, e.g. the control law, the control system processes Wave-Front Sensor measurement data in realtime to determine setpoints for the actuators. In most cases this involves post-processing of the WFS measurements as they come from CCD detectors to the desired quantities and by the use of spatial and temporal models of the wavefront corrector and atmospheric turbulence.

For large AO systems the control laws are implemented on dedicated FPGA boards that can perform many calculations in parallel. These processors obtain the measurements via a fast, usually digital communication link to the sensor and output the commands via Digital to Analog Convertors (DACs) to the actuators.

AO systems can be configured in both open loop (Figure 1.9) as well as closed loop (Figure 1.8). Both configurations have their advantages and both are used in practice. In the open loop configuration the measurements are not influenced by the shape of the corrector and provide direct information on the wavefront distortion. However in case of strong turbulence the wavefront distortion may exceed the range of the WFS, leading to poor performance. Further, the effect of the control actions is not observed by the control system, which has

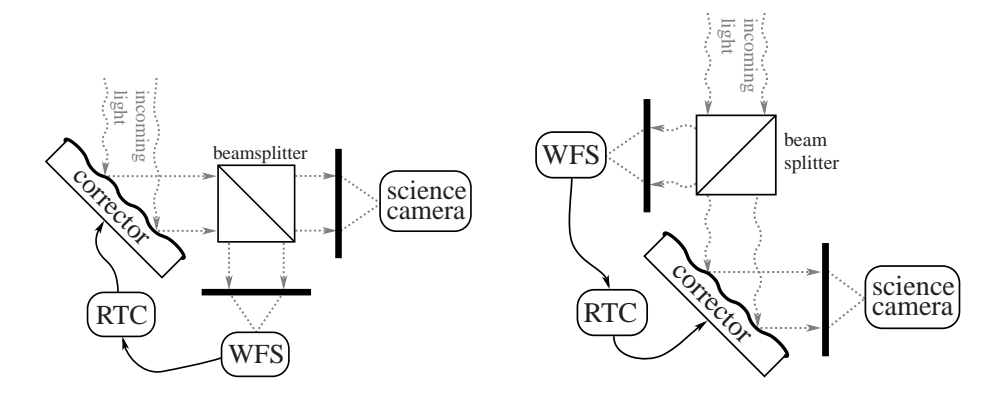


Figure 1.8: Schematic of an AO system configured in closed loop.

Figure 1.9: Schematic of an AO system configures in open loop.

to rely on a model that accurately describes the behavior of the wavefront corrector. For obvious reasons, this model cannot be calibrated in this configuration. On the other hand, an inaccurate model cannot lead to instabilities as long as the open loop controller itself is stable. This in contrast to the closed loop case, which – if not properly tuned – can become unstable. But this seems a reasonable price to pay for solving all previously mentioned issues of the open loop configuration. Therefore, throughout this thesis a closed loop control system will be considered.

1.3 Challenges

The largest optical telescopes built today have a 10m primary mirror. Examples are the VLTs, the LBT, the Keck telescopes and the SUBARU telescope. To explore the universe further and further, telescopes with more collecting area and higher resolution are desired. Both can be achieved by enlarging the telescopes primary mirror diameter. Telescopes are currently being designed with these extremely large aperture diameters (Extremely Large Telescopes (ELTs)). A consortium in the USA has conceived the Thirty Meter Telescope (TMT) with an aperture diameter of 30m [178]. Another recent American initiative is the Giant Magellan Telescope (GMT) [113]. The primary mirror of this 22-meter telescope is made out of 7, 8-meter class, segments. The European project called Overwhelmingly Large Telescope (OWL) started as a 100m telescope [52], but is recently downsized to a 42m telescope called the E-ELT [74]. Another initiative by the Swedish Lund University called the EURO-50, is now superseded by the E-ELT.

It does not make sense to design and build such large telescopes without the use of adaptive optics. One would only gain by the collecting area and able to observe fainter objects, but without increased resolution. The design of AO systems for such large telescopes involves serious challenges for all parts of the AO system. For the scope of this thesis only the challenges for the wavefront corrector and the control system will be addressed.

1.3 Challenges 11

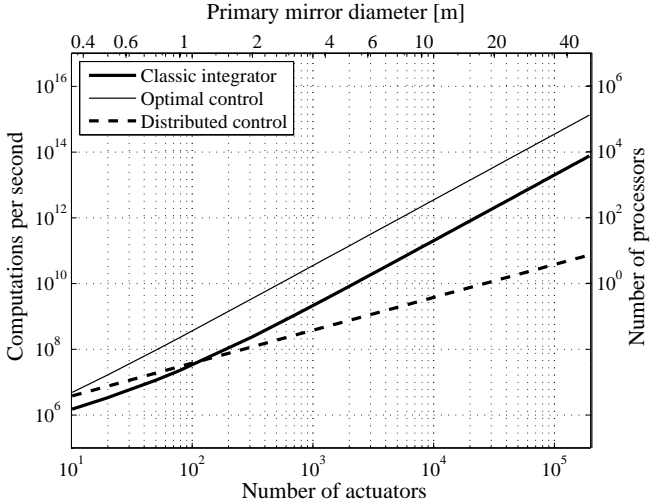
1.3.1 Challenges for the wavefront corrector

The number of controllable degrees of freedom of DMs for such large telescopes must be in the order of ten of thousands, because - as discussed in the next chapter - the actuator density remains constant for a given optical quality. The highest number of actuators currently available for DMs is $\approx \! 1000$ and the costs are around $1k \in$ per actuator. It is not trivial to extend current designs to larger actuator numbers. A few reasons can be identified.

- Extendability. Straightforward extension of many current DM designs leads to an
 increase in mass that cannot be matched by stiffness and thus leads to a severe reduction of the resonance frequencies. Low resonance frequencies reduce the achievable
 control bandwidth and thus the achievable wavefront correction performance. Extendability is not only needed in its mechanics but also for the control system and
 electronics involved.
- Scalability. DMs are needed with a wide range of actuator pitch. The first generation
 AO systems for the E-ELT will have 30mm actuator pitch and around 8000 actuators
 [107]. Later generations will have an actuator pitch down to 1mm with over a 100.000
 actuators. No current design is available that matches these requirements. DMs are
 needed with a wide range of actuator pitch.
- Power dissipation. Most DM designs involve substantial power dissipation. As a consequence e.g. the temperature of the DM surface with respect to its environment will rise with detrimental air flow in the path of light as a result. So active cooling is required. Active cooling systems add complexity to the system and have the risk of leakage. The fluid flow will introduce vibrations on the nm level that affect the wavefront correction performance as well.
- Failure probability. As the number of actuators increases, the probability of defect actuators also increases. When an actuator has high stiffness it fixes the displacement in the facesheet at one point, a so-called hard point and this will affect a large fraction of the mirror area and thus its performance. So besides developing actuators with a high Mean Time Before Failure (MTBF), actuators should not cause a significant decrease in the optical surface quality after failing.
- The price per channel. The budget for a whole ELT is 500M€. With current cost per channel a full size AO system for these telescopes will not be affordable.

In this thesis a design will be proposed that is driven by above-mentioned reasons. Extendable and scalable mirror design is needed, in mechanics, electronics and control with lightweight construction with high resonance frequencies, low power dissipation and soft and cheap actuators. As a starting point for further requirements an 8m class telescope on a representative astronomical site is chosen.

Figure 1.10: The computational load for different control algorithms as function of the number of DOFs to be controlled



1.3.2 Challenges for the control system

Already since the first AO system, the speed at which the control system has to operate has formed a serious challenge. At that time, a shearing interferometer was used to measure the wavefront. Similar to the SHS described above, this sensor also does not provide direct information on the wavefront phase, but via a spatial transformation. Inversion of this transformation and subsequent calculation of suitable actuator command signals are computationally costly operations, which would have taken more than a day on a contemporary computer [98]. Instead, an analog electronic circuit was designed in which measurements were introduced as controlled currents, yielding the actuator commands as measurable voltages. Although this controller structure was very inflexible, it allowed for update rates of around 1kHz, which is respectable even for today's standards.

Currently, SHSs are the most widely used and digital control systems have become sufficiently fast to do the required computations. For the future large telescopes, this will not be trivial to maintain. Digital processors may continue to increase in computational power, but this may not be sufficient. Without efficient algorithms, the required computational power increases approximately with the square of the number of actuators and thus to the fourth power in the telescope aperture. This is plotted in Figure 1.10 and based on a desired Strehl ratio of 0.87. It shows that without efficient numerical algorithms an AO system for the 42m E-ELT with over 100.000 actuators would require almost 10.000 processors each capable of 10 giga-flops. It requires a careful design for both hard- and software to achieve an efficient parallel computer system. In [59, 73, 195] control algorithms are shown with a computational complexity of $\mathcal{O}(N_a^{3/2})$. But even these would require many processors to compute the setpoints for the 100.000 actuators at a rate of 1kHz.

Besides computational problems, increasing the number of actuators yields many practical problems. Usually the actuation has at least two connection wires. In case of 100.000 actuators, this leads to 200.000 wires and thus a large probability of defects, disturbances, etc. To keep the lengths of these wires to a minimum and obtain a straightforward multi-processor hardware architecture, a modular, distributed control system is proposed:

each actuator or small group of actuators is driven by a separate hardware module that has direct communication links to only a few neighboring modules. Each module receives a small fraction of the wavefront sensor measurements and all modules are identical in hardware. This allows cost efficient production of the modules, enables the straightforward construction of a control system for a new, larger AO system and quick replacement of defective modules.

By assigning computational power per actuator, the total computational power increases only linearly with the number of actuators, which is less than is required by current efficient algorithms. In [183] is shown that these algorithms are not suitable for the distributed architecture and research into new algorithms, whose prime design driver is the distributed structure, is needed. The performance achieved by the use of these algorithms is subjected to the choice for specific properties of the structure, but should approximate that of traditional, centralized architectures. These properties are what neighbors the modules can communicate with, what information they exchange and which measurements they receive. A suitable choice for these properties requires insight into how they affect the AO system's performance. More details on these issues can be found in the PhD thesis of Rogier Ellenbroek [183]. The temporal part of the traditional controller is an integrator structure that despite its limited tuning freedom usually yields sufficient performance. Firstly because the frequency content of the wavefront disturbance can be well approximated by a first order low-pass characteristic. Secondly because the high gain of an integrator at low frequencies provides the means to compensate mismatches between the real DM and the model used.

1.4 Problem formulation and outline

Existing large and future even larger telescopes can only be utilized to the full extend, when they are equipped with AO systems that enhance the telescopes resolution to the diffraction limit. The development of new DM technology that meets these requirements is therefor essential. This thesis will focus on the design, realization and testing of a new DM that is extendable and scalable in mechanics, electronics and control. Since this thesis is a result of a joint research project there is an accompanied thesis, by Rogier Ellenbroek, on the development of a distributed control framework. In Chapter 2 the requirements will be deduced based on typical atmospheric turbulence conditions. The requirements are made quantitative and the design concept is presented. Chapter 3 will focus on the deformable element, the facesheet. The design, realization and testing of the actuators and dedicated driver electronics is presented in Chapter 4 and Chapter 5. In Chapter 6 results of a 61 actuators and a 427 actuators prototype will be presented and validated on developed models. Finally in Chapter 7 conclusions and recommendations will be given.

Design requirements and design concept

The main requirements for the adaptive deformable mirror and control system are derived for typical atmospheric conditions. The spatial and temporal properties of the atmosphere are covered by the spatial and temporal spectra of the Kolmogorov turbulence model and the frozen flow assumption. The main sources for the residual wavefront aberrations are identified. The fitting error, caused by a limited number of actuators and the temporal error, caused by a limited control bandwidth, are considered to be the most important for the mirror design. A balanced choice for the number of actuators and the control bandwidth is made for a desired optical quality after correction. Then the actuator requirements are defined, such as the pitch, total stroke and inter-actuator stroke, resolution and power dissipation. Requirements are derived for the control system and the electronics. Finally, the full DM system design concept is presented, consisting of the thin mirror facesheet, the mirror-actuator connection, the actuators, the control system, the electronics and the base frame.

2.1 Requirements

The goal is to make a DM that can correct a wavefront of an 8-meter telescope in visible light, which is aberrated by atmospheric turbulence to the diffraction limit. The mirror's main requirements will be derived from the spatial and temporal properties of typical atmospheric conditions as they exist on astronomical sites such as Cerro Paranal in Chile. These conditions will be shown to determine the number of actuators, the (inter) actuator stroke and the control bandwidth. Further, the mirror should have low roughness and high reflection for the wavelengths utilized and be functional in a temperature range between $-10\,^{\circ}\mathrm{C}$ and $30\,^{\circ}\mathrm{C}$ [87].

The mirror surface may not heat up more than 1K relative to the environment to prevent the deformable mirror itself to become a significant heat source. Finally, the number of sensors and actuators in the AO system will be of such order of magnitude that efficient control algorithms are required to prevent problems in the realization of suitable computation hardware. Known efficient control algorithms such as proposed in [59, 73, 130, 196] exploit the structure present in a system to obtain efficient implementations. For AO applications, such algorithms exploit sparsity or spatial invariance of the DMs influence matrix and generally comprehend its temporal dynamics only in terms of a number of samples delay. The DM to be designed should behave accordingly up to a sampling time scale defined in Section 2.4.

2.1.1 Atmospheric turbulence

In Section 1.1 it is explained that refractive index variations of the atmosphere cause wavefront aberrations. Based on the work of Edlén [57] several contributions have been made to describe the dependence of the refractive index n_{air} on temperature, pressure, humidity and CO_2 -concentration [13, 39, 114, 142, 148]. Many different formulations exist, which are often aimed at specific wavelength of interest. Because of the weak dependence on the relative humidity (for vertical propagation through the atmosphere) and CO_2 -concentration, these are often neglected [98]. The dependence of the refraction index on pressure and temperature is given by [44]:

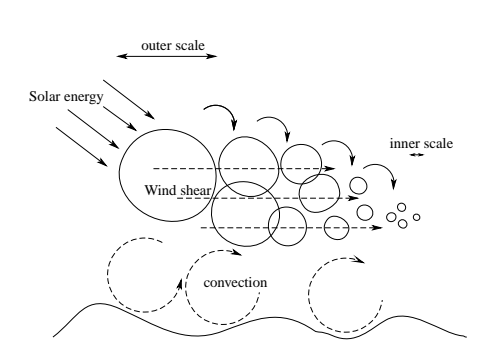
$$n_{air} = 1 + 7.76 \cdot 10^{-5} \frac{P}{T} \left(1 + \frac{7.52 \cdot 10^{-3}}{\lambda^2} \right)$$
 (2.1)

Where P is the pressure in millibars, T the temperature in K and λ the wavelength in microns. As a result of the change in the refractive index some parts of the initially flat wavefront are advanced and some parts of the wavefront are retarded.

2.1.2 The Kolmogorov turbulence model

The work of Kolmogorov in 1941 [117] formed the basis for currently used atmospheric turbulence models. Kolmogorov concluded that in a turbulent flow the kinetic energy is fed into the system at the outer scale L_0 and decreases till it is dissipated in heat at the smallest, inner scale l_0 . The outer scale corresponds to the radius of the largest air bubbles and the inner scale to that of the smallest. Outside the outer scale the isotropic behavior of the

2.1 Requirements 17



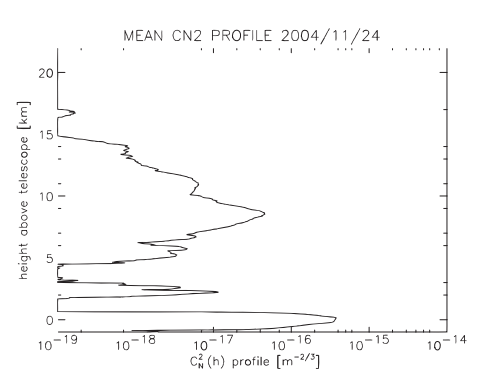


Figure 2.1: Schematic of Kolmogorov turbulence. Energy is fed into the system at the outer scale and cascades till dissipated in heat at the inner scale.

Figure 2.2: A typical profile measured with a SCIDAR instrument at Mt. Graham (profile taken from S.E.Egner [58]).

atmosphere is violated and inside the inner scale viscous effects are dominant and kinetic energy is dissipated in heat. This is schematically shown in Figure 2.1.

Spatial model of atmospheric turbulence

Kolmogorov described the random movement of the wind with statistical quantities by means of structure functions. Structure functions describe the mean squared difference between two randomly fluctuating values. With the assumption that the atmosphere is locally homogeneous, isotropic and incompressible he concluded from a dimensional analysis that the kinetic energy decreases with the spatial frequency to the power $-\frac{5}{3}$. Tatarski [182] related Kolmogorov's velocity structure function to the index of refraction structure function $D_n(h,r)$ given by:

$$D_n(h,r) = \langle |n(h,r') - n(h,r'+r)|^2 \rangle$$

= $C_N^2(h)r^{\frac{2}{3}}$, for $l_0 \ll r \ll L_0$

where $\langle \rangle$ denotes the variance of the enclosed expression at height h and distance r. $C_N^2(h)$ is used to take into account the atmospheric turbulence contributions from all altitudes above the telescope. Figure 2.2 gives a typical $C_N^2(h)$ profile. From this refractive index structure function profile it becomes clear that the ground layer and the high wind speed at the jet stream at about 10 km height strongly contribute to the wavefront aberrations.

To quantify the effect of variations in index of refractions in terms of wavefront phase, another structure function is used: the phase structure function $D_{\phi}(r)$. For the values of the phase ϕ at any two points in the wavefront that are separated by a distance r this structure function is given by [98]:

$$D_{\phi}(r) = \langle |\phi(r',t) - \phi(r'+r,t)|^2 \rangle,$$

$$= 2.91 \left(\frac{2\pi}{\lambda}\right)^2 \frac{1}{\cos(\zeta)} r^{\frac{5}{3}} \int_0^\infty C_N^2(h) dh,$$

$$= 6.88 \left(\frac{r}{r_0}\right)^{\frac{5}{3}}$$
(2.2)

where ζ is the angle with zenith and r_0 is the Fried parameter defined as:

$$r_0 = \left[0.423 \left(\frac{2\pi}{\lambda} \right)^2 \frac{1}{\cos(\zeta)} \int_0^\infty C_N^2(h) dh \right]^{-\frac{3}{5}}.$$

The Fried parameter r_0 is the characteristic spatial scale, which for λ =550nm typically ranges between 5 and 20cm [98]. The Fried parameter corresponds to the aperture diameter D_t of a telescope for which the variance σ_{wf}^2 of the wavefront aberrations is roughly 1 rad². This variance can be expressed as [141]:

$$\sigma_{wf}^2 = 1.03 \left(\frac{D_t}{r_0}\right)^{\frac{5}{3}} \tag{2.3}$$

Other important statistics are described by the spatial Power Spectral Density (PSD), which is a measure for the relative contribution of aberrations with spatial frequency $\kappa = \sqrt{\kappa_x^2 + \kappa_y^2 + \kappa_z^2}$ to the total wavefront distortion. For the Kolmogorov turbulence model this is given by [141]:

$$\begin{split} &\Phi(\kappa,h) = 0.033 C_N^2(h) \kappa^{-\frac{11}{3}}, \\ &\Phi(\kappa) = 0.023 r_0^{-\frac{5}{3}} \kappa^{-\frac{11}{3}} \quad \text{(assuming isotropy)}. \end{split} \tag{2.4}$$

This spatial PSD is often truncated at the outer and inner scale of the turbulence in which the Kolmogorov model is valid. This is mostly done using the Von Karmann model:

$$\Phi(\kappa) = \frac{0.023r_0^{-\frac{5}{3}}}{(\kappa^2 + \kappa_0^2)^{\frac{11}{6}}} \exp\left(-\frac{\kappa}{\kappa_i}\right)^2$$
 (2.5)

where $\kappa_o = 2\pi/L_0$ corresponds to the boundary set by the outer scale L_0 and $\kappa_i = 5.92/l_0$ corresponding to the lower boundary set by the inner scale l_0 . The outer boundary is in the order of tens of meters [42] and the inner scale is in the order of tens of millimeters [56, 122]. The outer scale constrains the lower order wavefront distortions. Since these are dominant, the outer scale also determines the total stroke requirements for the actuators in adaptive mirrors. Knowledge of the outer scale at a certain telescope location for ELTs is therefore of great importance. For intensity variations (scintillation) the inner scale is more relevant. In Figure 2.3 the Kolmogorov PSD defined by Equation (2.4) and the Von Karmann PSD defined by Equation (2.5) is shown.

Temporal model of atmospheric turbulence

In analogy with the refractive index structure function a temporal structure function $D_{\phi}(\delta t)$ can be defined between two wavefront phase values separated in time by δt :

$$D_{\phi}(\delta t) = \langle |\phi(r,t) - \phi(r,t+\delta t)|^2 \rangle,$$

2.1 Requirements

19

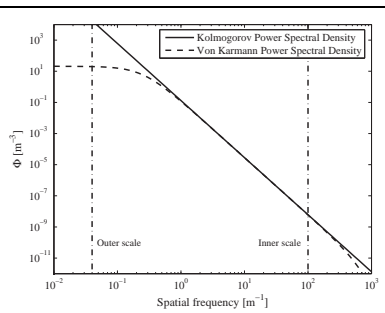


Figure 2.3: The spatial PSDs of the wavefront aberrations for the Kolmogorov and Von Karmann turbulence models.

where $\langle \cdot \rangle$ denotes the variance of the enclosed expression over space (r) and time (t). Under the assumption that the wavefront aberrations are fixed and turbulence layers at altitude h are moving with a wind speed v(h) over the telescope aperture – the frozen flow assumption – the temporal structure function can be expressed in the spatial frequency κ as [41]:

$$D_{\phi}(v,\kappa) \propto \int_{0}^{\infty} \frac{1}{v(h)} \left(\frac{\kappa}{v(h)}\right)^{-\frac{8}{3}} C_{N}^{2}(h) dh.$$

This function integrates the effect of all turbulence layers. When this integration is performed for a single turbulent layer at altitude h of thickness δh traveling with a wind speed v_w , the temporal power spectrum P of the phase value ϕ observed at a certain point in space can be expressed in terms of the temporal frequency f as:

$$P(f,h) \propto C_N^2(h) \frac{\delta h}{v_w} \left(\frac{f}{v_w}\right)^{-8/3}$$
.

This -8/3 power law is often used in the context of controller design for AO [98, 187], where integrator structures approximate the -8/3 power law by -2.

In the previous paragraph, the characteristic spatial scale r_0 was introduced to quantify the spatial variance of atmospheric turbulence. A similar value exists that describes the characteristic timescale for changes in wavefront aberrations [160]: the coherence time τ_0 . Various definitions exist [27, 187], but let it here be defined as the time for wind to carry frozen flow turbulence over an aperture of size r_0 . Based on the mentioned assumptions, this would imply that the wind speed is indicative of the coherence time τ_0 . This is in fact the case, even though the validity of the frozen flow assumption is questionable: it is e.g. shown in [48, 160] that the so-called boiling effect plays a major role in the evolution of phase errors on the timescales of practical interest. Let the coherence time τ_0 be expressed through its inverse, the Greenwood frequency f_G [78]:

$$f_G = \frac{1}{\tau_0} = 2.31\lambda^{-\frac{6}{5}} \left[\frac{1}{\cos(\zeta)} \int_0^\infty C_N^2(h) v^{\frac{5}{3}}(h) dh \right]^{\frac{3}{5}}.$$

For a single turbulence layer with constant wind speed v_w the Greenwood frequency can be approximated as:

$$f_G = 0.43 \frac{v_w}{r_0}.$$

For representative values of the wind velocity $v_w=10 {\rm m/s}$ and the Fried parameter $r_0=0.166 {\rm m}$ the Greenwood frequency is approximately 25Hz. Since the Greenwood frequency

is a measure for the rate of change of the wavefront distortion, it is related to the required control bandwidth of an AO system.

2.2 Error budget

The atmospheric conditions and the desired optical quality after correction are the main design drivers for the AO system. They determine the number of actuators and the control bandwidth. The optical quality is often expressed by a Strehl-ratio S. This ratio can be related to the variance σ^2 of the wavefront measured in radians using the extended Maréchal approximation [15, 98, 187]:

$$S \approx e^{-\sigma^2}$$

This approximation is valid up to $\sigma=2\mathrm{rad}$ [98]. For the design of the DM the practical limit to the diffraction limited level is set at a Strehl ratio of 0.85. This leads to a total error budget of $\sigma\approx\frac{2\pi}{16}\mathrm{rad}$, which for $\lambda=550\mathrm{nm}$ corresponds to $550/16\approx34\mathrm{nm}$. Assuming that all error sources are independent, the total variance can be approximated as the sum of the variances corresponding to the main contributing sources:

$$\sigma^2 = \sigma_{fit}^2 + \underbrace{\sigma_{temp}^2 + \sigma_{meas}^2 + \sigma_{delay}^2}_{\sigma_{tel}^2} + \sigma_{angle}^2 + \sigma_{cal}^2. \tag{2.6}$$

The fitting error σ_{fit} arises from the limited number DOF of the DM and thus the limited number of spatial frequencies that it can correct. The temporal error σ_{temp} is due to the limited control bandwidth of the AO-system.

If the light source used for wavefront sensing (i.e. the reference star), is not the same as the object for which the correction is used (the science object), a so called anisoplanatic error is made. The variance of this error is related to the angle θ_a by which the two objects are separated as $\sigma_{angle}^2 \propto \theta_a^{5/3}$. Further, σ_{meas}^2 covers all the measurement errors (e.g. measurement noise in the wavefront sensor) and σ_{delay}^2 the errors due to delays in the wavefront sensor and the controller. As will be discussed in Section 2.4, a closed loop controller influences not only the temporal, but also the measurement and delay related errors, hence in Equation (2.6) the combination of these sources is related to the controller and denoted σ_{ctrl}^2 . Finally, σ_{cal}^2 consists of all calibration errors. Calibration is needed for the correction of static aberrations that are not seen by the wavefront sensor and are called Non Common Path Aberrations (NCPAs) [166]. A good review of the main errors in an AO system can be found in [98]. Since a large part of the total error budget is consumed by σ_{fit}^2 and σ_{temp}^2 which both can be influenced by the DM and controller design, the other error sources will further be neglected. The fitting and temporal errors will be considered in the next two paragraphs to derive requirements for inter-actuator stroke and control bandwidth.

2.2 Error budget 21

2.2.1 The fitting error

The variance of the fitting error can be approximated by [98]:

$$\sigma_{fit}^2 = \kappa_f \left(\frac{d_t}{r_0}\right)^{\frac{5}{3}},\tag{2.7}$$

where d_t is the inter actuator distance projected onto the primary aperture and r_0 the Fried parameter. The fitting error coefficient κ_f depends on the type of mirror that is used:

$$\kappa_f = \begin{cases} 1.26 & \text{for segmented mirrors with only piston correction,} \\ 0.18 & \text{for segmented mirrors with tip, tilt and piston correction,} \\ 0.28 & \text{for membrane mirrors.} \end{cases}$$

In [125] it is shown that for piston, continuous face-sheet and membrane mirrors for an equal number of actuator the correction quality does not significantly depend on the actuator geometry as long as the actuator distribution is fairly homogenous. This means that Equation (2.7) gives an estimate for the fitting error variance to be expected for a specific DM on a telescope with known diameter at a site with a certain r_0 . Although κ_f given above is the smallest for segmented mirrors with tip, tilt and piston correction, this type of mirror has three actuators per segment whereas the inter actuator distance d_t is assumed to be the segment size. For a more fair comparison, let the fitting error be expressed in terms of the total number of actuators N_a , which can be achieved by writing the inter actuator spacing d_t as a function of N_a . For piston and membrane type mirrors, the inter actuator spacing can be approximated as $d_t \approx D_t/2\sqrt{\pi/N_a}$, whereas for segmented mirrors with piston, tip and tilt correction the number of actuators must be scaled by three, yielding $d_t \approx D_t/2\sqrt{3\pi/N_a}$. After substitution into Equation (2.7), σ_{fit}^2 can thus alternatively be expressed as:

$$\sigma_{fit}^2 = \kappa_{f,N_a} D_t \left(\frac{\sqrt{\pi/N_a}}{r_0} \right)^{5/3},$$

where

$$\kappa_{f,N_a} = \begin{cases} 0.63 & \text{for segmented mirrors with only piston correction,} \\ 0.23 & \text{for segmented mirrors with tip, tilt and piston correction,} \\ 0.14 & \text{for membrane mirrors.} \end{cases}$$

This implies that for the same number of actuators, the fitting error is the smallest for a membrane type mirror.

2.2.2 The temporal error

Although in practice the temporal error depends on all components of the AO system as well as on actual atmospheric conditions, Greenwood [78] showed that the variance of the temporal error can be related to the Greenwood frequency f_G as:

$$\sigma_{temp}^2 = k \left(\frac{f_G}{f_c}\right)^{\frac{3}{3}},\tag{2.8}$$

where f_c is the control bandwidth and k a scaling constant. For the ideal – though unrealistic – case that the controller fully suppresses the wavefront disturbance up to the bandwidth f_c and does not affect higher frequencies, the scaling constant k is equal to 0.191. For a more realistic integrator type controller it is equal to 1, which means that Equation (2.8) gives an estimate for the temporal error to be expected for a given type of controller and a given temporal behavior of the wavefront disturbance.

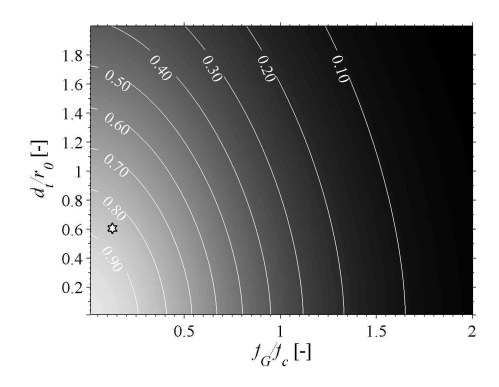
However, the derivation of this relation is based on many assumptions. Starting point is a wavefront disturbance with a Kolmogorov spectrum and a frozen flow behavior, which is corrected by a DM system that is able to track a command signal up to the bandwidth f_c . The temporal error is then defined as the servo tracking error of the DM with respect to the assumed type of wavefront disturbance. This means that the estimate of the temporal error variance in Equation (2.8) does not take into account the ability of a (closed loop) control law to reduce the detrimental effects of measurement noise or DM dynamics. It does not consider the dynamics of the wavefront sensor or delays in the disturbance signal to track. In AO literature, the latter is considered as a separate effect on the eventual performance and is quantified as the variance σ_{delay}^2 between wavefronts measured τ seconds apart [66]:

$$\sigma_{delay}^2 = 28.44 \left(f_G \tau \right)^{\frac{5}{3}}.$$

By considering control system delays as a separate source of errors, it is not taken into account that the control system can exploit spatio-temporal correlations of the wavefront distortion to make accurate short term predictions to compensate delays [104]. However, as the latter strongly depends on the atmospheric turbulence conditions, Equation (2.8) will further be used for the estimation of the expected error. Since the wavefront sensor is regarded as a given part of the AO system and delays in a controller affect its already considered bandwidth, the effect of delays will further be neglected as a separate source of errors.

2.2.3 Error budget division

If the main atmospheric parameters (r_0 and f_G) are known for a specific telescope location and only the fitting and temporal errors are considered, the actuator spacing d_t and control bandwidth f_c can be related to a desired Strehl ratio (Figure 2.4). When also the diameter D_t of a telescope is known, the number of actuators N_a can be calculated in approximation as $N_a = \frac{\pi}{4}(D_t/d_t)^2$. For an 8-meter telescope ($D_t = 8$ m), Figure 2.5 shows the Strehl ratios for the number of actuators N_a and control bandwidth f_c based on $f_G = 25 \mathrm{Hz}$ and $r_0 = 0.166$ m (λ =550nm). Observe from Figures 2.4 and 2.5 that the same Strehl ratio can be achieved by different combinations of control bandwidth f_c and number of actuators N_a . According to Figure 2.5 the effect of increasing the number of actuators is limited when this it not matched by an increase in control bandwidth and vice versa. A combination of actuator count and control bandwidth should be chosen for which the fitting and temporal errors are approximately equal. For a desired Strehl ratio of 0.85 this leads to a combination of 5000 actuators and 200Hz control bandwidth, which is marked by a white star in Figures 2.4 and 2.5. The corresponding RMS fitting and temporal errors are $\sigma_{fit} = \sqrt{0.28} (D_t / \sqrt{4N_a / \pi} / r_0)^{5/6} = 0.34$ rad and $\sigma_{temp} = \sqrt{f_G / f_c} = 0.17$ rad, which for $\lambda = 550$ nm corresponds to 30nm and 15nm respectively.



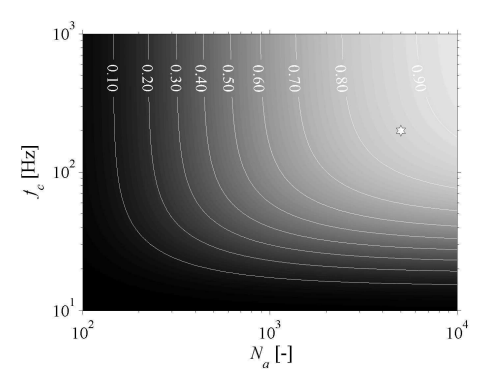


Figure 2.4: The Strehl ratio as function of the relative actuator density d_t/r_0 and control bandwidth f_G/f_c .

Figure 2.5: The Strehl ratio as function of the number of actuators N_a and control bandwidth f_c based on $D_t = 8m$, $r_0 = 0.166m$ and $f_G = 25Hz$.

2.3 Actuator requirements

Before stating the requirements for the actuators, it should be noted that the Optical Path Difference (OPD) of the light is the double of the facesheet displacement. This is explained in Figure 2.6 and implies that the magnitude of the mirror deflection required to correct a wavefront needs to be half the magnitude of the wavefront unflatness. For the nearly diffraction limited correction of an 8 meter telescope in the visible part of the light spectrum the main requirements for the actuators are as follows:

• Mirror diameter and actuator spacing Given a number of actuators N_a , the actuator spacing depends on the diameter of the DM. The location of a DM is not restricted to a single position in the optical path of a telescope system. Because of the dynamic requirements and the ease of manufacturing, usually a flat surface with a smaller diameter is chosen. The lower limit is set by the Smith-Lagrange invariant. This optical invariant is explained in Figure 2.7 and states that at all cross-sections in the optical path the product $D\Theta$ is constant. Herein is D the illuminated diameter or the envelope of all rays and Θ the

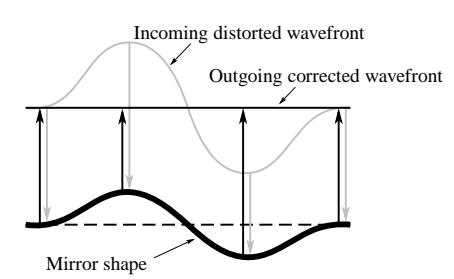


Figure 2.6: The magnitude of the mirror deflection required to correct a wavefront needs only be half the magnitude of the wavefront unflatness because the deflection distance of the mirror is traveled twice. The summed lengths of all pairs of black and grey arrows are equal.

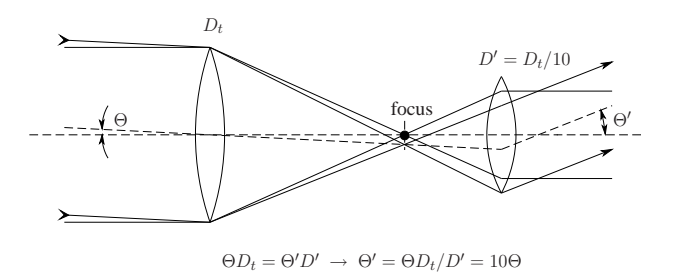


Figure 2.7: The optical Smith-Lagrange invariant, which states that at all cross-sections in the optical path the product $D\Theta$ is constant. D is herein the illuminated diameter, the envelope of all rays and Θ the angle between the optical axis and the chief (outer) ray. When D increases, Θ must decrease and vice versa.

angle between the optical axis and the chief (outer) ray of the beam. At the primary mirror of this telescope the invariant is equal to $D_t\Theta$, where Θ equals the Field Of View (FOV) and at apertures further along the optical path the angle Θ' will become $\Theta' = \Theta D_t/D'$. To keep Θ' within realizable values for e.g. the 8m VLT with a half degree FOV and the 42m E-ELT with 10 degree FOV, a realistic lower bound for the DM diameter lies in the order of 500mm. This will be chosen as a starting point in the design. With the 5000 actuators this defines a $500 \cdot 10^{-3}/\sqrt{4 \cdot 5000/\pi} \approx 6$ mm actuator spacing.

• Total actuator stroke

The total actuator stroke can be derived using Equation (2.3) describing the RMS unflatness of the wavefront. With $D_t=8\mathrm{m}$ and $r_0=0.166\mathrm{m}$ (λ =550nm) this gives $\sigma_{stroke}^2=\sigma_{wf}^2=1.03(D_t/r_0)^{5/3}=657\mathrm{rad}^2$. The square root of this variance relates to the RMS actuator position, whereas in fact the Peak To Valley (PTV) value is sought that forms the total actuator stroke. For AO applications the RMS and PTV values are often related via a scaling factor 5, yielding a total actuator stroke of $5\cdot\sqrt{657}=128\mathrm{rad}$. Considering the reflection doubling the OPD (Figure 2.6) for $\lambda=550\mathrm{nm}$, this corresponds to a required actuator stroke of $\lambda/2\pi\cdot128/2=\pm5.6\mu\mathrm{m}$. In addition to this stroke a few $\mu\mathrm{m}$ are added to be able to deal with misalignment of the DM in the optical system.

• Inter actuator stroke

The inter actuator stroke can be calculated using the structure function in Equation (2.2) describing the mean square difference between two wavefront phase values separated by a distance r. Substitution of $r=d_t$ and using $r_0=0.166$ m (λ =550nm) then yields the required mean square inter-actuator stroke as $\sigma_{ia}^2=6.88(d_t/r_0)^{5/3}=2.8\cdot 10^{-2} {\rm rad}^2$. Using the factor 5 between the RMS and PTV strokes, the latter becomes $5\cdot \sqrt{2.8}=8.3 {\rm rad}$. Due to the reflection doubling the OPD (Figure 2.6) for $\lambda=550 {\rm nm}$ this corresponds to a required inter-actuator stroke of $\pm 0.36 {\rm \mu m}$.

Actuator resolution

The actuator resolution should be well below the error budget as derived in Section 2.2 of $\frac{2\pi}{16}$ rad (for $\lambda=550$ nm this is 34nm RMS). The design value for the actuator displacement resolution is therefore set significantly smaller at 5nm.

· Power dissipation

To avoid the need of active cooling, all energy dissipated in heat should be convected from the mirror surface by natural convection. The temperature difference between the mirror surface and the surrounding air of 1K is usually allowed. A typical value for the heat transfer coefficient h_n is $1 < h_n < 40 \text{W/m}^2$ [10]. Using $h_n = 12 \text{W/m}^2$ and 5000 actuators on the \varnothing 500mm DM, this allows for $\approx 0.5 \text{mW}$ per actuator. Assuming that only half of the heat dissipated in the actuators is transferred to the mirror surface, the maximum heat dissipation per actuator is set to $\approx 1 \text{mW}$.

Dependence on telescope diameter D_t

Observe that according to Equation (2.7) and Equation (2.8) an increase of the telescope diameter D_t only affects the fitting error variance σ_{fit}^2 and not the temporal error variance σ_{temp}^2 . To maintain the desired Strehl ratio, the actuator spacing d_t must therefore remain constant and the number of actuators N_a must increase with D_t^2 . For the E-ELT this would result in $5^2 \cdot 5000 = 625000$ actuators.

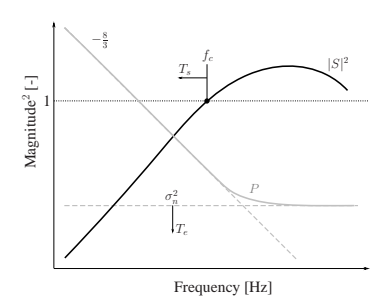
However, Equation (2.7) and Equation (2.8) do not consider any beneficial effects that a scale increase may have on the achievable controller error σ_{ctrl} . For instance, a larger number of correlated sensor inputs may lead to better short term predictions and a lower sensitivity to measurement noise. It is therefore likely that the actual number of actuators required at the E-ELT for the same Strehl ratio is smaller.

2.4 Control system and electronics requirements

The goal of the control system is to calculate suitable actuator commands based on wavefront sensor measurements. The AO system performance ultimately depends on the accuracy with which the control system can match the mirror shape to half that of the actual wavefront disturbance. In Section 2.2.3 a desired control bandwidth of 200Hz was specified. As a rule of thumb this requires a sampling frequency f_s at least five times higher, i.e. $f_s \approx 1 \, \text{kHz}$. This rule of thumb is based on classical control theory of a Single-Input Single-Output (SISO) system, where it is assumed that the loop gain has a first order roll-off and thus -90° phase lag around the bandwidth. The sampling (Zero Order Hold (ZOH) plus delay) at $1 \, \text{kHz}$ adds another 72° at the bandwidth of $200 \, \text{Hz}$, leaving an 18° phase margin. Although this reasoning does not directly apply to general Multi-Input Multi-Output (MIMO) systems, it is used for AO systems under the assumption that the loop gain is diagonalized – i.e. decoupled into SISO systems – by the inverse DM influence matrix.

However, the sampling frequency cannot exceed the frame rate of the CCDs camera in the wavefront sensor. For current state-of-the-art devices 1kHz is a realistic rate, but as this leads to very short exposure times, measurement noise becomes more significant. The

Figure 2.8: Influence of sampling time T_s and exposure time T_e . The black line represents $|S(2\pi f)|^2$ and the grey line the disturbance spectrum P(f) that has a horizontal asymptote on the measurement noise level σ_n .



variance σ_n^2 of the measurement noise of a SHS consists of several components that are related to the exposure time T_e in various ways. For instance, photon noise is attenuated by increasing T_e , whereas dark current and read-out noise are attenuated by decreasing it [109, 110, 140]. When measurement noise becomes significant for $T_e \leq T_s$ and its variance is added to the temporal error variance in Equation (2.8), this sum may not strictly decrease with the sampling frequency f_s . This can be illustrated using Figure 2.8, which sketches the disturbance spectrum P(f), white measurement noise with variance σ_n^2 and a disturbance rejection characteristic of sensitivity function $|S(2\pi jf)|^2$ of the control system. Assuming the AO system to be Linear Time-Invariant (LTI), the disturbance suppression characteristic $S(2\pi i f)$ is the transfer function between disturbance and residual error. The external disturbance acting on the control loop does not only include the wavefront disturbance with temporal spectrum P(f), but also the measurement noise with variance σ_n^2 . In contrast to the servo tracking point of view that forms the basis for the temporal error variance discussed in Section 2.2.2, a realistic disturbance suppression characteristic $|S(2\pi jf)|$ is here used that includes the effect of loop delays and obeys the Bode-sensitivity integral. This integral states that the disturbance rejection at low frequencies must be matched by amplification at higher frequencies.

When the filter $S(2\pi jf)$ is applied to a disturbance signal with temporal spectrum $P(f) + \sigma_n^2$, the output (i.e. the residual error) spectrum can be expressed as $|S(2\pi jf)|^2(P(f)+\sigma_n^2)$. Using Parseval's theorem, the control error variance σ_{ctrl}^2 introduced in Equation (2.6) on page 20 can then be expressed as:

$$\sigma_{ctrl}^2 = \int_{0}^{\infty} |S(2\pi jf)|^2 \left(P(f) + \sigma_n^2\right) df.$$

Now let this be applied to Figure 2.8. Accordingly, a decrease of the sampling time T_s may lead to an increased bandwidth f_c , but also to an increased disturbance amplification at high frequencies and since $0 < T_e \le T_s$ also to higher measurement noise σ_n . As a result, the error variance σ_{ctrl} may not diminish by a decrease of T_s . The same error may be achieved using various choices for T_s and T_e .

In fact, the T_e and T_s form control loop delays, as do communication delays and computation time. In contrast to the exposure time, a reduction of the communication delays or computation time will always be beneficial to performance. However, communication speeds have limits and more computational power will result in limited performance gain at significant costs. A detailed specification of T_e and T_s is complicated by the fact that the

measurement noise σ_n and read-out time are highly device specific, whereas the WFS is not included in the AO system to be designed. Moreover, model based controller designs are able to predict (to some extent) future wavefront disturbances and so compensate for loop delays. In an optimal controller design the effects of measurement noise are also minimized with respect to some – usually a quadratic – cost function. The noise residual then becomes dependent also on the DM dynamics and the accuracies of the models used.

Due to these a priori unknowns, the temporal error variance in Equation (2.8) will further be used to express the worst case error. An indicative sampling time of $T_s=1 \mathrm{ms}$ will be assumed, equal to the exposure time T_e and communication and computation delays are assumed to be small compared to T_s . This leads to a total loop delay of 1 sample or 1 ms. As discussed in [67, 68], the best performance is obtained when the number of measurement positions of the wavefront sensor is proportional to the number of actuators. In the supplied references the location of the actuators with respect to the wavefront sensors is not explicitly analyzed, whereas it is known from control theory that performance may degrade

supplied references the location of the actuators with respect to the wavefront sensors is not explicitly analyzed, whereas it is known from control theory that performance may degrade when actuators and sensors are not collocated. On the other hand, the gradient measurement concept of a SHS versus the deflection based DM actuation already clouds the notion of collocation.

Nevertheless, for a SHS with two measurements per lenselet, it will be assumed that the number of measurements N_s is approximately equal to twice the number of actuators N_a . The total processing power of the control system must then be sufficient to evaluate the command update equations from ~ 10000 measurements to 5000 command signals within a fraction of the sampling time T_s of 1ms. This also involves the processing of the CCD of the SHS image to obtain the actual gradient measurements [110, 184]. A detailed discussion can be found in [183].

The displacement of each actuator is changed by a current through the actuator coil. This current will be generated by dedicated electronics with sufficient accuracy to meet the specified 5nm actuator position accuracy. Further, the dynamics introduced by these driver electronics should not affect the lowest eigenfrequency or rise time of the system that may lead to a lower achievable control bandwidth.

2.5 The design concept

The design concept for the adaptive deformable mirror that meets the requirements, as listed in the previous sections, is schematically given in Figure 2.9. The design concept is based on [83]. In the design a few layers are distinguished, which will be discussed in more detail:

- the mirror facesheet,
- the actuator grid,
- the base frame.

The first layer consists of the thin reflective facesheet, which is the deformable element. The facesheet is continuous and stretches out over the whole mirror. In the underlying layer - the actuator grid - low voltage electro-magnetic push-pull actuators are located. The actuator grid consists of a number of identical actuator modules. Each actuator is connected via

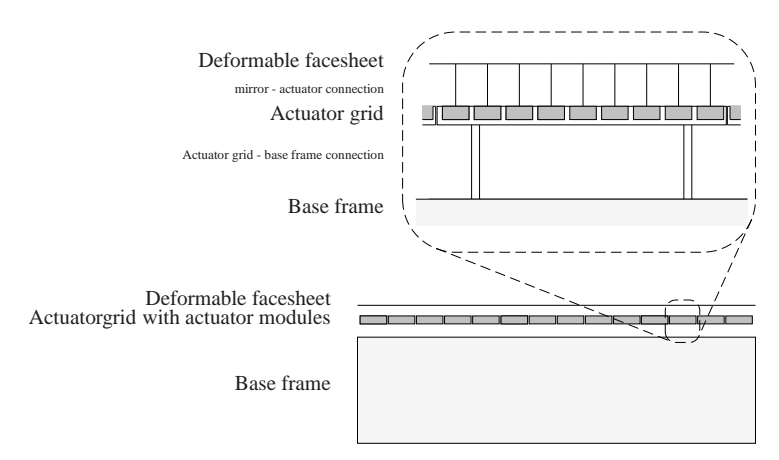


Figure 2.9: Schematic of the adaptive deformable mirror design.

a strut to the mirror facesheet. The mirror facesheet, the mirror-actuator connection and the actuator modules form a thin structure with low out-of-plane stiffness so a third layer is added, the base frame, to provide a stable and stiff reference plane for the actuators. This base frame is a mechanically stable and thermally decoupled structure. Besides these distinguished layers a control system and electronics is present which is also described briefly.

2.5.1 The mirror facesheet

A membrane-type mirror is chosen because of its low moving mass and low out-of-plane stiffness. This results in low actuator forces and the best wavefront correction for a given number of actuators (Section 2.2.1). Because of the low out-of-plane stiffness of the thin facesheet, the inter-actuator coupling and the width of the influence functions can be kept small. This is desirable for currently available efficient control algorithms [59, 73, 196] and facilitates the implementation of a distributed control system [183]. Finally, the limited thickness leads to a short thermal time constant that allows for quick adaptation to changing environmental temperatures.

The mirror-actuator connection

The connection between the actuators and the mirror facesheet is made by struts. Via these struts, the actuators impose the out-of-plane displacements on the facesheet. The struts constrain one DOF since their bending stiffness is significantly lower than the local bending stiffness of the facesheet. Because the struts leave the ϕ and φ rotation free, the bending stiffness of the facesheet can form a smooth surface through the imposed z-positions, as is shown schematically in Figure 2.11. The piston-effect, shown schematically in Figure

2.10 is thereby avoided. As a result no higher order aberrations are introduced into the wavefront.

The struts neither constrain the x- and y-positions of the mirror facesheet. Differences in the thermal expansion coefficient of the facesheet material and the actuators and/or a temperature difference between them is therefore possible without unwanted deformation of the mirror surface. The struts are glued with small droplets to both the mirror facesheet as the actuators.

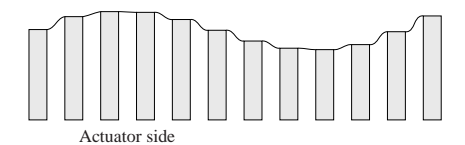
The mirror facesheet and mirror-actuator connection is discussed in detail in [84–87] and in Chapter 3 of this thesis.

2.5.2 The actuator modules

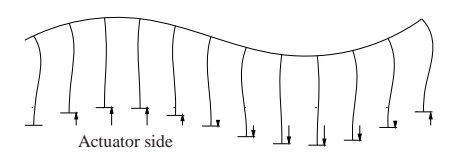
Because a large number of actuators is needed it is attractive to produce actuator arrays with a layer based construction instead of single actuators, where each of them is positioned with respect to its neighbors. Therefore, a standard actuator module with 61 low voltage electromagnetic actuators in hexagonal arrangement is designed. More than 80 of such actuator modules are needed for a DM with 5000 actuators. Figure 2.12 shows the mirror facesheet with the mirror-actuator connections and the working principle of the actuators in schematic. The actuators are of the variable reluctance type and consist of a closed magnetic circuit in which a PM provides static magnetic force on a ferromagnetic core that is suspended in a membrane. This attraction force is influenced by a current through a coil, which is situated around the PM to provide movement of the core. Figure 2.12 shows that with the direction of the current the attractive force of the PM is either increased or decreased, allowing movement in both directions.

The efficient actuators are free from mechanical hysteresis, friction and play and therefore have a high positioning resolution with high reproducibility. The stiffness of the actuator is determined by the membrane suspension and the magnetic circuit. There exists a large design freedom for both. The stiffness of the actuators is chosen such that, if one should fail, no hard point will form in the mirror surface.

The coil wires are soldered to a flex foil. This flex foil is connected to a Printed Circuit Board (PCB) with dedicated electronics for 61 actuators. Each actuator module is connected



Actuator - facesheet connections with high bending stiffness



Actuator - facesheet connections with low bending stiffness

Figure 2.10: A connection, between the actuators and the facesheet, with high bending stiffness constrains the local ϕ - and φ -rotation in the mirror surface, causing local flattening.

Figure 2.11: A connection, between the actuators and the facesheet, with low bending stiffness results in a smooth surface and allows lateral expansion between the facesheet and the actuators.

to the base frame via three A-frames. The actuator grid is scalable, so the actuator pitch can be chosen freely and extendable since many modules can form large grids of actuators. The actuator module design is described in [90–93] and in Chapter 4 of this theses.

2.5.3 The control system and electronics

To make the control system and the electronics of the AO system extendable without a full redesign, a modular structure is foreseen for these components. Each grid of 61 actuators is given a dedicated electronics module to supply each actuator with its current. These modules include 61 PWM drivers implemented using FPGAs and 61 2^{nd} order analog lowpass filters. For the DM prototypes, the FPGAs receive their setpoint updates from a PC via a custom designed, multi-drop LVDS communication link (Chapter 5). A distributed control system is to be implemented in the FPGAs of the electronics modules [183]. These modules communicate with a limited number of neighboring modules instead of the complete set, corresponding to a centralized controller.

This architecture has consequences for the controller design, which is discussed in detail in [183].

2.5.4 The base frame

To support the 80 actuator modules, a light and stiff and thermally stable base frame has been designed. The diameter of this support structure is 500mm, its height 150mm and its mass 5kg with a first mechanical resonance frequency of 1kHz. This base frame is a welded hexagonal box with ribs made of 2mm thick aluminium plates. The cover of the box is a 25mm thick aluminium honeycomb plate, which supports the actuator modules. Aluminium is chosen because of its good thermal properties. Since the box is well ventilated, it will adapt quickly to changes in the ambient temperature and hereby expand and contract homogeneously. Finally, the box can contain the electronics for the mirror modules.

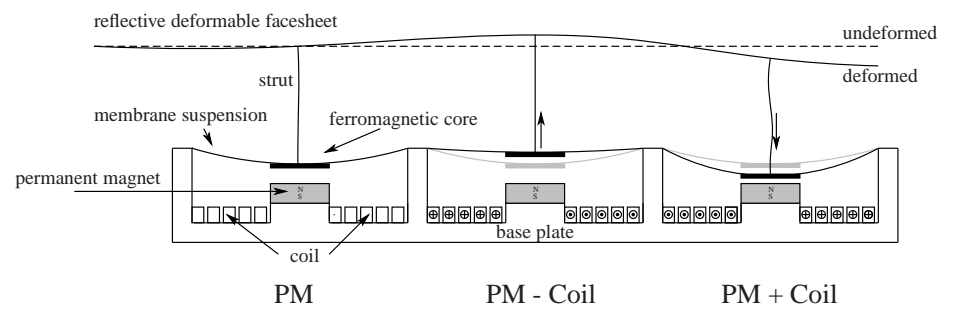


Figure 2.12: Three actuators shown in schematic.

Chapter three

The mirror facesheet

An overview of materials and fabrication techniques for thin, large scale, rigid, active and adaptive mirrors is given. The thickness of the mirror facesheet is shown to be very relevant to minimize actuator forces F_a and actuator power dissipation P_a . The scaling laws for F_a and P_a are derived, depending on the size op the uncompressed wavefront D_t , the compression factor $c_D = \frac{D_t}{D_{DM}}$, the number of actuators N_a , the thickness of the mirror t_f and Kolmogorov turbulence. To reduce power dissipation, beryllium is shown to be the favorable material for mirror facesheets. For the prototype developments, Pyrex facesheets with $100\mu \text{m}$ thickness are used as a best, practical, alternative. Three folded leafsprings constrain the in-plane DOFs of the mirror facesheet and the actuators form the out-of-plane constraints. The influence of the actuator stiffness c_a on the mirror's first resonance frequency f_e is shown. A smooth influence function is achieved by the use of connection struts between the actuators and the mirror facesheet. Tooling is developed to assemble grids of struts to the facesheet and actuators, for mirrors up to $\varnothing 200 \text{mm}$.

3.1 Overview of thin mirrors

In this section an overview is given of developments in thin, large scale mirrors. This overview is not intended to be complete, but meant to present current technologies, available and applicable for a wide range of mirror types. Static, active and adaptive, thin plate and membrane mirrors are included in this listing. Their application and main characteristics and potential usage is discussed. This section serves as a starting point in the design by creating insight in the difficulties and trivial aspects on thin, large mirrors.

3.1.1 Thin and ultra thin glass mirrors

Since the invention of the telescopes in the beginning of the 17th century, glass is used for mirrors. First used as a material for transmissive and later, with a coating applied, for reflective optics. Some of the latest developments in thin, flat and curved, static and adaptive, mirrors are summarized below.

Adaptive Secondary Mirrors

Adaptive Secondary Mirrors were briefly discussed in Section 1.2.3. ASMs are built since the '90s and today present in several telescopes. The first ASM was built for the Multiple Mirror Telescope, which is located on Mount Hopkins, Arizona and is followed by two ASMs for the Large Binocular Telescope. A fourth one is currently under development and is aimed to replace one of the four solid secondaries at the Very Large Telescope. All the ASMs have a convex glass mirror shell with a thickness of 1.5-2mm.

Production of the shell is done at the Steward Observatory Mirror Lab. Each shell starts as a thick zerodur block, that is ground to a thick meniscus. The concave side of this meniscus is then attached to a more rigid convex blocking body with a $100\mu m$ thick layer of pitch, for example Gugolz 73. Blocked on this body it is made thinner by grinding and finally polishing. The bond with pitch provides a stiff support for the polishing forces but allows the glass to relax under internal stress that may change as material is removed during the thinning process. The pitch is a visco-elastic material with a Young's modulus of ≈ 5 GPa and very high viscosity at room temperature (≈ 1 GPa·s). A 30cm stressed lap and small passive tools are used to polish the aspheric surfaces. The glass shell is released from its rigid support by heating and melting of the pitch. This is done in a slowly heated bath of oil

The surface accuracy achieved is better than 19nm RMS [129]. For the large shells with \emptyset >1m, the support and handling requires additional tooling. The smaller one, for the MMT, could still be held at the edge by a single person.

The production of an ASM is expensive and time consuming. Further thickness reduction is difficult with the increased risk on breakage. The production technique allows for strongly curved, aspheric shapes and is thereby usable to replace many existing rigid secondary mirrors.

NGST Mirror System Demonstrators

The desire for large collecting area and higher resolution is, as in ground-based telescopes, also present for space telescopes. The successor of the Hubble Space Telescope (HST), with its 2.4m monolithic primary mirror, is the James Webb Space Telescope (JWST) with a segmented primary mirror of 6.5m. The primary mirror assembly of the HST weighed $1860 \, \text{kg}$, with an areal density of $410 \, \text{kg/m}^2$ and its primary mirror weighed $830 \, \text{kg}$ with an areal density of $180 \, \text{kg/m}^2$. By comparison, the entire JWST optical telescope assembly is required to weigh less than $1300 \, \text{kg}$ and the primary mirror assembly has an areal density of $< 30 \, \text{kg/m}^2$ [173]. This has driven the development of Next Generation Space Telescopes (NGST) Mirror System Demonstrators with low areal density. A few of these designs make use of a thin glass facesheet (t $\approx 2 \, \text{mm}$), which is supported by a grid of support points, that connect the thin glass sheet to a stiff and lightweighted, non-glass structure.

At the Steward Observatory Mirror Lab a 53cm demonstrator with a 2mm zerodur shell is made. This NGST Mirror System Demonstrator (NMSD) is a concave spherical mirror with 1.5m radius of curvature, which results in a sagittal depth of 25mm. The mirror is supported by 36 actuators and connected to a carbon fiber composite support structure. The total areal density is 20kg/m^2 . The shell started as a 7cm thick zerodur block. This block is ground and polished using conventional methods while it was blocked to an 8cm thick zerodur blocking body [21].

After the 53cm prototype, a demonstrator that consists of a 2m hexagonal segment is made with an areal density of 12kg/m^2 . In this demonstrator, the shell is 2mm thick and fabricated out of a 50mm thick piece of Borosilicate. This block is squeezed on a 0.75mm layer of pitch on a blocking body. After the facesheet is released it is cut with diamond in a hexagonal. Whiffle tree supports connect the face sheet to the composite support structure. Further refinement of the NMSD design would result in an areal density of 5kg/m^2 [23].

A third mirror is developed based on the previous 53cm and 2m mirror. It has an aluminum-coated reflective glass facesheet of 1mm and is supported by 31 actuators. It was fabricated out of a 6" thick zerodur block. First the optical surface was polished and glued to a granite block of the desired curvature using pitch. Then it was reduced in thickness and as a last step loadspreaders were attached to the facesheet while it was still supported on the granite block.

Even thinner, 0.4mm thick, glass membranes were produced for adaptive mirrors [22]. Since the production process of the described NMSD is comparable to that of the ASMs, the same disadvantages are present. Because most NMSDs are not strongly curved the facesheets can be made thinner than for the ASMs.

Slumped glass membranes

Thermal shaping of glass, also referred to as 'glass slumping', brings an alternative to grinding a thin shell from a much thicker piece, which is time consuming, costly and not without risk.

With its application in the Flat Panel Display (FPD) industry, high quality, thin glass (<1mm) is available for example by Schott under the tradenames D-263 and AF-45. With the planned 10th generation FPDs the maximum size of a single glass sheet is

2850mm×3050mm. The glass is smooth for length scales up to the size of a single display and has sub nm surface roughness. Thickness variation, particularly present in the direction of production, is in the order of 10% of the total thickness. Furthermore a 200μm thick glass sheet has a typical 200μm warpage over an area of 100x100mm². This makes the facesheets not directly applicable in high precision optics. Due to the amorphous structure of glass the low-spatial frequency figure and waviness can be improved through thermal shaping [135].

Glass slumping is used for the fabrication of precision conical mirrors for hard X-ray optics [82, 101] and in the preshaping of strongly curved, gas bonded, glass honeycomb mirrors by the Hextek corporation.

In the slumping process the glass sheet is placed on top of a mandrel and heated in a oven. Gravity causes the glass sheet to slump over the mandrel. For the mandrel several materials are used, for example fused silica, pure silicon [135] and special zerodur [53]. For good results, temperature uniformity and a prescribed thermal profile is required.

There are a few difficulties with slumping. The flatness close to the edges is usually worse than in the central part. With the use of a slightly larger sheet and cutting the edges off after slumping, is dealt with this problem. The second problem is that the glass sheets sticks to the mandrel. If heated and in close contact with the mandrel Van der Waals forces make the glass stick to the mandrels surface. Additional TiO_2 coating with increased surface roughness reduces this problem [135]. The third issue is related to dust particles. If trapped between the glass and the mandrel they will cause a bump of typically 5μ m high and 5μ m across. More thorough cleaning will usually not entirely solve this problem and has the negative side effect that sticking is increased. One solution is found in a silicon chuck with a grid of pins of 25μ m x 25μ m each, on a orthogonal grid with 0.25μ m pitch. The underlying idea is that dust particles fall into the space between the pins that is deep enough for the dust particles. The chance that a dust particle is trapped between a pin and the facesheet is reduced with respect to a conventional mandrel.

The unflatness of FPD glass can, with slumping, be reduced by a factor 100 [135]. The shape quality comes hereby in the μm regime. To obtain a better surface shape special polishing techniques have been developed. Besides this shape correction, techniques like Epoxy Replicated Aluminum Foil (ERAF) can be used as well.

Slumping is considered as an alternative for the previously described ASM manufacturing [7].

3.1.2 Beryllium X-ray windows

Beryllium has a high specific stiffness (E/ρ) and good thermal properties, as a low Coefficient of Thermal Expansion (CTE) and high thermal conductivity λ . This makes it a superior material compared to widely used mirror materials like glass and aluminium.

However, beryllium processing is also known to be toxic. Small particles that come into contact with oxygen can cause berylliosis, a lung decease, when inhaled. Special precautions need to be taken when beryllium is manufactured, which results in only a few companies in the world that are properly equipped.

Examples of high precision optics made from beryllium are the lightweighted primary mir-

ror segments for the JWST and the secondary mirrors for the VLTs.

Besides good mechanical and thermal properties, beryllium has a low mass absorption coefficient, which means that it is highly transmissive to X-rays. Therefor beryllium is used in X-ray equipment as a window. A thin beryllium sheet or foil is used between the X-ray source in vacuum or inert gas and atmospheric conditions. Beryllium windows are mostly used in medical and industrial equipment, such as computed tomographic (CT) scanning, mammography and in X-ray tubes for baggage inspection.

Several grades of beryllium exist. Beryllium windows can be made by extruding, slicing and/or hot rolling ingots or hot-pressed blocks. Beryllium windows of 100μ m thickness up to 140μ m diameter are available. Specials with a diameter of 16μ cm and 127μ m are also reported [99, 121]. Smaller beryllium foils with 25mm diameter with high optical quality are available in 50μ m thickness. Beryllium coatings and structural elements can also be produced by means of plasma spraying [31]. With additional coatings, beryllium, can be used as a mirror material.

3.1.3 Existing membrane deformable mirrors

Membrane DMs were first reported in 1977. A titanium membrane $\varnothing 50$ mm and $1.4\mu m$ thick was proposed by [81]. Underneath the membrane 53 hexagonally arranged electrostatic electrodes are located. A next milestone was set in 1991 by [32] who proposed a bias voltage to create a static parabolic shape. Several membrane adaptive mirror have been developed afterwards. Although the list below is by no means complete, the list should bring some insight in what current continuous facesheet deformable membrane mirrors exist.

OKO Technologies

OKO Technologies makes micro machined membrane DMs since the mid '90s with a clear aperture of 10 to 50mm. The membranes are $0.5\mu m$ thick and etched from bulk silicon nitride and coated with $0.2\mu m$ aluminium. The membranes are mounted with a 20 to $100\mu m$ gap between the membrane and the electrodes that actuate the membrane [188].

ALPAO

As a spin-off company from the Université Joseph Fourier in Grenoble and supported by the Laboratoire d'Astrophysique of Grenoble, ALPAO makes silicon membrane deformable mirrors with voice coil actuators. They have several DMs ranging from $\varnothing 15$ -40mm and 52 to 241 actuators. The inter actuator stroke is $\approx 1 \, \mu m$.

Polymer membrane mirror from the Laboratoire d'Electrotechnique de Grenoble

The mirror has a polymer membrane with 2-5 μ m thickness. At the back small SmCo₅ PM of $\varnothing 0.85 \times 0.25$ mm are glued. An array of planar micro coils that interact with the PMs are positioned underneath.

The polymer membranes are developed at the Institut d'Electronique et Micro Electronique du Nord [163]. The membrane is produced by spinning of a liquid polymer (Ultradel 3112 Coating) onto a polished 50mm GaAs substrate. The liquid film is solidified in an oven and then released by wet-etching of the central part of the GaAs substrate. The roughness of the membrane is copied from the GaAs surface and \approx 10nm. The membrane is finally coated with a thin layer of aluminium.

Ø100mm aluminized nitrocellulose membrane mirror

The reflective membrane in the mirror assembly presented in [25] is a $2.5\mu m$ thick, $\varnothing 100 mm$ aluminized nitrocellulose membrane. This is similar to beamsplitter pellicles. Such a pellicle is a very thin, optical-grade nitrocellulose membrane stretched over a lapped aluminum ring and bonded in place. These pellicles are desirable in interferometric applications since they don't produce ghost images and optical path length change and no chromatic aberrations when converging beams are used. Pellicles have a typical thickness uniformity of 2λ per 25mm.

The nitrocellulose membrane used for the electrostatic DM has a tension applied of ≈ 50 N/m. It is shown by [180] than hereby good optical membranes are realized. From the $\varnothing 100$ mm mirror only the inner $\varnothing 42$ mm can be used for correction. Approximately 400μ m under the membrane a $\varnothing 56$ mm concentric array of 31 electrodes is present. The large, very thin membrane is sensitive for air-coupled vibration, therefor an additional entrance window is used [25].

A few limitations to these membrane deformable mirrors exist. Firstly, the scaling to large mirror diameters is limited. The deformable mirrors have a first resonance frequency $\propto \frac{1}{r_f} \sqrt{\frac{Q}{\rho_f t_f}}$, where Q is the membrane tension, ρ_f the membrane material density, r_f the mirror radius and t_f the mirror thickness. Without additional measures, a high resonance frequency cannot be achieved easily for large mirror diameters. A low mechanical resonance frequency can be dealt with by the use of a complex control system, where local sensors exist and local feedback is realized, as with the ASMs. More on this subject can be found in Section 3.3.1. Secondly cleaning of the mirrors is hardly possible since they are very fragile. The mirrors are sensitive for air-coupled vibration as well.

3.1.4 Thin and ultra thin wafers

A wide variety of wafer materials and sizes exist that have the potential to be used -with additional coating- as a continuous facesheet for a deformable mirror. Silicon and Pyrex are the most obvious ones. Standard silicon wafers are available up to 12" and usually $\approx\!600\mu m$ thick. $\varnothing200mm$ Silicon wafers can be ground and polished down to $20\mu m$ [147, 165]. A $\varnothing300mm$ silicon wafer with $5\mu m$ thickness is reported by [1]. Wafer scale silicon adaptive mirrors have been reported in [208]. Besides silicon, Pyrex wafers with large diameters are also available. Thinning $\approx\!600\mu m$ thick 6" wafers down to $100\mu m$ is well possible on a commercial scale.

μms [106].

3.1.5 Thin CFRP mirrors

With the same drivers that initiated the NMSD projects, the use of Carbon Fiber Reinforced Plastic in large, thin (deformable) mirrors is initiated. Fiber reinforced plastics are strong, low density materials, vacuum compatible and stable at cryogenic temperature. The carbon fiber reinforcements allow the CTE to be controlled since the CTE of the fiber is -1 $\mu m/m/K$. Although other fiber materials as aramid (kevlar), aluminium and glass, exist, carbon is often chosen for its superior stiffness. The individual fibers are usually between 5 and $10\mu m$ thick.

Mirrors made from CFRP are made by replication. A mandrel is needed on which several layers of carbon fibre material and cyanite ester resin are stacked. When cured, the mirror is released from its mandrel. With replication a high volume at low costs is achievable. Several mirrors, with optical quality have been reported in literature ([157], [106], [204]). For example, a 0.9m flat mirror, with areal density of $6kg/m^2$ is made [157]. The figure accuracy is $\lambda/20$ RMS, at 632.8nm and roughness <10nm RMS is reported. Additional SiC and Al/MgF₂ coatings for high Ultra Violet (UV) reflectivity can be added. Another example is a 0.5m flat mirror with 0.5mm thickness with a replication accuracy of a few

One of the main issues with CFRP is the fibre print through, caused by a difference in resin and fiber cure shrinkage, CTE and Coefficient of Moisture Expansion (CME). Several solutions to this have been found. A thicker, resin-rich, outer layer is used to damp this mismatch in properties. Another solution involves additional coating over the replicated surface with a harder material which can be polished. The harder material damps out the resin/fiber mismatch errors more effectively than the extra thick resin-rich layer. Another solution is to apply a layer of nano-fiber reinforced polymer composite between the main composite fibers. The smaller diameter fibers will cause a print-through effect of smaller magnitude. These nano carbon fibres can be as thin as Ø50nm and have a Young's modulus of 600GPa.

Even the replication figure can be improvement by polishing an additional layer of SiO_2 [204].

Although CFRP is often cited as a material with exceptionally high specific stiffness this needs additional attention. The ratio of mass density, 1800kg/m^3 and stiffness, 190 GPa, of carbon fibre itself is high, but cannot be obtained in CFRP constructions. All stiffness in a CFRP comes from the high Young's modulus of the carbon fibre, but with a typical fill factor of 0.6, the effective stiffness is already reduced. Secondly since stiffness is needed in more than one direction, not all fibers will contribute significantly. If, for example, in a 8 layer stack, only the outer layers are 'well' oriented, the in plane stiffness, will further decrease by a factor of 4. It is clear that the theoretical specific stiffness is therefor easily a factor 10 lower than initially expected and its advantage over other materials, even aluminium, is not present in planar applications.

3.1.6 Nanolaminate deformable mirrors

Nanolaminates are foils, up to a few hundred μ m thick, produced by sputtering layers of alternating materials, where each layer is only a few nm thick. As with the CFRP, slumping

and ERAF, shapes are replicated from mandrels. First the mandrel is coated with a separation layer, than the reflective coating and nanolaminate is sputtered. The foils can have high ultimate tensile strength and toughness due to its very small grains, which size is limited by the individual layer thickness.

The Lawrence Livermore National Laboratory (LLNL) has developed nanolaminate foil for adaptive deformable mirror facesheets [103, 144–146]. One of their nanolaminates is made out of alternating layers of copper, with 60nm thickness and thinner layers of an amorphous copper-zirconium alloy, with 8nm thickness. The latter has an approximate composition of Cu_3Zr [103]. From a 25 μ m thick foil of this nanolaminate mechanical properties are measured. The Young's modulus is 100GPa and the CTE is 13μ m/m·K. The LLNL has developed a series of 0.25m and 0.5m spherical nanolaminate mirrors that have less than 0.5kg/m² areal density. Actuators, comparable with the electrostatic MEMS actuators from Boston Micromachines can be added to make a large adaptive deformable mirror. This is already shown on small scale [146].

Other nanolaminate materials developed are Pt/Cr and 304 stainless steel/Zr laminates.

3.1.7 Epoxy Replicated Aluminum Foil (ERAF)

Epoxy Replicated Aluminum Foil is a foil made by replication with its main application in X-ray optic fabrication. An aluminium foil ($\approx 400 \mu m$) is rolled or stress-relieved on a mandrel to obtain its figure. The foil is then pressed onto an Au-coated mandrel with a thin ($\approx 40 \mu m$) layer of epoxy to smooth out the surface ripple in the foil. This is done in vacuum to avoid air to be trapped. With this replication technique very good reflecting surfaces with low X-ray scatter can be obtained at low cost.

3.1.8 Space membrane mirror technologies

Interest in membrane mirrors for space has grown in the recent years. Research on radio and radar antennae, optical telescopes, and solar power and propulsion applications is carried out [80]. Initiatives have been taken by National Aeronautics and Space Administration (NASA) [11], the Air Force Research Laboratory (AFRL) [29, 38, 127, 128, 201], the Optical Sciences Center and Steward Observatory from the University of Arizona [24, 175] and the Massachusetts Institute of Technology (MIT) Space Systems Laboratory [49, 50].

At the University of Arizona research on future space telescopes designs with 50-500m apertures is conducted. As in ground-based ELTs these designs use a primary reflector made from flat or near flat membrane segments. The secondary reflector and subsequent optics would fly in formation with the primary reflector [175].

A good overview of membrane technology for space is given in [30, 111, 158, 198].

Polyimide plastic and nickel are already being used for reflectors in space. Solar reflectors and multilayered insulation are made from polyimide. Electroformed nickel has been used for X-ray telescopes such as the XMM satellite. Both materials can be formed using glass as a mandrel. Surface roughness and waviness is hereby copied.

Up to two meter wide films from polyimide are available from Dupont and SRS Technologies with thicknesses of $10\text{-}20\mu\text{m}$ and thickness variations $\approx 1\mu\text{m}$. Any thickness variation

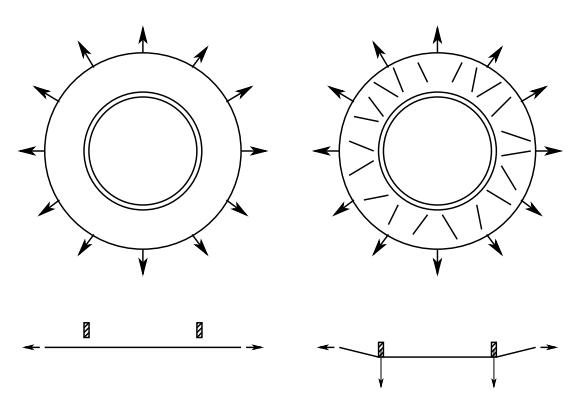


Figure 3.1: The assembly of a Stretched Membrane with Electrostatic Curvature mirror is shown in schematic. The central part of the membrane is made wrinkle free by the pretension caused by the weight of the ring

will cause an equivalent wavefront error and should therefor be further reduced [24]. Besides this, the plastics exhibit creep [175].

Membranes have no stiffness, so tension is required to make them flat. The simplest method of controlling the surface of the membrane is to constrain the entire boundary, similar to a pellicle. The perimeter defines the plane for the membrane. Via positive tension in the membrane buckling and wrinkling is avoided. Discrete attachment points are sufficient to tension the material. Results of useable flat area as a function of the number of attachment points is given in [175]. Besides flat mirrors, mirrors with a small curvature have been created by the use of an electrostatic force between the membrane and an electrode behind it. The electrostatic shaping of membranes was already described by [134] in 1980. An electrostatic attractive force distributed over the area is balanced with the membrane tension to create a concave optical surface [5, 60]. These Stretched Membrane with Electrostatic Curvature (SMEC) mirrors are reported in [5, 60]. The SMEC mirror consists of a thin membrane film attached to a ring. The membrane is a 10µm thick CP1-1 polyimide material developed by SRS Technologies. The 6" ring is an aluminum ring with a 8 degree bevel along the top surface. Two grooves were machined in the ring to prevent the glue from entering the landing area and thereby affecting the membranes shape. Piezo actuators are able to deform the ring and electrostatic electrodes placed 1.5mm behind the membrane are able to force the membrane in a 32m radius of curvature with 1200V applied.

It is essential to ensure uniform tension in the membrane. To achieve this a much larger, 12" membrane, is stretched by means of 12 discrete attachment points. Once the membrane is uniformly stretched, the 6" ring is placed on top of the membrane. Weight from the ring provides adequate tension to pull out wrinkles in the central part of the membrane. This is shown in schematic in Figure 3.1. A two component viscous glue is then flowed into the gap between the bevel and the membrane. The measured surface quality over the central 4" was better than $\lambda/20$ RMS.

At the AFRL the feasibility of a membrane as a primary mirror surface is considered [38, 127, 128, 201]. [29] shows precise surface measurement of a \varnothing 28cm diameter, 125 μ m

thick polyimide membrane mirror that is shaped by pressure to form a concave mirror with 4.47m radius of curvature. The circular membrane is thereby mounted to an optically-polished ring and then figured using gas pressure and axisymmetric tension. The high shape quality of the ring greatly reduces shape errors that propagate towards the mirror center. The error between the achieved shape and the desired paraboloid is shown to be in the hundreds of wavelengths.

At MIT research is done to predict the static behavior of axisymmetric, doubly-curved membranes accurately by [49, 50].

Membranes are also considered for transmission and reception (T/R) antennas. T/R antennas made from Dupont's copper-clad all-Polyimide flexible circuit material, Pyralux®AP TM and 50 μ m thick with 9 μ m copper layers. These antennas are described in [137]. Tension springs connected between the edges of the antenna's catenary-shaped boundary and a metal frame keep the antenna taut and flat. Other membrane antenna arrays, also with catenary systems, up to 8m with 2.5 μ m membranes, are presented in [61].

Most polymeric membranes are formed by spin casting on a solid or liquid mandrel or they are cast on a mandrel with high optical quality. Spin casting on a liquid mandrel allows scalability, but a limited number of materials can be used. Spin casting on a solid concave mandrel increases the cost significantly though the mandrel does not need to be of optical quality to form a surface with high optical quality. The back side of the mirror will take on the shape of the mandrel while the front of the membrane will form the parabolic figure dictated by the spin rate. By casting or depositing the film on a non spinning mandrel a larger number of membrane materials is available since this method does not rely on the flowability of the material [28].

3.2 Design of the mirror facesheet

From the overview in the previous section it can be concluded that for large thin mirrors different fabrication techniques and materials are available. In this section the consequences of the material choice are discussed. The effects of material parameters as Young's modulus E_f and density ρ_f and actuator spacing d on the mirrors inter actuator gravitational sag σ_g and deflection caused by wind σ_w is shown. Consequences of the facesheet thickness t_f for the actuator stiffness c_a , force F_a , power dissipation P_a and mirror resonance f_e , will be explained.

3.2.1 The facesheet thickness

40

The shape that the mirror must take is given by the wavefront distortions caused by atmospheric turbulence and is often represented by the Kolmogorov spatial spectrum (Equation (2.4) and Equation (2.5)). This and the out-of-plane stiffness of the facesheet determine the forces that the actuators have to generate for the mirror deformation (see Section 3.2.2). With the efficiency of the actuators these forces will result in energy dissipated in heat.

The out-of-plane stiffness of a plate is $\propto E_f t_f^3$. This stiffness should be kept to a minimum, but with the mirror only supported by an actuators grid with pitch, the inter actuator deflection caused by gravity or wind pressure should be limited as well. This maximum allowable

inter actuator deflection will set the lower limit on the mirror thickness.

The gravitational sag is maximal when the mirror is placed horizontally and can be neglected when placed vertically as in most breadboard setups. The deflection, when placed horizontally, should not be significant in comparison with the residual wavefront error. The limit for the RMS deflection σ_g is 1nm. Under the assumptions of a infinitely extended, thin mirror, actuated by orthogonally arranged point forces, the analytic formula for the RMS gravitational sag σ_g is given by [18]:

$$\sigma_g = \frac{12\left(1 - \nu_f^2\right)}{E_f t_f^2} \rho_f g \left(\frac{d}{2\pi}\right)^4 \sqrt{4\zeta\left(4\right)\beta\left(4\right)}$$
(3.1)

where E_f , ν_f and ρ_f are respectively the Young's modulus, the Poisson-ratio and the density of the facesheet material. t_f Is the mirror thickness, d the actuator pitch, g the gravitational acceleration, ζ the Riemann Zeta function and β de Catalan Beta function: $\xi(4)\beta(4) \simeq 1.07$. From Equation (3.1) the minimum mirror thickness, for a given orthogonal actuator grid, mirror material and maximal RMS gravitational deflection is:

$$t_{f_{min}} = \left(\frac{d}{2\pi}\right)^2 \sqrt{\frac{12(1-\nu_f^2)g\rho_f\sqrt{4\xi(4)\beta(4)}}{\sigma_q E_f}}$$
(3.2)

Wind pressure p_w , if present, will cause additional deflection. The wind pressure on the mirror surface can be modeled by [18]:

$$p_w = 2\sin(\theta)\sqrt{\frac{1+\sin(\theta)}{2}}\rho_a\bar{v}^2$$

where θ the angle between the wind direction and the mirror surface, ρ_a the air density and \bar{v} the average windspeed. If the average windspeed \bar{v} is > 1m/s the wind loading becomes dominant over the gravitational sag and Equation (3.1) can be approximated with

$$\sigma_{w} \approx \frac{12\left(1 - \nu_{f}^{2}\right)}{E_{f}t_{f}^{3}} \left(p_{w}\right) \left(\frac{d}{2\pi}\right)^{4} \sqrt{4\zeta\left(4\right)\beta\left(4\right)}$$

The minimal mirror facesheet thickness is then calculated by:

$$t_{f_{min}} \approx \sqrt[3]{\left(\frac{d}{2\pi}\right)^4 \frac{12(1-\nu_f^2)p_w\sqrt{4\xi(4)\beta(4)}}{E_f\sigma_w}}$$
 (3.3)

Since the mirror is not intended to have any optical power, it is most likely placed further in the optical path, without any significant wind pressure. For the dimensioning of the mirror facesheet thickness only gravitational sag is taken into account. Since the mirror might be placed as a folding mirror (e.g. the folding mirror needed in a Nasmyth telescope design) calculations are made with a worst case gravitational deflection.

3.2.2 Actuator forces for mirror deformation

The RMS actuator force $F_{a_{rms}}$ needed to deform the mirror surface for the Kolmogorov spatial spectrum is given by [18]:

$$F_{a_{rms}} \simeq \sqrt{10.9} \frac{E_f t_f^3}{12\left(1 - \nu_f^2\right)} \lambda \left(\frac{r_0}{c_D}\right)^{\frac{-5}{6}} d^{\frac{-7}{6}}$$
 (3.4)

Herein is λ the wavelength to correct for and c_D the compression factor between the primary mirror aperture and the DM diameter. $F_{a_{rms}}$ addresses only the forces needed to deform the mirror surface. Other actuator forces, that are needed for the actuator stiffness or dynamic forces are not included. This actuator stiffness is also related to the facesheet thickness, since that determines the mass per actuator and for a given resonance frequency, the actuator stiffness.

For Kolmogorov turbulence, 83% of the total actuator stroke is needed for the correction of the tip/tilt component of the wavefront aberration [141]. For this correction no mirror deformation is needed. Only the mirrors mass and the stiffness of the actuator is felt. With a high actuator stiffness this can become dominant. For a detailed analysis of the actuator stiffness one is referred to Section 3.3.1.

3.2.3 Power dissipation

This section will show the dependence of the total actuator force F needed to deform the mirror and power dissipation P on:

- the size of the uncompressed wavefront, determined by the telescopes primary aperture diameter D_t ,
- the compression factor c_D , which is the ratio between D_t and the diameter of the DM D_{DM} ,
- the number of actuators or DOFs that need to be corrected N_a ,
- the thickness of the mirror t_f ,
- the atmospheric conditions r_0 with its corresponding wavelength λ .

Two cases will be considered. In the first case the mirror facesheet thickness is determined by the maximum inter actuator deflection caused by gravity (Equation (3.2)). In this case, the mirror is placed in a environment with wind speeds <1 m/s.

In the second case the mirror facesheet thickness is determined by the maximum inter actuator deflection caused by wind pressure (Equation (3.3)). In this case, the mirror is placed in a environment where the inter actuator deflection induced by wind pressure is dominant over the gravitational sag.

In both cases the RMS actuator forces needed to deform the DM are related to the Kolmogorov wavefront statistics according to Equation (3.4).

For all cases the power dissipation is assumed to depend on F^2 , which is valid for Lorentz actuators (Section 4.2.1).

Case 1: scaling laws for F and P when gravity determines the facesheet thickness

The minimum mirror facesheet thickness is determined by a maximum inter actuator deflection caused by gravity as in Equation (3.2). From this equation the facesheet thickness as function of the actuator pitch d and material properties ρ_f and E_f can be written. The actuator pitch d on the DM can also, more general, be expressed by the primary aperture diameter D_t , the diameter ratio with the DM c_D and the number of actuators in the orthogonal grid N_a . The sum of all the actuator forces F and dissipation P is then expressed as:

$$d \propto \frac{D_t}{c_D \sqrt{N_a}}$$

$$t_f \propto d^2 \sqrt{\frac{\rho_f}{E_f}} \propto \left(\frac{D_t}{c_D}\right)^2 \frac{1}{N_a} \sqrt{\frac{\rho_f}{E_f}}$$

$$F \propto N_a \cdot \frac{E_f t_f^3}{d^2} \propto \left(\frac{D_t}{c_D}\right)^4 \frac{1}{N_a} \rho_f \sqrt{\frac{\rho_f}{E_f}}$$

$$P \propto F^2 \propto \left(\frac{D_t}{c_D}\right)^8 \frac{1}{N_a^2} \frac{\rho_f^3}{E_f}$$
(3.5)

In the force and power dissipation three different contributions are noted.

In the first contribution, the telescope size and design is addressed. If the DM diameter D_{DM} (= D_t/c_D), is smaller, the total force and total power dissipation will reduce dramatically.

The second contribution relates to the number of DOFs or N_a corrected in the wavefront. More DOFs result in a smaller actuator pitch, which will, for the same gravity induced deflection, result in a decreased mirror facesheet thickness. This thickness reduction will result in a lower out-of-plane stiffness and therefor lower actuator forces and power dissipation. The last contribution is related to the material properties ρ_f and E_f of the mirror facesheet material. A low mass density and high elastic modulus are favorable material properties for mirror materials. A comparison of material properties and its consequences is shown in Table 3.1.

If, in Equation (3.5), the Kolmogorov wavefront statistics, similar to 3.4, are included the scaling laws become:

$$\begin{split} F &= N_a \cdot F_{a_{rms}} \propto N_a E_f t_f^3 \lambda \left(\frac{r_0}{c_D}\right)^{\frac{-5}{6}} d^{\frac{-7}{6}} \\ &\quad F \propto D_t^{\frac{29}{6}} c_D^{-4} N_a^{\frac{-17}{12}} \rho_f^{\frac{3}{2}} E_f^{\frac{-1}{2}} \lambda r_0^{\frac{-5}{6}} \\ &\quad P \propto F^2 \propto D_t^{\frac{29}{3}} c_D^{-8} N_a^{\frac{-17}{6}} \rho_f^3 E_f^{-1} \lambda^2 r_0^{\frac{-5}{3}} \end{split}$$

Note that P is also proportional to the actuator efficiency. For this efficiency one is referred to Chapter 4.

Case 2: Scaling laws for ${\cal F}$ and ${\cal P}$ when wind pressure determines the facesheet thickness

Here the minimum mirror facesheet thickness is assumed not to be determined by the gravitational sag but by a more relevant wind pressure p_w and is calculated with Equation (3.3). In analogue with Equation (3.5) the scaling for F and P can be written as:

$$d \propto \frac{D_t}{c_D \sqrt{N_a}}$$

$$t_f \propto \sqrt[3]{\frac{d^4 p_w}{E_f}} \propto \sqrt[3]{\frac{\left(\frac{D_t}{c_D}\right)^4 \frac{p_w}{N_a^2}}{E_f}}$$

$$F \propto N_a \cdot \frac{E_f t_f^3}{d^2} \propto \left(\frac{D_t}{c_D}\right)^2 p_w$$

$$P \propto F^2 \propto \left(\frac{D_t}{c_D}\right)^4 p_w^2 \tag{3.6}$$

Unlike Equation (3.5), only the DM diameter and wind pressure p_w are relevant. The total actuator force does not depend of the number of actuators and not on the mirror material. A certain out-of-plane stiffness is required to match the wind pressure. For the total actuator force or power dissipation it does not matter whether this is achieved by a material with a high elastic modulus and low facesheet thickness of vice versa. For the total actuator force an actuator number increase, with a decreased facesheet stiffness, is matched by the actuator number increase. So there is no dependance on the number of DOFs N_a as well.

If, in Equation (3.6), the Kolmogorov wavefront statistics are included, the scaling laws become:

$$F = N_a \cdot F_{a_{rms}} \propto N_a E_f t_f^3 \lambda \left(\frac{r_0}{c_D}\right)^{\frac{-5}{6}} d^{\frac{-7}{6}}$$

$$F \propto D_t^{\frac{17}{6}} c_D^{-2} N_a^{\frac{-5}{12}} p_w \lambda r_0^{\frac{-5}{6}}$$

$$P \propto F^2 \propto D_t^{\frac{17}{3}} c_D^{-4} N_a^{\frac{-5}{6}} p_w^2 \lambda^2 r_0^{\frac{-5}{3}}$$

Compared with Equation (3.6), a small dependance of N_a and a more significant dependence on D_t is found.

3.2.4 Mirror facesheet material comparison

The materials used in the technologies as described in Section 3.1 and other common materials are listed in Table 3.1. For these potential facesheet materials the density ρ_f , the Young's modulus E_f , the Poisson ratio ν_f , the CTE and the thermal conductivity λ is listed. In addition the specific stiffness E_f/ρ_f and the ratio E_f/ρ_f^3 is listed. The latter is relevant for Equation (3.5). Equation (3.2) and Table 3.1 are used to calculate the minimum mirror facesheet thickness. The results are listed in Table 3.2 and are calculated for an orthogonal grid with 6mm pitch and an allowed inter actuator deflection caused by gravity of 1nm RMS. Besides the minimum facesheet thickness, the relative actuator force and power dissipated is calculated based on Equation (3.4). The values are relative to the values of beryllium. In Table 3.2 it is shown that large differences exist in thickness, force and power dissipation. The choice of facesheet material is clearly of importance. As much as a factor of 200 is to be gained or lost. When low forces and power dissipation are required, the application of e.g. Cu/Zr nano laminate, stainless 316 or nickel is not favorable when compared to beryllium, CFRP, silicon or Pyrex. Beryllium is superior, but with the thickness of 35µm extremely thin and will be an expensive piece to make with significant lead time. CFRP is, due to its low density, close to beryllium. When the thickness of a single carbon fibre is considered, an isotropic facesheet without print through with a thickness of 53 µm will however be hard to make. Silicon and Pyrex serve as an good practical alternative.

For DMs where wind pressure determines the facesheet thickness no difference exist in force and power dissipation for different materials.

In the mirror facesheet selection many aspects should be taken into account. Material properties E_f and ρ_f and the consequence for the mirror thickness, force and power dissipation are discussed in Section 3.2.4. Besides the drive for low out-of-plane stiffness, low actuator forces and power dissipation other aspects, such as manufacturability and availability as described in Section 3.1 are also relevant. For the mirror it is furthermore relevant that the mirror is flat on length scales corresponding to the inter actuator pitch, since the actuator can not correct for this unflattness. Unflattness corresponding to the lowest spatial frequencies is allowed since very little force is needed since its corresponding stiffness is low. It will be clear from Section 3.6 how is dealt with unflattness that is present. The roughness however should be in the order of nm and depending on the wavelength spectrum of interest the mirror should have a coating with suitable reflectivity.

Beryllium with a coating is superior when low forces and dissipation is required, but in this research several tests and prototypes with many facesheets are needed so this is not chosen at this stage. Form Table 3.2 silicon and Pyrex both are alternatives and form a good compromise between low actuator forces and power dissipation and obtainability, combined with short lead times and low costs.

Since for Pyrex a larger thickness is allowed, this material is chosen. In this thesis calculations will be made for both the Pyrex and the beryllium facesheet.

Material ^a	$ ho_f$	E_f	ν_f	α	λ	$\frac{E_f}{\rho_f}$	$\frac{E_f}{\rho_f^3}$
	$\left[\frac{\mathrm{kg}}{\mathrm{m}^3}\right]$	$\left[\frac{N}{m^2}\right] \cdot 10^9$	[-]	$\left[\frac{m}{m \cdot K}\right] \cdot 10^{-6}$	$\left[\frac{W}{m \cdot K}\right]$		$\begin{bmatrix} \frac{Nm^7}{kg^3} \\ \cdot 10^{18} \end{bmatrix}$
Beryllium ^b	1850	303	0.1	11.4	216	163	47.9
Aluminium 6061	2700	68	0.3	25	237	25	3.5
Titanium	4430	110	0.3	9.5	17	25	1.3
Nickel	8900	207	0.3	13	60	23	0.3
Stainless 316	8000	193	0.3	16	16	24	0.4
Pyrex ^c	2230	64	0.2	3.2	1	29	5.8
$Silicon^d$	2300	130	0.2	2.6	150	56	10.7
$CFRP^e$	1600	103	0.34	0.2	14	64	25.1
Nano laminate ^f	8000	100		13		12.5	0.2
CP1 Polyimide ^g	1430	2.1		51		1.5	0.7

 Table 3.1: Mechanical properties for different mirror facesheets materials.

Table 3.2: Mirror facesheet thickness comparison

Material	t_f	$t_{f_{rel}}$	$F_{a_{rel}}$	P_{rel}
	[µm]	[-]	[-]	[-]
Beryllium	35	1	1	1
Aluminium 6061	86	2.4	3.6	12.7
Titanium	86	2.5	5.9	34.8
Nickel	89	2.5	12.2	149.8
Stainless 316	87	2.5	10.8	116.7
Pyrex	82	2.4	2.8	8.0
Silicon	59	1.7	2.1	4.3
CFRP	53	1.5	1.3	1.7
Nano laminate	122	3.5	15.0	225.2
CP1 Polyimide	355	10.1	7.8	61.3

^a All properties are at 298 K.

^b O-30 grade from Brush Wellmann.

^c Borosilicate from Corning, in composition equal to Schott's 'Duran' glass or glass 8830.

^d Single crystal silicon in the <110> orientation, data taken from [202].

^e EX1515/M55J from Bryte Technologies Inc. 0° 45° 90° 135° woven laminate.

^f Cu/Zr nanolaminate, values taken from LLNL [103].

 $^{^{\}it g}$ Space grade polyimide by SRS Technology.

3.3 Constraining the mirror facesheet

This section will describe how the mirror facesheet is constrained. The out-of-plane DOFs constraints by the actuators and the constraints for the in-plane DOFs will be discussed.

3.3.1 The facesheet's out-of-plane DOFs

The mirror facesheet is supported by a grid of actuators. Each actuator adds stiffness c_a to the mirror facesheet. This stiffness, as will be shown below, will determine the resonance frequencies of the mirror facesheet. Besides an increase in resonance frequency, a higher stiffness will give rise to higher actuator forces.

These forces contribute to the previously mentioned actuator forces needed to deform the facesheet, which were mentioned in Section 3.2.2. The deformation of the mirror facesheet is small compared to the total actuator stroke, which is $\pm 10 \mu m$ as derived in Section 2.3 and largely needed for the tip/tilt correction of the aberrated wavefront.

The influence of the actuator stiffness on the mirrors first resonance frequency is calculated with a Finite Element Model (FEM) and is shown in Figure 3.3. Four different mirror facesheets have been analyzed. Two mirror facesheets are \emptyset 50mm and two are \emptyset 150mm. For each diameter, one facesheet is made of beryllium and 35 μ m thick and one is made from Pyrex and 100 μ m thick. Figure 3.2 shows the FEM model of the \emptyset 50mm mirror facesheet.

On a hexagonal grid with 6mm pitch, the actuator stiffness c_a is added to the mirror facesheet. 61 Actuators are added under the $\varnothing 50$ mm facesheet and 516 actuators for the $\varnothing 150$ mm facesheet. The in-plane DOFs are fixed by constraining x and y at the edge the mirror facesheet. Figure 3.3 is discussed and explained on the basis of the actuator stiffness.

• Zero actuator stiffness

When $c_a=0$ the first resonance frequency is determined by the bending stiffness of the facesheet. This frequency is low and its mode shape is shown in seen in Figure 3.3 on the left. It is a global bending mode of the facesheet. For a circular plate, simply supported at the edge, this first resonance frequency can be calculated with [14]:

$$f_e = \frac{4.977t_f}{2\pi r_f^2} \sqrt{\frac{E_f}{12\rho_f (1 - \nu_f^2)}}$$
 (3.7)

Where r_f is the mirror radius, t_f the thickness and E_f and ρ_f the Young's modulus and density of the mirror facesheet material. The FEM results: 212, 150, 26 and 20Hz for respectively $\varnothing 50$ mm Pyrex, $\varnothing 50$ mm beryllium, $\varnothing 150$ mm Pyrex and $\varnothing 150$ mm beryllium are close to the analytical results form Equation (3.7): 205, 167, 23 and 18 Hz. With $c_a=0$ the actuators are pure force actuators. Since the first mechanical resonance is low, additional control stiffness will be needed to control the many internal modes of the mirror facesheet. The local sensors and a control loop increase the overall complexity significantly.

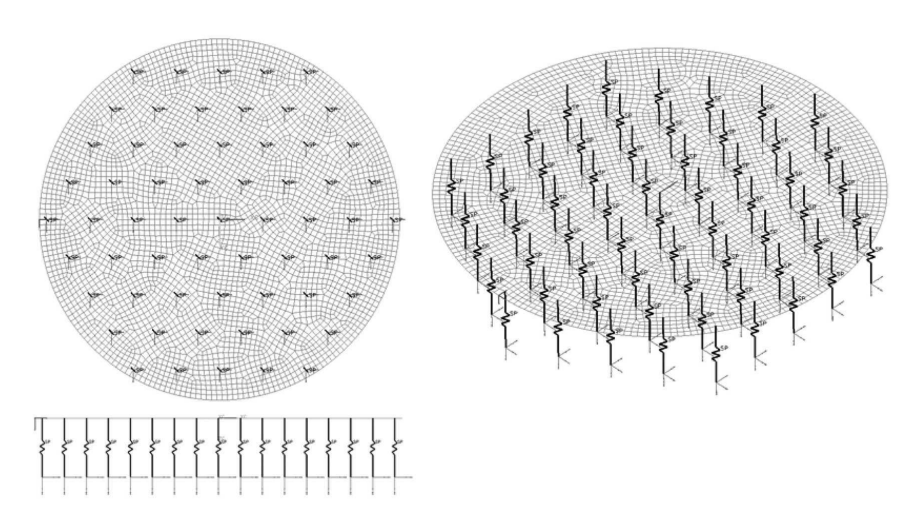


Figure 3.2: The FEM model to calculate the resonance frequencies in a $\varnothing 50$ mm mirror facesheet. The model is made of 2D plate elements that represent the mirror facesheet and 1D linear elements that represent the actuator stiffness. The in-plane DOFs are fixed by constraining x and y at the edge. Furthermore the edge is constrained in z to make it a simply supported circular plate. On the actuator positions, arranged in a hexagonal grid with 6mm pitch, the linear elements constrain z with the actuator stiffness c_a .

• Actuator stiffness: $0 < c_a < 5e3$ N/m

When any actuator stiffness is added to the facesheet stiffness this soon becomes significant over the bending stiffness of the mirror membrane. Since the mass of the 35 μm beryllium facesheet is less then the $100 \mu m$ Pyrex, the resonance frequency increase is larger. For all facesheets the resonance frequency in this regime can be approximated with $f_e=\frac{1}{2\pi}\sqrt{\frac{c_a}{m_{a_f}}}$, where m_{a_f} is the total mass of the facesheet divided by the number of actuators carrying the facesheet. This approximation is plotted in Figure 3.3 for the Pyrex and beryllium facesheets. There exist no difference in the first resonance frequency between the $\varnothing 50 mm$ and $\varnothing 150 mm$ facesheets. With a diameter increase, the added facesheet mass is matched with more support points with actuator stiffness. For the Pyrex facesheets the first mode shape remains a global bending until $c_a\approx 10^4$ N/m and for the beryllium facesheet until $c_a\approx 10^3$ N/m. The actuator can still be considered soft. Limited force is needed to overcome the actuator stiffness.

• Actuator stiffness: $5e3 < c_a < 1e5 \text{ N/m}$

When $5\mathrm{e}3 < c_a < 1\mathrm{e}5$ N/m there is a transition between the global, previously described modes and the more local modes as described below. The stiffness of the actuators is of the same order of magnitude as the facesheet between the actuators. The modes shapes are not global as before, but local bending of the facesheet is visible. An example of such a mode shape is visible in Figure 3.3. The force needed to move the actuators is significant.

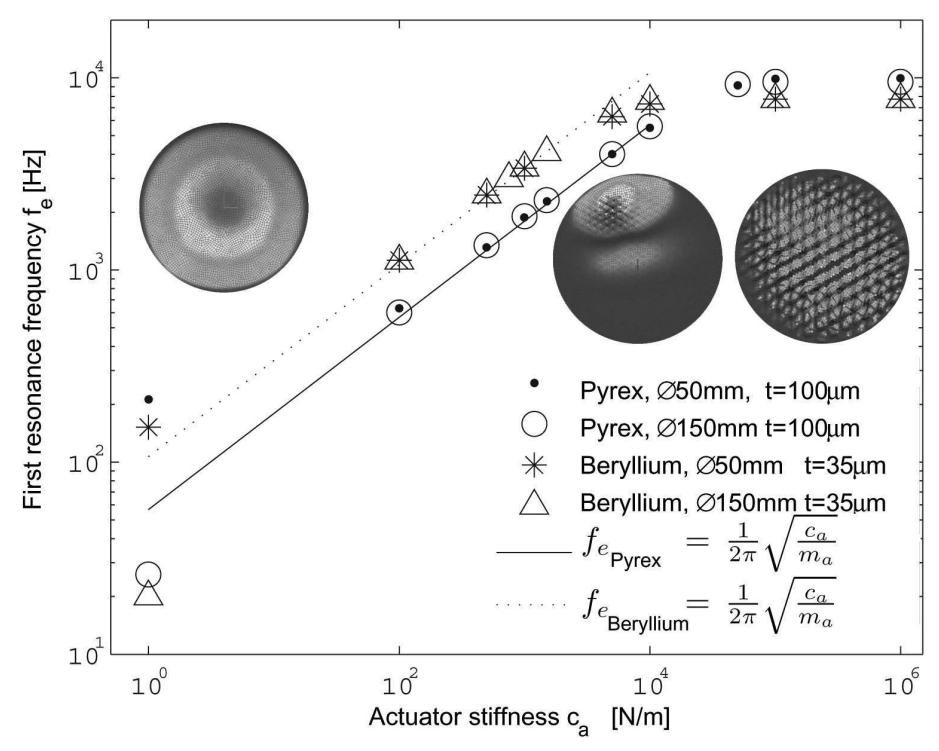


Figure 3.3: The first resonance frequency f_e as function of the actuator stiffness c_a for a $\varnothing 50$ mm and $\varnothing 150$ mm mirror facesheet made from Pyrex and beryllium. The Pyrex facesheets are 100μ m thick and the beryllium facesheets are 35μ m thick.

• Actuator stiffness > 1e5 N/m

When the actuator stiffness is significantly higher than the facesheet between the actuators, the facesheet starts to resonate first. The facesheet can be considered fixed on the actuator positions. Adding even more stiffness to the actuators will not increase the first resonance. This resonance is higher for the $100\mu m$ Pyrex facesheet as for $35\mu m$ beryllium. The bending of the facesheet is local as can be seen in Figure 3.3. The actuator is an stiff actuator and actuator forces will be high. There will be a hard point in the mirror facesheet if one fails.

With 200Hz control bandwidth as a goal, the first mechanical resonance frequency of the assembled mirror is aimed at 1kHz. With the moving mass of the actuators still to be added to the previously discussed calculations, an actuator stiffness of 500N/m will be needed. This is sufficient for both a 35 μ m beryllium and and 100 μ m Pyrex facesheet. With this there will be no additional local control loop needed and the actuator stiffness is not higher than needed thereby avoiding excessive power dissipation. In Chapter 4 the actuator and the actuator stiffness design is shown.

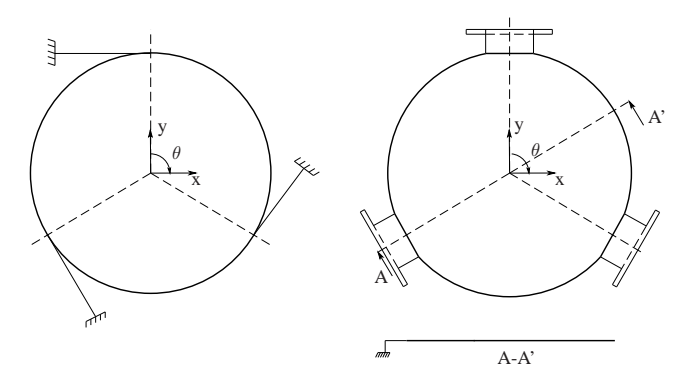


Figure 3.4: On the left, three tangentially placed struts constrain the x and y translation and θ rotation. On the right, the three tangential rods are replaced by three folded leafsprings.

3.3.2 The mirror's in-plane DOF

Each actuator will only constrain one DOF in the mirror facesheet. The actuators together will constrain all the out-of-plane DOFs. The facesheet can be considered stiff in-plane, therefor only three additional constraints for the in-plane DOFs of the facesheet are needed: x, y and θ . Figure 3.4 will show two implementations. On the left three tangentially placed rods constrain the x and y translation and θ -rotation. The thermal center coincides with the optical axis, but thermal expansion will lead to a small rotation θ of the mirror facesheet. When folded leafsprings replace the tangential rods as shown on the right in Figure 3.4, this is avoided. Each folded leafspring will constrain one DOF: along its fold line. Because lateral expansion is possible without rotation the folded leafsprings are implemented. The next section will describe the detailed design.

The folded leafspring

The required stiffness in the direction of the fold line c_f is determined. For the translations x and y and the θ -rotation of the mirror facesheet, the first mechanical resonance $f_{e_{x,y}}$ and $f_{e_{\theta}}$ should be >1 kHz. The minimum stiffness c_f needed to constrain a $\varnothing 150$ mm Pyrex mirror facesheet with 0.1mm thickness is:

$$\begin{split} f_{e_{x,y}} &= \frac{1}{2\pi} \sqrt{\frac{3c_{f_{x,y}}}{2m_f}} = \frac{1}{2\pi r_f} \sqrt{\frac{3c_{f_{x,y}}}{2\pi t_f \rho_f}} > 1 \text{kHz}, \qquad \rightarrow c_{f_{x,y}} > 1.1 \cdot 10^5 \frac{\text{N}}{\text{m}} \\ f_{e_{\theta}} &= \frac{1}{2\pi} \sqrt{\frac{k_{\theta}}{J_{\theta}}}, \qquad J_{\theta} = \frac{1}{2} m_f r_f^2, k_{\theta} = 3c_{f_{\theta}} r_f^2 \\ f_{e_{\theta}} &= \frac{1}{2\pi r_f} \sqrt{\frac{6c_{f_{\theta}}}{\pi t_f \rho_f}} > 1 \text{kHz}, \rightarrow k_{\theta} > 4.5 \cdot 10^2 \frac{\text{Nm}}{\text{rad}}, \rightarrow c_{f_{\theta}} > 2.7 \cdot 10^4 \frac{\text{N}}{\text{m}} \end{aligned} \tag{3.8}$$

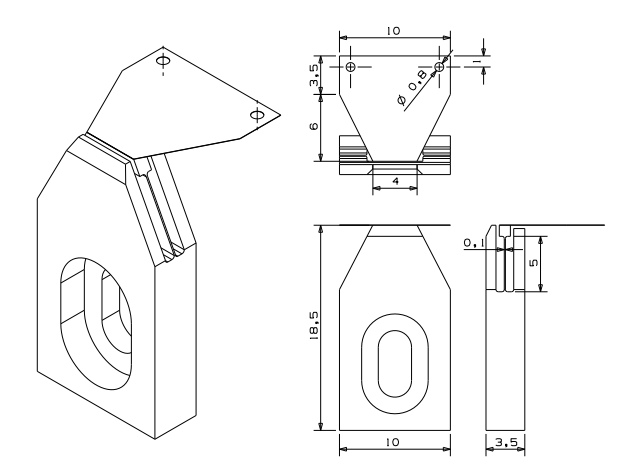


Figure 3.5: The dimensions of the folded leafsprings as used to constrain the in-plane DOFs

where m_f is the mirror facesheet mass and J_θ is the moment of inertia of the mirror facesheet around z. Equation (3.8) shows that the minimum stiffness c_f is determined by the resonance frequency in x and y direction. The stiffness should therefor be $1.1 \cdot 10^5$ N/m. Figure 3.5 shows the folded leafspring with its dimensions. The folded leafspring is made out of two parts. An aluminium part forms the short, vertical part of the folded leafspring. This leafspring is made with wire Electrical Discharge Machining (EDM). The second part is a 15-5 PH steel foil. The steel foil is glued to the thickened end of the aluminium leafspring. The steel foil is glued with two spots to the back of the mirror facesheet.

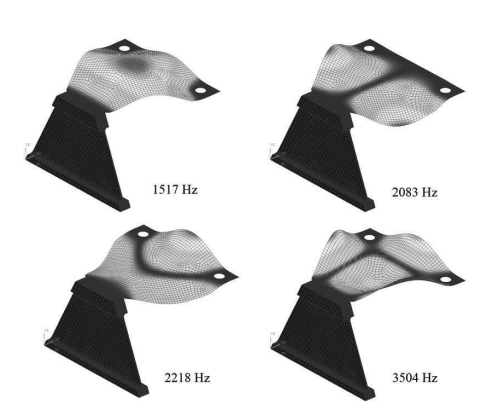


Figure 3.6: The first four resonance frequencies in the folded leafspring at 1517, 2093, 2218 and 3504 Hz.



Figure 3.7: Photo of five folded leafsprings placed on a carrier.

The aluminium part is provided with end stops that avoid excessive bending and provide protection. FEM analysis shows a stiffness of $4.8 \cdot 10^5$ N/m in the direction of the fold line. The steel foil should be less stiff in bending then the mirror facesheet. Since the bending stiffness scales $\sim Et^3/L^3$ a 20μ m thick steel foil with 9mm bending length will have two orders of magnitude lower stiffness than the 0.1mm thick Pyrex facesheet on a 6mm actuator pitch.

Besides the stiffness properties, the first resonance frequency of the folded leafspring should be >1kHz as well. Figure 3.6 shows the results of a FEM analysis of the first four resonance frequencies and corresponding mode shapes. For this model the aluminium leafspring is fixed at the base and the holes for the glue are fully constrained. The FEM analysis shows a sufficiently high resonance. Figure 3.7 shows five folded leafsprings placed on an aluminium carrier.

Alternatives

Besides the mirror facesheet suspension, where the out-of-plane DOFs are constrained by the actuators and x,y, and θ by the folded leafsprings, a few alternatives will be discussed. Instead of a free edge, the mirror facesheet could also be simply supported of even clamped at the edge. One possible way is to clamp the edge with a ring, similar to Figure 3.1, the pellicle beamsplitter and a membrane in drums. The rigid ring can be adjusted in z, φ and ψ and aligned with respect to the actuator grid. The facesheet can be fixed to the ring with glue or allowed lateral expansion over the edge while kept taut by pretension. With this pretension wrinkling is avoided and the facesheets resonance frequency is increased. In the next section different ways to pretension the facesheet will be shown. Under what conditions wrinkling will happen and how this can be avoided is discussed as well.

3.3.3 Wrinkling and pretension in the membrane

With pretension wrinkling of the facesheet can be avoided. If not properly done however, this pretension will induce wrinkling. The wrinkling phenomenon is a subject of research for many years. [112, 154] and [71] give an extensive overview on various aspects of wrinkling. To avoid wrinkling it is necessary to know under what conditions wrinkling will exist. A common way to approach this question is by the use of the principal stress criterion. When the principle stresses in the membrane are considered, the state of the membrane can be predicted:

taut	$\sigma_{22} > 0,$	$\sigma_{11} > 0$,
wrinkled	$\sigma_{22} \leq 0$,	$\sigma_{11} > 0$,
slack	$\sigma_{22} < 0$.	$\sigma_{11} < 0$.

In other words, if a membrane is not taut, it is regularly wrinkled if one principal stress is positive. A membrane is slack if it is neither taut nor regularly wrinkled.

If a wrinkled region is found, the wrinkle frequency and amplitude can be determined analytically by methods described in [205, 206].

For the design of a wrinkle free facesheet, isotropic positive stress should be in the facesheet

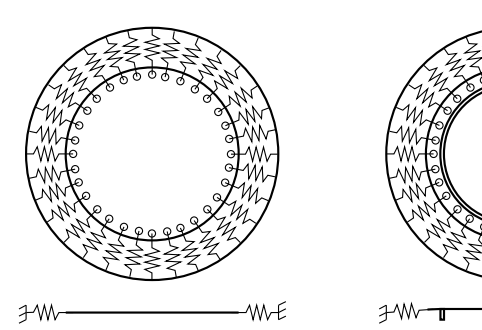


Figure 3.8: Soft springs at the circumference pretension the mirror facesheet (Left). This can be combined by a ring whereby the central part of the mirror will be kept wrinkle free (Right).

under all conditions. When a facesheet is pre-tensioned by pulling at discrete points at the circumference, small wrinkles will occur, but they die out over a short range [5]. The left of Figure 3.8 shows how this pretension can be brought into the facesheet, similar to a trampoline. The soft springs can pull under a small angle when combined with a ring at the edge of the aperture as shown on the right in Figure 3.8. The central part within this ring will be wrinkle free. To reduce the radial dimensions, the soft springs at the circumference can also be placed 90° rotated, parallel to the optical axis. Still local regions with wrinkles, outside the ring, will exist.

For isotropic stress over the full aperture an alternative is found in the use of a catenary [79]. By pulling a catenary or tension cord, attached to the edge of the mirror facesheet, the full aperture is pretensioned. Depending on the cord shape different loads are applied on the facesheet [79]. When the edges of the facesheet are perfectly circular shaped this will result in a uniform load locally perpendicular to the cord and will result in a uniform isotropic stress. This is shown in Figure 3.9. The number and size of the arcs may differ as long as they are all perfectly circular. To work properly the cord and mirror facesheet should have equal stiffness. It is thereby avoided that any shear is transferred between the cord and mirror facesheet. The required cross section stiffness $(EA)_{cord}$ for a support arc radius R_i is: $(EA)_{cord} = \frac{E_f R_i t_f}{(1-\nu_f)}$ where E_f and ν_f are the mirror facesheet Young's modulus and Poisson ratio. If the material of the cord and the facesheet are equal no additional thermal problems will rise. Another possibility is to apply a shear compliant transition between the

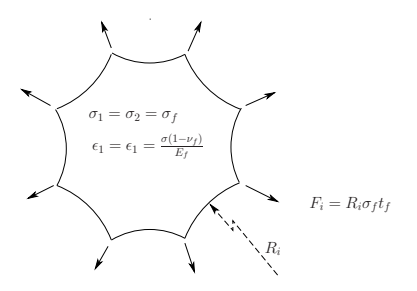


Figure 3.9: At the perimeter of the facesheet a tension cord, or catenary, is attached that in perfect circular shapes brings uniform isotropic tension in the mirror facesheet.

cord and the mirror facesheet. For polyamide membranes by SRS this is done by perforating slots to create a series of 'struts' [181].

3.4 The influence function

In Section 3.3.1 the effect of different actuator stiffness c_a on the first resonance frequency of the mirror facesheet is shown. The actuator stiffness is also relevant for the mechanical coupling between actuators and thereby for the shape op the influence function. The influence function for an actuator describes the shape the mirror facesheet takes when only this actuator is actuated. The mirror shape is made by a linear superposition of all the influence functions.

When the actuator stiffness is low, there will be a large coupling between adjacent actuators and the influence function will be wide. With a high actuator stiffness the coupling will be low and the influence function will be narrow.

Figure 3.10 shows a model of the mirror facesheet with the attached actuators. In this model $z_{a,1}$ is the position of the central actuator and $z_{a,2}$ are the positions of N adjacent actuators. The positions are linked by the actuators stiffness c_a , the connection struts stiffness c_s and the mirror facesheet stiffness c_f . Since $c_s \gg c_f$, c_a , the axial compliance of the connection strut can be ignored and the model further simplified.

The actuator coupling η can then be written as:

$$\eta = \frac{z_{a,2}}{z_{a,1}} = \frac{c_f}{c_f + N \cdot c_a}$$

 c_f is calculated with FEM and found to be 1200N/m for a 35 μ m beryllium facesheet and 6300N/m for a 100 μ m Pyrex facesheet with a 6mm hexagonal actuator pitch.

For a hexagonal grid with 6mm pitch the coupling is calculated for different actuator stiffness for both the $35\mu m$ thick beryllium and $100\mu m$ thick Pyrex mirror facesheet. The results

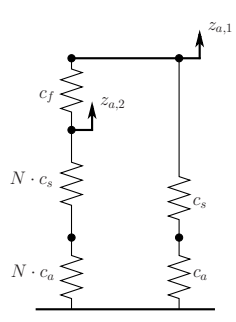


Figure 3.10: Model of the mirror facesheet with attached actuators to determine the actuator coupling.

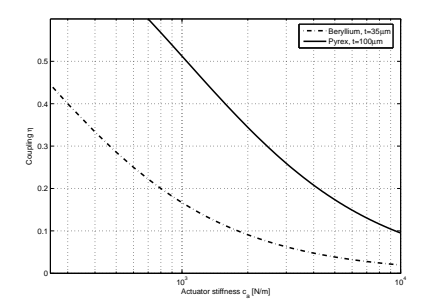


Figure 3.11: The actuator coupling in a hexagonal actuator grid with 6mm pitch for the 35 µm beryllium and 100 µm Pyrex facesheet as function of the actuator stiffness.

are shown in Figure 3.11. With c_a =500N/m as described in Section 3.3.1 this would give η_{Be} =0.28 and η_{Pyrex} =0.65. This is an appropriate value for the beryllium facesheet but rather large for the Pyrex. In the prototypes Pyrex is used, but beryllium is considered more ideal and a realistic material for further developments. Therefor the actuators will be designed for 500N/m.

Besides the width of the influence function, its shape is also relevant. The shape should be smooth to prevent higher order aberrations to be introduced in the wavefront. With the use of struts between the actuators and the facesheet, the bending stiffness of the facesheet will be able to form this smooth shape. More details on the influence function can be found in Chapter 6.

3.5 The connection struts

As explained in Section 2.5 struts couple the actuators to the mirror facesheet. This section will govern the dimensioning of the struts. Four aspects are hereby considered. First the struts should be less stiff in bending than the mirror facesheet, secondly the struts should be stiff enough axially to impose the axial position of the actuator on the mirror facesheet. The third aspect will govern the struts own first resonance frequency. As last, the struts should not buckle under load. All these aspects will have their consequences for the length L_s and diameter D_s combinations of the struts. Goal is to make a suitable choice taking these aspects into account.

The bending stiffness of the strut

The bending stiffness k_{φ_s,ψ_s} of the strut needs to be significantly lower than that of the mirror facesheet to prevent the pistons as in Figure 2.10. At the actuator side, the strut is considered to be fixed in φ and ψ . This is schematically shown in Figure 3.12. The

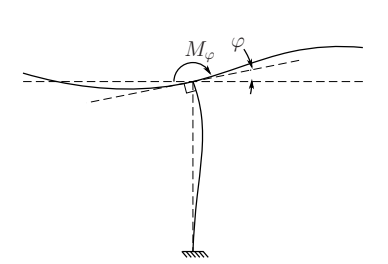


Figure 3.12: The mirror facesheet imposes a moment M_{φ} and since its bending stiffness is low, the mirror will impose φ and ψ to the connection strut (only φ is shown).

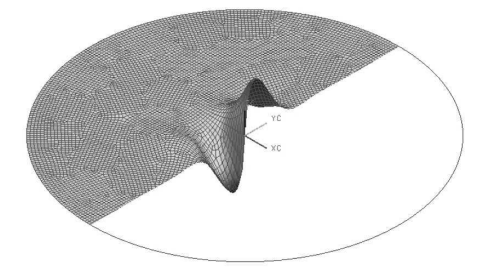


Figure 3.13: A cut through shows the deformed mirror facesheet due to an applied moment M_{φ} (made with FEM). From the deformation, the local rotation is found and the mirror rotational stiffness k_{φ_f,ψ_f} is calculated.

3 The mirror facesheet

bending stiffness k_{φ_f,ψ_f} of the mirror facesheet is determined by FEM analysis. In the FEM analysis a $\varnothing 50$ mm Pyrex facesheet of $100\mu m$ is fixed in z on the hexagonal actuator grid with 6mm pitch. On the central actuator position a moment M_φ is applied. Figure 3.13 shows a cut through of the deformation that results. From this analysis the bending stiffness $k_{\varphi_f,\psi_f}=0.05$ Nm/rad is found. The design goal is to make the connection strut 20 times more flexible. With this the required L_s and D_s of the strut from Figure 3.12 is determined:

$$k_{\varphi,\psi} = \frac{4E_sI_s}{L_s}, \qquad I_s = \frac{\pi D_s^4}{64}, \qquad \to k_{\varphi,\psi} = \frac{\pi E_sD_s^4}{16L_s}$$
$$\frac{D_s^4}{L_s} = \frac{16k_{\varphi_s,\psi_s}}{\pi E_s}, \qquad k_{\varphi_s,\psi_s} < \frac{k_{\varphi_f,\psi_f}}{20}$$

Where E_s is the Young's modulus of the strut material and I_s is the second moment of inertia of a strut with round cross section.

The axial stiffness of the strut

The frequency f_{e_z} where the mass of the mirror facesheet carried by an actuator m_{a_f} starts to resonate on the axial stiffness of connection struts c_s needs to be significantly higher than the first resonance of the mirror facesheet and is set on 5kHz. From this the $\frac{L_s}{D_s}$ requirements can be determined:

$$\begin{split} f_{e_z} &= \frac{1}{2\pi} \sqrt{\frac{c_s}{m_{a_f}}}, \qquad c_s = \frac{E_s A}{L_s} = \frac{\pi E_s D_s^2}{4L_s}, \qquad m_{a_f} \approx \frac{\pi d^2 t_f \rho_f}{4} \\ f_{e_z} &= \frac{D_s}{2\pi d} \sqrt{\frac{E_s}{t_f \rho_f L_s}}, \qquad \frac{D_s^2}{L_s} > \frac{4\pi^2 f_{e_z}^2 \rho_f t_f d^2}{E_s} \end{split}$$

Where d is the actuator pitch, t_f the mirror facesheet thickness and ρ_f the mirror facesheet material.

The first resonance frequency of the strut itself

When the struts become more slender, the struts first resonance f_{e_s} can become undesirably low. The strut is designed such that this bending mode not occurs under 2kHz. For the strut in Figure 3.12 f_{e_s} is calculated with [14]:

$$f_{e_s} = \frac{25\pi}{32L_s^2} \sqrt{\frac{E_s I_s}{m_s}}, \qquad m_s = \frac{\rho_s \pi D_s^2}{4}$$

$$\frac{D_s}{L_s^2} = \frac{128 f_{e_s}}{25\pi} \sqrt{\frac{\rho_s}{E_s}}$$

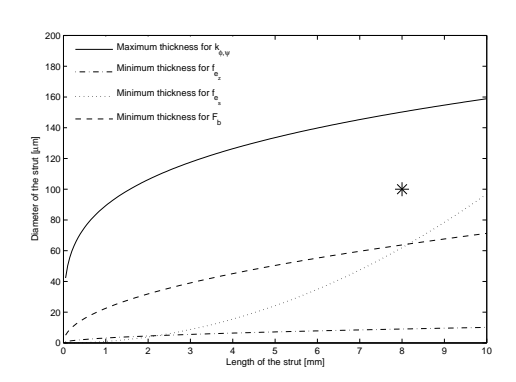


Figure 3.14: Combinations of length L_s and diameter D_s for the connection struts to satisfy the design criteria from Section 3.5. The design choice is marked with an asterisk: *.

Buckling of the strut

Buckling of the struts needs to be prevented. The buckling force F_b for the strut in Figure 3.12 and suitable $\frac{L_s}{D_o}$ requirements are calculated by:

$$F_b = \frac{2\pi^2 E_s I_s}{L_s^2} = \frac{\pi^3 E_s D_s^4}{32 L_s^2}$$
$$\frac{D_s^4}{L_s^2} \ge \frac{32 F_b}{\pi^3 E_s}$$

With the actuator forces in the order of mN's, the 50mN is a safe value for the buckling force.

For all the previously mentioned aspects the different $\frac{L_s}{D_s}$ ratios are plotted in Figure 3.14. The figure is made for stainless steel struts and f_{e_s} =3kHz, f_{e_z} =5kHz, F_b =50mN and $k_{\varphi,\psi}$ is 20 times less stiff than the facesheet. From Figure 3.14 the dimensions \emptyset 0.1×8mm is chosen. Straight wires of \emptyset 0.1×200mm made of AISI 302 are obtained and cut to length (in bundles), by wire EDM.

3.6 Assembly of the connection struts

Glue is considered for the attachment of the strut to the mirror facesheet and actuators. In the glued connection tolerances, such as strut length and axial actuator position, are taken care of. The most basic idea to join the struts is seen in Figure 3.15. The strut is first glued with a small droplet at the back of the mirror facesheet. Any length variation is handled at the actuator side where the droplet is bigger. The axial gap between the tip of the strut and the actuator is filled with glue and can vary from strut to strut. Axial shrinkage differences will result in mirror facesheet unflattness. Figure 3.16 shows a more complex version of Figure 3.15. Here the strut is made out of two parts. Both parts are first joint to the facesheet and actuators. A small tube will act as the stiffened central part of the strut and has a joint where length tolerances can be handled. Any radial shrinkage is this joint will not result in mirror facesheet unflattness. Since this is a more complex version, first the basic version is tested.

The joint at the mirror facesheet side should not result in significant facesheet deformation. Deformation is the result of shape of the droplet and the glue shrinkage and Young's modulus. Since a stiff connection in z-direction is needed and the glue area is limited a glue with relative high Young's modulus is needed. With a stronger glue, the surface area on the facesheet and the cylindrical face of the struts can be reduced. Therefor a strong, low shrinkage and stiff glue is wanted.

From a practical point of view the glue should have a relatively long pot life (\approx 1 hour) and should be suitable for use with dispensing needles. A glue with low viscosity is thereby favorable. The assembly can not easily be baked in an oven, therefor room temperature hardening is desired. Glue that cures with UV can not be used, since the joint will be difficult to illuminate.

Epoxies based on two components are considered. Many epoxies exist. In Table 3.3 three common industrial epoxies with relevant properties are shown. Araldite 2011 is a tough epoxy with a long pot life and a good resistance to dynamic loading. The glue is suitable for bonding a wide variety of materials, e.g. metals, ceramics, glass, rubber and rigid plastics. Araldite 2020 has an extremely low viscosity, which makes it easy to use. It is colorless and with a refractive index close to glass, especially designed for glass bonding. The glue is suitable for bonding metals, ceramics, rubbers and rigid plastics. DP460 from 3M is a high strength epoxy. All epoxies cure relatively slowly at room temperature. Araldite 2020 reaches half shear strength at 24 hours. All others are fully cured by that time. During curing, the epoxies will shrink. All manufactures claim a shrinkage <1%. All epoxies are amine-cured epoxies. If polymerized in conditions of low ambient temperature or high humidity, amine-cured epoxy resins can develop a surface oiliness or exudate, commonly

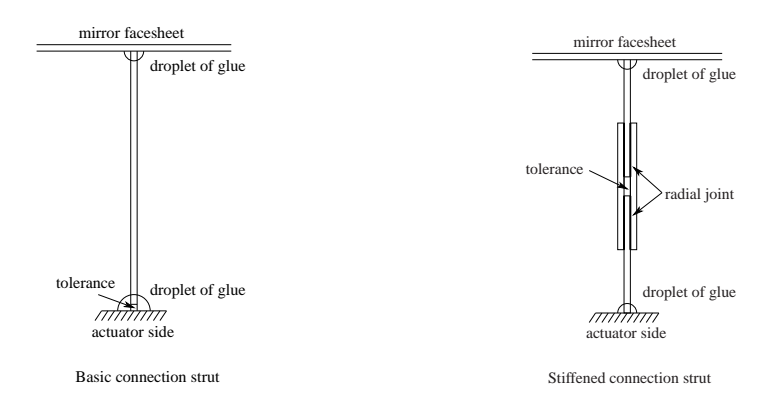


Figure 3.15: The most simplified version of the strut joint. The strut is first glued with a small droplet at the back of the mirror facesheet. Any length variation is handled at the actuator side, where the droplet can be bigger. The axial gap between at the tip of the strut can vary from strut to strut, resulting in shrinkage differences and mirror facesheet unflattness.

Figure 3.16: An alternative to Figure 3.15. Here the strut is made out of two parts. Both parts are first joint to the facesheet and actuators. A small tube will act as the stiffened central part of the strut and has a joint where length tolerances can be handled. Any radial shrinkage is this joint will not result in mirror facesheet unflattness.

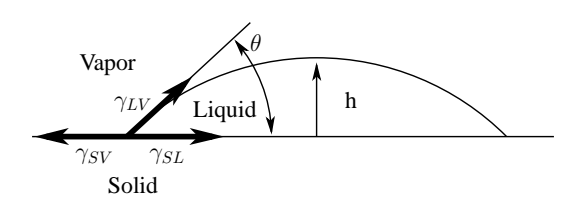


Figure 3.17: The shape of a glue droplet.

referred to as 'amine-blush' or 'sweating'. The amine component reacts with moisture and atmospheric carbon dioxide to form ammonium bicarbonate and/or ammonium carbamate [26]. Araldite 2020 proved to be sensitive to the environmental conditions. In several tests the small droplets did not harden although properly mixed. This is attributed to the amine blushing, since the small droplets have a relatively large exposed surface area with respect to its volume. Because of its high strength and the lack of amine blushing, DP460 is finally chosen.

When a droplet of glue is placed on the mirror facesheet, the droplet can spread out completely or form an almost perfect sphere like a water droplet on a waxed surface. In the first case the droplet fully wets the surface and in the second case there is no wetting at all. Figure 3.17 gives a generalized shape of a droplet on a flat solid surface. The contact angle θ represents the wettability and is related to the interfacial tensions of the system. From Figure 3.17 the contact angle in the thermodynamic equilibrium is given by the Young's equation [209]:

$$\gamma LV \cdot \cos \theta = \gamma SV - \gamma SL$$

Where γSL , γSV , and γLV are the solid-liquid, solid-vapor and liquid-vapor interfacial tensions. These tensions are a measure of the free energy per unit area. Since the droplets are small, gravity forces can be ignored. If $\theta=0^{\circ}$, there is complete wetting, when $0<\theta<90^{\circ}$ the surface is partially wet, when $\theta>90^{\circ}$ the surfaces is non-wetting and

Table 3.3: Epoxy glue properties.

Epoxy	E_g	LSS^a	Viscosity ^b	Shrinkage	Mix ratio ^c	Pot life ^d
	$\left[\frac{GN}{m^2}\right]$	$\left[\frac{N}{mm^2}\right]$	[Pa·s]			[min]
Araldite 2020	2.5	17	$150 \cdot 10^{-3}$	<1%	100:30	40-50
Araldite 2011	1.9	19	30-45	<1%	100:80	90
DP460 from 3M	1	31	80	<1%	100:48	60

 $[^]a$ Lap Shear Strength at 23°. Typical value for a lap joint of 170 x 25 x 1.5mm aluminium strips.

The joint area is thereby $12.5 \times 25 \text{mm}^2$.

^b Values at 25°.

^c In weight %.

^d For 100g at 25°.

when $\theta=180^\circ$ the surface is completely non-wetting. The droplet should partially wet the surface. When fully wetted the droplet height h is small and there is a good chance that the tip of the strut will not be in the glue. No meniscus will be formed. The timescale on which the droplet will take its equilibrium shape is determined by the viscosity of the glue. When the viscosity is very high, the equilibrium shape may not be reached by the time hardening of the epoxy has already started.

Figure 3.36 and Figure 3.37 show the results of struts placed in small droplets of DP460. By pulling at the struts in axial direction, the strength of the connection is tested. The forces that could be applied before breakage are >500mN. When the joint is broken, the glue droplet remains at the back of the mirror surface and the strut is pulled out of the droplet.

The optical effect of the attachment is tested. The goal is to measure the mirror facesheet's deformation caused by the glued connection. Figure 3.18 shows an interferogram of the print through. The interferogram shows the central hexagon of a \emptyset 50mm mirror. Underneath this hexagon 7 connection struts are glued on a 6mm pitch. One central and 6 on the outer edges of the hexagon. The surface unflatness is 25nm PTV and 3nm RMS. The deformation is considered small enough. The deformation will be proportional to the bending stiffness of the mirror facesheet.

Assembly procedure

Assembly of the thin, flexible and fragile mirror facesheet, the connection struts and the soft actuators is a challenge. This section describes all assembly steps and additional tooling needed. To see whether the assembly procedure will do and to gain experience, first a Ø150mm Pyrex facesheet is connected with connection struts to a rigid dummy instead of a more expensive actuator array. In Chapter 6 assembly to the actuator array will be shown. From Chapter 4 it will be clear that the actuators are arranged in hexagonal actuator modules containing 61 actuators each. Under a Ø150mm facesheet, 7 of these modules will be placed. That arrangement with 427 actuators is used in this assembly procedure. The tooling developed is identical for the dummy and for the actuator arrays. With small modifications, other actuator arrangements and pitches are possible. Furthermore the tooling allows mirrors with diameters up to 200mm to be assembled.

Goal of the assembly is to end up with an initially flat mirror facesheet. This means that the mirror unflattness should be $\pm 1 \mu m$ and the actuator forces needed to flatten the mirror will be $\approx 10\%$ of the total available force. To make the assembly possible, the mirror facesheet is attached to a reference flat. This reference flat is provided by the porous graphite air bearing. A vacuum pump connected to the air bearing will ensure the mirror facesheet to copy the shape of the air bearing.

With the mirror facesheet attached to the air bearing, the struts are first attached to the mirror facesheet and in a second step the struts are attached at the actuator side. Finally the air bearing can be removed.

All individual steps are shown and discussed in detail below.

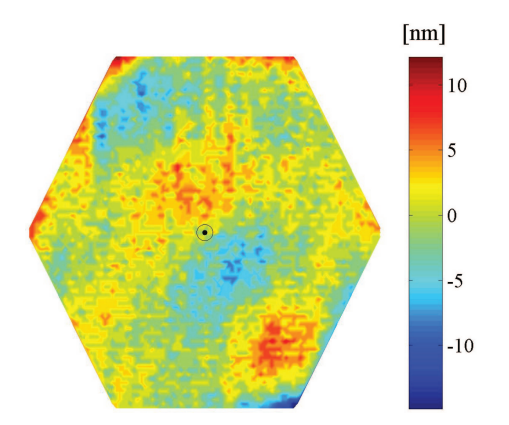


Figure 3.18: An interferogram of a central hexagon of $\varnothing 50$ mm, 100μ m thick, Pyrex mirror. At the back of this hexagon, 7 struts are glued on the 6mm pitch. A central one and 6 on the edges. The total unflatness is 25nm PTV and 3nm RMS.

1 Placement of the mirror facesheet on the porous graphite air bearing.

With the use of a porous graphite air bearing and a vacuum pomp it is possible to 'suck' the mirror facesheet to the air bearing's reference surface. Since the air bearings in normal application are used with air gaps of $\approx 5\,\mu m$ the air bearing's flatness is expected to be good. The flatness of the air bearing is measured with an interferometer and shown in Figure 3.19. For the $\varnothing 200mm$ air bearing 12 interferograms were stitched together. Figure 3.19 shows the air bearing to be $\approx 4\mu m$ concave. Superimposed on this global concave shape, concentric grooves with 150nm PTV are present. This is probably print through caused by the glue, which joints the slice of graphite to the aluminium housing. The shape of the air bearing when the focus term is removed is shown on the right in Figure 3.19. From the

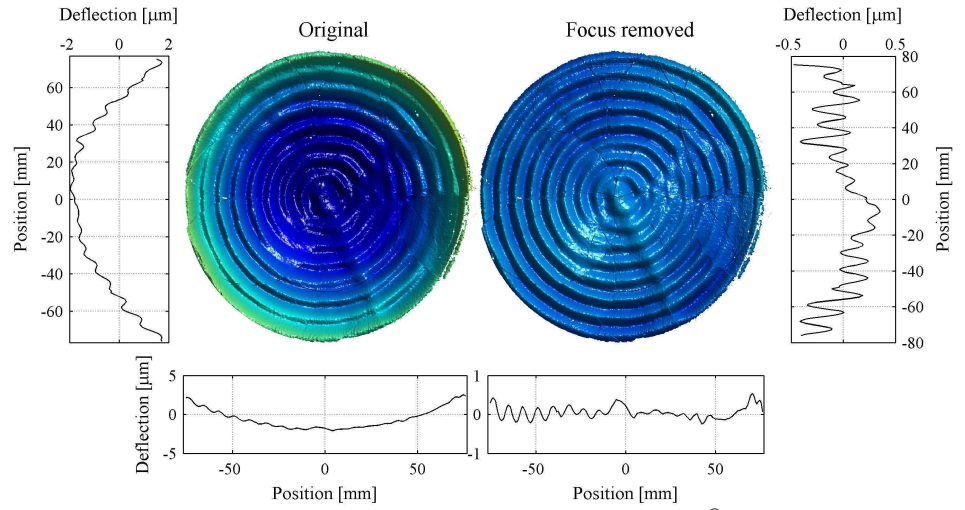
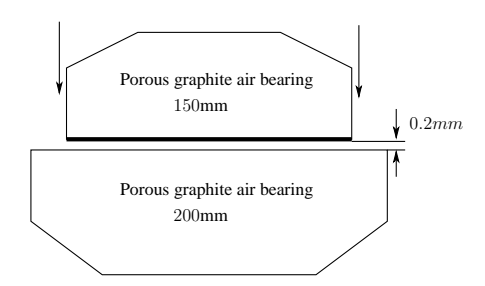


Figure 3.19: The flattness of the central $\varnothing 150$ mm of a $\varnothing 200$ mm NewWay[®] air bearing. On the left the stitched interferogram. On the right the measurement with the focus term removed.

62 3 The mirror facesheet

Figure 3.20: Vacuum pressure clamps the mirror facesheet to the upper air bearing. The upper air bearing is lowered to a few tenths of a mm above the reference air bearing. When the vacuum is removed the mirror facesheet will 'fall' down. Vacuum pressure connected to the lower air bearing will hold the mirror facesheet.



interferograms it is clear that the air bearing will only copy low spatial frequencies with significant amplitude into the mirror facesheet. These frequencies correspond with a low facesheet stiffness and will therefor, when corrected, result in low actuator forces. The air bearing therefor serves as a suitable reference for the mirror facesheet.

The Pyrex facesheet is manufactured by LightMachinery in Ottawa, Canada and provided with a single sided protected aluminium coating. This $\emptyset 150$ mm facesheet is only 0.1mm thick and therefor vulnerable and should be handled with care. Handling and placement on the reference air bearing is done in a clean room. Goal is to avoid dust to be trapped between the air bearing reference surface and the mirror facesheet. This is done with the following steps.

- The Pyrex mirror is placed with the non-coated side facing upwards. This side of the facesheet is cleaned with Whatman Grade 105 lens cleaning tissues and isopropanol.
- A second, in this case Ø150mm porous graphite air bearing is cleaned with isopropanol. With the vacuum pump connected to this air bearing, the mirror facesheet is sucked onto this air bearing.
- Supported by the air bearing the coated side of the mirror facesheet can now be cleaned. After cleaning, the mirror and air bearing are suspended with the mirror facing down.
- The \(\times 200\)mm air bearing is cleaned. This air bearing is, with the reference surface upwards, placed under the air bearing holding the mirror facesheet. The latter is lowered to a few tenths of a mm above the \(\times 200\)mm reference air bearing. When properly cleaned, no dust particles are present between the mirror facesheet and the reference air bearing.
- The vacuum pump is turned off and the mirror facesheet will 'fall' on the reference air bearing. This is schematically shown in Figure 3.20. A small overpressure can be used to release the facesheet from the top air bearing. In case air is trapped under the fallen facesheet, a few pieces of scotch tape at the circumference prevent the mirror facesheet from sliding off. In Figure 3.21 a photo of the Ø150mm Pyrex facesheet placed on the Ø200mm air bearing is shown.

An alternative for isopropanol and lens cleaning tissues is CO₂ snow cleaning. In this surface cleaning method a combination of high velocity small dry ice particles and carbon



Figure 3.21: Photo of the aluminium coated, $\varnothing 150mm$ Pyrex mirror facesheet placed on the $\varnothing 200mm$ air bearing. The filter of the air flow cabin is visible in reflection.

dioxide gas streams are directed towards the mirror facesheet. The interactions between the solid and gaseous CO_2 and the surface particles and hydrocarbon contamination lead to surface cleaning [135]. Cleaning with CO_2 snow leads to removal of micron and submicron sized particles.

But even in a clean room environment it is difficult not to trap any dust particles. A typical dust particle will cause a bump of a few micron high and a few mm across. Besides thorough cleaning, a possible solution is to make grooves in the graphite surface where particles can be embedded. The grooves should be small to avoid significant quilting of the mirror facesheet under the vacuum pressure.

The porous graphite can be machined well by fly cutting and lapping. The possibility to make a flatter reference surface with additional grooves is therefor considered realistic.

2 Attachment of the connection struts to the mirror facesheet.

A few possible ways to attach the connection struts to the back of the mirror facesheet exist. A first option is to dip the tips of the struts in glue. When the struts are pulled out of the glue a residue is left on the tip of the struts, similar to the phosphor tip of a match. The strut tips are then placed on the backside of the mirror facesheet. This step could be done for all struts simultaneously. The struts need therefor be pre assembled in a holder with all the strut tips at equal height. An advantage is that the alignment between droplet and strut tip is guaranteed and a short lead time is present, independent of the number of struts. Practice with Araldite[®] 2020 showed that the droplet will not stay at the tip, like the phosphor tip in a match, but move over the struts cylindrical face. Therefor a meniscus is not formed between the strut and the mirror facesheet.

Alternatively the droplet is placed on the mirror facesheet first and the strut is pushed through the surface tension of the droplet. A good meniscus is thereby formed, but additional alignment between the droplet and strut should be provided. When the strut is not placed concentrically with the droplet, the surface tension of the droplet will force the droplet towards a more rotationally symmetric meniscus. When the droplets are placed sequentially, the lead time increases with every strut added. With large numbers, significant epoxy curing may be present. When the struts are placed directly after each droplet or when a screen printing technique is used, no significant curing will be present. Still alignment

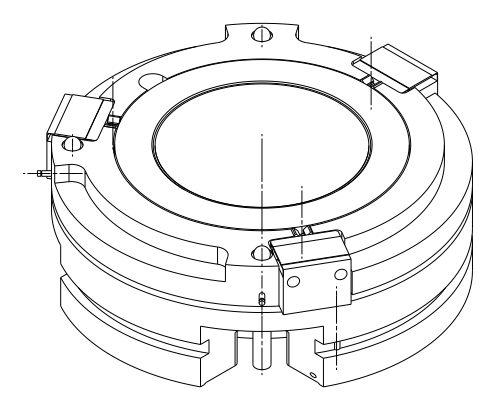




Figure 3.22: Overview of the aluminium housing, which contains the air bearing and the alignment ring.

Figure 3.23: Photo of the droplets placed by a dispensing needle, which is mounted in the machines z-axis.

between droplet and struts is needed.

In the prototype development, the number of actuators does not exceed 427, therefor sequential placement of the glue droplets is still possible in 5-10 minutes without significant curing.

2a The air bearing with the mirror facesheet is placed in a housing and aligned.

The air bearing with the mirror facesheet is placed in an aluminium housing. Figure 3.22 shows this housing with the reference air bearing and mirror facesheet. Figure 3.24 shows the exploded view. The drawings show that the airbearing with the mirror facesheet is assembled from the back. A cover and a rubber ring will press the air bearing to ensure proper clamping of the reference side to the aluminium housing. An alignment ring is connected to the aluminium housing by three folded leafsprings. These folded leafsprings constrain, similar to Figure 3.4, x, y and θ . Three micro spindles are placed orthogonally to the alignment ring and allow adjustment with respect to the housing in z, φ and ψ . The round spindle tips make contact with tungsten carbide plates, which are glued in the aluminium alignment ring. Springs ensure contact. In the ring three V-grooves are also present, placed under 120°. The V-grooves are made from tungsten carbide plates, which are glued to the alignment ring. On the machine, which places the glue droplets, the mirror facesheet is aligned with the machines x- and y-axis. By measuring the position of the three V-grooves, the θ -rotation is adjusted. A groove at the circumference of the aluminium housing enables clamping on the Computer Numerical Control (CNC) machine bed.

When the housing is aligned and fixed, the droplets are placed on the mirror facesheet.

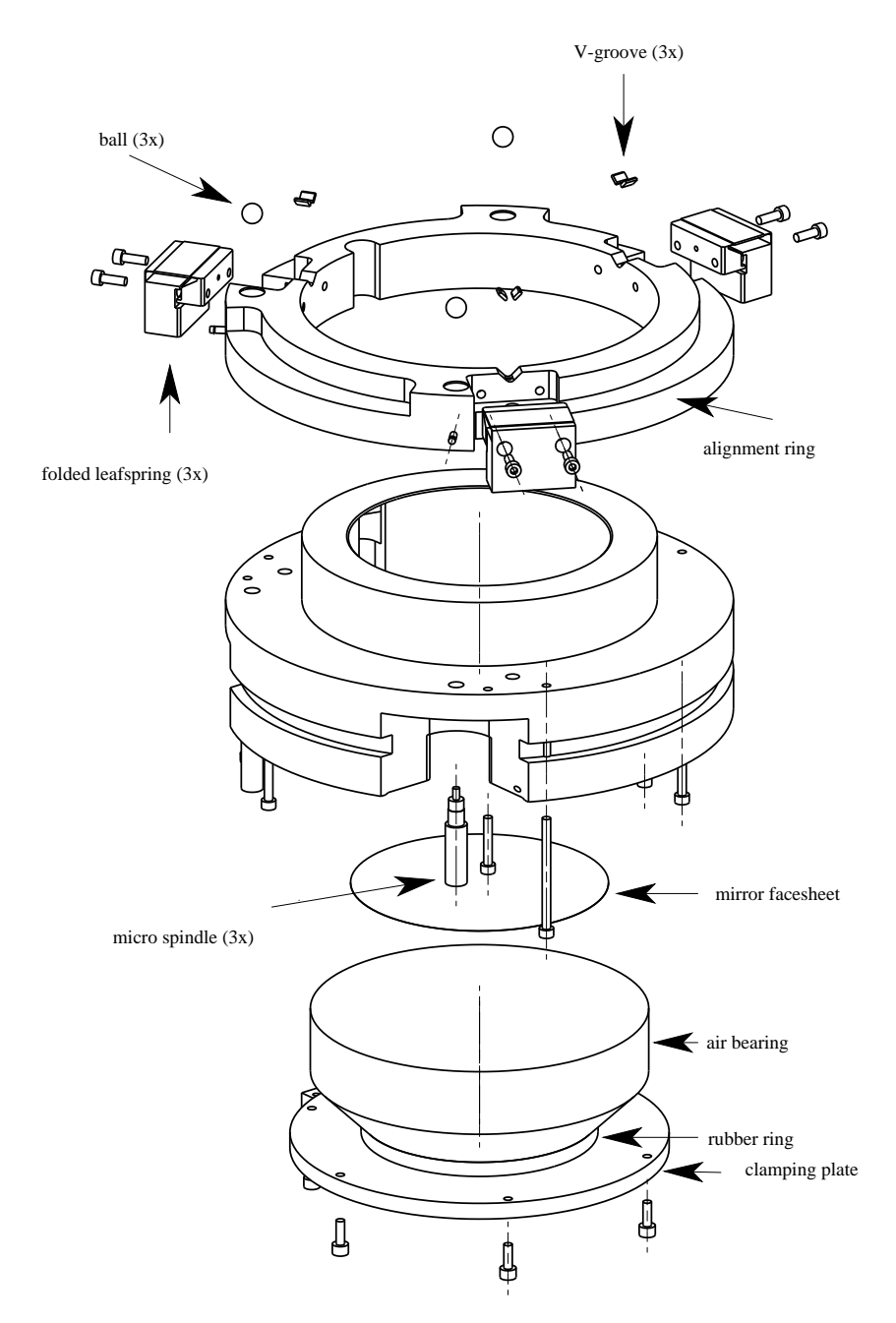


Figure 3.24: Exploded view of the assembly in Figure 3.22.

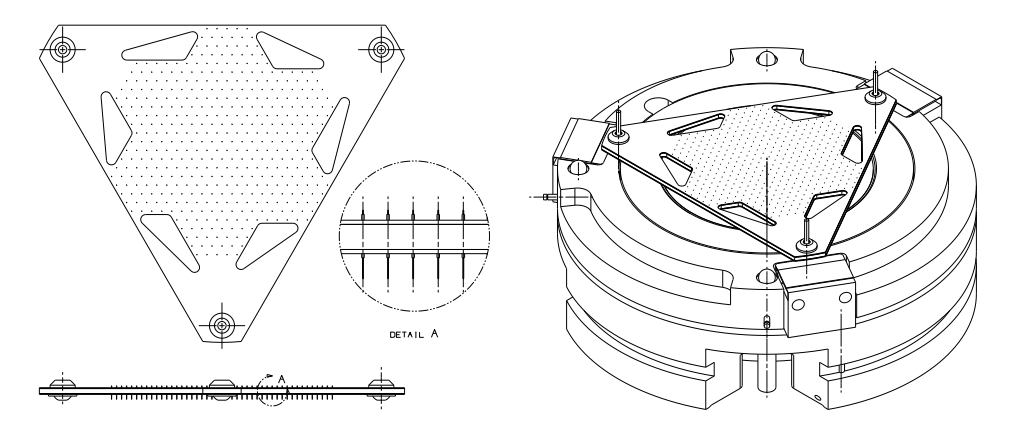


Figure 3.25: Drawing of the strut holder.

Figure 3.26: The strut holder connected to the alignment ring.

2b Droplets of glue are placed on the mirror facesheet.

A CNC program moves the needle from actuator position to the next. On each position the needle is lowered. With an EFD Pressure Dispenser a positive pressure is applied for a short time period. The glue is forced through the gauge 30 needle. This needle has a 0.15mm inner diameter. The positive pressure is followed by a short time period with under pressure that prevents excessive glue from flowing out. When the droplet is placed, the needle retracts and moves to the next actuator position. Figure 3.23 shows a photo of the syringe in its holder, mounted to the machine z-axis and the droplets placed on the $\varnothing 150$ mm Pyrex mirror facesheet.

2c The holder with struts is placed.

To place all struts orthogonally to the mirror facesheet they are placed in a holder. This holder consists of a plate that contains 427 tubes, made from needles. The needle tubes are used because it is hard to drill a hole with $\emptyset 0.1$ mm with sufficient length to guide the struts. Even with the $\emptyset 0.3$ mm thick needle tubes a hole over several mm is costly. Therefor the plate is assembled from three layers. The 0.5mm thick aluminium outer layers hold the pattern with $\emptyset 0.3$ mm holes and are glued on a 3mm thick aluminium core with larger holes. This pattern is modified when a different actuator grid is needed. The needle tubes are threaded through the sandwich plate and glued. Figure 3.25 shows the drawing of the holder filled with connection struts. Additional slots are made, which make it possible to observe the glued connection.

At the corners of the holder, three balls are glued in cups for alignment of the holder with respect to the alignment ring. Each ball contains a hole for a bolt. A spring is added to ensure contact between the ball of the holder and groove in the alignment ring.

Figure 3.26 shows the holder connected to the alignment ring by the three balls and V-grooves. Each tube is filled with a connection strut before the gluing starts. A thin plate





Figure 3.27: Photo of the strut holder in place.

Figure 3.28: Photo of a few struts guided by the needle tubes while placed in the glue droplets.

underneath prevents the struts from falling through. When placed above the droplets this plate is laterally retracted. A rubber layer and a weight is placed on the struts to press the tips into the glue droplets.

Figure 3.27 shows a photo of the holder with the struts in place. Figure 3.28 shows a photo of a detail where a few struts can be seen, guided by the needle tubes and placed in the droplets.

2d The glue is hardened and the strut holder is removed.

When the glue is hardened the strut holder is removed. By rotation of the spindles, the alignment ring with the strut holder is moved in z until the needle tubes are above the struts. Then the holder can be removed manually. The grid with struts, glued to the mirror facesheet, remains. Figure 3.29 shows all the 427 struts placed on the back of the mirror facesheet after removal of the strut holder. In Figure 3.30 a detail of the grid with struts is



Figure 3.29: With the strut holder removed the grid of struts becomes visible.

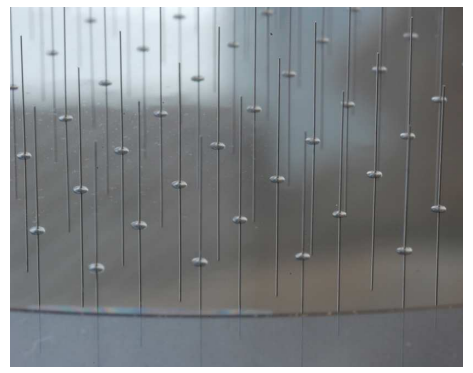
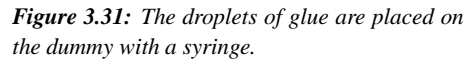


Figure 3.30: Detail of the struts placed in droplets of glue.





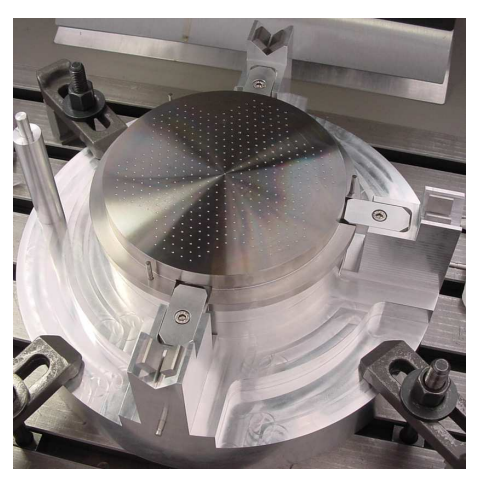


Figure 3.32: The droplets of glue after placement on the dummy.

shown. The mirror facesheet with struts is now ready to be attached to the actuator side.

3 Attachment of the struts to the actuator side.

To gain practice a first mirror facesheet with connection struts will be attached to an actuator dummy. In analogue to step 2, the dummy is placed on an aluminium base that is aligned to the CNC machine. Figure 3.32 shows the dummy placed on this base. The aluminium base holds three V-grooves. These V-grooves are made from tungsten carbide and glued to the base. Alignment on the machine is carried out with respect to these V-grooves. The dummy, which consists of a $\varnothing 165 \times 25 \,\mathrm{mm}$ stainless steel disc is placed on a thick aluminium spacer

Figure 3.33: The assembly in the last step. The upper part contains the air bearing, which holds the mirror facesheet and connection struts. The lower part contains the actuator dummy. Three balls in the upper part fit in three radially placed V-grooves in the lower part. The upper part is lowered until the strut tips are in the droplets of glue placed on the actuator dummy.

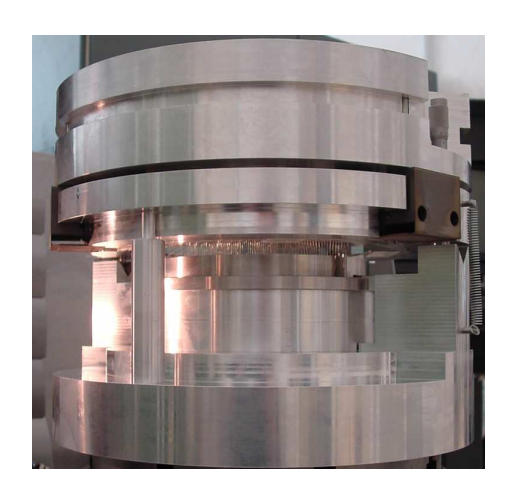




Figure 3.34: The Ø150mm, 0.1mm Pyrex mirror facesheet successfully connected with 427 struts to an actuator dummy.

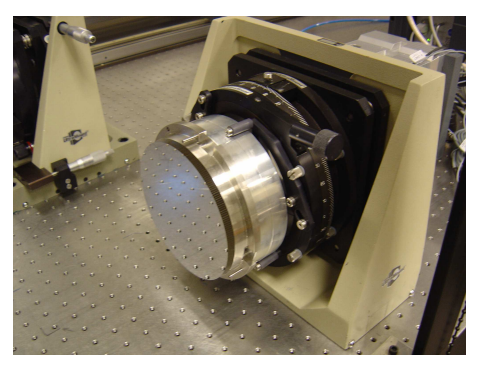


Figure 3.35: The assembled prototype placed vertically in front of the Wyko 400 interferometer.

and clamped on the base. When the base with the dummy is aligned, the base is clamped to the machine. The droplets can be placed. This is done in a way similar to the droplets on the mirror facesheet side. Figure 3.31 and Figure 3.32 show photos of the droplets being placed and the finished grid. When the droplets have been placed, the assembly, which consists of the aluminium housing with reference air bearing, mirror facesheet, connection struts and alignment ring, is placed above the droplets. The three balls in the alignment ring connect hereby to the three V-grooves in the base. When placed, contact is ensured by springs, which pretension the contact. The three spindles attached in the housing, align the mirror facesheet and struts in z, φ and ψ with respect to the dummy's front surface. The tips of the struts are hereby placed in equal distance to the surface and lowered into the droplets.

When the strut tips break through the surface tension and enter the droplets, it is difficult to see how close they are to the front surface of the dummy. Lowering the struts is therefor first done without the droplets present. The tips of the struts are observed through a binocular microscope that is placed at the circumference of the housing. The spindle's micro scale

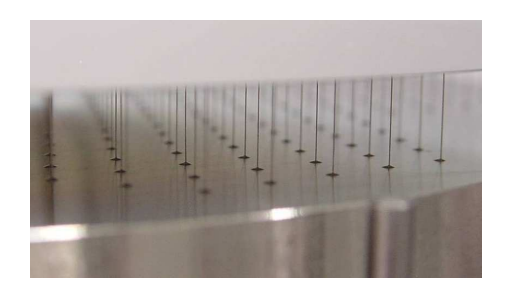


Figure 3.36: Photo of the connection struts placed in rows on a 6mm pitch. Each connection strut is $\emptyset 0.1 \times 8mm$.



Figure 3.37: Photo of a detail of the 427 connections struts between the mirror facesheet and the actuator dummy. The meniscus at the facesheet and actuator side are visible.

is read when the struts are 0.1mm above the front surface. The assembly is then taken off, droplets are placed, and the spindles lower the struts to the previously found spindle settings. To prevent the upper assembly from tipping over, an extra strut is placed. The strut will not support the alignment ring, but only serve as a safety stop. Figure 3.33 shows the final assembly with the safety strut in front.

4. Removal of the reference air bearing and its housing.

When the glue is hardened, the top assembly with the air bearing reference is removed. First the vacuum pump is disconnected. The upper assembly is slowly moved upwards by the spindles. This is done very slowly because air should be given time to flow in the narrow gap between the mirror facesheet and the air bearing. When sufficiently separated the upper assembly can be removed entirely. The mirror assembly becomes visible. Figure 3.34 shows the mirror facesheet with 427 struts successfully attached to a stainless steel actuator dummy. Figure 3.36 and Figure 3.37 show details of the connection struts glued to the mirror facesheet and the actuator dummy.

3.7 Results

The assembled prototype is placed vertically in front of a Wyko 400 interferometer with Intelliwave wavefront reconstruction software. The assembly placed in the measurement mount is shown in Figure 3.35. Since the maximum diameter that can be measured with the interferometer is 4", a full interferogram is realized through stitching. The stitched result of the measurement is shown in Figure 3.38 on the left. Since the 427 actuators do not support the whole $\varnothing 150$ mm facesheet, the unsupported edges are removed from the interferogram. In the interferogram the actuator locations are plotted as black dots.

The result is a facesheet with a PTV unflattness similar to the reference air bearing, although no direct relation is visible with Figure 3.19. The actuator dummy is rigid and as a consequence all axial shrinkage will result in displacement of the mirror facesheet. With the rigid dummy replaced by the actuator stiffness this effect will be reduced since the actuator stiffness is significantly lower than the facesheet out-of- plane stiffness.

When the initial facesheet shape is theoretically corrected with the actuators influence functions a best flat is made. This flattening procedure is described in detail in Section 6.3.2. Here only the results are shown. After the flattening only the high spatial frequencies that can not be corrected by the actuators remain. The residue shown in Figure 3.38 on the right shows an unflatness of 20nm RMS. In Section 6.21 the actuator forces needed for this flattening are shown to be 0.4mN RMS.

3.8 Conclusions and recommendations

Materials and fabrication techniques for thin, large scale, rigid, active and adaptive mirrors have been summarized. Thin and ultra thin glass mirrors conventionally machined for ASMs and NMSDs and slumped glass mirrors from FPD substrates are discussed. Thinned silicon and Pyrex wafers up to $\varnothing 300$ mm are well suited for membrane deformable mirrors. Also high specific stiffness materials as beryllium, used for X-ray windows and CFRP are considered. Newly developed nanolaminates, ERAF replication and space membrane technologies conclude the list.

The DM design is driven by minimizing the power dissipation P. A thin mirror facesheet is needed for low actuator forces F_a and power dissipation. The facesheet thickness t_f lower limit is set by the inter actuator deflection σ . This deflection is determined by gravity or when wind speeds >1m/s are present, by wind pressure. For both situations the scaling laws for F and P are derived, depending on the size of the uncompressed wavefront D_t , the compression factor c_D , which is $\frac{D_t}{D_{DM}}$, the number of actuators N_a and the thickness of the

mirror. For gravity induced deflection the total actuator force is $F \propto \frac{1}{N_a} \left(\frac{D_t}{c_D}\right)^4 \rho_f \sqrt{\frac{\rho_f}{E_f}}$. With the telescope's optical design and desired optical quality fixed, the power dissipation is minimized by selecting a facesheet material with high $\frac{E_f}{\rho_f^3}$. When significant wind pres-

sure is present, the total actuator force is $F \propto \left(\frac{D_t}{c_D}\right)^2 p_w$. F and P are independent of the facesheet material properties and the number of actuators.

For this deformable mirror, only gravity induced deflection is taken into account. Minimum power dissipation is achieved when beryllium is used for the mirror facesheet. With $35\mu m$ facesheet thickness and an actuator grid with 6mm pitch 1nm RMS inter actuator deflection is present. Since thin beryllium facesheets are expensive and several are needed for the prototype developments, Pyrex facesheets with $100\mu m$ thickness are chosen as a best practical, alternative.

The actuators are the out-of-plane constraints for the mirror facesheet and determine the mirror's first resonance frequency f_e . When the actuator stiffness c_a is smaller than the mirrors bending stiffness of the facesheet between two actuators, f_e is well approximated with $=\frac{1}{2\pi}\sqrt{\frac{c_a}{m_{a_f}}}$, where m_{a_f} is the total mass of the facesheet divided by the number of

actuators carrying the facesheet. The first resonance is independent of the mirror diameter and the mode shape is a global bending of the mirror. When c_a is further increased, local modes appear and more stiffness will not increase the resonance. The actuator is now a stiff actuator and there will be a hard point in the mirror facesheet.

The design goal for the actuator stiffness is $c_a = 500 \text{N/m}$. Hereby the first resonance is >1kHz, which is needed for the 200Hz closed loop bandwidth, but not higher than the necessary to avoid excessive actuator forces and dissipation.

The in-plane DOFs of the mirror facesheet are constrained with three tangentially placed folded leafsprings. With the actuator stiffness, the actuator coupling is 0.65 for the thicker Pyrex mirror and 0.28 for the beryllium facesheet.

A smooth influence function is achieved with the connection struts between the actuators and the mirror facesheet. The connection struts allow the mirror facesheet to form a smooth surface over the imposed heights. When the bending stiffness, axial stiffness, resonance fre-

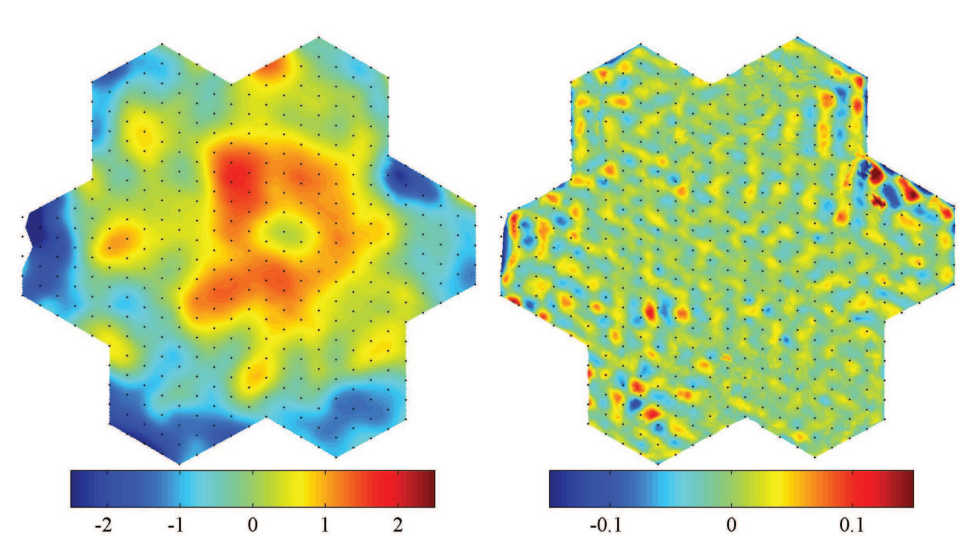


Figure 3.38: The stitched interferogram on the left shows the shape of the mirror facesheet of the assembly shown in Figure 3.34. The edge of the facesheet is not supported by the struts is removed. The strut positions are plotted as black dots. On the right the residue is shown after a theoretical flattening with 427 actuators.

quency and buckling load of the strut are considered, the diameter and length of the struts are determined. A round stainless steel strut with $\emptyset 0.1 \times 8 mm$ is chosen.

The struts are glued, with DP460 epoxy, to the backside of the mirror facesheet and actuators. Interferometric measurements show a 3nm RMS surface unflattness caused by the glued attachment. Tooling is developed to assemble the struts to the mirror facesheet and the actuators for mirrors up to $\varnothing 200$ mm. A dummy prototype is made with a $\varnothing 150$ mm Pyrex facesheet, connected with 427 struts to an actuator dummy. The goal is an initially flat mirror facesheet. Therefor the facesheet is supported by a porous graphite air bearing during the assembly. The 427 struts are placed in a holder and placed in small glue droplets at the backside of the mirror facesheet. With the glue hardened and the holder removed, the facesheet with struts is placed in droplets of glue placed at the actuator side. The flatness of the assembly is measured to be $4\mu m$ PTV, which is in the same order of the unflattness of the air bearing reference. The assembly tooling and procedure is also suited to assemble the struts to the actuator grids.

One of the most difficult steps is to place the mirror facesheet on the reference air bearing without dust being trapped. By adding grooves in the air bearing, the chance that a dust particle causes a bump in the mirror surface, is reduced.

Chapter four

Modular actuator grid

This chapter describes the low voltage electromagnetic variable reluctance actuators, which are used in the adaptive Deformable Mirror. The actuators are arranged hexagonally in a module of 61 actuators on a 6mm pitch. The actuators have a stroke of $\pm 10\mu m$, nm resolution and high efficiency. Each actuator consists of a Permanent Magnet surrounded by a coil, a ferromagnetic moving core in a membrane suspensionand a baseplate. The magnetic force from the PM attracts the ferromagnetic core, which causes the membrane suspension to deflect. A current through the coil will, depending on its direction, decrease or increase the electromagnetic force and thereby cause a translation of the core. In the design there is force equilibrium between the mechanical spring and the electromagnetic force. The positive stiffness of the membrane suspension together with the negative stiffness of the magnetic circuit determine the actuator stiffness. Static and dynamic electromagnetic models of the actuator are derived. These models include leakage flux. For 7 actuator modules, each individual actuator is measured in an automated set-up. The measurements of the motor constant, actuator stiffness and resonance frequency show reasonably good agreement with the analytical models. The sensitivity of parameters, such as dimensions and material properties, for variation of the motor constant, actuator stiffness and resonance frequency is analyzed and differences between the model and measurements are explained.

4.1 Actuator requirements

In Section 2.2, the actuator requirements that result from the atmospheric conditions, telescope aperture and desired optical quality are derived. For an 8-meter wavefront in the visible (380< λ <750nm) the aim is to reduce the wavefront error in medium seeing conditions (r₀=0.166m at λ =550nm) to $\frac{\lambda}{16}$. The main requirements for the actuators are enumerated.

- The number of actuators N_a . To reduce the fitting error ≈ 5000 actuators are needed.
- Actuator pitch d and arrangement.
 The diameter goal of the DM is 500mm. For 5000 actuators this results in a ≈6mm pitch. A hexagonal arrangement is chosen, because this results in the most actuators per unit area and the most rotationally symmetric influence function.
- The actuator stroke.
 For the atmospheric disturbance correction ±5.6μm mechanical stroke is needed. A few micron is added to prevent saturation when alignment errors are present. The total actuator stroke needed is therefor ±10μm.
- The inter actuator stroke. The inter actuator stroke is determined by the atmospheric conditions and the actuator pitch and is $\pm 0.4 \mu m$.
- The actuator resolution.

 The resolution should be a fraction of the wavelength and is set on 5nm.
- The first resonance frequency and actuator stiffness. In Section 3.3.1 is shown that an actuator stiffness c_a = 500N/m is needed. With this stiffness the first resonance frequency of the mirror facesheet is \approx 1kHz and will thereby enable 200Hz control bandwidth. The actuator stiffness is significantly lower than the out-of-plane stiffness of the mirror facesheet between two actuators. The actuator is therefor called a soft actuator.

Besides these requirements, the actuators should be free of drift and hysteresis. If not, this can lead to a significant complexity increase for the mirror control system. Local position sensors would be needed.

When a large number of actuators is needed, the MTBF and the consequences of an actuator failure become relevant. A simple and robust actuator, which is preferably replaceable, is ideal. Since the actuators are soft, the optical degradation is case of an actuator failure is limited: the facesheet will take the mean position of the adjacent actuators.

The actuators design should be suited for large numbers. Therefor it is chosen not to make individual actuators and positions each with respect to each other, but to manufacture the actuators in modules of several actuators. With these modules, the actuator grid can be extended without much effort.

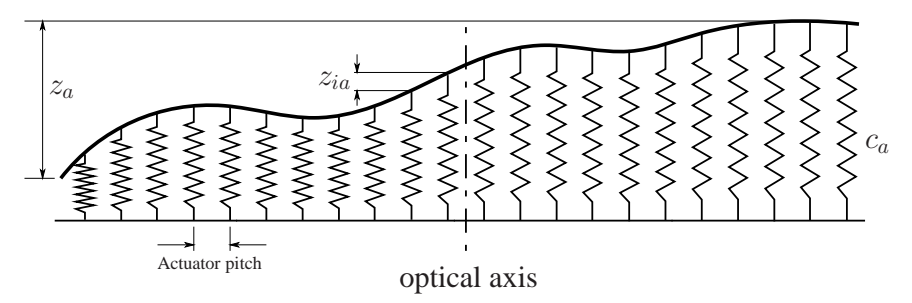


Figure 4.1: The actuator force is determined by the actuator stiffness c_a , the facesheet stiffness c_f , the actuator stroke z_a and the inter actuator stroke z_{ia} .

4.1.1 The actuator force

The inertial and damping forces are at least one order of magnitude smaller than the stiffness forces. The actuator force requirements are therefore only determined by stiffness and stroke. Figure 4.1 shows that the actuator force F_a can be approximated by:

$$F_a = c_a z_a + c_f z_{ia} (4.1)$$

where c_a and c_f are the actuator and mirror facesheet stiffness and z_{ia} and z_a are the inter actuator and actuator stroke. Typical values are $c_a=500\text{N/m}$ and $c_f=6000\text{N/m}$. The actuator force is calculated with and $z=\pm5.6\mu\text{m}$ and $z_{ia}=\pm400\text{nm}$. This results in $F_a\approx\pm5\text{mN}$, the RMS force is thereby estimated to be 1mN.

4.2 Electromagnetic actuators

Electromagnetic actuators are considered an alternative to the stiff, widely used, piezo electric actuators. Electromagnetic actuators can be produced at very low cost. A widely known example is found in a CD or DVD player.

Two types of electromagnetic actuators will be discussed here. First, the voice coil or Lorentz actuator and second the (variable) reluctance actuator.

4.2.1 The Lorentz actuator

The Lorentz force F_L is the force on an electrical current in a carrier in the presence of a magnetic field. The force on a coil, with current I_a , and resulting Ohmic loss P_a is calculated with:

$$F_L = B \times I_a L_w, \qquad J_a = \frac{I_a}{A_w}, \qquad V_a = A_w L_w$$

$$F_L = B \times J_a V_w, \qquad R_a = \frac{\rho_e L_w}{A_w}$$

$$P_a = I_a^2 R_a = J_a^2 V_w \rho_e = \frac{F_L^2 \rho_e}{B^2 V_w}$$

where B is the magnetic field density, I_a the current through the actuator coil, L_w the length of the coil wire in the magnetic field, J_a the current density in the coil windings, A_w the cross section of the winding, V_w the coil volume and R_a the electrical resistance of the actuator coil. In most designs the magnetic field is made by a PM. For the coil, the fill factor has to be taken into account. The fill factor depends on the method of winding, the coil wire's cross section and size and the isolation layer on the wire. The fill factor will reduce the effective coil density.

When the current density J_a is under 10 A/mm² usually no thermal problems exist and a long lifetime is guaranteed.

The efficiency η of the voice coil actuator is expressed by:

$$\eta = \frac{F_L}{\sqrt{P_a}} = B\sqrt{\frac{V_w}{\rho_e}}$$

An efficient actuator is achieved with a high flux density, a large coil volume and coil wires made of material with a low electrical resistance, such as copper, aluminium or silver.

The coil or the PM can be the moving part in the voice coil actuator. Since the mass of the coil is much smaller this is often preferred. A linear current to force relation can be obtained when the product of B and I_a is equal in all coil positions. This can be realized with an uniform magnetic field throughout the total stroke, or with a smaller magnetic field in which a constant number of windings pass. Of course the latter is less efficient.

With an elastic suspension for the moving part, the actuator is free from friction, mechanical hysteresis and play and its resolution is mostly determined by the driver electronics and/or measurements system.

The actuator has no stiffness, except for the stiffness of the suspension. In for example the ASMs [18–20] such actuators are used. The PM moves with the mirror facesheet and the actuators have no mechanical stiffness. In the ASMs additional control stiffness is added by local position feedback and a complex control system [159].

With the low stiffness desired, a disadvantage of a moving coil is the parasitic force that the connection wires exert. A second disadvantage is the limited heat transfer from the coil. The heat developed has to cross the air gap before it is removed by conduction. This results in a higher coil temperature.

An alternative to the voice coil actuator is the reluctance actuator. In this actuator the advantages of a low moving mass and a fixed actuator coil are combined with a high actuator efficiency.

4.2.2 Reluctance actuators

In the reluctance actuator, ferromagnetic material is attracted by a magnetic force. It is often called a hybrid actuator, when - besides coils -, a PM is present for magnetic preloading. The main advantage of a reluctance actuator is the lower power dissipation. Figure 4.2 shows the initial reluctance actuator design. A similar actuator design can be found in [152]. In the actuator, a PM attracts a ferromagnetic membrane. This causes the ferromagnetic membrane

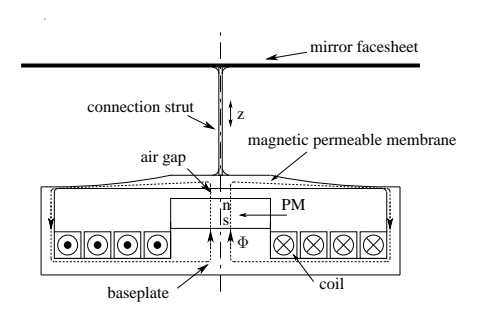


Figure 4.2: Schematic of the variable reluctance actuator. A PM attracts a ferromagnetic membrane. The magnetic flux crosses the axial air gap, passes radially through the ferromagnetic membrane and returns to the PM via the baseplate. The magnetic force provides a position bias to the ferromagnetic membrane. A current through the coil can, depending on its direction, decrease or increase the electromagnetic force and can thereby provide movement in both directions. This movement is transferred by the connection strut to the mirror facesheet.

to deflect. The magnetic flux crosses the axial air gap, passes radially through the ferromagnetic membrane and returns to the PM via the baseplate. The ferromagnetic membrane acts as a flux carrier and by its mechanical stiffness it determines, together with the negative stiffness from the magnetic circuit, the total actuator stiffness. A current through the coil can, depending on its direction, decrease or increase the electromagnetic force and can thereby provide movement in both directions. The coil is fixed and any heat is directly conducted through the baseplate. Movement of the central part of the ferromagnetic membrane is transferred by the connection strut to the mirror facesheet.

Force equilibrium and actuator stiffness

In the actuator there is a force equilibrium between the electromagnetic attraction force F_m and the ferromagnetic membrane's restoring force F_s . A good value for the initial air gap, when the current through the coil is 0, is between 50 and 100 μ m. Small enough for high efficiency and large enough to allow for sufficient actuator stroke. The airgap should also be large enough to allow particles, like dust, to be present in the airgap without malfunction of the actuator. In the equilibrium position there should be a positive stiffness c_a in the order of 500 N/m (See Section 3.3.1). This stiffness is the sum of the positive stiffness of the membrane suspension and a negative stiffness from the electromagnetic circuit:

$$F_s + F_m = 0$$
$$\frac{\partial F_s}{\partial z} + \frac{\partial F_m}{\partial z} = c_a$$

On the design as shown in Figure 4.2 two remarks need to be made concerning the membrane thickness profile and the occurrence of magnetic saturation.

1. The thickness profile of the ferromagnetic membrane. To achieve the low actuator stiffness of 500N/m, the out-of-plane stiffness of the ferromagnetic membrane should be limited. The thickness t_m should be kept small, since the bending stiffness scales with t_m^3 . For the design in Figure 4.2 all magnetic flux passes through the membrane. If saturation occurs, this will first occur at the central part of the membrane. To avoid saturation and to maintain low out-of-plane stiffness,

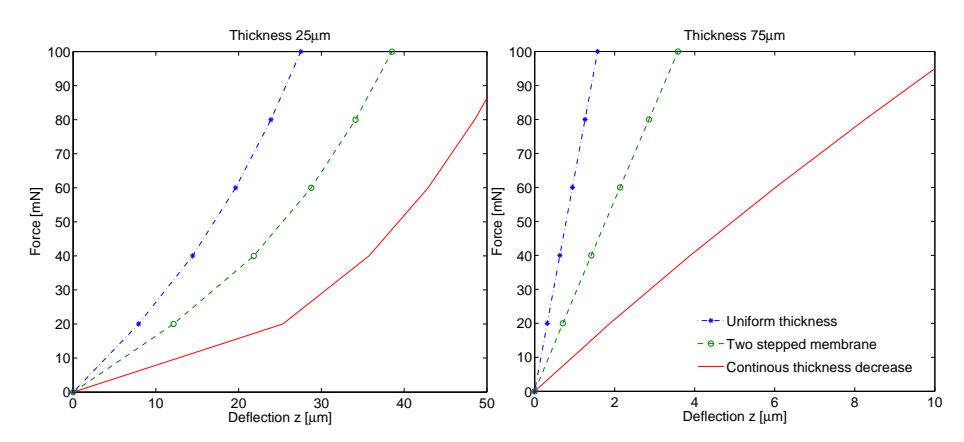


Figure 4.3: Nonlinear FEM analysis shows the deflection of a Ø5mm, clamped, 25μm and 75μm thick, centrally loaded, ferromagnetic membrane. A uniform thick, a two stepped membrane and a membrane designed for uniform flux density are analyzed.

the thickness of the membrane in inward radial direction can be increased. This is shown in the schematic design in Figure 4.2. The thickness $t_m(r)$ of the membrane is chosen such that the area A for the flux to cross is kept constant: $A=2\pi r\cdot t_m(r)$. The influence on the out-of-plane stiffness is, for these non-uniformly thick membranes, shown in Figure 4.3. The deflection of a $25\,\mu\mathrm{m}$ and $75\,\mu\mathrm{m}$ non-uniformly thick membrane is compared with the deflection of a uniform thick membrane. Furthermore as a crude but easy to manufacture approximation of the membrane with constant flux density, a two stepped membrane, is added. The results from a nonlinear analysis with Algor®, are shown for a $\varnothing 5\,\mathrm{mm}$ membrane, clamped at the edge and loaded with a central force. Figure 4.3 shows that the out-of-plane stiffness can be reduced by a factor of two without decreased flux carrying capability compared to the uniform thick membrane.

Besides the higher stiffness, the stiffness of the $75\mu m$ thick membrane is more linear. The linear bending stiffness is dominant over the nonlinear stiffness which is a result of the in-plane stretching of the membrane. More on this nonlinear stiffness can be found in Section 4.3.1.

2. Magnetic saturation.

Magnetic saturation should be avoided. The example below shows that this saturation occurs quickly without the use of materials with a high saturation limit such as CoNiFe with B_s =1.8T [151] or Vacoflux with B_s =2.2T [3].

The magnetic flux density in the membrane can be estimated when the thickness and required force and corresponding flux are known. An estimate of the thickness t_m follows from the actuator stiffness requirement. A first estimate is made, with only the bending stiffness taken into account. The bending stiffness of a constant thickness

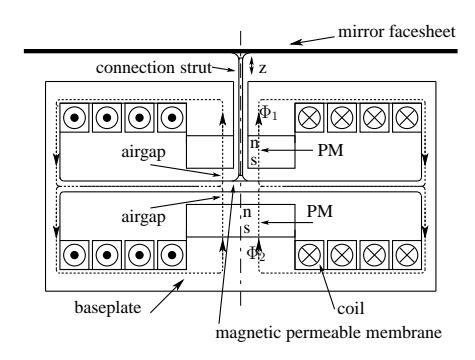


Figure 4.4: Schematic of the balanced reluctance actuator based on [153]. The actuator consist of two magnetic circuits, each with its own PM. Both PMs are magnetized in the same direction. From each PM flux travels through an axial air gap through the central membrane and back via the baseplate. Only the difference of the magnetic fluxes travels through the central membrane. Planar coils surround the PMs and are driven such that the produced magnetic fluxes are in opposite direction. This causes a decreased flux across one air gap and an increased flux across the other. In the upper PM a hole is made for the strut which connects the movement of the membrane to the mirror facesheet.

membrane, centrally loaded and clamped at the edge, is given by [185]:

$$c_m = \frac{4\pi E_m t_m^3}{3r_m^2 (1 - \nu_m^2)}$$

Where c_m is the out-of-plane bending stiffness of the thin plate, E_m and ν_m are the Young's modulus and Poisson ratio of the suspension material and r_m and t_m are the maximum radius and thickness of the membrane. As shown above, the out-of-plane stiffness roughly doubles when a membrane with non-uniform thickness, designed for constant flux density is used, due to the thickened central part. Since this will be needed to avoid saturation the out-of-plane stiffness aimed for in this calculation with the constant thickness membrane is therefor 250N/m. With E_m =2e11N/m², ν_m =0.3 and r_m =2.5mm, a membrane thickness t_m =12 μ m is found at the edge. With the dimensions of membrane known, an estimate of the maximum magnetic flux density is made when the maximum force is applied on the membrane. The relations between magnetic force F_m , flux Φ and flux density B is given by:

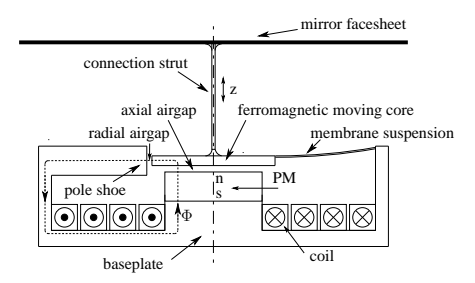
$$F_m = -\frac{\Phi^2}{2\mu_0 A_{g_a}}$$

$$B = \frac{\Phi}{A_m} = \frac{\Phi}{2\pi r_m t_m}$$

Where μ_0 the permeability of vacuum and A_{g_a} the cross-sectional area of the axial air gap for the flux to cross and A_m is the cross-sectional area for the flux to cross in the actuator membrane suspension. F_m is the bias force by the PM and the electromagnetic force created by the coil. The bias force is taken a factor 10 larger than the electromagnetic force needed for the wavefront correction (Section 4.1.1). The force F_m is therefor -55mN. With the membrane dimensions this would require membrane materials with B_s =1.8T.

From these design considerations it becomes clear that thin (\approx 12 μ m) membranes are needed to achieve c_a =500N/m and membrane materials with high saturation limit are re-

Figure 4.5: Schematic of the variable reluctance actuator used in the adaptive DM. In contrast to Figure 4.2, the membrane suspension will only serve as a mechanical spring on which the ferromagnetic core is suspended. The magnetic flux from the PM passes through the axial air gap, the ferromagnetic moving core and a radial air gap to the three pole shoes (one shown) located in the baseplate and finally back to the PM.



quired. Magnetic materials with high saturation limit have usually a low stress level allowed, typically 250N/mm^2 [3], and will therefor result in vulnerable actuators. A variant of the initial reluctance actuator, where saturation can be avoided, is shown in Figure 4.4. This is the balanced variable reluctance actuator, similar to the design proposed in [153]. The actuator consist of two PMs, which are magnetized in the same direction. From each PM flux travels through an axial air gap through the membrane back via the baseplate. Only the difference of the magnetic fluxes travels through the membrane itself. Planar coils surround the PMs and are driven such that the produced magnetic fluxes are in opposite direction. This causes a decreased flux across one air gap and an increased flux across the other. For this actuator the electromagnetic force F_m becomes [153]:

$$F_m = \frac{\Phi_2^2 - \Phi_1^2}{2\mu_0 A_m}$$

 Φ_1 and Φ_2 are the magnetic flux across air gap 1 and 2, μ_0 is the permeability of vacuum and A_m is the cross-sectional area of the air gap. F_m results from the difference of the magnetic fluxes across the two air gaps and is 0 for equal fluxes. The additional force generated by the coils is constant for a constant coil current and independent of the position of the membrane [153].

Disadvantages of the design are the number of parts and increased complexity. For example, a hole is needed in the upper PM for the strut that connects the movement of the membrane to the mirror facesheet. This makes assembly more difficult. Furthermore, when the membrane is very thin and some negative stiffness is present due to internal stresses, its use around the central position is not advisable.

To avoid both the thin vulnerable membrane with high flux densities from the initial design and the complexity of the balanced reluctance actuator, yet another alternative is proposed in the next section.

4.3 The variable reluctance actuator

Figure 4.5 shows the schematic of the variable reluctance actuator which is used in the adaptive DM. In this actuator design the membrane suspension is no longer part of the magnetic circuit. The membrane suspension will only serve as a mechanical spring by which the ferromagnetic core is suspended. The position of the moving core is coupled by a connection strut to the mirror facesheet. The magnetic flux from the PM passes through the axial air

gap, the ferromagnetic moving core and a radial air gap to one of the three pole shoes located in the baseplate and finally back to the PM. In contrast to the design in Figures 4.2 and 4.4 it is possible to select a high strength material for the membrane suspension and high magnetic permeable materials for the moving core. Figure 4.6 shows the CAD drawing of the actuator and Figure 4.9 shows a photo of a single actuator. An insert which contains the PM, the coil and part of the iron circuit is shown on the left of the photo. As in the actuators from Figures 4.2 and 4.4, a match is made between a positive stiffness from a mechanical spring and a negative stiffness from the magnetic circuit. At the cost of an extra radial air gap and increased complexity, design freedom is obtained where the membrane suspension design is separated from the magnetic flux circuit design.

In the remainder of this chapter, first the relevant actuator parts are discussed and mathematical equations for their behavior derived. This leads to nonlinear models describing both the static and dynamic behavior of the actuator. A series of measurements is performed on a single actuator prototype, whose results are used to validate the derived model. The sensitivity of the actuator behavior is then analyzed w.r.t. geometric, magnetic and electric properties, which is used to improve the actuator design before manufacturing them in modules. Finally, measurement results will be shown for the actuator module prototypes

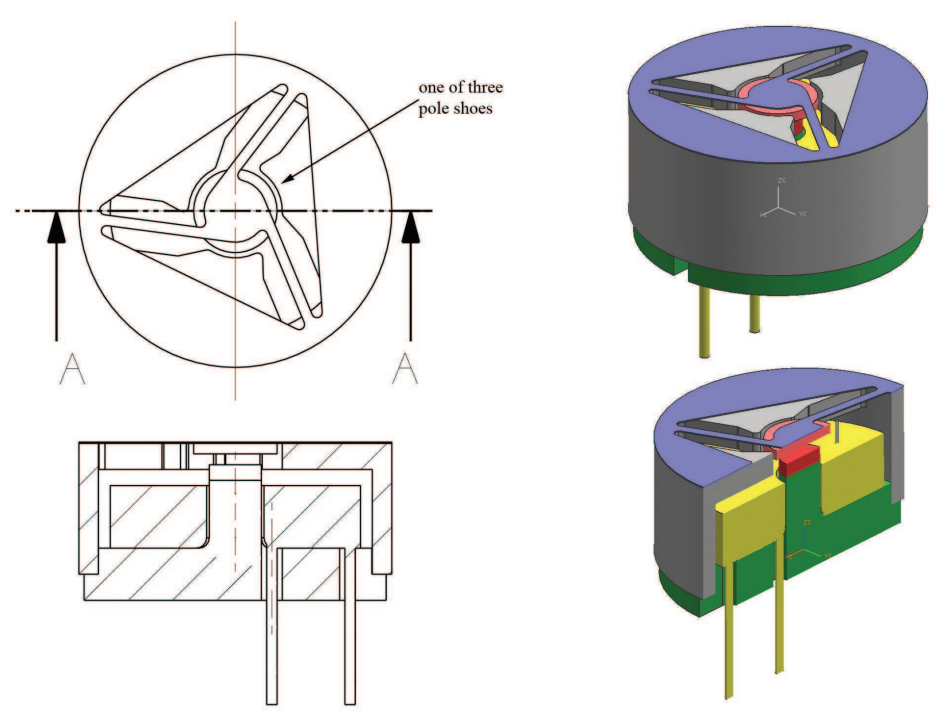


Figure 4.6: CAD drawing of the variable reluctance actuator. The membrane suspension, with three leafsprings and the ferromagnetic core is shown. The magnetic flux from the PM passes through the axial air gap, through the ferromagnetic moving core and through a radial air gap the three pole shoes located in the baseplate, back to the PM.

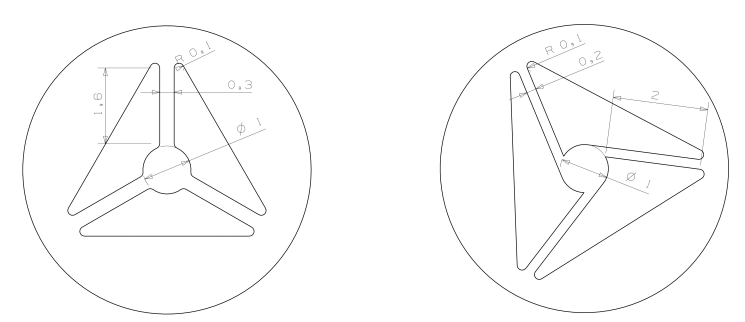


Figure 4.7: Dimensions in mm of the tested membrane designs.

and conclusions and recommendations will be formulated.

4.3.1 The actuator membrane suspension

The stiffness of the membrane, in which the moving core is suspended, largely determines the actuator's resonance frequencies and thereby the resonance frequencies of the adaptive deformable mirror Chapter 3. The magnetic force generated by the PM and the coil acts on the moving core and pre-tensions the membrane suspension. According to [185], the nonlinear relation between spring force F_s and membrane deflection z_s can be approximated by:

$$F_s(z_s) = -C_1 \frac{E_m t_m^3}{r_m^2} z_s - C_2 \frac{E_m t_m}{r_m^2} z_s^3$$
(4.2)

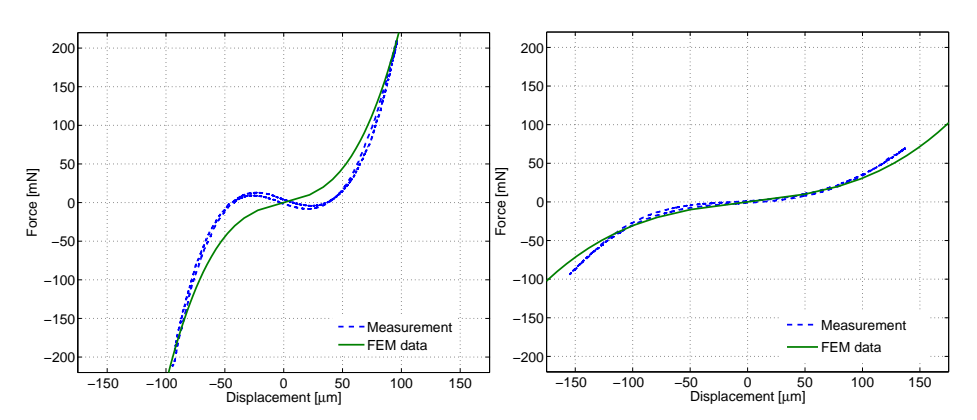


Figure 4.8: Comparison of the nonlinear spring characteristic of the suspension designs as shown in Figure 4.7, as calculated with FEM and as measured. The measurements were performed using the test setup described in Appendix B.

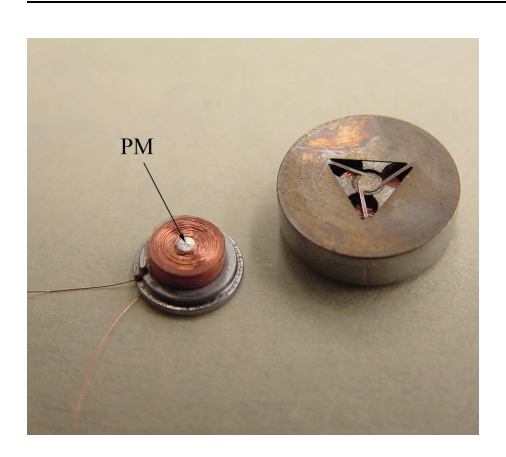


Figure 4.9: Photo of a single actuator. On the left, the insert is shown that contains the PM and the coil.

where t_m and r_m are the suspension membrane thickness and radius and E_m is the membrane material's Young's modulus. The coefficients C_1 and C_2 depend on the design and boundary conditions and will be estimated from FEM results and measurements. The membrane deflection z_s follows the sign definition as indicated in Figure 4.12 and is always negative due to the PM pretension. Since the resulting deflection is larger than the membrane thickness, a linear approximation of the stiffness is no longer valid: not only the bending stiffness $\left(E_m t_m^3/r_m^2\right)$, but also the nonlinear stiffness due to in-plane stretching becomes relevant.

Figure 4.7 shows on the left a design with springs placed radially towards a central disc. Results from both FEM analysis and measurements depicted in Figure 4.8 show that the radially placed springs cause the suspension to stiffen quickly. This nonlinear effect is undesirable as this will complicate the design of a control system for the DM and reduce the achievable optical correction quality. One way to reduce the nonlinearity is to use a relatively thick membrane as was already noticed from Figure 4.3. Another way to reduce the nonlinearity is to allow rotation of the central part to reduce the tensional forces. This leads to the design shown on the right in Figure 4.7. Here the springs are placed tangentially. Due to the out-of-plane displacement, bending in the leaf springs occurs and the central part will rotate with typically 2° per Newton [4]. Since the glued connection strut has a low rotational stiffness (Figure 2.12 on page 30), this rotation will not lead to an actuator malfunction after assembly of the DM.

Stiffness measurements

To verify the FEM analysis a test set-up was designed to measure the nonlinear stiffness for different membrane suspensions. This measurement setup is described in [126] and in Appendix B. In the setup the displacement is measured optically with a Philtec D21 sensor with sub- μ m resolution. The force required to enforce the displacement is measured with a Kistler 9203 piezo sensor, with mN resolution. The membrane suspensions are placed in containers ($\varnothing 25x8mm$) to be able to handle them and place them in the measurement setup. In the containers the membranes are clamped at the outer edge. In the setup the suspensions

are subjected to an out-of-plane displacement of ± 100 -150 μm . For the suspensions shown in Figure 4.7 the results of the nonlinear FEM analyses are compared with the measurements and shown in Figure 4.8. A few remarks on the measurements are given below:

- FEM prediction of the stress in the membrane is needed prior to the measurement to avoid plastic deformation during measurement.
- Around the central position a negative stiffness is observed. This can be explained, partly from the stress present in the material due to the production of the foil, which is rolled, and partly from the clamping forces in the container. However, the membrane suspension will not be used in this position as the PM pre-tensions the membrane suspension. To deal with the negative stiffness, the membrane is placed a little higher above the magnet than originally designed. The spring force model in Equation (4.2) is well able to describe a negative stiffness around $z_s = 0$ and only the coefficient C_1 needs to be adapted. By using a single rolled sheet for all actuators, the variation in membrane material stresses between the actuators is minimized.
- The measurements are made using slow back and forward motion. A small difference
 between the two directions is observed, which is attributed partly to hysteresis in the
 clamp and partly to charge leakage in the piezo based sensor.

The suspension membranes of the first actuators (e.g. Figure 4.9) were made with titanium rolled sheets. The titanium sheets had limited yield strength (250N/mm²) and yielded vulnerable actuators. In later designs, sheets of Havar®, a non-magnetic, cobalt based, high-strength alloy, were used. Its yield strength is 1860N/mm^2 and its Young's modulus 200GPa [2]. The available choice in sheet thickness is limited. The design on the right in Figure 4.8 was made with a $25\mu\text{m}$ Havar® rolled sheet. The constants C_1 and C_2 were estimated using a least squares fit as:

$$C_1 = -0.12, \qquad C_2 = 0.02.$$

The 'bowleg' membrane suspension

A further improvement to the membrane design on the right in Figure 4.8 is the 'bowleg'-design [4] shown in Figure 4.10. This suspension design has a more linear stiffness, has less parasitic rotation of the central part and has a more uniform stress distribution in the leaf springs. The curved legs allow bending and avoid high stresses and stiffening. Each leg can be represented by two beams and three rotation points. Rotation of the central part of the membrane can now be minimized since both beams will rotate.

Figure 4.10: The 'bowleg' membrane suspension proposed by [4]. The nonlinear stiffness and the parasitic rotation of the central part is decreased and a more uniform stress distribution in the leaf springs is obtained.



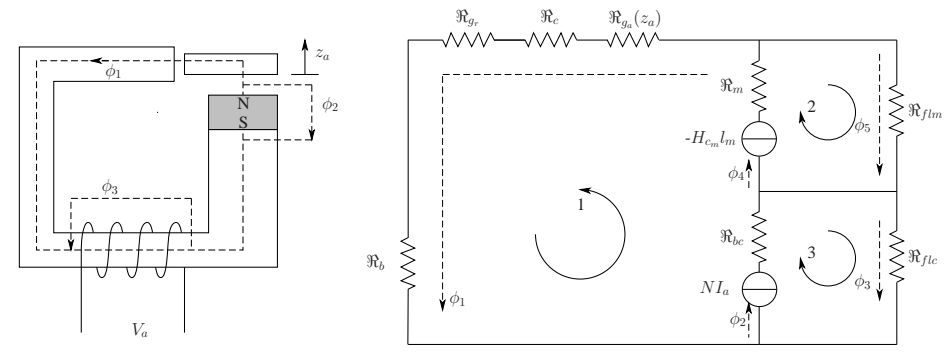


Figure 4.11: Left: a schematic representation of the variable reluctance actuator from Figure 4.6.

Right: the electrical equivalent circuit including two leakage flux paths.

4.3.2 The electromagnetic force

The axial magnetic force acting on the ferromagnetic core will be modeled as a function of the actuator deflection z_a (Figure 4.12) and the actuator current I_a . First the magnetic flux density in the axial air gap is determined, followed by a force derivation based on magnetic coenergy.

The magnetic circuit of the actuator from Figure 4.6 is shown schematically in Figure 4.11. The model includes leakage flux paths: one that short-circuits the coil and one that short-circuits the PM. As will be shown later, the first one mainly affects the actuator coil inductance, whereas the latter affects many properties such as motor constant and actuator stiffness. The indicated flux paths contain two sources – the PM and the coil – and eight reluctances: the reluctance \Re_m of the PM itself, $\Re_{g_a}(z_a)$ of the axial air gap, \Re_c of the ferromagnetic core, \Re_{g_r} of the radial air gap, \Re_b of the baseplate, \Re_{bc} of the part of the baseplate that forms the core of the coil and \Re_{flc} and \Re_{flm} of the leakage flux paths that short-circuit the coil and PM respectively. Based on first principles, the reluctances of the PM, the axial and radial air gaps and the coil core are expressed as:

$$\Re_m = \frac{l_m}{\mu_0 \mu_{r_m} A_m}, \Re_{g_a}(z_a) = \frac{z_0 + z_a}{\mu_0 A_{g_a}}, \Re_{g_r} = \frac{l_{g_r}}{\mu_0 A_{g_r}}, \Re_{bc} = \frac{l_c}{\mu_0 \mu_{r_b} A_m}, \tag{4.3}$$

where μ_0 is the permeability of vacuum and μ_{r_m} and μ_{r_b} are the relative permeabilities of the PM and the baseplate material respectively.

Since the thickness of the pole shoe is larger than the thickness of the ferromagnetic core plus the displacement range, the reluctance \Re_{g_r} of the radial air gap is considered to be independent of the displacement z_a . A_m and A_{g_r} are the cross sectional areas of the flux paths through the PM and the radial air gap respectively and (z_0+z_a) , l_{g_r} and l_c are the axial air gap height and the lengths of the flux paths through the radial air gap and coil core respectively. A schematic of the actuator with the definitions of z_a and z_0 is depicted in Figure 4.12. The effective lengths and areas of the flux paths through the base plate and the ferromagnetic core are estimated from the actuator geometry, leading to the reluctances \Re_b and \Re_c as listed in Table 4.1. Their values lie two orders of magnitude below the reluctances

of the air gaps and the PM and will be combined into a single reluctance $\Re_r = \Re_c + \Re_b$ with a characteristic path length l_r .

Figure 4.11 indicates five different magnetic fluxes $\phi_1 \dots \phi_5$ with positive directions. Since the sum of the fluxes towards each node must be equal to zero, these fluxes are related as:

$$\begin{cases}
\phi_1 - \phi_2 + \phi_3 = 0, \\
\phi_2 - \phi_3 - \phi_4 + \phi_5 = 0, \\
\phi_4 - \phi_5 - \phi_1 = 0.
\end{cases}$$
(4.4)

The PM is represented as a source with an internal reluctance and the coil as a source of magnetomotive force. According to Ampère's law, the magnetomotive forces $\mathfrak{F}_1 \dots \mathfrak{F}_3$ can be derived for the three different flux paths indicated in the figure as:

$$\begin{cases} \mathfrak{F}_{1} &= \oint Hdl = NI_{a} = H_{m}l_{m} + H_{g_{a}}(z_{a} + z_{0}) + H_{r}l_{r} + H_{g_{r}}l_{g_{r}} + H_{bc}l_{bc}, \\ \mathfrak{F}_{2} &= \oint Hdl = 0 = H_{m}l_{m} + H_{flm}l_{flm}, \\ \mathfrak{F}_{3} &= \oint Hdl = NI_{a} = H_{flc}l_{flc} + H_{bc}l_{bc}, \end{cases}$$

where H_m , H_{g_a} , H_{g_r} , H_r and H_{bc} are the magnetic field intensity in the PM, the axial air gap, the radial air gap, the combined baseplate and moving core and the coil core respectively.

Assuming that all flux conductors represent linear magnetic materials, their flux densities B are related to their magnetic field intensity H via the material's magnetic permeability μ as $B=\mu H$. For the PM, this relation includes an offset:

$$B_m = \mu_0 \mu_{r_m} (H_m - H_{c_m}), \tag{4.5}$$

where H_{c_m} is the coercivity of the PM. According to Gauss's law, flux ϕ is the integral of the flux density B over an area A:

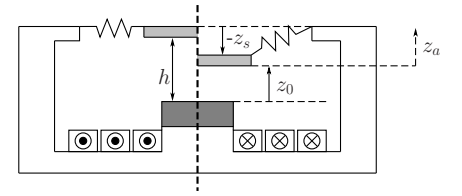
$$\phi = \int_A B \cdot dA = BA,\tag{4.6}$$

where the latter equality assumes that the flux density is constant over the cross-sectional area A.

When substituted into Equation (4.5), this allows the magnetic field intensity of the PM to be expressed as:

$$H_m = \frac{B_m}{\mu_0 \mu_{r_m}} + H_{c_m} = \frac{\phi_4}{\mu_0 \mu_{r_m} A_m} + H_{c_m}.$$
 (4.7)

Figure 4.12: Definition of the axial air gap height through the initial gap z_0 and the displacement z_a . The height h is the axial air gap when the suspension membrane is not deflected, i.e. $z_s = 0$. The membrane deflection z_s is related to the actuator displacement z_a as $z_s = z_a + z_0 - h$, and is negative for downward membrane deflection.



Substitution of Equation (4.7), Gauss's law from Equation (4.6), the definitions of the reluctances from Equation (4.3) and the linear relations between flux density and magnetic field intensity into the expressions for $\mathfrak{F}_1 \dots \mathfrak{F}_3$ then yields:

$$\begin{cases} \mathfrak{F}_{1} = NI_{a} &= \Re_{m}\phi_{4} + H_{c_{m}}l_{m} + (\Re_{g_{a}}(z_{a}) + \Re_{r} + \Re_{g_{r}})\phi_{1} + \Re_{bc}\phi_{2}, \\ \mathfrak{F}_{2} = 0 &= \Re_{m}\phi_{4} + H_{c_{m}}l_{m} + \Re_{flm}\phi_{5}, \\ \mathfrak{F}_{3} = NI_{a} &= \Re_{flc}\phi_{3} + \Re_{bc}\phi_{2}. \end{cases}$$

From these three relations and the three flux relations in Equation (4.4), five uncoupled expressions can be solved for the fluxes $\phi_1 \dots \phi_5$ as:

$$\phi_1(I_a, z_a) = \frac{NI_a \Re_{flc} \Re_2 - H_{c_m} l_m \Re_{flm} \Re_3}{\tilde{\Re}(z_a)}$$
(4.8a)

$$\phi_2(I_a, z_a) = \frac{NI_a \overline{\Re}(z_a) - H_{c_m} l_m \Re_{flc} \Re_{flm}}{\tilde{\Re}(z_a)}$$
(4.8b)

$$\phi_3(I_a, z_a) = \frac{NI_a \left(\Re_{flm} \Re_m + \Re_1(z_a) \Re_2\right) + H_{c_m} l_m \Re_{bc} \Re_{flm}}{\tilde{\Re}(z_a)}$$
(4.8c)

$$\phi_4(I_a, z_a) = \frac{NI_a \Re_{flc} \Re_{flm} - H_{c_m} l_m \underline{\Re}(z_a)}{\tilde{\Re}(z_a)}$$
(4.8d)

$$\phi_5(I_a, z_a) = \frac{NI_a \Re_{flc} \Re_m - H_{c_m} l_m \left(\Re_{bc} \Re_{flc} + \Re_3 \Re_1(z_a)\right)}{\tilde{\Re}(z_a)}$$
(4.8e)

where

$$\begin{split} \Re_1(z_a) &= \Re_{g_a}(z_a) + \Re_r + \Re_{g_r}, \\ \Re_2 &= \Re_m + \Re_{flm}, \\ \Re_3 &= \Re_{bc} + \Re_{flc}, \\ \overline{\Re}(z_a) &= (\Re_{flc} + \Re_1(z_a)) \, \Re_2 + \Re_{flm} \Re_m, \\ \underline{\Re}(z_a) &= (\Re_{flm} + \Re_1(z_a)) \, \Re_3 + \Re_{bc} \Re_{flc}, \\ \tilde{\Re}(z_a) &= (\Re_{flm} \Re_m + \Re_2 \Re_1(z_a)) \, \Re_3 + \Re_{bc} \Re_{flc} \Re_2. \end{split}$$

Note that the flux $\phi_4(I_a,z_a)$ through the PM will be zero when the winding current I_a is equal to $I_{a_{cc}} = -(H_{c_m}l_m\underline{\Re}(z_a)/(N\Re_{flm}\Re_{flc})$ or in absence of leakage flux to $I_{a_{cc}} = -H_{c_m}l_m/N$. For this current, the coil's magnetic field fully cancels that of the PM. For the values in Table 4.1 and in the absence of leakage flux, this corresponds to a current $I_a = 324$ mA. For the coil's $\varnothing 50$ µm copper wire this corresponds to an unrealistic current density of 165A/mm².

From the derived expressions for the fluxes, the operating point of the PM on its B-H curve is obtained. This operating point indicates how efficiently the volume of the PM is used to generate a desired flux density. Substitution of the flux $\phi_4(I_a,z_a)$ from Equation (4.8d) into the expression for the magnetic field intensity of the PM in Equation (4.7) provides the magnetic field intensity H_m of the PM as:

$$H_m = H_{c_m} - \frac{NI_a \Re_{flm} \Re_{flc} + H_{c_m} l_m \underline{\Re}(z_a)}{\mu_0 \mu_{r_m} A_m \tilde{\Re}(z_a)}.$$
(4.9)

In the unactuated state (i.e. $I_a=0$, $z_a=0$), with the use of the values from Table 4.1, this yields $H_m=-313 {\rm kA/m}$. Subsequent substitution into Equation (4.5) then leads to $B_m=0.33 {\rm T}$. The product of flux density B_m and magnetic field intensity H_m indicates the available PM energy per unit volume. Using Equation (4.5), the maximum of this product is found as:

$$|B_m H_m|_{max} = \left| \mu_0 \mu_{r_m} (H_m - H_{c_m}) H_m \right|_{max} = \mu_0 \mu_{r_m} H_{c_m}^2 / 4 = 106 \text{kJ/m}^3.$$

The value derived for the actuator is $|H_mB_m|=104 {\rm kJ/m^3}$, which is very close to the optimum. In fact, this optimum corresponds to the situation when $H_m=-H_{c_m}/2$ and thus – when considering Equation (4.9) for $I_a=0$ – to:

$$\frac{\Re(z_a)}{\Re(z_a)} = \frac{1}{2\Re_m}.$$

In absence of leakage flux (i.e. \Re_{flc} , $\Re_{flm} \to \infty$) this reduces to $\Re_m = \Re_{bc} + \Re_1 = \Re_{bc} + \Re_{g_r} + \Re_r + \Re_{g_a}(z_a)$, which implies that the highest volume efficiency of the PM is obtained when the internal reluctance \Re_m of the PM is exactly equal to the external reluctance felt by the PM.

The magnetic force on the ferromagnetic core is calculated via flux linkage and magnetic coenergy [62]. In this procedure the PM is modeled as a fictitious winding with the equivalent magnetomotive force. This means that $H_{c_m}l_m$ is replaced by $-N_fI_f$, where N_f is the number of turns of the fictitious winding and I_f the fictitious current through it. The flux linkages λ of the coil and λ_f of the fictitious winding are given by [62]:

$$\lambda(I_a, z_a) = N\phi_2(I_a, z_a) = L_{11}(z_a)I_a + L_{12}(z_a)I_f,$$

$$\lambda_f(I_a, z_a) = N_f\phi_4(I_a, z_a) = L_{21}(z_a)I_a + L_{22}(z_a)I_f,$$
(4.10)

where $L_{11}(z_a)$ and $L_{22}(z_a)$ are the self inductances of the coil and the PM and $L_{12}(z_a)$ and $L_{21}(z_a)$ the corresponding mutual inductances:

$$L_{11}(z_a) = \frac{N^2 \overline{\Re}(z_a)}{\tilde{\Re}(z_a)}, \qquad L_{12}(z_a) = \frac{N N_f \Re_{flc} \Re_{flm}}{\tilde{\Re}(z_a)},$$

$$L_{21}(z_a) = \frac{N N_f \Re_{flc} \Re_{flm}}{\tilde{\Re}(z_a)}, \qquad L_{22}(z_a) = \frac{N_f^2 \underline{\Re}(z_a)}{\tilde{\Re}(z_a)}.$$

$$(4.11)$$

As expected, the two mutual inductances $L_{12}(z_a)$ and $L_{21}(z_a)$ are equal. The magnetic coenergy can be expressed in terms of these (mutual) inductances as [62]:

$$W(I_a, z_a) = \frac{1}{2} L_{11}(z_a) I_a^2 + L_{12}(z_a) I_a I_f + \frac{1}{2} L_{22}(z_a) I_f^2,$$

$$= \frac{1}{2} L_{11}(z_a) I_a^2 + \frac{L_{12}(z_a)}{N_f} I_a H_{c_m} l_m + \frac{L_{22}(z_a)}{2N_f^2} H_{c_m}^2 l_m^2,$$

$$= \frac{1}{2\tilde{\Re}(z_a)} \left(N^2 I_a^2 \overline{\Re}(z_a) - 2N I_a H_{c_m} l_m \Re_{flm} \Re_{flc} + H_{c_m}^2 l_m^2 \underline{\Re}(z_a) \right).$$
(4.12)

Note that in the second step the magnetomotive force $N_f I_f$ of the fictitious winding is again replaced by the $-H_{c_m} l_m$ of the PM. After substitution of the inductances from Equation

(4.11) in the final step, the expression for $W(I_a,z_a)$ becomes independent of N_f and I_f . The electromagnetic force $F_m(I_a,z_a)$ is equal to the partial derivative of the coenergy with respect to the displacement z_a and can be expressed as:

$$F_m(I_a, z_a) = \frac{\partial W(I_a, z_a)}{\partial z_a} = \frac{-1}{2A_{q_a}\mu_0} \left(\frac{NI_a \Re_{flc} \Re_2 - H_{c_m} l_m \Re_{flm} \Re_3}{\tilde{\Re}(z_a)} \right)^2 \tag{4.13}$$

4.3.3 A static actuator model

Together, the derived equations for the electromagnetic force $F_m(I_a, z_a)$ in Equation (4.13) and the mechanical spring force in Equation (4.2) provide static relations for the behavior of the actuator. This provides insight in the nonlinear actuator stiffness, the required actuator current and voltage, its motor constant and power dissipation. However, the derived relations do not provide insight into dynamic properties such as resonance frequency, damping, inductance, etc. that affect the achievable controller performance and thus the correction quality of the AO system. Therefore, in Section 4.3.4 these equations are extended to also include dynamic behavior.

The static force equilibrium can be expressed as:

$$F_s(z_s) + F_m(I_a, z_a) = 0.$$
 (4.14)

Let the nominal operating point of the actuator be defined as the unactuated equilibrium point, where the air gap z_0 is such that the electromagnetic force $F_m(I_a=0,z_a=0)$ equals the membrane suspension spring force $F_s(z_s)$. The deflection z_s of the suspension membrane can be expressed in terms of the z_a , z_0 and h as defined in Figure 4.12 by:

$$z_s = z_a + z_0 - h.$$

Using this definition with $z_a = 0$, the initial gap z_0 can be solved from the force equilibrium in Equation (4.14) through substitution of Equation (4.13) and Equation (4.2):

$$-\frac{1}{2\mu_0 A_{g_a}} \left(\frac{H_{c_m} l_m \Re_{flm} \Re_3}{\tilde{\Re}(z_a)} \right)^2 - C_1 \frac{E_m t_m^3}{r^2} (z_0 - h) - C_2 \frac{E_m t_m}{r_m^2} (z_0 - h)^3 = 0, \quad (4.15)$$

This leads to a fifth order equation in z_0 with five solutions. The solution that corresponds to practise is real-valued. Moreover, it forms a stable equilibrium – i.e. the derivative of the sum of forces with respect to z_0 at the solution for z_0 is negative – and finally has a value within the range $0 < z_0 < h$. This solution is found numerically after substitution of the parameters from Table 4.1. Note that the values for some parameters in this table are determined from measurements as described in Section 4.3.5. The initial gap z_0 found is $z_0 = 109 \mu m$. The spring and electromagnetic forces of Equation (4.15) are plotted in Figure 4.13 as a function of z_0 .

Parameter	Value	Unit	Parameter	Value	Unit
H_{c_m}	-540^{a}	kA/m	C_1	-0.12^{c}	-
l_m	0.30	mm	C_2	0.02^{c}	-
A_{g_a}	0.79	mm^2	E_m	200	GPa
A_{g_r}	0.48	mm^2	t_m	25	μm
A_m	0.79	mm^2	r_m	2.5	mm
$\Re_{g_a}(0)$	111	$1/\mu H$	m_{a_c}	3.6	mg
\Re_m	262	$1/\mu H$	R_a	39.0	Ω
\Re_r	512	$1/\mu H$	h	230^d	μm
\Re_{g_r}	248	$1/\mu H$	z_0	109^{e}	μm
\Re_{bc}	1	$1/\mu H$	b_a	0.4^{f}	mNs/m
\Re_{flc}	100^{b}	$1/\mu H$	c_a	583^{e}	N/m
\Re_{flm}	600^{b}	$1/\mu H$			

Table 4.1: Electromagnetic and mechanical parameters of the variable reluctance actuator.

 $^{^{\}it f}$ Estimated from actuator measurements

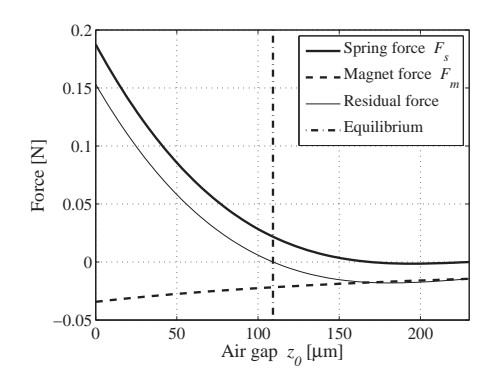


Figure 4.13: Forces exerted by the membrane suspension and the PM respectively as a function of the axial air gap.

Figure 4.14: The stiffness of the suspension membrane and PM as a function of the actuated displacement z_a around the equilibrium z_0 .

The relation between current I_a and displacement z_a is found by solving the force equilibrium equation in Equation (4.14) for the actuator current I_a , yielding:

$$I_{a}(z_{a}) = \frac{H_{c_{m}} l_{m} \Re_{flm} \Re_{3} \pm \sqrt{-2A_{g_{a}} \mu_{0} \tilde{\Re}^{2}(z_{a}) \left(\frac{C_{1} E_{m} t_{s}^{3}}{r_{m}^{2}} z_{s} + \frac{C_{2} E_{m} t_{m}}{r_{m}^{2}} z_{s}^{3}\right)}}{N \Re_{flc} \Re_{2}}$$
(4.16)

where z_s is used for brevity of the expression. Since Equation (4.13) and thus Equation

 $[^]a$ Estimated from PM measurements (Appendix A)

^b Value estimated from measurements on actuator prototypes

 $^{^{}c}$ Fitted on nonlinear FEM model with typical value for negative stiffness included

 $[^]d$ Design parameter

^e Derived value

(4.14) is quadratic in the current, there are two solutions $I_a(z_a)$ – as indicated by the \pm sign – of which only the solution with a plus sign is valid. Since a current yields a displacement z_a around the z_0 for which $I_a=0$, both positive and negative currents lead to realistic displacements. The solution for $I_a(z_a)$ with a minus sign could never lead to a positive current because the first term $(H_{c_m} l_m \Re_{flm} \Re_3)$ is always negative $(H_{c_m}$ is negative) and for realistic displacements the square root term is always positive. The viable relation for $I_a(z_a)$ is plotted in Figure 4.15 for the physical properties in Table 4.1. Note that despite the nonlinearity of the equations, the relation between current and deflection is highly linear within the intended operating range of $-10 \mu \text{m} < z_a < 10 \mu \text{m}$.

The mechanical stiffness c_a of the actuator can be derived by taking the partial derivative of the sum of forces in Equation (4.14) with respect to the deflection z_a . Although this remains a function of both I_a and z_a , these quantities are statically coupled through Equation (4.16). The dependence on I_a can therefore be replaced by an implicit constant $I_{a_z} = I_a(z_a)$ that denotes the static current required to reach the displacement $z_a = z_a'$. The mechanical stiffness $c_a(z_a)$ can thus be derived as:

$$\begin{split} c_{a}(I_{a_{z}},z_{a}) &= -\frac{\partial}{\partial z_{a}} \left(F_{s}\left(z_{a}\right) + F_{m}\left(I_{a} = I_{a_{z}},z_{a}\right) \right) \\ &= -\frac{\partial}{\partial z_{a}} \left(-C_{1} \frac{E_{m} t_{m}^{3}}{r_{m}^{2}} z_{s} - C_{2} \frac{E_{m} t_{m}}{r_{m}^{2}} z_{s}^{3} - \frac{\left(NI_{a_{z}} \Re_{flc} \Re_{2} - H_{c_{m}} l_{m} \Re_{flm} \Re_{3}\right)^{2}}{2\mu_{0} A_{g_{a}} \tilde{\Re}^{2}(z_{a})} \right) \\ &= C_{1} \frac{E_{m} t_{m}^{3}}{r_{m}^{2}} + 3C_{2} \frac{E_{m} t_{m}}{r^{2}} (z_{a} + z_{0} - h)^{2} \\ &- \frac{\Re_{2} \Re_{3} \left(NI_{a_{z}} \Re_{flc} \Re_{2} - H_{c_{m}} l_{m} \Re_{flm} \Re_{3}\right)^{2}}{\mu_{0}^{2} A_{a}^{2} \tilde{\Re}^{3}(z_{a})}. \end{split}$$

By substituting the relation between current I_{a_z} and displacement z_a from Equation (4.16), an expression for the actuator stiffness in terms of only z_a is found:

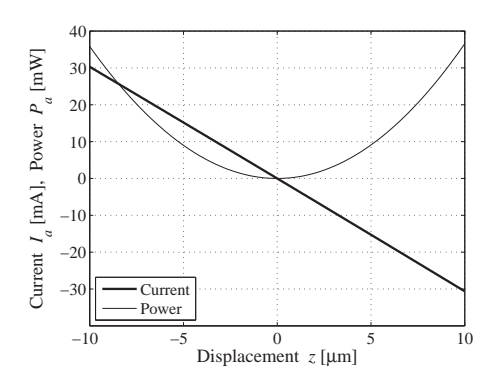
$$c_a(z_a) = -\frac{C_2 E_m t_m}{r_m^2 \mu_0 A_{g_a} \tilde{\Re}(z_a)} z_s^3 + \frac{3C_2 E_m t_m}{r_m^2} z_s^2 - \frac{C_1 E_m t_m^3}{r_m^2 \mu_0 A_{g_a} \tilde{\Re}(z_a)} z_s + \frac{C_1 E_m t_m^3}{r_m^2}, (4.17)$$

where z_s was resubstituted for brevity of the expression. Note that this expression is a function of the initial air gap z_0 , such that it does not fully reflect the effect of parameters affecting z_0 . Moreover, the stiffness is a third order polynomial in the deflection z_a , whereas without the PM this was second order. Based on the numerical solution for z_0 and the other properties shown in Table 4.1, the actuator stiffness has been plotted in Figure 4.14 for displacements z_a within the intended operating range. The stiffness decreases for positive z_a and increases for negative z_a and varies approximately 16.5% over the full intended operating range. At the equilibrium $z_a = 0$ and $z_s = z_0 - h$, the actuator stiffness is found as $c_a(0) = 583$ N/m.

Figure 4.15 also shows the dissipated power $P_a(z_a)$ calculated via Ohm's law:

$$P_a(z_a) = I_a^2(z_a)R_a,$$

where R_a is the resistance of the actuator coil that can be expressed in terms of geometry



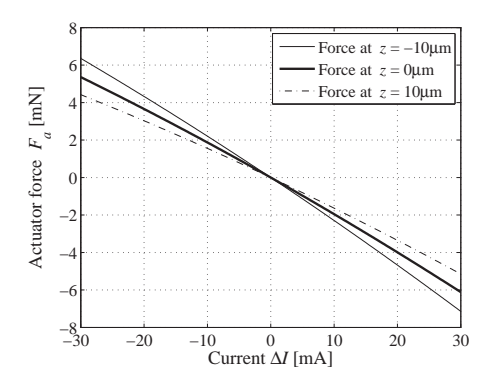


Figure 4.15: The actuator current I_a and corresponding power dissipation required for a displacement z_a .

Figure 4.16: The force that can be exerted by the actuator on the DM facesheet as a function of the current I_a at three deflections z_a .

and material properties as:

$$R_a = \frac{2\pi N r_{c_a} \rho_e}{A_w},$$

where r_{c_a} is the average coil radius, ρ_e the specific resistance of the coil's material and A_w the cross-sectional area of the coil's wire. For the $\varnothing 50\mu m$ copper wire used this leads to the value $R_a \approx 39.0\Omega$ found in Table 4.1.

In Figure 4.16 the generated actuator force F_a is plotted. This is the external force required to keep the actuator at a fixed operating point $z_a = z'_a$ as a function of a supplied current offset $\Delta I_a = I_a - I_a(z'_a)$. It is calculated by augmenting the static force equilibrium with an additional term $F_a(\Delta I_a, z'_a)$ and solving for it:

$$F_a(\Delta I_a, z_a') = F_m \left(I_a(z_a') + \Delta I_a, z_a' \right) + F_s \left(z_0 + z_a' - h \right). \tag{4.18}$$

The common relation between force and current in linear systems is through the motor constant defined in Newtons per Ampère, whereas Equation (4.18) expresses this relation for the derived nonlinear system. Figure 4.16 shows that the relation between the current offset ΔI_a and force $F_a(\Delta I_a,z_a')$ is highly linear within the intended operating range. According to this figure, the generated force due to a change in current is only marginally different at the intended extreme operating points. In fact, when nonlinearities are neglected, it can be observed from Figure 4.16 that the force per current unit – i.e. the motor constant – is approximately 0.2N/A.

4.3.4 A dynamic actuator model

The derived equations that describe the electromagnetic part of the actuator will be extended with the mechanical equations of motion to a (nonlinear) dynamic model. This model is linearized to obtain Bode plots of the actuator and linear electromechanical properties such as motor constant and coil inductance.

The terminal voltage $V_a(t)$ over the actuator coil can be expressed as a function of time t using the flux linkage term $\lambda(I_a, z_a)$ corresponding to the actuator coil as [62]:

$$V_a(t) = I_a(t)R + \frac{\partial \lambda(I_a, z_a)}{\partial t}$$
(4.19)

In the expression for the flux linkage in Equation (4.10), the magnetomotive force of the PM is expressed by that of a fictitious winding as $N_f I_f$. The latter can again be replaced by $-H_{c_m} l_m$ of the PM, leading to:

$$\lambda(I_a, z_a) = \frac{N}{\tilde{\Re}(z_a)} \left(N I_a \overline{\Re} - H_{c_m} l_m \Re_{flc} \Re_{flm} \right). \tag{4.20}$$

Since this expression for $\lambda(I_a, z_a)$ is a function of both current I_a and position z_a , the partial derivative in Equation (4.19) w.r.t. time t expands via the chain rule into:

$$V_{a} = I_{a}R_{a} + \frac{\partial \lambda}{\partial I_{a}} \frac{\partial I_{a}}{\partial t} + \frac{\partial \lambda}{\partial z_{a}} \frac{\partial z_{a}}{\partial t}$$

$$= I_{a}R + \frac{\partial \lambda}{\partial I_{a}} \dot{I}_{a} + \frac{\partial \lambda}{\partial z_{a}} \dot{z}_{a}$$
(4.21)

where the dependence on t has been omitted for brevity. The first partial derivative represents the self-inductance voltage term, whereas the second occurs in product with the actuator velocity \dot{z}_a and is called the speed voltage. The latter is common to all electromechanical energy-conversion systems and is responsible for energy transfer between the mechanical system and the electrical system.

Substitution of the flux linkage $\lambda(I_a, z_a)$ of Equation (4.20) into Equation (4.21) then leads to:

$$V_{a} = I_{a}R_{a} + \frac{N^{2}\overline{\Re}}{\tilde{\Re}(z_{a})}\dot{I}_{a} + \frac{N\Re_{flc}}{A_{a_{a}}\mu_{0}\Re_{2}\tilde{\Re}^{2}(z_{a})}\left(H_{c_{m}}l_{m}\Re_{flm}\Re_{3} - NI_{a}\Re_{flc}\Re_{2}\right)\dot{z}_{a} \quad (4.22)$$

This equation describes the electromagnetic part of the system that generates the force $F_m(z_a,I_a)$ in Equation (4.13) on the suspended mass. The equation of motion of this mass-spring-damper system can be expressed as:

$$m_a \ddot{z_a} + b_a \dot{z_a} = F_m(z_a, I_a) + F_s(z_a + z_0 - h),$$
 (4.23)

where b_a is the mechanical viscous damping, m the mass of the ferromagnetic moving core, $F_m(I_a, z_a)$ is defined in Equation (4.13) and $F_s(z_s)$ in Equation (4.2). Together with Equation (4.22) this equation forms a nonlinear dynamic actuator model. When assuming a state vector $\mathbf{x} = [I_a \ z_a \ \dot{z}_a]^T$, the time derivative of this state vector can be expressed as:

$$\begin{bmatrix} \dot{I}_{a} \\ \dot{z}_{a} \\ \ddot{z}_{a} \end{bmatrix} = \begin{bmatrix} \frac{\tilde{\Re}(z_{a})(V_{a} - R_{a}I_{a})}{N^{2}\overline{\Re}(z_{a})} - \frac{\Re_{flc}}{A_{g_{a}}\mu_{0}N\Re_{2}\tilde{\Re}(z_{a})\overline{\Re}(z_{a})} (H_{c_{m}}l_{m}\Re_{flm}\Re_{3} - NI_{a}\Re_{flc}\Re_{2}) \dot{z}_{a} \\ \dot{z}_{a} \\ \frac{1}{m_{ac}} \left(-F_{m}(z_{a}, I_{a}) - b_{a}\dot{z}_{a} - F_{s}(z_{a} + z_{0} - h) \right)$$

$$(4.24)$$

where \dot{I}_a was solved from Equation (4.22) and \ddot{z}_a from Equation (4.23) after substitution of Equation (4.13) and Equation (4.2). All state derivatives except \dot{z}_a are nonlinear equations

in terms of the state variables. However, if the effect of the nonlinearities on the actuator behavior is small, the nonlinear equations will only complicate the design of a controller. Therefore, this effect will be investigated in the next subsection through linearization of the nonlinear equations. This will also provide insight into (linear) dynamic properties such as inductance, resonance frequency and damping.

Linearization of the dynamic model

Linearization is a widely used technique that enables the application of linear, frequency domain tools on nonlinear systems. However, it can only provide useful insight when the nonlinearities play a negligible role around a certain operation point or state. To verify this for the nonlinear system in Equation (4.24), linearizations at several displacements $z_a = z_a'$ around the initial air gap z_0 will be derived and their frequency response functions plotted. The coil terminal voltage V_a serves as the system input and is assumed to be supplied by a voltage source. The system output is the displacement z_a , where no notational difference is made between the original and linearized system description as this is always clear from the context. The linearized system with state $\mathbf{x}_l = [I_a \ z_a \ \dot{z}_a]^T$ can thus be expressed as [72]:

$$\dot{\mathbf{x}}_l(t) = \frac{\partial \dot{\mathbf{x}}}{\partial \ \mathbf{x}^T} \Bigg|_{\mathbf{x} = \mathbf{x}_{z_a'}, V_a = I_{a_{z_a'}} R_a} \mathbf{x}_l(t) + \frac{\partial \dot{\mathbf{x}}}{\partial \ V_a} \Bigg|_{\mathbf{x} = \mathbf{x}_{z_a'}} V_a(t),$$

where the operating point $\mathbf{x}_{z_a'}$ is chosen as $[I_{a_{z_a'}} z_a' \ 0]^T$ where $I_{a_{z_a'}} = I_a(z_a')$ and the current required for the actuator displacement $z_a = z_a'$ as plotted in Figure 4.15. In the operating point used for linearization the velocity \dot{z}_a is assumed to be zero. The output of this system can then be chosen as displacement z_a , velocity \dot{z}_a and/or current I_a . After taking the partial derivatives, substituting $\mathbf{x} = \mathbf{x}_{z_a'}$ and $V_a = I_a R_a$ and omitting dependence on t for brevity this leads to:

$$\dot{\mathbf{x}}_{l} = \underbrace{\begin{bmatrix} -R_{a}/L_{a}(z'_{a}) & 0 & -K_{a}(z'_{a})/L_{a}(z'_{a}) \\ 0 & 0 & 1 \\ K_{a}(z'_{a})/m_{a_{c}} & -c_{a}(z'_{a})/m_{a_{c}} & -b_{a}/m_{a_{c}} \end{bmatrix}}_{\mathbf{A}_{l}} \mathbf{x}_{l} + \underbrace{\begin{bmatrix} 1/L_{a}(z'_{a}) \\ 0 \\ 0 \end{bmatrix}}_{\mathbf{B}_{l}} V_{a}, (4.25)$$

where $c_a(z_a')$ was defined in Equation (4.17) and the elements I_a , z_a and \dot{z}_a of the state \mathbf{x}_l now form small signal variations around the operating point $\mathbf{x}_{z_a'}$. Further, $K_a(z_a')$ and $L_a(z_a')$ are the motor constant and inductance at the operating point $z_a = z_a'$ respectively and can be expressed as:

$$K_{a}(z'_{a}) = \frac{N\Re_{flc}\Re_{2} (NI_{a}\Re_{flc}\Re_{2} - H_{c_{m}}l_{m}\Re_{flm}\Re_{3})}{\mu_{0}A_{g_{a}}\tilde{\Re}^{2}(z'_{a})},$$

$$L_{a}(z'_{a}) = \frac{N^{2} (\Re_{1}\Re_{2} + \Re_{flc}\Re_{2} + \Re_{flm}\Re_{m})}{\tilde{\Re}(z'_{a})}$$
(4.26)

Figure 4.22 shows the values of the motor constant and the coil inductance as function of the operation point $z_a = z_a'$. Both the motor constant and the inductance decrease as the air

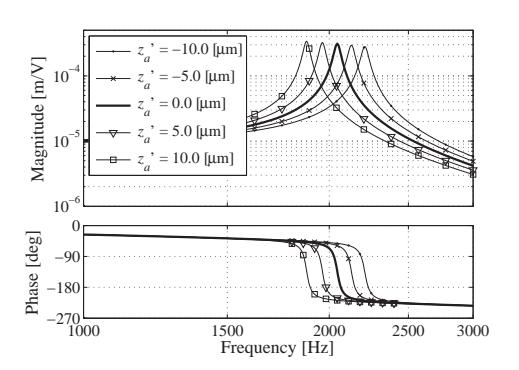


Figure 4.17: Bode plots of the modeled transfer function between actuator voltage V_a and displacement z_a for various operating points $z_a = z_a'$.

gap $z_0 + z_a$ increases, but for the latter the influence of the operating point is smaller. Bode plots of the actuator response are plotted for several operating points $z_a = z_a'$ in Figure 4.17. This shows a first resonance frequency of the system around 2.04kHz, which increases as the air gap $z_0 + z_a'$ increases. It should be noted that the ratio R_a/L_a between the electrical resistance and inductance of the actuator corresponds to a pole located at approximately 2.1kHz, which is very close to the mechanical resonance frequency. Although this pole will affect the two poles corresponding to the system's mechanics, this effect is small.

Although the dynamic system equations were mainly derived to gain insight into the dynamic behavior of the actuator, the Direct Current (DC)-gain of the linearized system also provides a direct relation between the supplied clamp voltage V_a and the deflection z_a . This DC-gain H(0) can be derived from the state-space model in Equation (4.25) by first rewriting it to transfer function form as:

$$H(s) = \begin{bmatrix} 0 & 1 & 0 \end{bmatrix} (s\mathbf{I}_3 - \mathbf{A}_l)^{-1} \mathbf{B}_l,$$

where the displacement z_a is chosen as the output and ${\bf A}_l$ and ${\bf B}_l$ are the system matrices defined in Equation (4.25). Further, $s=j\omega$ is the complex Laplace variable and ${\bf I}_3$ the identity matrix of size 3×3 . Subsequent substitution of $s=j\omega=0$ then yields the DC-gain H(0) as:

$$H(0) = \frac{K_a(z_a')}{R_a c_a(z_a')}. (4.27)$$

Observe that this gain depends on the coil resistance, the motor constant and the resulting actuator stiffness, which will all vary per actuator due to material and manufacturing tolerances. As a result, the DC-gain is expected to have a relatively large variation from actuator to actuator.

A simplified case: no leakage flux

The expressions describing the actuator behavior derived so far are complicated by the presence of the leakage flux around the coil and the PM. Although this leads to a more realistic model that is better able to describe the measurement results, it makes the physical interpretation of the expressions more difficult. Therefore, the case will be considered when the leakage flux is completely absent. This will provide a clearer understanding of the relations

between quantities such as geometric dimensions, number of coil turns and inductance, motor constant, etc.

The absence of leakage flux corresponds to the limit of all above electromagnetic equations for \Re_{flm} , $\Re_{flc} \to \infty$. For the fluxes $\phi_2(I_a, z_a)$ and $\phi_4(I_a, z_a)$ through the coil and the PM respectively, this leads to:

$$\phi_{2}'(I_{a}, z_{a}) = \lim_{\Re_{flm}, \Re_{flc} \to \infty} \phi_{2}(I_{a}, z_{a}) = \frac{NI_{a} - H_{c_{m}} I_{m}}{\mu_{0} A_{g_{a}} \Re'_{1}(z_{a})},$$

$$\phi_{4}'(I_{a}, z_{a}) = \lim_{\Re_{flm}, \Re_{flc} \to \infty} \phi_{4}(I_{a}, z_{a}) = \frac{NI_{a} - H_{c_{m}} I_{m}}{\mu_{0} A_{g_{a}} \Re'_{1}(z_{a})},$$

where $\Re'_1(z_a)$ denotes the sum of all remaining reluctances:

$$\Re_1'(z_a) = \Re_{g_a}(z_a) + \Re_r + \Re_{bc} + \Re_{g_r} + \Re_m.$$

Note that since there is only a single flux path left, fluxes ϕ_2 and ϕ_4 are equal. Similarly, for \Re_{flm} , $\Re_{flc} \to \infty$ the expression for the magnetic coenergy $W(I_a, z_a)$ in Equation (4.12) reduces to:

$$W'(I_a, z_a) = \lim_{\Re f_{lm}, \Re f_{lc} \to \infty} W(I_a, z_a) = \frac{(NI_a - H_{c_m} l_m)^2}{2\mu_0 A_{g_a} \Re'_1(z_a)}$$

and that for the magnetic force in Equation (4.13) to:

$$F'_{m}(I_{a}, z_{a}) = \lim_{\Re_{flm}, \Re_{flc} \to \infty} F_{m}(I_{a}, z_{a}) = \frac{-(NI_{a} - H_{c_{m}}l_{m})^{2}}{2\mu_{0}A_{g_{a}} (\Re'_{1}(z_{a}))^{2}}$$
$$= \frac{-1}{2}\mu_{0}A_{g_{a}} (\phi'_{2}(I_{a}, z_{a}))^{2}.$$

The fluxes, the coenergy and the magnetic force are all proportional to the total magnetomotive force in the system and inversely proportional to the total, position dependent reluctance $\Re_1'(z_a)$. In fact, the fluxes are linearly proportional to the total magnetomotive force, whereas the coenergy and force are both quadratically proportional to this. The resulting cross product between the magnetomotive force NI_a of the coil and the $H_{c_m}l_m$ of the PM amplifies the effect of the coil on the electromagnetic force, which is an advantage of using a PM to pre-load the spring.

Comparison of the derived limit equations for flux, magnetic coenergy and electromagnetic force with the original equations in Equation (4.8d), Equation (4.12) and Equation (4.13) shows that leakage flux leads to additional weights on the magnetomotive forces of the coil and the PM as well as on their cross products.

For the static actuator model, the absence of leakage flux leads to a simplified relation between current I_a and displacement z_a :

$$I_a'(z_a) = \lim_{\substack{\Re_{flm} \to \infty \\ \Re_{flc} \to \infty}} I_a(z_a) = \frac{H_{c_m} l_m}{N} + \frac{1}{N} \sqrt{-2 \left(\Re_1'(z_a)\right)^2 \left(C_1 \frac{E_m t_m^3}{r_m^2} z_s + C_2 \frac{E_m t_m}{r_m^2} z_s^3\right)},$$

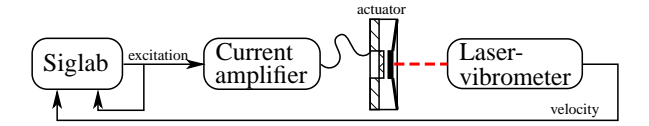


Figure 4.18: Experimental setup to measure the behavior of a single actuator using a SiglabTM system, a current source and a laser vibrometer.

where z_s is again used for brevity of notation. The relation between actuator stiffness $c_a(z_a)$ and displacement z_a becomes:

$$c'_{a}(z_{a}) = \lim_{\Re_{flm}, \Re_{flc} \to \infty} c_{a}(z_{a}),$$

$$= -\frac{2C_{2}E_{m}t_{m}}{r_{m}^{2}\mu_{0}A_{g_{a}}\Re'_{1}}z_{s}^{3} + \frac{3C_{2}E_{m}t_{m}}{r_{m}^{2}}z_{s}^{2} + \frac{2C_{1}E_{m}t_{m}^{3}}{r^{2}\mu_{0}A_{g_{a}}\Re'_{1}}z_{s} + \frac{C_{1}E_{m}t_{m}^{3}}{r_{m}^{2}}, (4.28)$$

where the dependence of \Re'_1 on the actuator deflection z_a has been omitted for brevity. Observe that the actuator stiffness remains a third order polynomial in the membrane deflection z_s , where only the first and third order terms depend on the magnetic circuit and are scaled by the total path reluctance $\Re'_1(z_a)$.

When the leakage flux is neglected for the equations describing the dynamic actuator behavior in Equation (4.24), the expression for \dot{I}_a becomes:

$$\dot{I}_a'(z_a) = \lim_{\Re_{flm}, \Re_{flc} \to \infty} \dot{I}_a(z_a) = \frac{-\Re_1'(z_a)}{N^2} \left(R_a I_a - V_a + \frac{N \left(H_{c_m} l_m - N I_a \right)}{A_{g_a} \mu_0 \Re_1'(z_a)} \dot{z}_a \right).$$

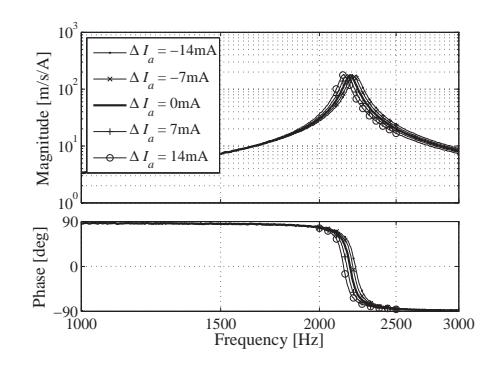
The expression for the linearized system in Equation (4.25) is unaffected, but the actuator stiffness $c_a(z_a')$ is given by $c_a'(z_a')$ in Equation (4.28) and the motor constant $K_a(z_a')$ and inductance $L_a(z_a')$ become $K_a'(z_a')$ and $L_a'(z_a')$ respectively, where:

$$K_a'(z_a') = \frac{-N\left(NI_a - H_{c_m}l_m\right)}{\left(\Re_1'(z_a')\right)^2}, \qquad L_a'(z_a') = \frac{N^2}{\Re_1'(z_a')}.$$

Both the motor constant and the inductance are thus inversely proportional to the total reluctance $\Re_1'(z_a')$. Since the motor constant is inversely proportional to the square of this reluctance, a modest reduction in reluctance will lead to a significant improvement of the motor constant.

4.3.5 Measurements and validation

Several prototypes of single variable reluctance actuators have been manufactured and measurements have been performed to determine their (dynamic) behavior. The quasi-static behavior of the actuator is governed by the force-displacement characteristic as derived in Equation (4.16), whereas its dynamics will be analyzed in terms of the parameters of the linearized system in Equation (4.25) and its mechanical resonance frequency. The measurements were performed using the test setup as depicted in Figure 4.18, consisting of a SiglabTM[43] system and a Polytec laser vibrometer. The Siglab system was used to generate an excitation signal that was fed to a current amplifier and also measured back at one of



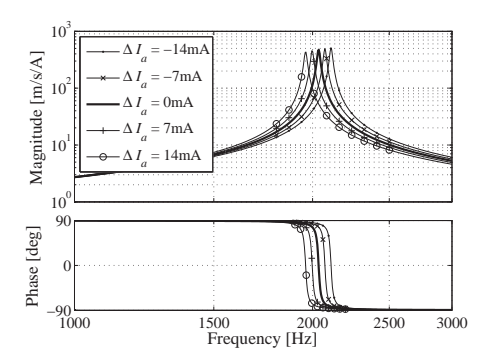


Figure 4.19: Measured frequency response functions of a single actuator for various current offsets ΔI_a .

Figure 4.20: Bode plots of the modeled transfer functions of a single actuator for various current offsets ΔI_a .

the Siglab inputs. The laser vibrometer was used to measure the velocity \dot{z}_a of the moving core and its output – an analog voltage – was also fed to a Siglab input. The sensitivity of the laser vibrometer was set to 25 mm/s/V with an output range of -10...10V.

To measure Frequency Response Functions (FRFs), a wide band, white noise excitation signal was used with an RMS level of ≈ 1.5 mA and DC offsets ΔI_a varying between -15 and 15mA. The FRFs are estimated using the Siglab software with a Hanning window of 8192 samples and 50 averages without overlap. The results are shown in Figure 4.19. Observe that the resonance frequency of the actuator lies around 2.1kHz and varies approximately 2Hz per mA current offset.

From the measured FRFs it is also possible to estimate the viscous damping, actuator stiffness and motor constant. This step requires the linearized model expressed in Equation (4.25) to be adapted from voltage to current input, as used in the test setup. When the current I_a is prescribed, the first state (I_a) of the system vanishes and the system is determined by the equations for the acceleration \ddot{z}_a and the velocity \dot{z}_a . This yields the following, second order state-space system:

$$\begin{bmatrix} \dot{z}_a \\ \ddot{z}_a \end{bmatrix} = \begin{bmatrix} 0 & 1 \\ -c_a(z_a')/m_{a_c} & -b_a/m_{a_c} \end{bmatrix} \begin{bmatrix} z_a \\ \dot{z}_a \end{bmatrix} + \begin{bmatrix} 0 \\ K_a(z_a')/m_{a_c} \end{bmatrix} I_a(t),$$

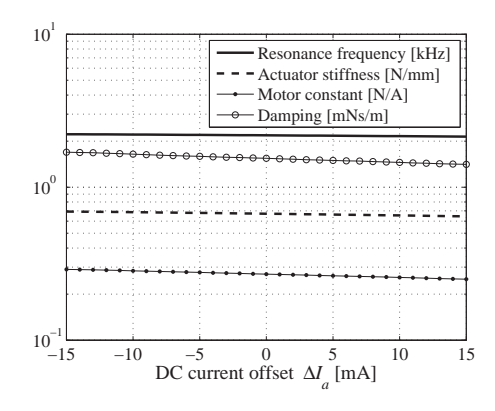
where \dot{z}_a is chosen as the system output corresponding to the type of laser vibrometer measurement used. This system can be rewritten into transfer function form as:

$$H_I(s, z_a') = \frac{K_a(z_a')s}{m_{a_c}s^2 + bs + c_a(z_a')}$$
(4.29)

and has an undamped mechanical resonance frequency f_e that depends on the operating point z_a' :

$$f_e(z_a') = \frac{1}{2\pi} \sqrt{\frac{c_a(z_a')}{m_{a_c}}}.$$

To obtain estimates for $K_a(z'_a)$, b_a and $c_a(z'_a)$, first a parametric identification on the FRF will be performed using Matlab's invfreqs function. However, to be able to derive the



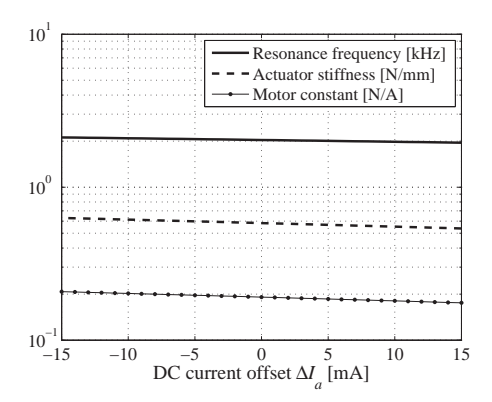


Figure 4.21: The viscous damping b_a , resulting actuator stiffness c_a , motor constant K_a and undamped mechanical resonance frequency f_e as a function of the DC current offset I_a' as identified from measurement data.

Figure 4.22: The modeled actuator stiffness c_a , motor constant K_a and resonance frequency f_e as a function of the DC current offset I'_a .

desired properties from the estimated coefficients, two modifications must be made to the above transfer function. Firstly, note that the lowest term of the numerator polynomial is zero. To prevent the need for a constraint in the parametric identification procedure, the numerator is divided by s. This corresponds to time domain integration that must be applied to the measured velocity signal prior to parametric identification. The second change is due to the fact that of the four coefficients only three can be uniquely identified and a fourth must be given. Since the value of m_{a_c} is well defined by manufacturing tolerances, this is further assumed to be known as listed in Table 4.1. The transfer function whose coefficients will be estimated can thus be expressed as:

$$H_I(s, z_a') = \frac{K_a(z_a')/m_{a_c}}{s^2 + (b_a/m_{a_c})s + c_a(z_a')/m_{a_c}}.$$
(4.30)

The Matlab function invfreqs is then used to estimate the three unknown coefficients from which $K_a(z'_a)$, b_a and $c_a(z'_a)$ are determined. The obtained values are plotted together with the damped resonance frequency corresponding to the poles of Equation (4.30) in Figure 4.21.

The following observations can be made by comparing the values obtained from the model in Figure 4.22 and from the measurements in Figure 4.21:

- the measured resonance frequency is higher than modeled and since the moving mass is known, this implies that the actuator stiffness must be higher,
- the stiffness and resonance frequency decrease with an increased axial air gap,
- the measured motor constant is higher than modeled,
- the measured viscous damping depends on the position of the core.

To explain the differences found, a sensitivity analysis of the variable reluctance actuator is performed.

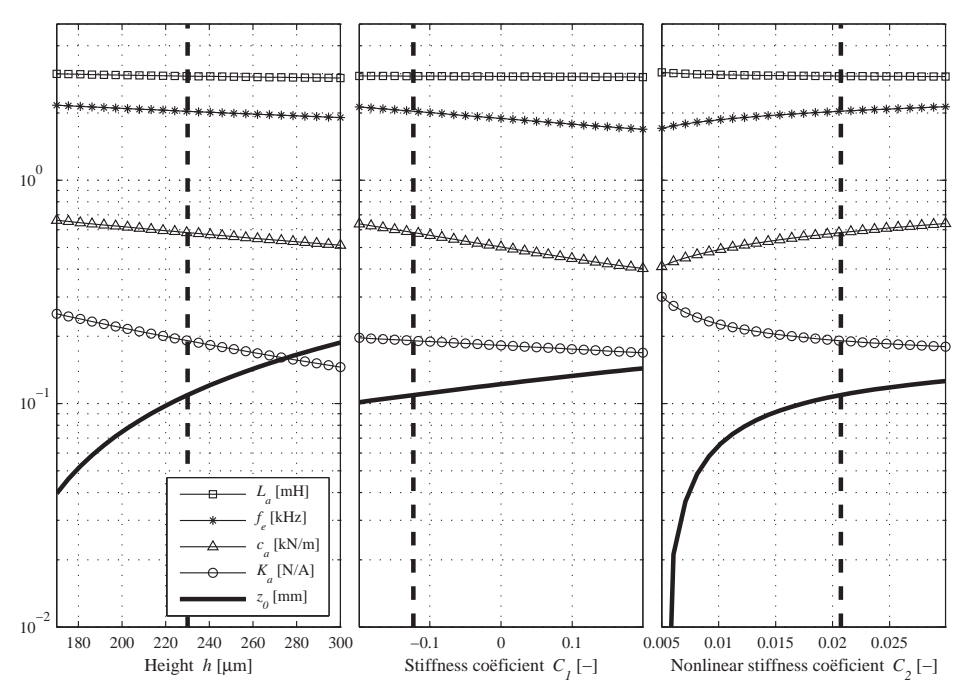


Figure 4.23: Sensitivity of the resonance frequency f_e , resulting stiffness c_a , motor constant K_a and inductance L_a of the actuator w.r.t. the height h and the stiffness constants C_1 and C_2 .

The thick, dashed vertical line represents the nominal value of the parameter, as listed in Table 4.1.

4.3.6 Sensitivity analysis

Figure 4.23 shows the sensitivity of the resonance frequency f_e , actuator stiffness c_a , motor constant K_a and inductance L_a of the actuator w.r.t. the height h and the stiffness coefficients C_1 and C_2 . This figure is obtained by evaluating the expressions for f_e , K_a , c_a and L_a derived in the previous subsections while varying a single actuator property and keeping all others at their nominal values as listed in Table 4.1. These values are marked by the thick, dashed vertical lines. The results include the effect of the parameters on the initial air gap z_0 on which all expressions implicitly depend. From Figure 4.23 the following remarks are made:

The height h.

An increase of the height h causes an increase of the initial air gap and a working point with less stiffness and lower motor constant.

The stiffness coefficient C_1 .

A change in the linear stiffness coefficient C_1 of the membrane suspension will result in a change in initial air gap z_0 . The magnetic force depends on the reluctance of

the magnetic circuit and therefore on the position of the moving core. In the equilibrium position, the spring force is equal to this magnetic force. The spring force is proportional to the deflection and the linear and nonlinear stiffness of the membrane suspension. If the linear stiffness coefficient decreases, the initial air gap z_0 will decrease and the contribution of the nonlinear stiffness on the actuator stiffness will increase. This effect is attenuated by the stiffness due to the magnetic circuit which also increases for smaller air gaps. However, this effect is linear with the decrease air gap whereas the effect on the mechanical spring stiffness is quadratic. The net effect is an increase in actuator stiffness and resonance frequency.

For a smaller air gap the magnetic reluctance drops, causing the magnetic flux, hence the force F_m and the motor constant K_a to increase.

The stiffness coefficient C_2 .

A decrease in the nonlinear stiffness coefficient C_2 of the membrane suspension will also result in a smaller initial air gap. In analogy with the linear stiffness coefficient C_1 this leads to a larger deflection to maintain force equilibrium, but this deflection increase is accompanied by a lower spring stiffness and will therefore – in contradiction to the stiffness coefficient C_1 – result in a lower overall stiffness.

Again with the smaller air gap the magnetic reluctance drops and the motor constant increases.

Figure 4.24 shows the sensitivity of the resonance frequency f_e , actuator stiffness c_a , motor constant K_a and inductance L_a w.r.t. the leakage flux reluctances \Re_{flc} and \Re_{flm} of the coil and the PM respectively and the radial air gap reluctance \Re_{g_a} . The figure was obtained the same way as Figure 4.23 and the thick, dashed vertical lines represent the parameter values listed in Table 4.1. From Figure 4.24 the following is observed:

The coil leakage flux reluctance \Re_{flc} .

The leakage flux reluctance of the coil has no significant effect on the initial air gap z_0 , actuator stiffness c_a or resonance frequency f_e . As the reluctance \Re_{flc} of the coil leakage flux decreases to the order of the reluctance \Re_{bc} of the coil core, the motor constant becomes affected. The major part of the flux generated by the coil will then flow into the leakage flux path.

The coil inductance L_a decreases for increasing \Re_{flc} , since this inductance is proportional to $N^2/\tilde{\Re}(z_a)$ and $\tilde{\Re}(z_a)$ is proportional to \Re_{flc} .

The PM leakage flux reluctance \Re_{flm} .

If the reluctance \Re_{flm} of the PM leakage flux is decreased, the attraction force on the ferromagnetic core decreases and the initial air gap will be larger. As illustrated by Figure 4.13, a lower equilibrium force will result in a lower stiffness of the membrane suspension and resonance frequency. The motor constant K_a decreases when \Re_{flm} decreases since the equilibrium force decreases and the air gap increases. As long as \Re_{flm} does not significantly affect the total reluctance experienced by the coil, there is little change in coil inductance.

The radial air gap reluctance R_{g_a} .

The reluctance of the radial air gap forms a significant part of the total reluctance

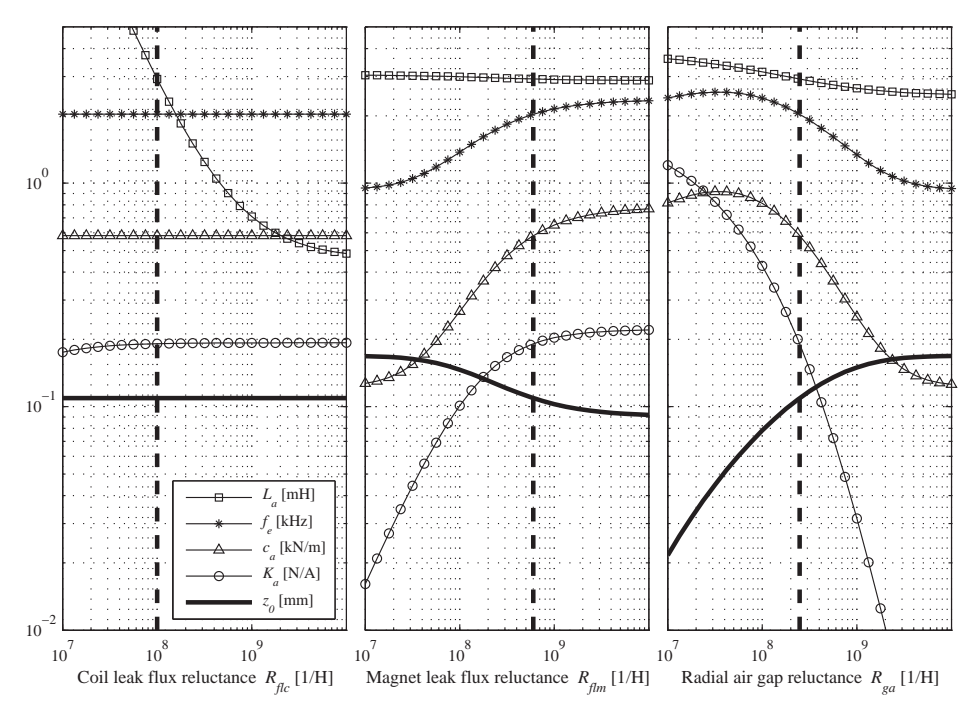


Figure 4.24: Sensitivity of the resonance frequency f_e , resulting stiffness c_a , motor constant K_a and inductance L_a of the actuator w.r.t. the leakage flux reluctances of the coil \Re_{flc} and the PM \Re_{flm} and the radial air gap reluctance \Re_{g_a} . The thick, dashed vertical line represents the parameter value listed in Table 4.1.

in the flux path through the axial air gap (ϕ_1) . This explains its significant effect of motor constant and initial air gap z_0 . When the total reluctance decreases, the flux, the force and the motor constant increase. The decrease of the axial air gap z_0 explains the increase in actuator stiffness and resonance frequency.

Figure 4.25 shows the sensitivity of the resonance frequency f_e , actuator stiffness c_a , motor constant K_a and inductance L_a of the actuator w.r.t. the axial air gap area A_{g_a} , the coercivity of the PM H_{c_m} and the PM thickness l_m . The figure was obtained the same way as Figure 4.23 and the thick, dashed vertical lines represent the parameter values listed in Table 4.1. From Figure 4.25 the following is observed:

The axial air gap area A_{g_a} .

Observe that the area A_{g_a} is present in the expression for the magnetic force F_m in Equation (4.13) and thus directly influences the initial air gap z_0 . However, A_{g_a} also affects the actuator properties indirectly via the reluctance \Re_{g_a} . This reluctance enters quadratically in Equation (4.13) and becomes the dominant term for small values of A_{g_a} . This leads to an increased magnetic force and a reduction of the nominal air gap

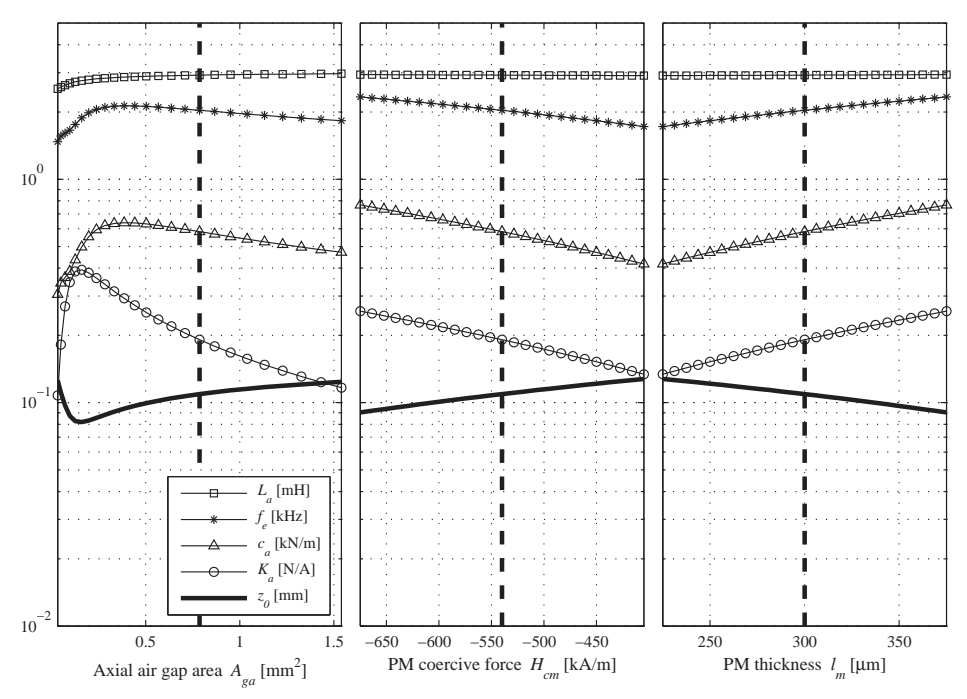


Figure 4.25: Sensitivity of the resonance frequency f_e , resulting stiffness c_a , motor constant K_a and inductance L_a of the actuator w.r.t. the axial air gap radius r_{g_a} , and the coercivity of the PM H_{c_m} and thickness l_m of the PM. The thick, dashed vertical line represents the parameter value listed in Table 4.1.

width that explains the minimum in the graph for z_0 . The initial air gap also affects the motor constant, leading to a maximum in the graph for K_a that corresponds to the minimum for the air gap z_0 . The actuator stiffness decreases as z_0 increases for small values of A_{g_a} . For larger values of A_{g_a} , the stiffness c_a is dominated by the nonlinear mechanical spring stiffness that decreases as the air gap z_0 increases. The decreased negative magnetic stiffness will not compensate for the mechanical spring stiffness reduction and an overall decrease in stiffness results.

The magnetic field intensity H_{c_m} of the PM.

If the coercive force of the PM is increased the magnetic force increases. This increase leads to a smaller air gap with a higher actuator stiffness, resonance and motor constant.

The thickness l_m of the PM.

A thickness increase of the PM has the same effect as a coercive force increase.

Besides sensitivity of the actuator properties f_e , c_a , K_a and L_a on the parameters h, C_1 , C_2 , \Re_{flc} , \Re_{flm} , \Re_{g_a} , A_{g_a} , H_{c_m} and l_m , it is relevant to know what causes the possible

differences in these parameters and how to minimize them. First of all, the predictability of the actuator properties is increased by the measurements performed to identify the coercivity H_{c_m} of the PMs and the stiffness coefficients C_1 and C_2 of the membrane suspension. Besides this, the manufacturing tolerances and assembly tolerances play an important role:

Manufacturing tolerances.

All dimensions of the actuator are subject to manufacturing tolerances. Manufacturing tolerances are typically in the order of tens of μm . These dimensions directly determine all modeled magnetic reluctances, the mechanical stiffness coefficients C_1 and C_2 and the moving mass m_{a_c} . Besides dimensions, the magnetic permeability of the ARMCO can be influenced by stresses caused by the manufacturing process. This is likely to play a role for the reluctances of the baseplate, the moving core and the radial air gap. As a result, all actuator properties will be affected and vary from actuator to actuator.

Assembly tolerances.

In addition to tolerances on the manufactured parts themselves, the design dimensions are affected by the assembly process. For instance, the thickness of the glue layers between (1) the PM and the coil insert and (2) between the baseplate and the membrane suspension and (3) between the moving core and the suspension membrane lead to a variation of the height h. Another example is the reluctance of the radial air gap, which is affected by the in-plane alignment of the moving core w.r.t. the pole shoes. Tolerances on the assembly process used are expected to be typically in the order of ten μ m. In Section 4.4 it will be shown how – by design and assembly – the effect of manufacturing and assembly tolerances on the actuator behavior is minimized.

In the next section, the results from the modeled actuator (Figure 4.22) and the measured actuator (Figure 4.21) will be compared and analyzed based on insights of the sensitivity analysis.

4.3.7 Lessons learned

Actuator stiffness c_a and resonance frequency f_e

The actuator stiffness c_a is directly coupled to the mechanical resonance frequency f_e via the mass m_{a_c} . The stiffness values derived from the measurements are higher than expected from the model. With the use of Figures 4.23 and 4.24 it is shown that the stiffness c_a varies significantly for all considered parameters except for the coil leakage flux reluctance. This is caused mainly by its dependence on the initial air gap z_0 , which is affected by all parameters. Note from Figure 4.14 that in general the stiffness increases as z_0 decreases. Variation of parameters that lead to an increase in z_0 will therefore lead to a decrease in c_a .

The same effect is observed in the variation w.r.t. the operating point. In accordance to the model, the stiffness is found to change with the deflection z_a (or I_a): it increases for negative z_a and decreases for positive z_a .

Motor constant K_a

The measured value ($\approx 0.28 \text{N/A}$) for the motor constant K_a is higher than the original design value of $\approx 0.2 \text{N/A}$. As can be observed in Figures 4.23 and 4.24, the motor constant shows considerable variation w.r.t. all analyzed parameters except the coil leakage flux reluctance \Re_{flc} . Most noticeable is the strong dependence of the radial air gap reluctance \Re_{g_a} . A higher motor constant can therefore be partially attributed to a lower reluctance of the radial air gap.

Finally, note from Figure 4.25 that there exists a value for the axial air gap area A_{g_a} where the motor constant has a maximum. This may be exploited in future designs to obtain a higher power efficiency.

Inductance L_a

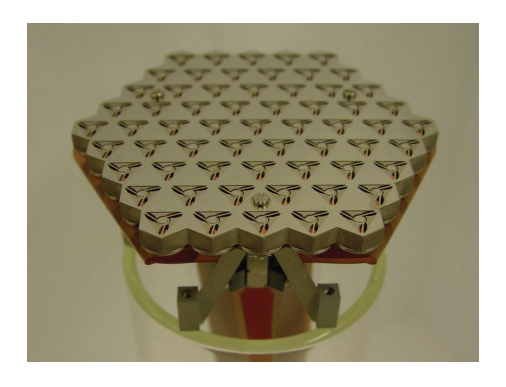
As can be observed in Equation (4.26), the inductance L_a of the actuator is a function of the number of turns N in the coil and the reluctances in the magnetic circuit. Consequently, only parameters that have a significant effect on the total reluctance will cause a significant change in L_a . The dominant reluctances are $\Re_{g_a}(z_a)$ of the axial air gap and \Re_{g_r} of the radial air gap and \Re_m of the PM.

Damping b_a

In the model, the damping is considered a constant, but the measurement results in Figure 4.21 indicate that the damping varies with the deflection of the moving core. A possible explanation for this effect is that a so-called squeeze film exists between the PM and the moving core. When the core moves, air is either expelled from or compressed between the two objects. Viscosity hampers the flow of air, which leads to both spring and damper behavior that depends on the distance between the two objects and the relevant time scale (i.e. frequency of motion) [119].

Although differences between the model and measurements exist and the analysis results indicate that improvement of the motor constant in particular is well possible, the results are good enough to proceed with design and integration of actuators in grids.

The design and realization of these actuator modules will be introduced in the next section. Measurement results, including the variation and spread in actuator properties, on all actuators of seven prototype grids will be presented in Section 4.4.3.



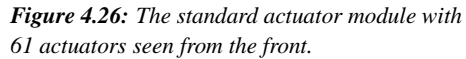




Figure 4.27: The standard actuator module with 61 actuators seen from the back.

4.4 The actuator module

In the transformation of the single actuator design into a grid actuator module, the philosophy is to design in layers that extend over many actuators and not to make many individual actuators that need to be placed and aligned individually. This reduces the number of parts and the complexity of assembly and improves the uniformity of the actuator properties. A hexagonal actuator layout is chosen since this gives the highest actuator areal density. The grids are also given a hexagonal shape to accommodate the assembly of large DMs from many actuator grids. The grid layout consists of a central actuator surrounded by a number of hexagonal 'rings' of actuators. This approach results in a total of 7, 19, 37, 61, 91 or 127 actuators for 1, 2, 3, 4, 5 or 6 rings respectively. For the prototype grids realized, four rings, corresponding to 61 actuators, are chosen. In this choice, several practical issues were taken into account, such as the size of the baseplate and its corresponding resonance frequency. A larger grid would require more thickness, or additional support points to avoid internal resonances. Further, the actuator coils are connected through flex foils. These will become more difficult to manufacture as the number of actuators per grid increases. When the line pattern is made on a single layer there is not enough area for more connections. Finally, the number 61 is close to a division factor of $2^6 = 64$, which is likely to be used in digital electronics for drivers and communication.

4.4.1 Actuator grid design

The actuator grid is shown in Figures 4.26 and 4.27. Figure 4.28 shows the exploded view of the actuator grid. The main parts shown in the exploded view are summarized and will be discussed in detail:

The baseplate

The baseplate serves a the flux carrier for the magnetic circuits for 61 actuators and is made from from ARMCO[®]. The baseplates are cut from bar and their front and

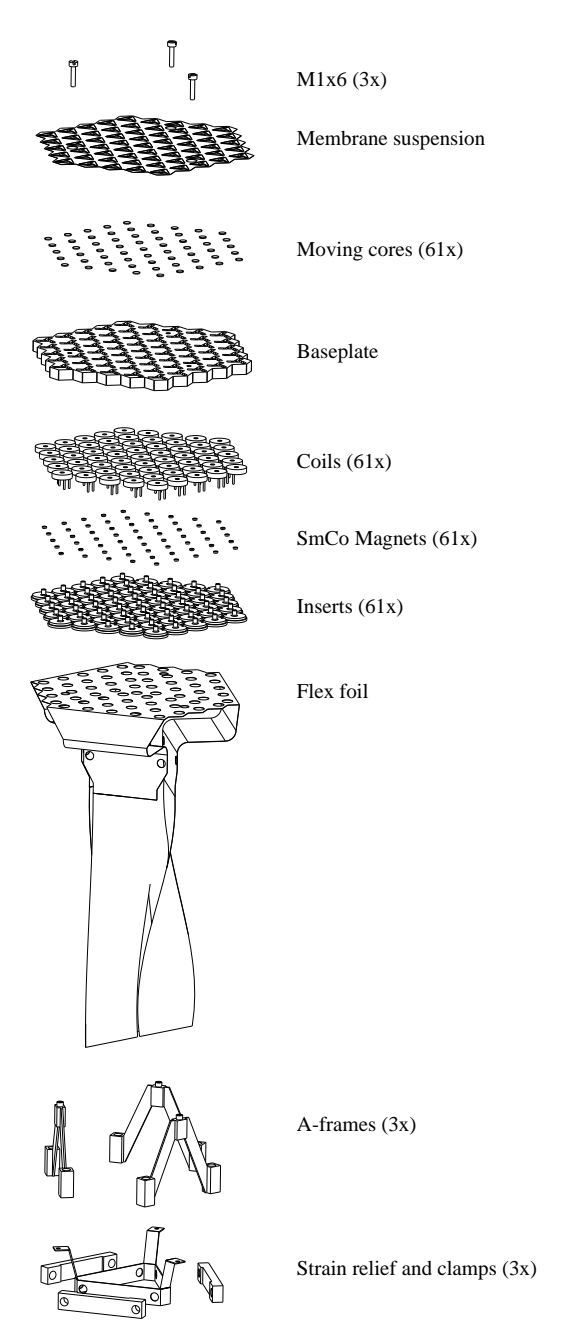


Figure 4.28: An exploded view of the actuator grid shown in Figures 4.26 and 4.27.

back surfaces are made plan parallel. The serrated circumference is made such that the actuator grids can be placed adjacent with a 0.3mm gap. The holes in the backside are made by milling, the circumference and pole shoe contours are made with wire EDM.

The membrane suspension with moving cores

The membrane suspension is made by laser cutting. The same sheet of rolled Havar® material is used for all actuator grids in the same orientation to obtain uniformity for the spring characteristic. The moving cores are laser cut and made from a 0.3mm thick ARMCO® sheet.

Inserts with the SmCo₅ PMs and coils

The inserts complete the magnetic circuit. The inserts are produced on a CNC lathe. After measurement and selection of the PMs described in Appendix A, the PMs are glued on the inserts with Araldite 2020. The coils, made of $50\mu m$ copper wire with 500 turns, are fabricated separately from the insert and have pre-leaded ends. The electrical resistance of each coil is measured before placement. The inner radius of the coil is made slightly larger than the insert core to avoid damage to the electrical isolation when placed. The bottom of the inserts contains a hole and a slot to provide an axial feed through for the coil wires.

The flex foil

A flex foil is designed to connect the coil wires to the driver PCB. This flex foil design is shown in Figure 4.43. Each of the three branches of the flex foil connects to a double row, 0.3mm pitch, connector. The central hexagonal part of the flex foil holds $\varnothing 2.5$ mm holes through which the coil wires emerge. At the circumference of the holes, the two wires of that coil are soldered each on a copper pad. After soldering, a droplet of silicon glue is placed to encapsulate the fragile coil wires. A strain relief (Figure 4.27) is added to avoid damage to the soldered connections.

The actuator grid supports

The actuator grid is connected with three A-frames to its support structure. Each A-frames is connected with one point to the baseplate and with two points to the support structure to avoid moments enforced on the baseplate. The A-frames are connected with M1 bolts. When the actuator grid is placed facedown on the table, with the membrane suspensions facing down, the bolt heads support the actuator grid and avoid damage to the suspension systems.

The next subsection will describe the assembly of an actuator grid.



Figure 4.29: Top view of the laser cut membrane suspension made from $25\mu m$ thick Havar[®].



Figure 4.30: A mould placed on top of the membrane suspension to position the ferromagnetic moving cores. The struts to align the mould and thereby the moving cores with respect to the membrane suspension are visible.

4.4.2 Actuator grid assembly

The assembly of the actuator grids is done in four steps.

- 1. The ferromagnetic cores are glued to the membrane suspension.
- 2. The membrane suspension with the ferromagnetic cores is assembled to the baseplate.
- 3. The PMs and coils are glued to the inserts and the inserts placed in the baseplate.



Figure 4.31: Struts are pressed to the cores to ensure a thin layer of glue between the cores and the membrane suspension. An elastomer foam and a weight is added on top of the struts (not shown).

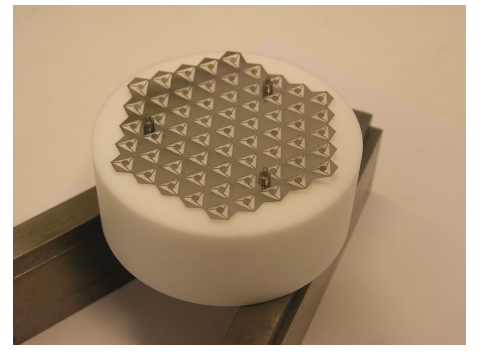


Figure 4.32: The cores glued on the membrane suspension visible after removal of the mould. The Havar[®] foil is seen to be slightly curved due to internal stress as a result of the foil rolling process.

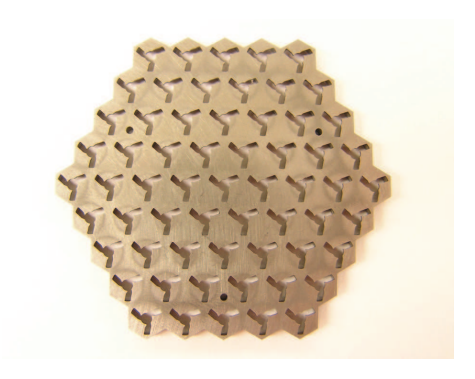




Figure 4.33: Front side of the baseplate.

Figure 4.34: Back side of the baseplate.

4. The flex foil is placed and the coil wires are soldered to the flex foil. Three A-frames and a strain relief are bolted to the actuator grid. The actuator grid is fully assembled and can be placed on the support structure.

Each assembly step is described in more detail and clarified by photo's.

Step 1: Assembly of the cores and the membrane suspension

Figure 4.29 shows the laser cut membrane suspension made from a $25\mu m$ Havar® rolled foil. For assembly this foil is placed on a flat base and laterally constrained by three metal struts. These struts can move up and down in the base. A 2.5mm thick mould, that contains 61 holes to position the cores, is placed on top of the foil. The struts align the mould and holes to the membrane suspension. Figure 4.30 shows the base with the mould placed on top of the membrane suspension. 61 Droplets of glue (Araldite 2020) are manually placed in



Figure 4.35: The baseplate is placed on the membrane suspension.



Figure 4.36: The baseplate is supported by the struts and lowered on the membrane suspension.



Figure 4.37: The baseplate placed on the membrane suspension. The cores are visible between the pole shoes.



Figure 4.38: A detailed view off one of the actuator suspensions with moving core and pole shoes in the baseplate. The air gap between the core and pole shoes is 0.1mm.

the holes of the mould followed by an iron core. Figure 4.31 shows 61 struts that are pressed to the cores to ensure a thin layer of glue between the cores and membrane suspension. An elastomer foam and a weight is added on top of the struts to ensure equal pressure. When the glue is hardened the struts and mould are removed. The result is shown in Figure 4.32.

Step 2: Assembly of the membrane suspension and baseplate

Figure 4.33 and Figure 4.34 show the front and back side of the baseplate. Droplets of glue are placed on the membrane suspension at the end of each leafspring of the suspension.



Figure 4.39: Top view of the baseplate with membrane suspension and cores.

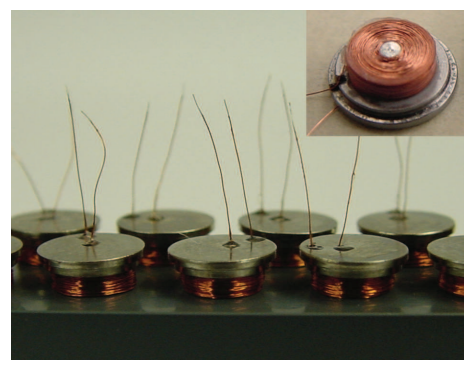


Figure 4.40: The assembled inserts with PM and coil placed in a container. Note the droplets of glue on the wires to avoid damage to the insulation.

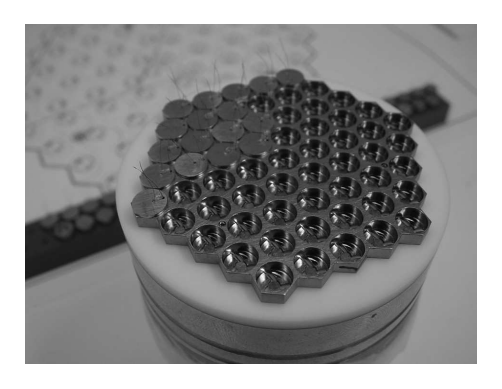


Figure 4.41: Assembling the inserts in the base-plate.

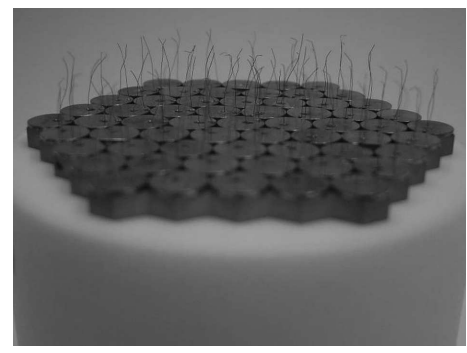


Figure 4.42: All inserts placed in the baseplate. The coil wires extend over 8mm and are tin plated.

The baseplate is placed on the thinned ends of the struts and lowered on the membrane suspension. This is shown in Figures 4.35, 4.36 and 4.37. Figure 4.38 shows a detail of the baseplate. The pole shoes, membrane suspension and core are shown for a single actuator. The air gap between the core and the pole shoes is 0.1mm. Figure 4.39 shows the top view of the baseplate with membrane suspension and cores as removed from the assembly base. All air gaps are checked before proceeding.

Step 3: Assembly of the inserts

On the iron inserts, a PM and coil is placed. All magnets are placed with their magnetization in the same direction. In the bottom part of the insert, a hole and slot has been prepared for

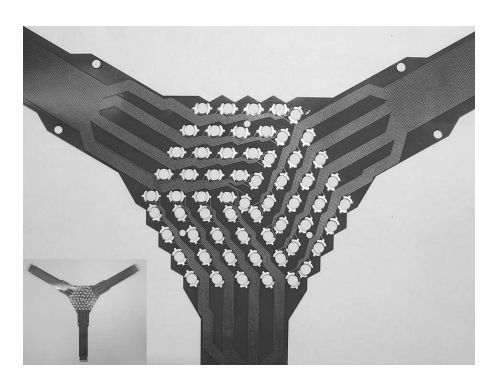


Figure 4.43: The flex foil that provides two electrical connections per actuator between the driver electronics PCB and the actuators.

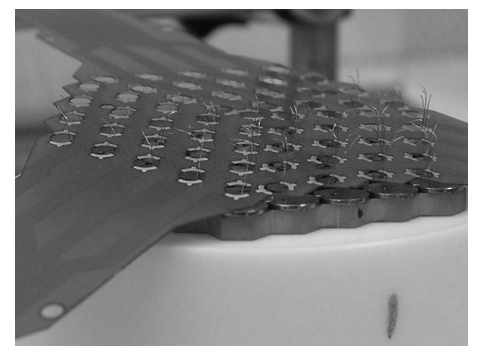


Figure 4.44: The coil wires pass through the holes in the flex foil.





Figure 4.45: The flex foil connected to the actuator grid.

Figure 4.46: Detail view of the actuator grid.

the coil wires. Figure 4.40 shows a photo of the inserts prepared awaiting assembly in a container. Figure 4.41 and Figure 4.42 show the inserts being placed in the baseplate.

Step 4: Flex foil assembly

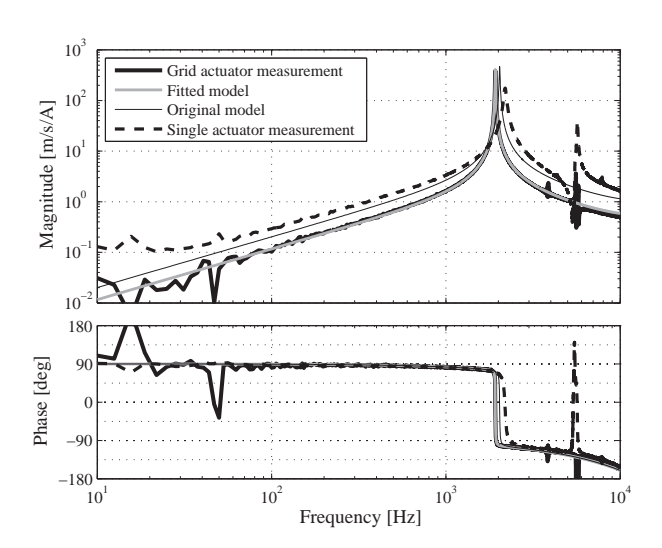
The flex foil is shown in Figure 4.43. Figure 4.44 shows the flex foil lowered over the coil wires. The two wires of each coil pass through a hole in the flex foil and are soldered onto a copper pad at the circumference of the holes. Silicone glue is added to protect the wires and soldered connection from damage. The A-frames are bolted on the baseplate and the strain relief is added. The flex foil is folded and clamped on the frame. The result is shown in Figures 4.26 and 4.27. The grid is then bolted on the three A-frames. Figure 4.46 shows a detail of the actuator grid.

4.4.3 Measurement results

A batch of seven grids was realized using the above procedure. The only difference in nominal dimensions with respect to the single actuator is an additional 25µm for the height h. Although this is known to have a negative effect on the motor constant, actuator stiffness and resonance frequency, more margin is hereby built in for manufacturing errors and the risk on ferromagnetic cores to snap down on the PMs is avoided. The reduced motor constant, actuator stiffness and resonance frequency are estimated from Figure 4.23 as K_a =0.17 N/A, c_a =550N/m and f_e =1980 Hz.

For each grid all actuators are measured with the same experimental setup as shown in Figure 4.18. Figure 4.47 shows a typical transfer function with a parametric model fit of one of the actuators in the grid. As a reference, the figure also shows the nominal transfer function derived from the analytical model depicted previously in Figure 4.20. Besides the first resonance frequency around 2kHz, a second resonance is visible at approximately 5kHz. This is the tip/tilt mode of the ferromagnetic core in its membrane suspension that can only

Figure 4.47: Bode plot of the measured transfer function $H(z_a)$ from a single actuator in a grid, together with the fitted model and the analytic model. The measured transfer function of the single actuator as shown in Figure 4.19 is also plotted for comparison.



be observed when the laser vibrometer is not perfectly aligned to the center of the moving core.

Estimates for the actuator stiffness c_a , resonance frequency f_e , motor constant K_a and viscous damping b_a are obtained from the measurement data using the same procedure as described in Section 4.3.5. The average and standard deviation values are listed in Table 4.2 and more detailed results are shown in Figures 4.48, 4.49, 4.50 and 4.51. The values in the figures are sorted to provide insight into the statistical spread and differences in median values between grids. The mean actuator stiffness and resonance frequency are 471N/m and 1.83kHz respectively, which is lower than expected. In Figure 4.48 it is shown that the spread in stiffness values within a grid is similar for all grids, but that the mean differs from grid to grid. This can be caused by manufacturing and assembly variations that directly

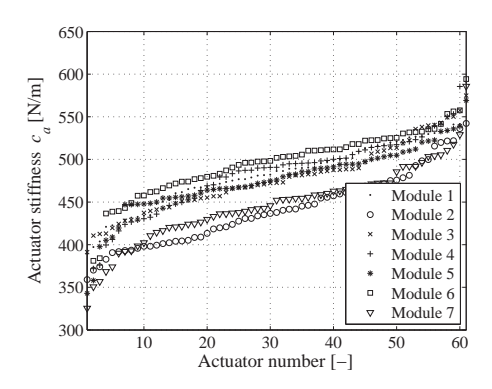


Figure 4.48: The identified actuator stiffness c_a , for $m_{a_c}=3.6$ mg sorted for each measured actuator grid separately.

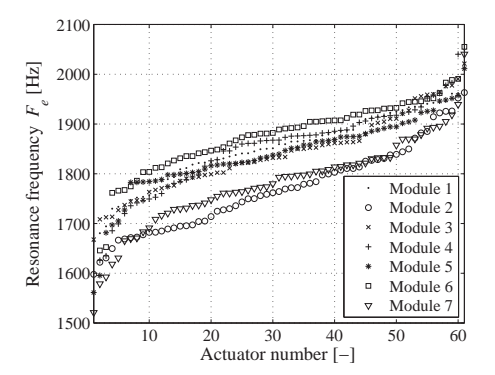
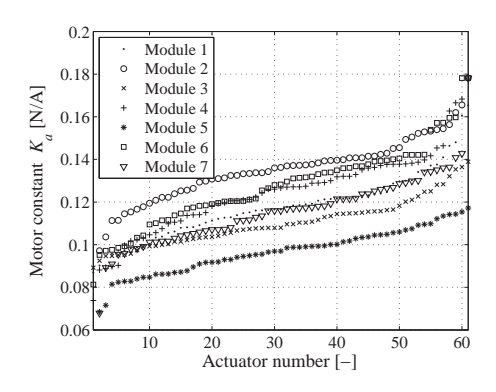


Figure 4.49: The identified actuator resonance f_e , for $m_{a_c} = 3.6$ mg sorted for each measured actuator grid separately.



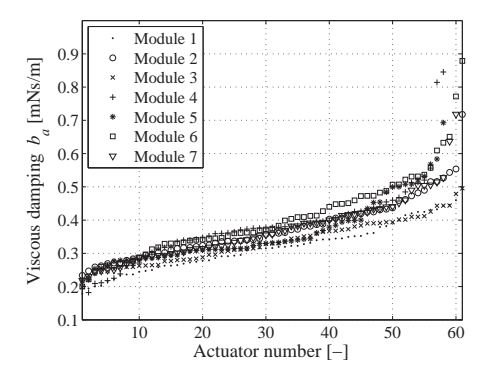


Figure 4.50: The fitted motor constants K_a , for $m_{a_c} = 3.6$ mg sorted for each measured actuator grid separately.

Figure 4.51: The fitted damping b_a , for $m_{a_c} = 3.6$ mg sorted for each measured actuator grid separately.

Table 4.2: Average values and standard deviations of the actuator properties measured over all grid actuators.

Property	K_a	c_a	b_a	f_e
Average	0.12N/A	471N/m	0.36mNs/m	1.83kHz
Std.dev.	0.02N/A	48N/m	0.10mNs/m	95Hz

affect all actuators in a module, such as baseplate or suspension membrane thickness variations.

Figure 4.50 shows the values of the motor constants, which are lower than expected. The analytic model predicted K_a =0.17N/A, whereas 0.12N/Ais measured. A possible explanation for the measurement results is that the leakage flux reluctances for the PM and coil are smaller in the actuator module baseplate than for the single actuator. The few high values for damping are explained by rests of glue in between the moving core and baseplate.

4.4.4 Power dissipation

To analyze the expected power dissipation of the actuator, only its static response is considered and assumed to be linear. The validation measurements have shown this to be an accurate approximation at least up to approximately 1600Hz, where effects such as viscous damping and eddy currents play a negligible role.

The power dissipated by the current I_a through the actuator coil with resistance R_a can be expressed as:

$$P_a = I_a^2 R_a = \left(\frac{F_a}{K_a}\right)^2 R_a,$$

where for the second step the linearized case $F_a = K_a I_a$ was used. In Chapter 2 the expected RMS actuator force was derived as 1mN, which was based on an actuator stiffness

 c_a of 500N/m. Since the stiffness of the realized actuator was found to be very close to this value, the 1mN RMS force remains a valid basis to evaluate power dissipation. For 1mN RMS actuator force and a measured average motor constant K_a of 0.12N/A this yields an RMS actuator current I_a of approximately 8mA. Via the coil resistance $R_a\approx 39\Omega$, this corresponds to a power dissipation of approximately 3mW per actuator. This means that the realized actuators meet the specification in Chapter 2 that the power dissipation must be in the order of mW's.

4.5 Conclusions

The application of electromagnetic actuators for adaptive deformable mirrors has several advantages. Electromagnetic actuators can be designed with a limited stiffness, such that failure of an actuator will cause no hard point in the reflective surface and thus a small optical degradation compared to e.g. stiff piezo-electric elements. Other advantages over the latter type of actuators at the relatively low cost, low driving voltages and negligible hysteresis and drift.

Variable reluctance type actuators were primarily chosen because of their high efficiency and low moving mass. A nonlinear mathematical model of the actuator was derived describing both its static and dynamic behavior based on equations from the magnetic, mechanic and electric domains. The nonlinear spring force characteristic of the membrane suspension was modeled and verified via measurements in a dedicated measurement setup (Appendix B). This indicated that FEM analysis can predict the nonlinear behavior well, but could not predict the effect of internal stresses resulting from the production of the rolled Havar[®] foil. The model was linearized, leading to expressions for the actuator transfer function and linear electromechanical properties such as motor constant, coil inductance, actuator stiffness and resonance frequency.

Single actuator prototypes were realized and transfer functions were estimated from measurement data, based on white noise current excitation. This was done for various operating points by adding static current offsets to the excitation signal, which showed that the effect of the nonlinearities is indeed small. The resonance frequency and the DC-gain of the transfer functions showed only marginal variation with respect to the operating point. This means that a control system will be able to use an LTI control law without sacrificing performance. The measured nominal resonance frequency is higher than modeled: 2.1 kHz instead of 2 kHz, corresponding to an actuator stiffness of $\approx 680 \text{N/m}$. The measured motor constant is also higher than modeled 0.27 N/A instead of 0.2 N/A.

Due to the satisfactory measurement results, the design for single actuators was applied with little modification to the design of standard hexagonal modules with 61 actuators. Only the nominal height h of the moving core above the PM was increased by $25\mu m$ to limit the risk of the ferromagnetic cores snapping down onto the PM. Based on the results of a sensitivity analysis, this modification was expected to reduce the motor constant, actuator stiffness and resonance frequency to K_a =0.17N/A, c_a =550N/m and f_e =1980Hz respectively.

In this sensitivity analysis the effect was determined of variation in a number of model parameters on several actuator properties (i.e. stiffness, resonance frequency, motor constant and inductance) as derived from the mathematical model. In particular, this indicated a

4.6 Recommendations 117

strong influence of the radial air gap reluctance on the motor constant and actuator stiffness, which can explain the deviation between the modeled and measured properties.

Seven actuator module prototypes were made of which all actuators were measured with the same setup as the single actuator prototypes. All actuators were found to be functional, indicating that the manufacturing and assembly process is reliable. From transfer function measurements, the motor constant, actuator stiffness and resonance frequency were identified. These properties showed slight deviations from the values derived from the model, but the statistical spread for the properties was small, stressing the reliability of the manufacturing and assembly process. The mean actuator stiffness and resonance frequency were 471N/m and 1.83kHz respectively, which are very close to their design values of 500N/m and 1885Hz. The value derived from the model for the motor constant K_a was 0.17N/A, whereas on average only 0.12N/A was measured. This may be the result of leakage flux reluctances in the baseplate being lower – and thus the leakage flux being larger – than for the single actuator.

Despite the motor constants of the actuators realized being lower than expected, the RMS power dissipation of the actuators is still low during operation and expected to be ≈ 3 mW.

4.6 Recommendations

In a redesign, the large influence of the radial air gap reluctance can be used to increase the motor constant and reduce power dissipation. A factor of two reluctance reduction will increase the motor constant to 0.37N/A and increase the actuator stiffness to 750N/m. This can be realized by a smaller gap width or by a larger gap area.

A reduction of the axial air gap area will lead to a further increase in motor constant. With these changes, an improvement by a factor four is feasible. Since power dissipation is inversely proportional to the squared motor constant, a power dissipation reduction by a factor 16 is achieved. A convenient side effect is the increased electronic damping of the mechanical resonance frequency. This is illustrated in Figure 4.52. The magnitude peak of the two systems is almost equal, whereas the DC-gain of the improved system is four times higher. This implies that the resonance mode is much better damped and will be less limiting for the controller performance.

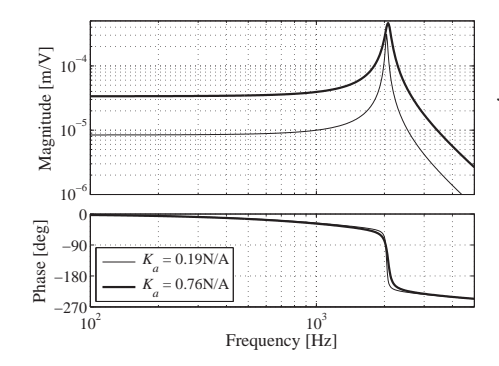


Figure 4.52: Bode plot of the voltage to position actuator model with the currently measured and four times higher motor constant. Note the increased relative damping of the resonance mode.

Chapter five

Electronics

This chapter describes the design and realization of the actuator driver electronics and communication system. PWM based voltage drivers are selected and implemented in three FPGAs for 61 actuators (one actuator module). A high base frequency of 61kHz and an additional analog 2^{nd} order low-pass filter is used to reduce the actuator position response ripple due to harmonics of the PWM signal to less than a quarter of the Least Significant Bit (LSB) of the setpoint. The driver electronics of each actuator module are contained on a single PCB, which is placed behind the actuator module to preserve the modular concept. The FPGAs receive the voltage setpoints via an LVDS communication link from the control system. As no commercial LVDS interface board was available for a standard PC, an ethernet-to-LVDS communications bridge is developed that translates ethernet packages into LVDS packages and vice versa. A single flat-cable connects up to 32 driver PCBs to this communications bridge.

The actuator model from Chapter 4 is extended with models for the communication and driver electronics. The communication is modeled as a pure delay and the driver electronics as an ideal voltage source with a linear, analog 2^{nd} order low-pass filter. The dynamic model is validated using white noise identification measurements on the actuator system. The system is evaluated on control aspects, showing the dependance of achievable bandwidth on the sampling frequency. Finally, the power dissipation of the FPGAs is evaluated and found to exceed the power dissipation in the actuator coils. Concepts are proposed and analyzed to reduce power dissipation in the digital electronics.

120 5 Electronics

5.1 Introduction

In this chapter, the design and realization of the electronics required to generate the currents through the coils of the actuators is described. The actuators were described in Chapter 4 The electronics consist of two parts: a communication system and driver electronics. The communication system transmits the current value calculated by the control system to the driver electronics, which generate the actual currents. The main difficulty of the driver electronics is the required number of channels combined with the desired high power efficiency. After the realization of these electronics, the behavior of the full actuator system is analyzed by comparing it to a first principles model. This model is obtained by extending the model from Chapter 4 to include the components of the electronics systems.

In the next two sections design concepts for the driver and communication electronics will be presented, followed by their implementation and realization in Section 5.4. The first principles model is derived in Section 5.5 and compared to measurement results in Section 5.6. Since the driver electronics and the actuators are located close to the DMs reflective surface, power dissipation is an important design driver. Therefore, in Section 5.7 the power dissipation of the prototype actuator system is analyzed and compared to the design requirements. Finally, the main conclusions will be formulated.

5.2 Driver electronics

The driver electronics provide currents through the coils of the variable reluctance actuators. In the actuator, the current converts into forces that deform the mirror facesheet. In this section the requirements, design concepts and implementation of the driver electronics will be discussed.

5.2.1 Requirements

In Section 2.3 the required actuator positioning resolution is derived as 5nm. From this value, the worst-case required range and resolution will be derived of the currents and voltages that must be provided by the driver electronics. Since the resolution requirement is in terms of displacement, the mechanical stiffness, motor constant and circuit resistance must be considered. The mechanical stiffness depends on the resulting deformation of the reflective surface. The minimal stiffness is used to determine the required resolutions and the maximal stiffness is used to determine the required ranges. Inertia forces and other dynamic effects are neglected. The stiffness is minimal when all actuators have the same displacement and the reflective membrane does not deform. The worst case force resolution for the actuator stiffness c_a =583N/m can thus be derived as F_{res} = 2.9 μ N. Via a motor constant K_a of 0.19N/A (Figure 4.16) and an actuator coil resistance R_a of 39.0 Ω (Table 4.1), this leads to required current and voltage resolutions of 15 μ A and 0.60mV respectively.

The required current and voltage range follows from the maximum actuator force, motor constant and coil resistance. The actuator force is calculated with Equation (4.1), where c_f is \approx 6kN/m (Section 3.4), $z_a=10\mu m$ and $z_{ia}=0.36\mu m$ as derived in Chapter 2. This

5.2 Driver electronics 121

results in a range of the required force of ± 8 mN. Via the motor constant and actuator coil resistance previously used, this leads to the required current and voltage range of ± 42 mA and ± 1.6 V respectively.

This implies that the dynamic range (the total range divided by the resolution) of the driver electronics must be at least $2\cdot 8\cdot 10^{-3}/(2.9\cdot 10^{-6})\approx 5.5\cdot 10^3$. For a digital driver system, this would require at least 13 bits of accuracy. This is a minimum and does not provide any margin for a stiffer facesheet, initial flattening and alignment of the mirror and variation in motor constant between actuators. To account for this and acknowledge that the digital implementation in 16 bits is likely to be more efficient, this is the starting point in the design. The consequences for the driver electronics from this requirement will be elaborated in Section 5.2.2.

The DM actuators are designed to have a high efficiency. In combination with the low actuator force requirement, this minimizes power dissipation. As a result no active cooling is needed and vibrations introduced by such systems are avoided. Through natural convection, heat is convected without adding significantly to the wavefront disturbances that are to be corrected. By placing the driver electronics near the electromagnetic actuators the number of wires to the DM can be limited and spacious connectors avoided. With the short length of the wires, sensitivity to environmental loads (e.g. lead breakage, magnetic fields from nearby power sources, etc.) is reduced. However, it also means that the power dissipation of the driver electronics must be in the order of mW's, similar to the actuators.

Finally, the electronics should be compact in size, have low cost/actuator and preferably replaceable. Since the actuator grid is made extendable by means of the standard modules that hold 61 actuators each, the same should hold for the electronics. All drivers for a single actuator module should therefore be placed on a single PCB.

5.2.2 Concepts

For the driver electronics concept, two categories are distinguished: current and voltage sources. A current driver converts the digital setpoint from the control computer into a controlled current through the electromagnetic actuator. A voltage driver converts this setpoint into a voltage over the actuator clamps, upon which the circuit resistance determines the current. The current may therefore vary due to dynamics or time variance in the electronic circuit. The L_a/R_a time constant is approximately $2.93 \, \mathrm{mH}/39.0\Omega \approx 75 \, \mu \mathrm{s}$ (Section 4.3.5), which is small compared to the intended sampling time of 1ms. Therefore, an applied voltage will result in a current without significant delay.

The DC-gain of the actuator system including driver electronics depends on the actuator's motor constant K_a , stiffness c_a and – in the case of a voltage source – the resistance R of the actuator circuit. All three properties vary from actuator to actuator and vary with temperature, causing slow gain variations. A current source will compensate for variations in the resistance R_a , but variations of K_a and c_a must still be compensated by the AO control system. Therefore, the conceptual advantage of a current driver over a voltage driver is small, but concrete designs of both driver types will be discussed before a choice is made.

122 5 Electronics

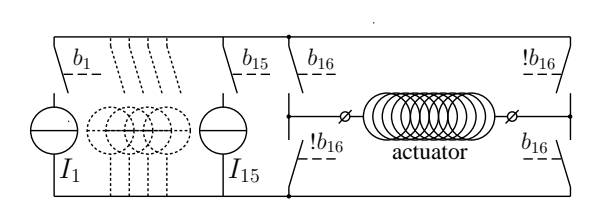


Figure 5.1: A design based on current sources that can be efficiently implemented in an ASIC using current mirrors. The "!" denotes a logical not.

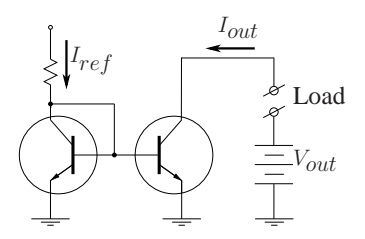


Figure 5.2: Schematic of a single current mirror. The reference current I_{ref} – here determined by a resistor – is mirrored to the output current I_{out} .

Current mirrors

In practice, a current source regulates its voltage output based on measurement of the actual current. This feedback can be done with a linear amplifier circuit, but for this application this approach has several drawbacks. Firstly, the circuit needs two supply voltages to generate positive and negative currents. Secondly, the required number of components is relatively high since no standard ASICs are available that compactly house a large number of accurate, efficient and low power linear amplifiers. Finally, the amplifier obtains its setpoint current from an analog voltage input that must be generated from the digital value of the control system by an additional component such as a DAC.

These drawbacks can be circumvented using a design based on current mirrors, which is schematically represented in Figure 5.1. This design holds 15 current mirrors and can be efficiently implemented in CMOS technology. A single current mirror (Figure 5.2) consists of two parts: in the first part a reference current is generated that is mirrored with a certain ratio to the second part that includes the load. The reference currents of the current mirrors will be permanently flowing, whereas the mirrored load currents can be switched according to the setpoint bits. The physical dimensions of the current mirror's two transistors determine the ratios between the reference and load currents. These ratios can be designed to minimize the permanently flowing reference currents and thus optimize power efficiency. The total current can be constructed with 15 fixed current mirrors and a sign-switch corresponding to the Most Significant Bit (MSB) of the setpoint. The sign-switch is obtained using the full bridge configuration as depicted in Figure 5.1, where the four switches are driven by the MSB of the setpoint and its inverse. This design is relatively simple, has a linear setpoint to current characteristic and many of these circuits can be implemented in a single Integrated Circuit (IC). However, it requires an ASIC, which is expensive to design and manufacture. Its power efficiency is comparable to that of linear amplifiers and dependent on the ratio between the RMS and PTV currents: the crest factor. The current sources regulate their output voltage, leading to internal voltage drops and thus dissipation. When neglecting internal current paths of the current sources, the total power consumption P_{tot} can be expressed in terms of the supply voltage V_{cc} and the desired actuator current I

5.2 Driver electronics 123

as $P_{tot} = V_{cc}I$. The power P_{load} dissipated in the load with resistance R_{load} is equal to $P_{load} = I^2 R_{load}$ and can be expressed relative to P_{tot} as:

$$\frac{P_{load}}{P_{tot}} = I \frac{R_{load}}{V_{cc}} = \frac{I}{I_{max}}.$$

This means that for low currents, almost all power is dissipated by the current source and for the maximum current $I_{max} = V_{cc}/R_{load}$ all power is consumed by the load.

For the RMS current of 8mA (Section 4.4.4), a load resistance of 39.0Ω and a supply voltage of 1.6V, this yields a power efficiency of approximately 20%. This low efficiency could be improved by adapting the supply voltage V_{cc} in accordance with the desired actuator current by dividing the output range over a number of supply voltages. However, as this leads to an even more complex design that can only be realized in an ASIC, a PWM voltage driver with a higher power efficiency is considered as an alternative in the next section.

Pulse Width Modulation

The absence of a feedback path to regulate a current simplifies the design in comparison with linear amplifiers although this advantage is limited when compared to the current mirror design. A regulated voltage source that generates an analog voltage for the actuator from the digital setpoint value is essentially a DAC. There exist many types of DACs, but the high accuracy and low power consumption required for this application limit the options. For instance, the low accuracy of the resistors of the common resistor ladder network DAC limits the useful accuracy of this type of converter to 8 bits or less.

For high accuracy applications the PWM principle is often used, in which a digital output is modulated between high and low states to yield a desired average DC value of the output voltage. The desired output voltage is translated into a duty cycle r_{PWM} , which is the time fraction that the digital output is high during a certain time period T_{PWM} . This time period forms the base frequency $f_{PWM} = 1/T_{PWM}$ of the PWM.

The advantage of a PWM based voltage source over the proposed mirror concept is twofold. Firstly the PWM generators can be implemented in FPGAs, which reduces the number of components and does not require the expensive and complex design and realization of an ASIC. Moreover, its power efficiency is superior to the current mirror driver because it has no internal voltage drop that leads to dissipation. Dissipation is limited to switching losses and indirect losses of the PWM signal generator and does not significantly depend on the desired output voltage. Finally, PWM design and implementation is well understood, which limits development risks. A drawback of PWM is that it outputs a signal with high-frequency components, which causes a corresponding ripple on the system output. Using the Fourier series expansion shown in Appendix C, for a constant duty cycle $r_{PWM} \in [0...1]$ the PWM output voltage \tilde{V}_{PWM} that modulates between 0 (low) and V_{cc} (high) can be expressed as the following infinite sum of cosines:

$$\tilde{V}_{PWM}(t) = V_{cc} \left\{ r_{PWM} + \sum_{n=1}^{\infty} \frac{\sin(n\pi r_{PWM})}{n\pi} \cos(2\pi n f_{PWM} t) \right\}, \tag{5.1}$$

where V_{cc} is the switched supply voltage. The spectrum of this PWM signal thus only contains power at frequencies $2\pi n f_{PWM}$ for $n=1,2,\ldots\infty$. These harmonic frequencies

124 5 Electronics

Table 5.1: Properties of industrial communication standards as derived from data sheets of available driver ICs.

Standard	Bandwidth	Multi-drop	Predefined protocol
USB2	480Mb/s	no	yes, high overhead
FireWire 800	800Mb/s	no	yes, high overhead
CAN	1Mb/s	yes	yes
Gigabit Ethernet	1Gb/s	no	yes, high overhead
RS-485 (Profibus)	40Mb/s	yes	no
LVDS	$655 \mathrm{Mb/s}^a$	yes	no

^a According to LVDS standard as defined in ANSI/TIA/EIA-644-A

must be sufficiently attenuated by the dynamics of the driven system, such that the remaining ripple on the system's output is within the accuracy margin of a quarter of the LSB. To achieve this, not only the base frequency f_{PWM} can be suitably chosen, but also the system's response to the PWM signal harmonics can be tailored using additional filters.

As this drawback can thus well be handled, the driver electronics for the DM actuators will be based on PWM.

5.3 Communication electronics

The communication electronics send the actuator setpoints from the control computer to the driver electronics. The communication link should have low latency to allow a high control bandwidth (e.g. low phase lag) and a high reliability and bandwidth to allow a large number of actuators to be quickly updated. In addition, the power dissipation, flexibility and costs are relevant. If for example, the number of actuators, the bandwidth or the number of setpoint bits changes, the communication link and protocol should allow adaptation. Furthermore a protocol that can be chosen freely and with low overhead is preferred. To limit development costs, the choice is limited to industrial standards, such as RS-485 (Profibus), USB2, ethernet, LVDS, CAN and FireWire. A few relevant properties of these standards are listed in Table 5.1. When an update rate of 1kHz and 16 bit setpoint values are assumed, the minimum bandwidth for 5000 actuators is: $1000 \cdot 5000 \cdot 16 = 80$ Mb/s. With a protocol overhead of 10% and latency limited to one quarter of the sampling time (250µs), a minimum bandwidth of $(5000 \cdot 1000 \cdot 16 \cdot 1.1/0.250) \approx 350$ Mb/s is obtained. For the prototypes developed with actuator numbers up to 427 actuators, approximately 30Mb/s would already suffice, but with future, larger, systems the CAN bus and RS-485 are no option. Since the driver electronics will be placed on modules and located close to the DM the power consumption of the transceivers must be as small as possible and for practical reasons the number of wires leading to the modules should be small. Both arguments suggest the use of a multi-drop topology in which one transmitter communicates to many receivers on the same bus. The modules are given a unique identification code to allow messages to be passed to specific modules. For such topologies the modules do not require a power

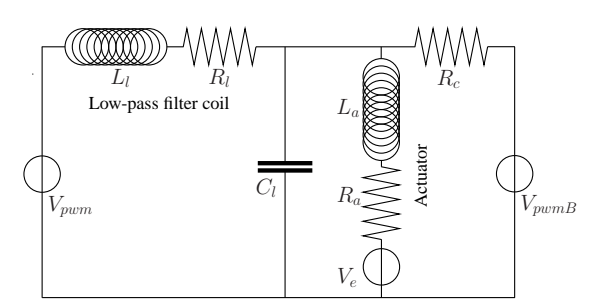


Figure 5.3: The analog electronic circuit, consisting of a coarse and a fine PWM generator, an analog low-pass filter and the actuator.

dissipating termination resistor and the number of communication wires is independent of the number of receiving modules. However, the power efficiency and speed of the communication link are not only determined by its hardware alone. If the method requires a specific protocol with a high overhead, both speed and power efficiency are reduced and flexibility for future upgrades limited. Both arguments favor the development of a custom protocol. Development costs of such a protocol will be limited, as a master-slave structure with a small command set will suffice and throughput is more important than guaranteed transmission.

The LVDS standard was chosen for the serial communication. In contrast to USB, this allows for a high bandwidth multi-drop topology for which low-power transceiver ICs are commercially available. Each transceiver dissipates only 15mW and requires no termination resistor. A custom communication protocol can be designed that has a small overhead compared to e.g. the USB, FireWire or ethernet protocols. Two LVDS wire pairs can be used to keep the protocol as simple as possible: one command line and one return line.

5.4 Implementation and realization

In this section the implementation of the chosen design concepts for the driver and communication electronics will be discussed.

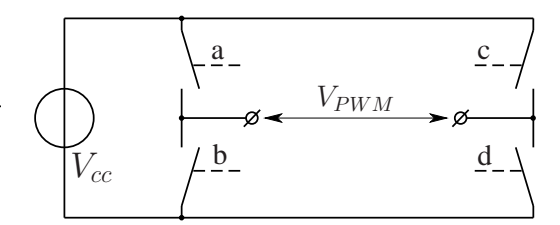
5.4.1 PWM implementation

For several reasons the PWM voltage drivers will be implemented in an FPGA. Firstly, because this leads to a compact design with few components because the FPGA can house many PWM generators. Moreover, no expensive ASIC has to be designed and realized and it allows modifications to the implementation through a software update.

As derived in Section 5.2.1, the driver electronics require a dynamic range of 16 bits. The PWM driver electronics will be designed such that the ripple magnitude due to the harmonic component in the PWM signal at the frequency f_{PWM} is less than a quarter of the system's response to the least significant bit for any duty cycle r_{PWM} . Let H(s) denote the transfer function between the PWM voltage \tilde{V}_{PWM} and the position z_a of a single actuator. Observe from Equation (5.1) that the worst case magnitude of the first harmonic (n = 1) occurs for

126 5 Electronics

Figure 5.4: H-bridge construction to allow the PWM voltage V_{PWM} of the coarse PWM to be both positive and negative.



 $r_{PWM} = 0.5$ and is equal to V_{cc}/π . The design condition can thus be formulated as:

$$\frac{V_{cc}}{\pi}|H(2\pi j f_{PWM})| < \frac{1}{4} \frac{V_{cc}}{2^{16}}|H(0)|$$

and thus:

$$|H(2\pi j f_{PWM})| < \frac{\pi}{2^{18}} |H(0)|.$$
 (5.2)

In Section 4.3.4, the frequency response function $H(j\omega)$ has been derived for the case that the PWM output is directly connected to the actuator coil. A Bode plot of $H(j\omega)$ is plotted in Figure 5.9, which shows that the f_{PWM} for which Equation (5.2) is satisfied lies above 100kHz.

When implemented in an FPGA, the PWM generator will consist of a 16 bit counter and a comparator. The counter value is increased by one at every FPGA clock cycle and resets to zero at the beginning of each PWM time period. The comparator compares the counter value to a value corresponding to the setpoint. The PWM output is high if the counter is higher than this value and low otherwise. The counting and thus clock frequency of the FPGA can be expressed as:

$$f_{FPGA} = f_{PWM} 2^{N_b} \tag{5.3}$$

where N_b is the number of bits of the counter. The clock frequency of currently available FPGAs is limited to approximately 200MHz, which implies that for $N_b=16$ the base frequency f_{PWM} is limited to approximately 3kHz. The dynamic power dissipation of digital electronics is for most designs linearly correlated with the clock frequency, which is an important drive to keep the base frequency as low as possible.

To keep f_{FPGA} below 200MHz while implementing 16bit PWM generators, two modifications are made. Firstly, an analog 2^{nd} order low-pass filter is added to reduce the system response magnitude at high frequencies and secondly the PWM is split into a fine part consisting of 5 bits and a course part of 11 bits. For 11 bits, the PWM base frequency can be increased to approximately 95kHz.

The analog low-pass filter consists of the inductor with inductance L_l and a capacitor with capacitance C_l (Figure 5.3). It is given a bandwidth of 5kHz that is high enough to have a negligible influence on the behavior of the system up to the mechanical resonance, but low enough to reduce the required PWM base frequency f_{PWM} to less than 95kHz. Assume that above the resonance at 2kHz the magnitude response of the actuator between driving voltage and position decays a factor 1000 per decade. Further, the response of the analog low-pass filter decays a factor 100 per decade above 5kHz. The minimum PWM frequency

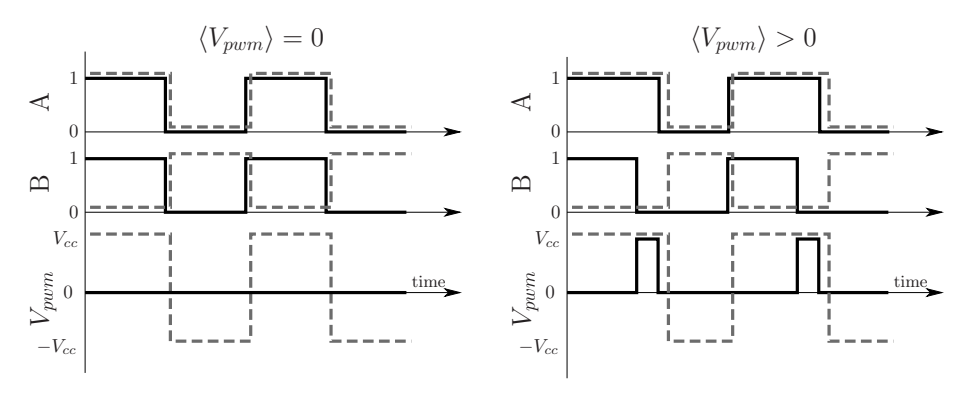


Figure 5.5: Comparison of the traditional and BD modulation schemes. The latter is represented by the black, solid lines and the first by the gray, dashed lines that are shifted slightly to the top-right for clarity.

 f_{PWM} that satisfies Equation (5.2) is then solved from:

$$\left(\frac{f_{PWM}}{2000}\right)^3 \cdot \left(\frac{f_{PWM}}{5000}\right)^2 = 2^{18}$$

yielding $f_{PWM} \approx 35 \text{kHz}$. Without the low-pass filter this would be 128kHz, such that this filter reduces the required PWM base frequency almost a factor 4.

However, this reduced base frequency is only achievable for currently available FPGAs when the number of bits is less or equal to 12. Therefore, the PWM has been split into two parts: the 11-bit course PWM provides V_{PWM} whereas the 5-bit fine PWM provides V_{PWMB} . The latter can re-use the lowest 5 bits of the course PWMs counter and is connected through an appropriately chosen resistor R_c to one of the actuator clamps (Figure 5.3). Evaluating Equation (5.3) for $N_b=11$ bits, the required FPGA clock frequency becomes approximately 125MHz. The number of bits of the PWM is split into unequal parts on purpose, as the resistance of R_c is in practise inaccurate and causes an output bias that increases with the magnitude of the fine PWMs highest bit.

To send positive and negative currents through the actuator coil, the PWM must provide positive and negative voltages. This is achieved with an H-bridge construction as shown in Figure 5.4. This construction has only been applied for the coarse PWM. Due to the limited range of the fine PWM, the added value of a sign change does not make up for the extra FPGA pins and PCB connections. The PWM signals control the switches a, b, c, and d such that current flows either via a and d or via b and c. Care must be taken that both a and b as well as c and d are never closed at the same time as this forms a short-circuit. By defining the PWM output 'low' as the closing of a and b and b and b and b the effective voltage over the actuator coil can be varied between a and a

128 5 Electronics

a BD modulation scheme.

For the BD modulation scheme, the a-d and b-c switches are driven by two different, but related PWM signals A and B, whereas otherwise these would be complementary (i.e. A=not B). For a zero effective voltage, both signals have a duty cycle of 50% and are fully in-phase (Figure 5.5). In this situation neither the a-d path nor the b-c path will ever conduct and cause dissipation. If a positive voltage is desired then the period of PWM signal A is increased whereas that of B is decreased and for a negative voltage vice versa. For both modulation methods, the signals A and B drive the switches according to a=A, b=not A, c=B and d=not B. Therefore, switches b=and b=and b=and b=and c=and b=and c=and c=an

A second advantage of the BD modulation method is that the output voltage swing is only V_{cc} , whereas for the traditional modulation this is $2V_{cc}$ (Figure 5.5). Consequently, the magnitudes of the harmonics in the frequency spectrum of the traditionally modulated signal are twice as high as suggested in Equation (5.1).

5.4.2 FPGA implementation

In Section 5.2.1 it is explained that for modularity of the DM system, the driver electronics should be made in PCB modules containing 61 driver circuits and connect to a single actuator module. To implement the 61 PWM generators and the LVDS communication protocol, three Altera Cyclone II (EP2C8) FPGAs are present on each electronics module. One master FPGA handles the LVDS protocol and two identical slaves implement 32 PWM generators each. The functionality is not realized in a single FPGA to limit the risk of the number of available logic cells or electrical connections being insufficient to implement the required functionality. Due to the two-level PWM solution discussed in Section 5.2.2, each actuator requires FPGA connections for each of the four H-bridge switches and one for the fine PWM signal. This results in 5 connections in total per actuator and thus 305 connections for 61 actuators.

The master FPGA decodes the LVDS signal using 5-times over-sampling (200MHz) and interprets the commands. If required, information is sent to or requested from the slaves via a 16-bit parallel data bus. The slaves each have one counter that is increased with the frequency of an externally supplied 125MHz clock. There the 11-bit counter signal is fed to 32 comparator circuits that generate the PWM signals. These circuits are divided into four blocks of eight circuits to prevent a large fan-out of connection wires that bring the counter to the comparators. Such fan-out limits the switching speed and leads to undesired dissipation.

Nevertheless, as will be discussed at the end of this chapter, the dissipation of the three FPGAs is dominant over the RMS dissipation in the actuator coils. In Section 5.7.1 several design concepts will be proposed to reduce this.

Figure 5.7 shows the double-sided PCB with 61 drivers and the PCB with the master FPGA, the DC/DC convertors and the LVDS drivers. The connector board that connects to the three flex foil flaps on one side and the analog electronics PCB on the other side is shown in the lower right photo in Figure 6.2.

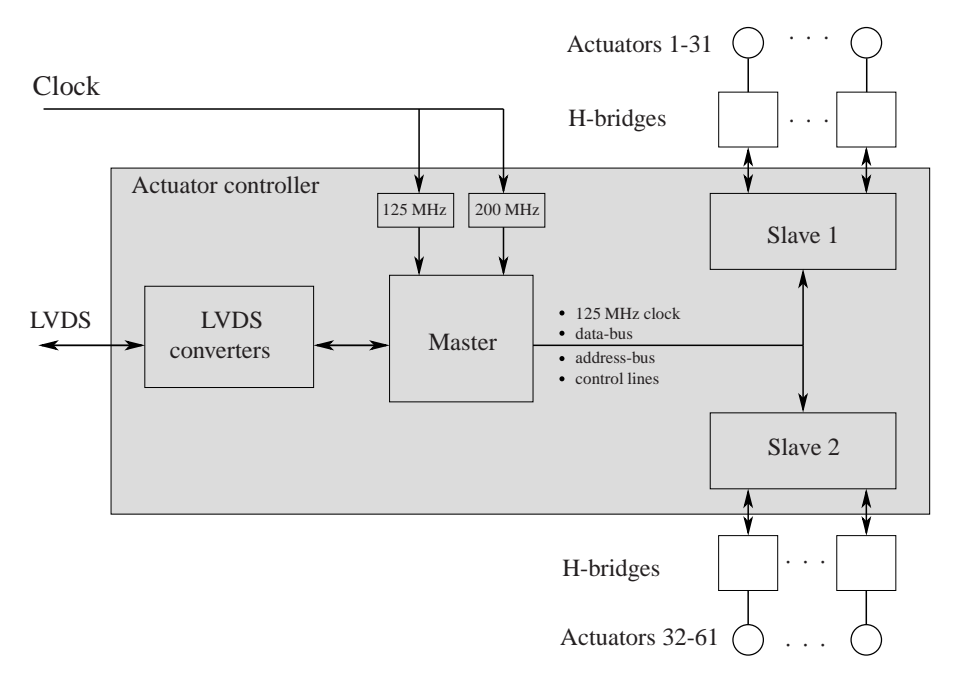


Figure 5.6: Actuator controller architecture.

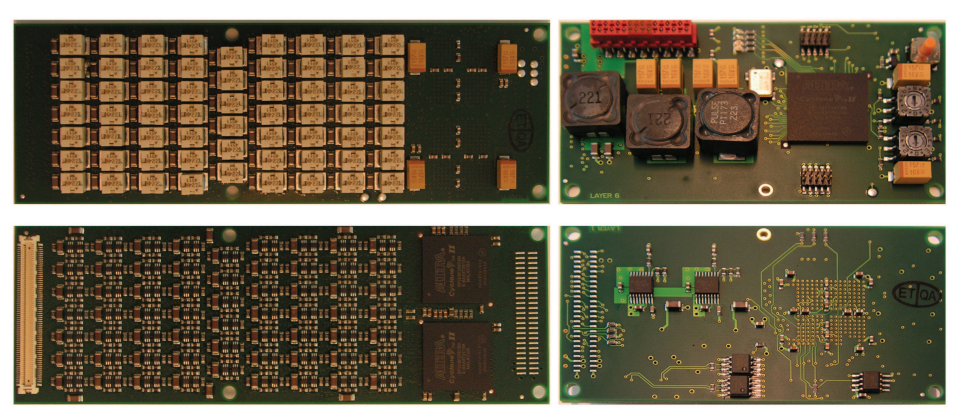


Figure 5.7: PCB (top and bottom) containing the analog filter electronics for 61 actuators. (left) PCB (top and bottom) containing the master FPGA, DC-DC convertors and LVDS drivers. (right)

5 Electronics

Figure 5.8: Top-view of the encased LVDS communications bridge.



5.4.3 The ethernet to LVDS bridge

At the time of design, no general purpose PC expansion card was available to provide an off-the-shelf PC with two LVDS connections and a fully customized communication protocol. Therefore, a communications bridge was conceived that bridges the 100Mb/s ethernet connection of a PC with the custom LVDS connection. The LVDS bridge must relay messages received over the ethernet connection to the LVDS on the other side and vice versa. The bridge should be reliable and add little latency - i.e. the delay between reception and transmission of the first bit of a data package - to the delay of the two-step communication chain. To limit development time, the LVDS bridge is based on an Altera NIOS-II FPGA development board (Figure 5.8). This board is extended with an ethernet PHY that implements the MAC layer of the ethernet protocol in hardware to limit latency. A second plug-in PCB contains the LVDS driver ICs. The NIOS FPGA implements a processor that executes an open source Internet Protocol (IP) stack that has been optimized for latency. As with any communication type, transmission errors may occur for which detection methods are usually implemented. However, for real-time application it is more important to limit latency than to detect or recover rarely occurring errors. Therefore, the UDP protocol has been chosen (Appendix E) for the ethernet communication, whose checksums to detect faulty data have been disabled or are ignored.

5.5 Modeling

The actuator and its electronic circuit are modeled to determine a suitable base frequency for the PWM signals and to check whether both the actuator and the electronics behave as designed. Furthermore it allows validation of the full DM system including its reflective facesheet (Chapter 6) and serves as input for a controller synthesis procedure.

Recall the analog electronic circuit depicted in Figure 5.3. Let the circuit be driven by the PWM voltage V_{PWM} . The effect of the fine PWM signal that connects to the system at a different location – leading to different dynamics – will further be neglected. The actuator has been modeled in Section 4.3.4, leading to the linearized system in Equation (4.25) on page 94. The 2^{nd} order analog low-pass filter consists of coil L_l with internal resistance R_l in series with capacitor C_l that is connected in parallel with the actuator. From Kirchoff's laws it follows that:

$$V_{PWM} = V_{L_l} + V_{R_l} + V_a, \qquad \text{and} \qquad I_{R_l} = I_{C_l} + I_a,$$

5.5 Modeling 131

Table 5.2: Properties of the components of the 2^{nd} order analog low-pass filter.

Parameter	Value	Unit	Parameter	Value	Unit
L_l	220	μH	C_l	4.7	μF
R_l	2.7	Ω	R_c	16.2	$k\Omega$
R'_l	2.4	Ω	R_a'	3	Ω

where V_{R_l} and V_{L_l} denote the potentials over R_l and L_l and I_{C_l} and I_{R_l} the currents through C_l and R_l respectively. They are defined through the following constitutional equations:

$$V_{R_l} = R_l I_{R_l}, \qquad V_{L_l} = L_l \dot{I}_{R_l}, \qquad I_{C_l} = C_l \dot{V}_a.$$

The mechatronic system will be modeled in the state-update form,

$$\dot{\mathbf{x}} = \mathbf{A}\mathbf{x} + \mathbf{B}V_{PWM},\tag{5.4}$$

with state vector $\mathbf{x}(t) = [I_a(t) \ z_a(t) \ z_a(t) \ V_a(t) \ I_{R_l}(t)]^T$. The time derivatives of the state elements can be derived from the constitutional equations together with the two Kirchhoff equations, leading to:

$$\begin{split} \dot{I}_{R_l} &= \left(V_{PWM} - R_l I_{R_l} - V_a\right) / L_l, \\ \dot{V}_a &= \left(I_{R_l} - I_a\right) / C_l. \end{split}$$

These two equations can be combined with the previously derived actuator system equation in Equation (4.25) and expressed in the state update form of Equation (5.4) as:

$$\begin{bmatrix} \dot{I}_{a} \\ \dot{z}_{a} \\ \dot{z}_{a} \\ \dot{V}_{a} \\ \dot{I}_{R_{l}} \end{bmatrix} = \begin{bmatrix} -R_{a}/L_{a} & 0 & -K_{a}(z'_{a})/L_{a} & 1/L_{a} & 0 \\ 0 & 0 & 1 & 0 & 0 \\ K_{a}(z'_{a})/m_{a_{c}} & -c_{a}/m_{a_{c}} & -b_{a}/m_{a_{c}} & 0 & 0 \\ -1/C_{l} & 0 & 0 & 0 & 1/C_{l} \\ 0 & 0 & 0 & -1/L_{l} & -R_{l}/L_{l} \end{bmatrix} \begin{bmatrix} I_{a} \\ z_{a} \\ \dot{z}_{a} \\ V_{a} \\ I_{R_{l}} \end{bmatrix} + \begin{bmatrix} 0 \\ 0 \\ 0 \\ 0 \\ 1/L_{l} \end{bmatrix} V_{PWM}.$$

The output signals that will be used for analysis and testing are the actuator displacement $z_a(t) = [0\ 1\ 0\ 0\ 0]\mathbf{x}(t)$ and the voltage $V_a(t) = [0\ 0\ 0\ 1\ 0]\mathbf{x}(t)$ that can be measured over actuator coil. Let the transfer function between the PWM voltage $V_{PWM}(t)$ and the actuator position $z_a(t)$ be denoted H(s). For properties of the actuator and the electronics as in Table 5.2, Figure 5.9 shows the Bode plots of the resulting transfer functions. Figure 5.9 also shows the transfer function when only the current-controlled mechanical system is considered. The static relation $I_a = V_a/R_a$ is used to scale the corresponding transfer function in Equation (4.29) on page 98 and allow comparison with the full mechatronic system. When omitting the nominal operating point z_a' , this yields the transfer function:

$$H_m(s) = H_I(s)/R_a = \frac{K_a}{m_{a_c}R_a s^2 + b_a R_a s + c_a R_a}.$$
 (5.6)

Observe in the Bode plot that the electronics provide a small amount of additional damping of the mechanical resonance, but have negligible influence on the low-frequent actuator behavior.

5 Electronics

The PWM base frequency

In Section 5.2.2 it was discussed that an 18-bit attenuation of the PWM ripple is desirable. To achieve this with an FPGA based implementation, an additional 2^{nd} order low-pass filter was added to the design.

The effect of this filter is illustrated in Figure 5.9, which contains Bode plots of the actuator system with and without the filter as described by Equations (5.5) and (4.25) respectively. The 18-bit ripple attenuation is shown in the magnitude plot of Figure 5.9 as the dash-dotted line. Observe that the application of the low-pass filter reduces the PWM frequency requirement from approximately 128kHz to approximately 35kHz.

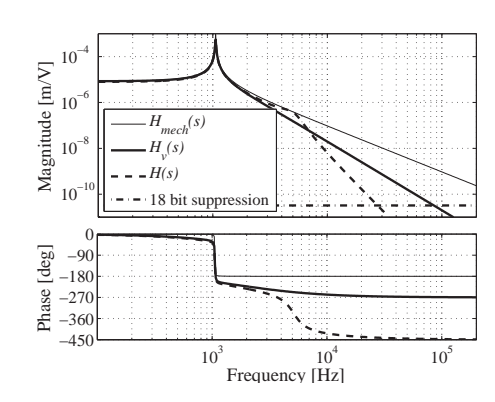
Although higher than necessary for DMs with Pyrex facesheets, the base frequency f_{PWM} is set at 61kHz. This is done because in future developments the replacement of the Pyrex mirror facesheet by beryllium is foreseen, demanding a higher base frequency. The specific stiffness of beryllium is more than five times higher (Chapter 3), which allows for thinner facesheets and thus less mass per actuator. With the same actuator stiffness this increases the system's eigenfrequency and decreases the attenuation of the PWM ripple.

For the foreseen update rate of 1kHz the base frequency of 61kHz provides 61 times over-sampling of the setpoint signal. This means that cross-harmonics in the PWM output voltage V_{PWM} resulting from non-constant setpoint signals can be neglected.

Serial communication

The serial communication via both ethernet (UDP) and LVDS will introduce a certain delay τ_c of the control output. This delay should be as small as possible and its variation (jitter) should be restricted to a negligibly small fraction of the delay itself. The communication latency is in the Laplace domain modeled as $H_{\tau_c}(s) = e^{-\tau_c s}$. Due to the definition of the communication protocol (Appendix E) and its serial nature, the latency τ_c will be different for each 61-actuator module.

Figure 5.9: Bode diagram of three transfer functions: $H_m(s)$ from Equation (5.6) (only the mechanics), $H_{mv}(s)$ from Equation (4.27) (mechanics including the actuator coil) and H(s) defined in Section 5.5 (mechanics with actuator coil and low-pass filter).



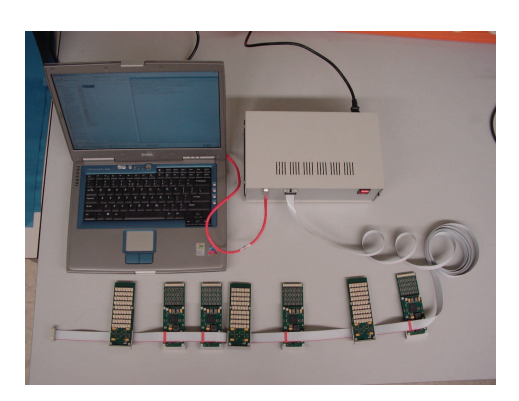


Figure 5.10: Seven PCBs connected to the LVDS bridge via the multi-drop flat-cable. The bridge is connected to the laptop via ethernet.

5.6 Testing and validation

The electronics and the actuator grids were tested. The dynamic response of the actuators was first measured using a controlled current source. These results were shown in Section 4.4.3. In this section, first the test results of the communication between a PC and the LVDS bridge and between the PC and the driver modules are shown (Figure 5.10) followed by a full system test. Here the dynamic response of the actuators is measured. At the end of the section the power dissipation of the electronics will be discussed.

5.6.1 Communications tests

To measure the latency of the communications bridge, two of its debug lines were connected to a logic analyzer. The first line is high while a UDP packet is being received and the second while an LVDS packet is being transmitted. A second computer was used to send burst packets (Appendix E). These are the most relevant in practise and contain 16-bit setpoint updates for all 61 actuators corresponding to 1024 bits in total. To minimize ethernet protocol overhead, each UDP burst packet can contain up to eight LVDS burst packets (Appendixs D and E).

Measurements taken by the logic analyzer show that the transmission time of a UDP burst packet can be expressed as:

$$\tau_{udp} \approx 4.7 \cdot 10^{-6} + 10.24 \cdot 10^{-6} N_m$$

where N_m is the number of actuator modules within the packet. The constant part is due to ethernet protocol overhead and the approximately $10\mu s$ per module corresponds to 1024 bits at a rate of 100Mb/s.

Further, the measurements show a time delay of approximately $85\mu s$ with a variation (jitter) of less than $10\mu s$ after reception of the UDP packet, before transmission of an LVDS packet. During this time the bridge processes the packet, splits it into LVDS packets and copies it to the transmit buffer. Since calculation of the UDP checksum takes a significant time – approximately $(10N_m)\mu s$ – this checksum is sacrificed for speed and ignored in the current implementation. Transmission of the 1024 functional bits over the 40Mb/s LVDS connection with 16-bit data words separated by 18 pause bits, one start-bit and one stop-bit

5 Electronics

should take $\tau_{lvds} \approx 28.8 \cdot 10^{-6} N_m$, which is confirmed by the measurements. The total communication latency τ_c can thus be expressed as:

$$\tau_c = \tau_{udp} + 85 \cdot 10^{-6} + \tau_{lvds} = 89.7 \cdot 10^{-6} + 39 \cdot 10^{-6} N_m$$

Since the communication chain consists of two sequential, buffered links, the maximum update rate is determined by the slowest link, in this case the LVDS line. This rate equals $1/28.8 \cdot 10^{-6}/N_m$, which for $N_m=1$ and $N_m=7$ is approximately 35 and 5kHz respectively. However, since the LVDS bridge may drop incoming packets during its $85 \mu s$ processing time, in practise this latency adds directly to the ethernet latency. For the case that $N_m=1$, this makes the ethernet latency dominant and reduces the maximum update rate to approximately 10 kHz.

5.6.2 Parasitic resistance measurements

Before the full actuator systems will be tested, first several properties of the electronics are measured. Deviations of the expected values measured in the next section can then be properly attributed to either the electronics or the mechanics.

In practise – due to wiring – the resistances R_l and R_a are assumed to increase by R'_l and R'_a respectively. Resistance measurements of the actuator coils show on average the design value of 39.0 Ω , but the average resistance measured over the capacitor C_l is found to be 42Ω , indicating that $R'_a \approx 3\Omega$. The resistance R'_l will be estimated from a few additional measurements. Firstly, the PWM setpoints are set such that the measured voltage over the capacitor C_l is $V_{C_l} = 1.001 \text{V}$. After reconnecting the actuators this yielded an average voltage drop over the capacitor of V=0.903V. Using the fact that the current through R_l , R'_l , R_a and R'_a is equal and the sum of the voltage drops is equal to the PWM voltage of 1.001V, the resistance R'_l is estimated as $R'_l = 2.4\Omega$. A 1Ω part of the latter can be attributed to a safety resistor present in the design for short-circuit protection, whereas the rest must be attributed to wiring and connector resistance.

Although the supply voltage variations will not have an effect for power dissipation – this will be compensated by a controller – the power dissipation increases linearly with the resistance of the current path. The total parasitic resistance of $R'_a + R'_l = 3 + 2.4 = 5.4\Omega$ will therefore lead to an undesired increase in power dissipation on the driver PCB of $(R'_a + R'_l)/(R_a + R_l) \cdot 100\% = 5.4/(39.0+2.7) \cdot 100\% \approx 13\%$.

5.6.3 Actuator system validation

Whereas dynamic measurements were performed on the single actuator prototypes using a Siglab system, the setup depicted in Figure 5.11 will be used for testing and model validation of the grid actuators. A MatlabTM xPC-target computer is used to generate a white noise sequence and send it in UDP burst packets (Appendix E) over an ethernet connection. The sequence is logged internally to be used for analysis later. The ethernet connection goes via a switch to allow both the xPC target and the dedicated electronics to be controlled and configured by a host computer. Although this doubles the ethernet latency, this is not critical for the open loop validation measurements.

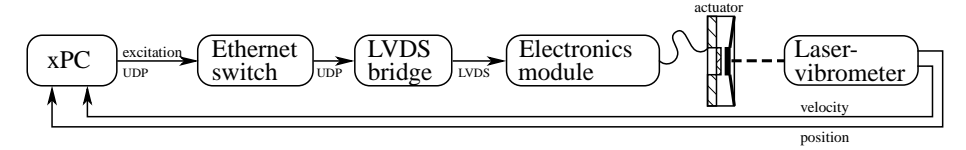


Figure 5.11: Setup used to perform the actuator response measurements using the custom built electronics.

The LVDS bridge then converts the packets into LVDS packets to be sent to the electronics module corresponding to the targeted actuator. Both the position and velocity response of the actuator are measured using a polytec laser vibrometer. This outputs the measurements as analog voltages that are fed back to the xPC target using a National Instruments Analog to Digital Convertor (ADC) card (NI-6025E) that does not contain any anti-aliasing filters. The measurements are performed for update rates of 1, 3, 5 and 10kHz to be able to evaluate the effects of sampling and aliasing.

Let the discrete time frequency response function between the PWM voltage output and the actuator position z_a that includes the effects of sampling and digital communication be denoted $H_{p,T_s}^*(z_a,\theta,\tau_c)$, where the subscript T_s indicates the corresponding sampling time and the vector θ contains the physical parameters m_{a_c} , b_a , c_a , L_a , R_a , K_a , L_l , R_l and C_l . Similarly, $H_{v,T_s}^*(z_a,\theta,\tau_c)$ denotes the transfer function to the actuator velocity $\dot{z_a}$. The effect of the sampling performed by the NI ADC card can be modeled by assuming a zero

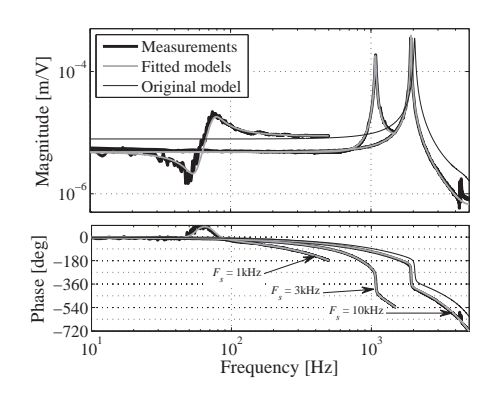


Figure 5.12: Bode plot of empirical frequency response function estimates $\hat{H}_{p,T_s}^*(f)$ together with the parametric fit $H_{p,T_s}^*(z_a,\hat{\theta})$ and the nominal model $H_{p,T_s}^*(z_a,\theta_0)$ at 1, 3 and 10kHz sampling frequencies.

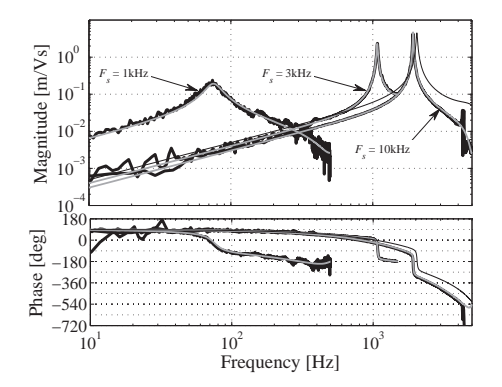
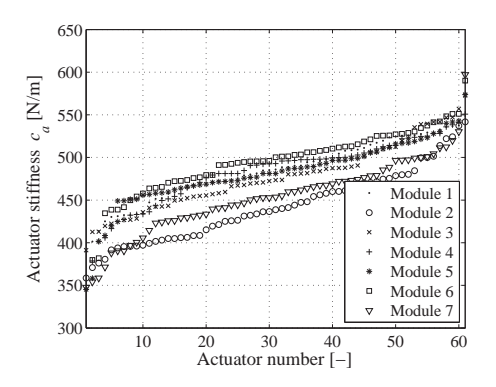


Figure 5.13: Bode plot of empirical frequency response function estimates $\hat{H}_{v,T_s}(f)$ together with the parametric fit $H^*_{v,T_s}(z_a,\hat{\theta})$ and the nominal model $H^*_{v,T_s}(z_a,\theta_0)$ at 1, 3 and 10kHz sampling frequencies.

5 Electronics



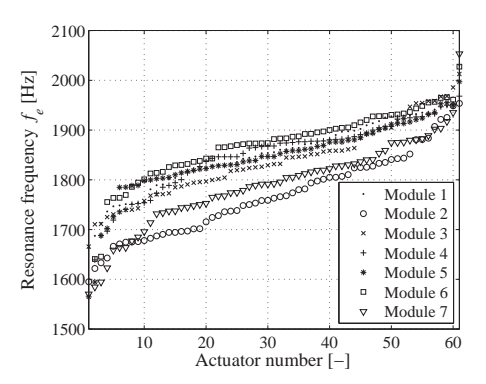


Figure 5.14: Identified actuator stiffness c_a when assuming $m_{a_c} = 3.6$ mg sorted on value for each measured actuator grid separately. The value predicted by the original model is 583N/m.

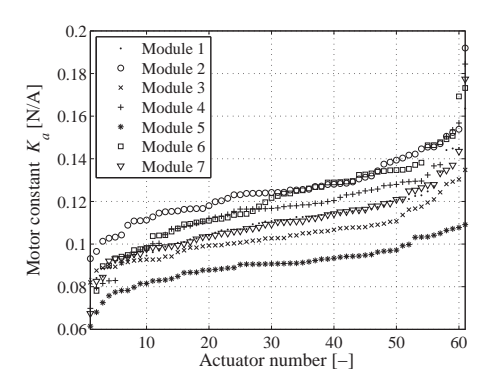
Figure 5.15: Resonance frequencies f_e when assuming $m_{a_c} = 3.6$ mg sorted on value for each measured actuator grid separately.

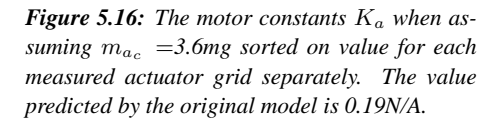
order hold on the excitation signal and applying the z-transform, yielding:

$$H_{p,T_s}^*(z,\theta,\tau_c) = \mathcal{Z}_{T_s} \left(\frac{1 - e^{T_s s}}{s} H(s,\theta) e^{-\tau_c s} \right) = (1 - z^{-1}) \mathcal{Z}_{T_s} \left(H(s) e^{-\tau_c s} / s \right),$$

$$H_{v,T_s}^*(z,\theta,\tau_c) = \mathcal{Z}_{T_s} \left(\frac{1 - e^{T_s s}}{s} s H(s,\theta) e^{-\tau_c s} \right) = (1 - z^{-1}) \mathcal{Z}_{T_s} \left(H(s) e^{-\tau_c s} \right),$$

where $H(s,\theta)$ denotes the transfer function H(s) based on the physical parameters in the vector θ . Let the empirical transfer function estimates of $H^*_{p,T_s}(z_a,\theta,\tau_c)$ and $H^*_{v,T_s}(z_a,\theta,\tau_c)$ be denoted $\hat{H}^*_{p,T_s}(f)$ and $\hat{H}^*_{v,T_s}(f)$ respectively, where f is the fre-





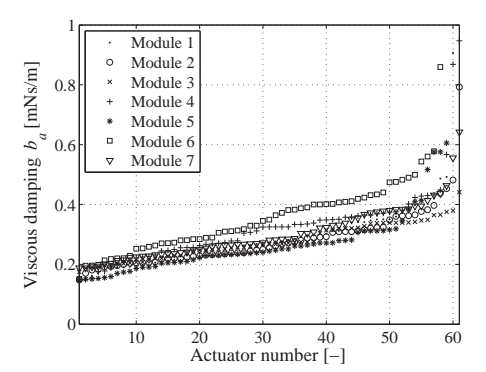
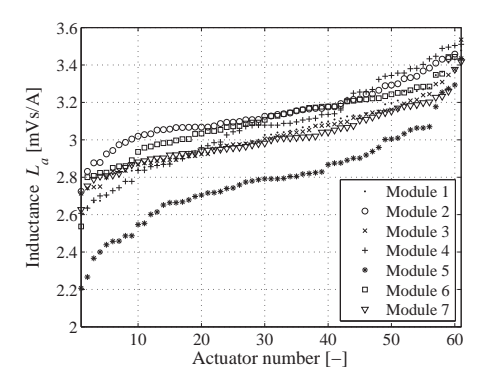


Figure 5.17: The viscous damping b_a when assuming $m_{a_c} = 3.6$ mg sorted on value for each measured actuator grid separately.



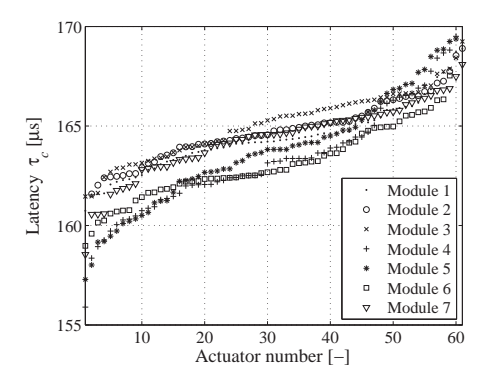


Figure 5.18: Identified actuator coil inductance L_a when assuming $m_{a_c} = 3.6$ mg sorted on value for each measured actuator grid separately. The value used for the original model is 2.93mH.

Figure 5.19: The communication latency τ_c sorted on value for each measured actuator grid separately.

Table 5.3: Average values and standard deviations of the actuator system properties measured over all grid actuators using the setup depicted in Figure 5.11.

Property	K_a	c_a	b_a	f_e	L_a
Average	0.11N/A	473N/m	0.30mNs/m	1.83kHz	3.0mH
Std.dev.	0.02N/A	46N/m	0.11mNs/m	91Hz	0.2mH

quency. These estimates together with the corresponding coherence functions $C_{p,T_s}(f)$ and $C_{v,T_s}(f)$ were obtained from 10s of input-output data logged by the xPC target using Welch's averaged periodogram method with a block size of 2048 samples with 70% overlap and a Hanning window. A typical set of estimates is shown in Figures 5.12 and 5.13 for actuator 10 of grid 1.

The model parameters c_a/m_{a_c} , K_a/m_{a_c} , b_a/m_{a_c} , L_a and the latency τ_c will be identified from the empirical transfer function estimates. The other model parameters R_l , L_l and C_l are assumed to be accurately known. A single set of parameters is fit against eight measurements series: four different sampling frequencies times two measurement outputs (position and velocity). The optimization is performed w.r.t. the cost function $J_p + J_v$, in which:

$$J_{p} = \sum_{T_{s} \in \mathcal{T}_{s}} \sum_{f \in \mathfrak{F}_{m}(T_{s})} \left(\frac{\hat{C}_{p,T_{s}}(f)}{\left| \hat{H}_{p,T_{s}}(f) \right|} \left| H_{p,T_{s}}^{*}(e^{2\pi j f}) - \hat{H}_{p,T_{s}}(f) \right| \right)^{2},$$

$$J_{v} = \sum_{T_{s} \in \mathcal{T}_{s}} \sum_{f \in \mathfrak{F}_{m}(T_{s})} \left(\frac{\hat{C}_{v,T_{s}}(f)}{\left| \hat{H}_{v,T_{s}}(f) \right|} \left| H_{v,T_{s}}^{*}(e^{2\pi j f}) - \hat{H}_{v,T_{s}}(f) \right| \right)^{2}.$$

The set \mathcal{T}_s consists of the sampling times corresponding to 1, 3, 5 and 10kHz update rates and the sets $\mathfrak{F}_m(T_s)$ contain the frequencies at which the transfer functions were estimated

5 Electronics

for the sampling time T_s . The values of the coherence functions $C_{p,T_s}(f)$ and $C_{v,T_s}(f)$ are used as weights to include the reliability of the transfer function estimates in the parametric optimization problem. To remove the bias introduced by the system magnitude response, the inverse of this response is applied as a second weight. In the optimization the properties of the electric components that form the analog low-pass filter are taken from Table 5.2 and include the parasitic resistances R_l' and R_a' . The z-transform is implemented using Matlab's C2D function, which also accounts for the latency τ_c . Since this cost function is non-linear w.r.t. the parameters to be estimated, the optimization is performed using Matlab's nonlinear least squares solver lsqnonlin.

Examples of the estimation result for an arbitrary actuator are depicted as the gray dashed lines in Figures 5.12 and 5.13, showing only very slight deviations between the model and the measurements. Moreover, it should be noted that both figures are based on the same set of parameter estimates. The average values and standard deviations of the estimates for K_a , c_a , b_a and L_a when assuming m_{ac} =3.6mg are listed in Table 5.3. These values agree well with the results obtained using the current source in the previous chapter as listed in Table 4.2 on page 115, which indicates the robustness of the measurement and identification process. Further, all estimates are plotted in Figures 5.16, 5.14, 5.17 and 5.18. For these plots the values are sorted per actuator module for better insight into their statistical spread and correspond well to the values estimated using the current source setup in Section 4.4.3 depicted in Figures 4.50, 4.48 and 4.51 on page 115. Each module has a few actuators with significantly different properties, but only a single actuator is malfunctioning. Moreover, the variation between actuators is not linked to the location of the actuator in the grid. This is illustrated for the resonance frequency and motor constant in the figures in Appendix F. These show the corresponding values for all actuator grids in relation to the location of the actuator in the module.

Although the resistance in the current path of an actuator affect this system's DC-gain, it cannot be separately estimated. The parasitic resistances R_a' and R_l' are only practically measurable for a few actuators per module. Measurements for approximately 20 actuators provided the average value used for the estimation of the actuator parameters. The several percent resistance variation affects the parameter estimates, which together with estimation errors explains the differences with the values obtained from current source measurements shown in Section 4.4.3.

In addition to the results shown in Section 4.4.3, the voltage excitation allows to estimate the actuator inductance L_a . Observe from Figure 5.18 that also the average of the inductance differs significantly per actuator module, which is most significant for module 5. This module also has a relatively low average motor constant (Figure 5.16). Based on the sensitivity analysis performed on the actuator design in Section 4.3.6, such variation can for instance be attributed to an increased radial air gap reluctance \Re_{g_r} . This reluctance depends strongly on the radial air gap width, which is e.g. equally affected for all actuators of a module by the radius of the mill used in the baseplate milling process.

Finally, the estimated latency varies between approximately 160 and 170 μs , of which $89.7+39=128.7\mu s$ can be attributed to the serial communication (Section 5.6.1). Another $8\mu s$ can be attributed to communication between the master and slave FPGAs and also $8\mu s$ to the implemented PWM update method that yields an average latency of half a period of the PWM base frequency. The remaining $20\mu s$ are likely caused by overhead in the XPC target computer, in which ethernet communication is performed by a background process

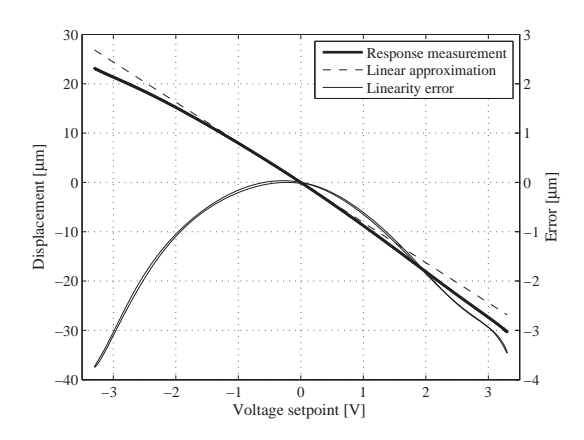


Figure 5.20: Non linearity and hysteresis measurements performed on a single actuator excited by a 4Hz sine excitation voltage with 3.3V amplitude. The response is plotted against the excitation for single (thick solid line) and the deviation from a linear response (dashed line) is plotted as the thin solid line on the right vertical axis.

and not strictly real-time.

5.6.4 Nonlinear behavior

So far only the linear system dynamics were considered, whereas it was shown in Section 4.3.3 that both the mechanical and magnetic stiffnesses of the actuator are nonlinear functions of current and deflection. This is particularly true for large deflections, when the difference with the operating point used for linearization becomes significant. However, measurement results show that no significant (i.e. measurable) hysteresis is present (Figure 5.20).

Measurements were performed to quantify both effects for the single actuator system. The previously described setup depicted in Figure 5.11 was used to excite the system with a low frequent sine signal and measure its deflection response. Differential measurement capabilities of the laser vibrometer were used to limit drift due to e.g. air motion and reduce external disturbances such as floor vibrations. The excitation frequency is chosen at 4Hz such that only the system's static behavior (stiffness) plays a role and not its resonances. An amplitude of 3.3V corresponding to the maximum available input voltage is used. The sampling frequency of the measurements is chosen as 10kHz to minimize effects of aliasing and the results depicted in Figure 5.20 have been compensated for the discussed latencies that yield a spurious hysteresis loop. The figure shows that hysteresis is negligible and of similar order of magnitude as the drift of the laser vibrometer. A linear function is fit to the response and shown as the dashed line. The difference with the actual response is plot as the dash-dotted line against the right y-axis. Although for large deflections the nonlinear actuator stiffness becomes visible, for the intended $\pm 10 \mu m$ deflection, the actuator linearity error is less than 5%.

140 5 Electronics

5.7 Power dissipation

As stressed in Chapter 2, power dissipation forms a design driver for the DM system. In this section, the power dissipation measured will be discussed.

For the analysis only the static response of the system is considered, which is assumed to be linear w.r.t. the PWM voltage setpoint. The validation measurements have shown this to be an accurate approximation at least up to approximately 1600Hz. Non-static dissipative effects such as viscous damping and eddy currents play a negligible role in this frequency range. The remaining power dissipation of the single actuator system consists of several parts. Firstly, there is the power dissipated as a direct consequence to the actuator current. This flows through the actuator coil with a resistance $R_a + R_a'$ and the coil of the analog low-pass filter with resistance $R_l + R_l'$. For the static case, the corresponding power dissipation can be expressed as:

$$P_a = I_a^2 (R_a + R'_a + R_l + R'_l) = \left(\frac{F_a}{K_a}\right)^2 (R_a + R'_a + R_l + R'_l),$$

where for the second step the system was assumed to be linear such that $F_a=K_aI_a$. For the expected RMS actuator force of 1mN, a measured average motor constant $K_a\approx 0.12 {\rm N/A}$ and $R_a+R'_a+R_l+R'_l\approx 39+3+2.7+2.2\approx 46.9\Omega$, this corresponds to $3.2 {\rm mW}$ per actuator. For the design values in Tables 4.1 and 5.2 this power dissipation would be $1.4 {\rm mW}$, which means that the actual dissipation will be approximately 2.3 times higher than expected.

Besides direct dissipation of the electronics, there is also indirect dissipation. This consists of the power dissipated by the FPGAs to generate the PWM signals and handle the communication and dissipation of the Field Effect Transistor (FET) switches of the H-bridges, LVDS drivers and voltage converters. These contributions have been quantified by measuring the supply current to a single electronics module for various configurations using a Fluke digital multi-meter.

The static power dissipation of the three FPGAs is provided by the manufacturer as approximately 40mW. The summed power dissipated by the master FPGA, the voltage converter and the LVDS driver has been obtained by measuring the supply current with only the master print connected. The power dissipated by the slave FPGAs that generate the PWM signals has been obtained by measuring the supply current with the resulting PWM outputs disabled. Losses in the analog part of the electronics and due to the switching of the H-bridge were obtained by measuring the supply current for various actuator setpoints, but without the actuators being connected. This prevents DC currents from flowing and allows the measuring of parasitic effects only. Further, the difference in supply current to the case that the actuators are connected can be attributed to actuator currents and resulting dissipation. Finally, for all measurements the DC-DC convertor was assumed to have an efficiency of 85%, leading to the results plotted in Figure 5.21.

For an output voltage of 0V the dissipation consists only of the mentioned indirect losses, whereas for non-zero voltages the dissipation is proportional to the square of the voltage setpoint divided by the total resistance. The results in the figure confirm this resistance to be around 40Ω . The RMS voltage setpoint expected in practise is derived from the expected RMS actuator force of 1mN derived in Chapter 2 by division by the motor constant

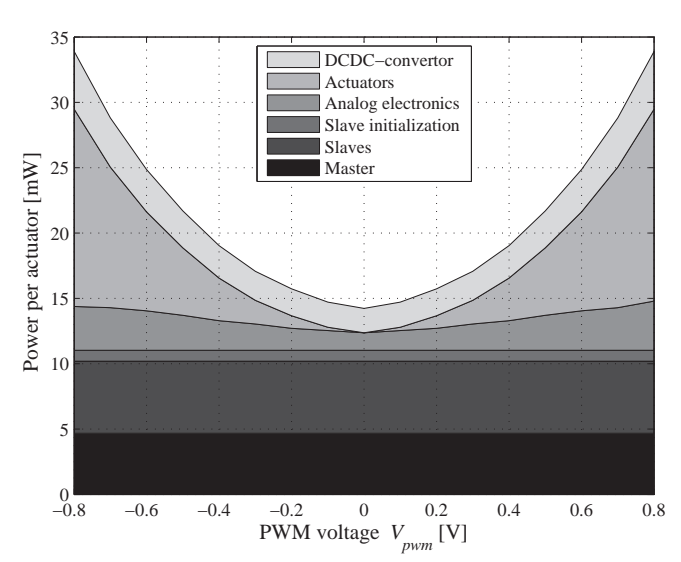


Figure 5.21: Measured power dissipation of the single actuator system including driver and communication electronics. Results are split into the contributions of several components.

 $K_a \approx 0.12 {\rm N/A}$ and multiplication by the total resistance $R_a + R_a' + R_l + R_l' \approx 46.9 \Omega$, yielding 0.39 V. Observe in Figure 5.21 that for this voltage setpoint value the power dissipated in the FPGAs dominates the power dissipated in the actuator to generate force. A reduction of the total power consumption will thus be most effectively achieved by a reduction of the power consumption of the FPGAs. The FPGA implementation has been analyzed in detail by William de Bruijn, who also proposed design modifications to improve the power efficiency. His work has been documented in detail in [51], but only the main findings and design proposals will be summarized.

5.7.1 Optimizing the FPGA power efficiency

The driver electronics developed for the DM system use three FPGAs to implement 61 PWM signal generators and the LVDS communication with a control computer. The power dissipated by an FPGA can be divided into static and dynamic dissipation. The first is dissipated regardless of the program loaded or configuration, but depends highly on the specific IC. For each of the Altera ICs this dissipation is approximately 40mW. The dynamic dissipation depends on the program loaded and can be approximated as:

$$P_{dyn} = P_{sc}(f_{clk}) + \alpha C V_{cc}^2 f_{clk}, \tag{5.7}$$

where P_{sc} is the short-circuit power dissipation that is linearly proportional to the clock frequency f_{clk} . Further, α denotes the switching activity (the average number of 0 to 1 transitions per clock cycle), V_{cc} the supply voltage and C the total capacitance. The latter is a measure for the amount of hardware (transistors, interconnection wires, etc.) in use. The static power dissipation and the supply voltage V_{cc} are determined by the choice for a particular FPGAs. Both are likely to decrease for future models due to technological progress. A reduction of the dynamic power dissipation can be achieved by reducing the

142 5 Electronics

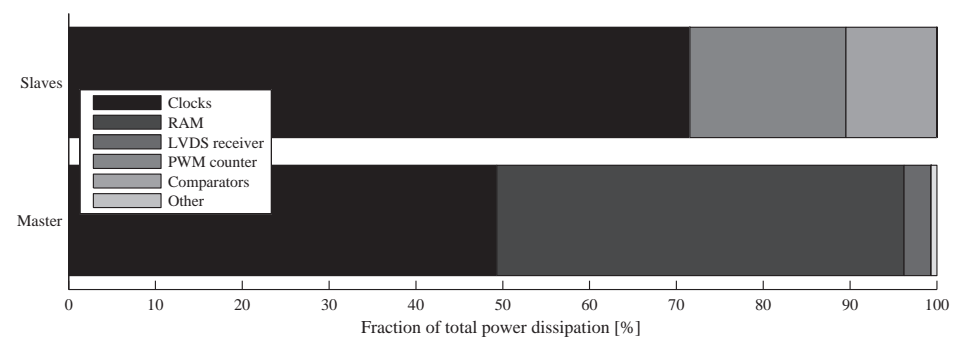


Figure 5.22: The power usage of the master and slave FPGAs subdivided into several functional categories.

capacitance C and the total number of state switches per second expressed by the product αf_{clk} . Such a reduction requires more insight into the distribution of the dissipation over specific parts of the current FPGA program.

To determine the contribution of code parts, the existing FPGA programs were first ported to a Xylinx University Program (XUP) development board. This development board contains a single Xylinx chip instead of the three Altera's, but measurements confirmed that the dynamic FPGA power dissipation is of the same order of magnitude: approximately 550mW instead of 673mW. The latter is derived from Figure 5.21 by summing the contributions of the master, the slaves and the initialization thereof at $V_{PWM}=0$. These measurements were used as a benchmark to compare with the output of the XPower simulation tool [207] by Xylinx that uses the post-place and routing net-lists of the ModelSim PE simulator [133]. Since the simulation results corresponded well to the measurements [51], the more detailed results of the XPower tool were trusted to provide an accurate subdivision of the total dissipation. This is shown graphically in Figure 5.22 for the master and slave FPGAs. Observe that the dissipation of the master FPGA can be mainly attributed to a RAM module and that the dissipation of both FPGA types is for over 50% attributable to clock signals. This means that power dissipation is reduced by:

- 1. Removing the Random Access Memory (RAM) module.
- 2. Reducing the clock frequency f_{clk} .
- 3. Reducing the amount of clocked hardware.

The RAM module is currently used to buffer the incoming LVDS messages, which is not necessary. According to Equation (5.7) the dynamic dissipation is linearly proportional to the clock frequency f_{clk} . A reduction is not possible for all functionality of the FPGA, since this is linked to the PWM base frequency (Section 5.2.2), but for some parts it is. The dissipation due to clock signals can be significantly reduced using an asynchronous design in which logic cells are synchronized using local handshakes instead of *global* clock signals. Such an asynchronous design can be efficiently written in a parallel language such as Tangram or HASTE [95], but the achievable reduction in dissipation depends highly

on the software tools used for mapping this code onto a specific FPGA. For maximum effect the design should be mapped to an ASIC instead of an FPGA. Nevertheless, three new designs were proposed that have been conceptually analyzed and evaluated using both simulations and implementations on the XUP development board. This has lead to the following observations:

- The master functionality can be efficiently expressed in an asynchronous language.
 After implementation without RAM module, a reduction in the power dissipation of the master FPGA of 40% was measured.
- Although asynchronous designs have a high potential for power reduction, this cannot be fully exploited by implementation on FPGAs, because these devices are inherently synchronous and must in fact simulate asynchronous programs.
- The slave functionality was most efficiently implemented using a recursive PWM driver designs. This design has no central counter, but uses a counter for each channel.
 A power reduction is achieved via a recursive counter design in which the bits are clocked at their rate of change (lower bits have a higher clock frequency).
- A combination of a recursive counter implementation for each PWM driver and the asynchronous master lead to a reduction in overall power dissipation of approximately 29%. This reduction is significantly larger when the design is mapped to an ASIC.

5.7.2 Cooling

The improvements proposed in Section 5.7.1 are not yet implemented. The power dissipation in the FPGAs will therefor still exceed the power dissipation of the coils by far. To avoid this heat to be transferred to the ambient air with detrimental air flow in the path of light as a result, a possibility for active cooling is added. This cooling system consists of an aluminium fin which is placed between the master and two slave FPGAs. The aluminium fan is connected with a the aluminium block, which holds the cooling channels. The cooling liquid cools the block and thereby the aluminium fan. In case of, for example, an electronic



Figure 5.23: The cooling system seen from the back.



Figure 5.24: The cooling system seen from the front.

5 Electronics

failure, the PCB together with the aluminium fin can be disconnected from the cooling system without disconnection of the fluid system. The flow is regulated by a commercial Central Processing Unit (CPU) cooling system. The aluminium block is suspended in a thin plate to allow dimensional change of the PCB as well as tolerances on the PCB size. In Figures 5.24 and 5.23 the active cooling system for the FPGAs is shown.

5.8 Conclusions

The electronics for the prototype DMs consist of two parts: the communication electronics that supply the setpoints as computed by the control system and the driver electronics that generate the corresponding actuator voltages. The requirements for both part are derived. Both current and voltage drivers are considered. Current mirrors were not implemented because of their complexity to produce them and the lower efficiency, especially with the large dynamic range required. Since the L_a/R_a time of the actuator is short: 75 μ s, the advantage of current control over voltage control is limited. The motor constant K_a , stiffness c_a and — in the case of a voltage source — the resistance R of the actuator circuit, will vary from actuator to actuator and vary with temperature, causing slow gain variations. A current source will compensate for variations in the resistance R, but variations of K_a and c_a must still be compensated by the AO control system. PWM based voltage drivers are chosen because of their high efficiency and capability to be implemented in large numbers with only a few electronic components.

A LVDS based serial communication bus was chosen for its low power consumption (15mW/transceiver), high bandwidth (up to 655Mb/s) and consequently low latency, low communication overhead and extensive possibilities for customization. The driver electronics for 61 actuators are located on a single, multi-layer PCB and consist of FPGAs to generate the PWM signals, FETs for the H-bridge switches and a coil/capacitor pairs that form 2nd order low-pass filters. The FPGAs that generate the PWM signals also control two LVDS communication connections – one up- and one downlink – to receive setpoint updates and to report status information. A 16-wire flat-cable connects up to 32 electronics modules to a custom designed communications bridge, which translates ethernet packages into LVDS packages and vice versa. The ethernet side of the communications bridge is connected to the control computer at a speed of 100Mbit/s and uses the UDP protocol to minimize overhead and latency.

The actuator model from Chapter 4 was extended with models for the communication and driver electronics. The communication is modeled as a pure delay and the driver electronics as a voltage source with an analog 2^{nd} order low-pass filter. The model is used to select a suitable PWM base frequency for which the position response from the voltage ripple due to higher harmonics of the PWM signal is less than a quarter of the LSB of the setpoint. This frequency should be higher than 40kHz for the DMs with Pyrex facesheets, but is set at 61kHz to be suited for the replacement of these facesheets by beryllium. The actuator model including its communication and electronics was validated by measurements. The measurements include communication tests, static and dynamic response measurements and power dissipation measurements. It is shown that the communication latency is well represented by $\tau_c = 89.7 \cdot 10^{-6} + 39 \cdot 10^{-6} N_m$, where

5.8 Conclusions 145

 N_m is the number of the actuator grid. With the actuator response measurements, actuator properties as stiffness ($c_a=473\pm46\mathrm{N/m}$), motor constant ($K_a=0.11\pm0.02\mathrm{N/A}$), damping ($b_a=0.30\pm0.11\mathrm{mNs/m}$), inductance($L_a=3.0\pm0.2\mathrm{mH}$) and resonance frequency ($f_e=1.83\pm91\mathrm{Hz}$) are verified. These properties showed some variation between actuators, but this could not be attributed to the location of the actuator in the grid (Appendix F).

The time domain response of an actuator to a 4Hz sine voltage was used to determine hysteresis and semi-static nonlinear response of the actuator. This showed the first to be negligible and the second to remain below 5% for the intended $\pm 10 \mu m$ stroke.

Finally, power dissipation was measured. Unintended resistances in the paths between the voltage source and the actuator, combined with the lower motor constant showed to lead to 2.3 times higher power consumptions of the actuators: 3.2mW instead of 1.4mW. Measurements also showed that in the expected operating range, the total power dissipation is dominated by indirect losses in the FPGAs. An alternative FPGA implementation is investigated. A reduction of 40% in the master FPGA and 29% in the slave FPGAs is thereby achieved.

System modeling and characterization

The developed actuator modules and electronics will be integrated with the reflective facesheet to form a complete DM system. The static and dynamic system behavior is modeled and compared to measurement results. The reflective deformable facesheet, which couples all actuators, is modeled with a biharmonic plate equation and an analytic solution for the surface shape under a regular actuator grid is found. The model is used to derive the actuator influence functions. The static model is extended with lumped masses to include the dynamic behavior. From the model, the transfer functions, impulse response functions and mode shapes are derived. The verification of the static behavior of the DM system is done using an interferometer setup. The dynamic system identification is performed using white noise excitation on the actuators and displacement and velocity measurement of the mirror facesheet with a laser vibrometer. With these measurements the model modal analysis is compared with the measurements.

6.1 Introduction

In this chapter the developed actuator modules (Chapter 4) and electronics (Chapter 5) will be combined with a reflective facesheet (Chapter 3) into a complete prototype DM system. First, the integration of these parts is described, after which the behavior of the DM system will be analyzed. An analytical model for the reflective facesheet is derived that – combined with the DC-gain of the single actuator system provides a static model for the DM system. This model describes the actuator influence functions that will be compared with measurements on the DM system. Further, measurement results are presented that show the initial flatness of the DM and its ability to form Zernike mode shapes. Finally, the DC model is used to determine the expected average power dissipation of the DM when correcting Kolmogorov type wavefront disturbances.

An analytical dynamic model for the system is then derived based on the available model for a single actuator system from Chapter 5. From this model the expected resonance frequencies and modal shapes are derived that will be compared to measurement results on the DM system. Finally, the dynamic behavior of the DM system will be evaluated w.r.t. discrete time control aspects.



Figure 6.1: The DM prototype with 61 actuators shown during final assembly. The upper left figure shows 61 struts attaching the mirror facesheet to the actuator module. The module is connected to the (black) base with three A-frames. The flex foil is fed through a central hole in the base. On the right, the folded leafsprings that constrain the facesheet's in-plane DOFs are shown prior to assembly. In the lower left, one of the folded leafsprings is located a little below the mirror facesheet, before it is translated to make the glued connection with the facesheet.

6.2 DM integration

A single actuator grid with 61 actuators is integrated with a $100\mu m$ thick $\varnothing 50mm$ Pyrex facesheet and a single PCB to form the first prototype. In a second, larger prototype, 7 actuator modules are placed on a reference base and connected to a single, $\varnothing 150mm$ Pyrex facesheet.

6.2.1 Integration of the 61 actuator mirror

In Figure 6.1 the integration the first DM prototype is shown at different stages. Similar to the procedure described in Section 3.6, the actuator struts are first connected to the back of the mirror facesheet and then connected to the actuator grid. With the struts attached, only the out-of-plane DOFs of the facesheet are constrained. The in-plane DOFs are still free and will be constrained by the three folded leafsprings described in Section 3.3.2 and shown in Figure 3.7. The folded leafsprings are placed in their aluminium mount and glued to the

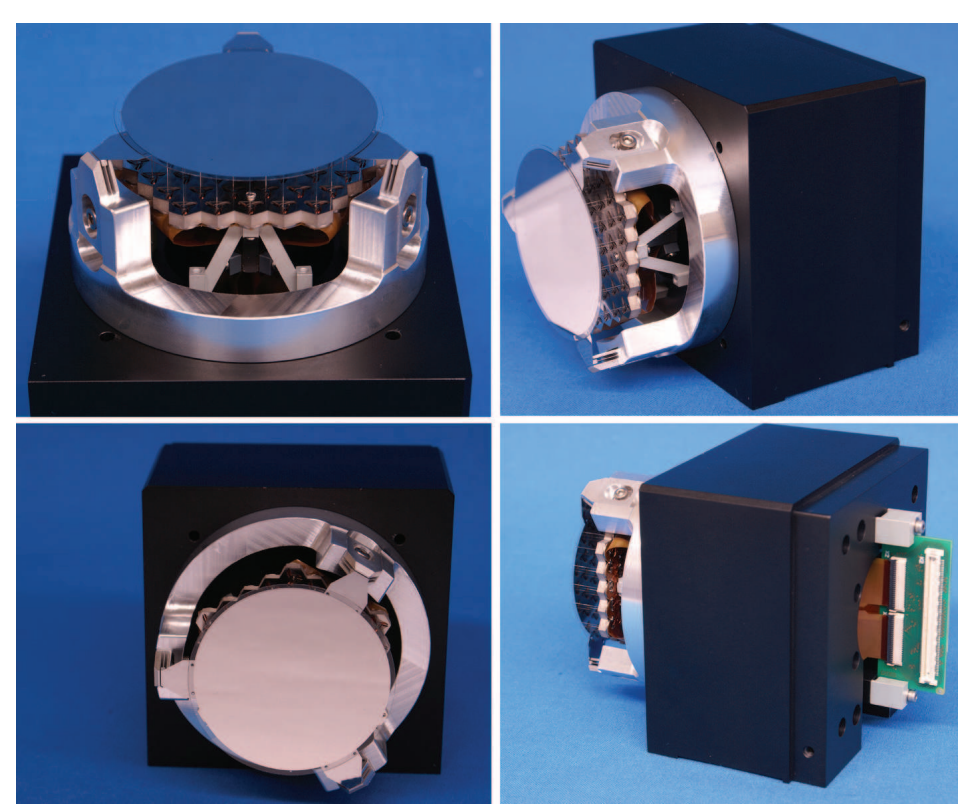


Figure 6.2: The 61 actuator DM. The protective cover is not shown, to see the inner parts. The connector board, described in Section 5.4.2 is shown in the lower right photo.

Figure 6.3: The 61 actuator DM including its electronics.



backside of the facesheet. Figure 6.2 shows the DM with the folded leafsprings in place and Figure 6.3 shows the 61 prototype DM including its electronics and protective cover.

6.2.2 Integration of the 427 actuator mirror

The second DM prototype with 427 actuators is assembled similar to the single actuator grid DM. First the 7 actuator grids are placed on a reference base (Figures 6.4 and 6.5). The corrugated edges of the actuator grids are separated by 0.3mm. The base is made from a 40mm thick aluminium block, perforated with 7 large holes (\varnothing 30mm) and a pattern of small holes to accommodate the M2-bolts to attach the A-frames that connect to the actuator grids. These bolts are mounted from the back. The base itself is placed vertically and supported by three larger A-frames.

The PCBs with the driver electronics are placed in one box (Figure 6.6). The PCBs are mounted similar to Figures 5.24 and 5.23. Via the slits in the front plate, the flex foils connect to the connector boards and PCBs. Figure 6.7 shows the electronic box connected to

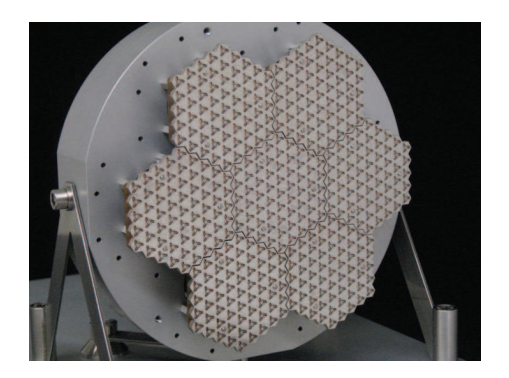


Figure 6.4: Seven actuator modules placed on the reference base. The actuator grids are separated by 0.3mm.

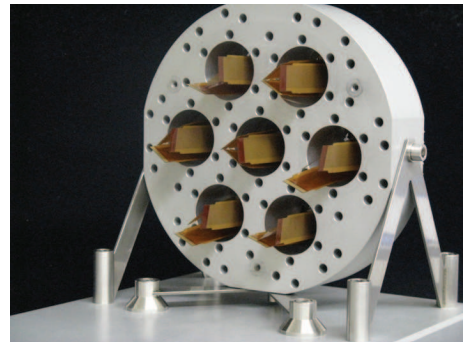


Figure 6.5: The backside of the reference base with the 7 actuator modules mounted. The flex foils are visible through the larger holes.



Figure 6.6: The 7 PCBs with driver electronics assembled in the electronics box. The cooling, similar to Figure 5.24 is visible. Via the slits in the front plate, the flex foils connect to the connector boards and PCBs.

the actuator grids.

The electronic box is decoupled before the mirror facesheet is connected to the actuator grids by means of the actuator struts and small droplets of glue. The procedure, described in Section 3.6 to mount the facesheet is again followed. First the connection struts are glued to the backside of the mirror facesheet, during which the mirror facesheet is supported by a

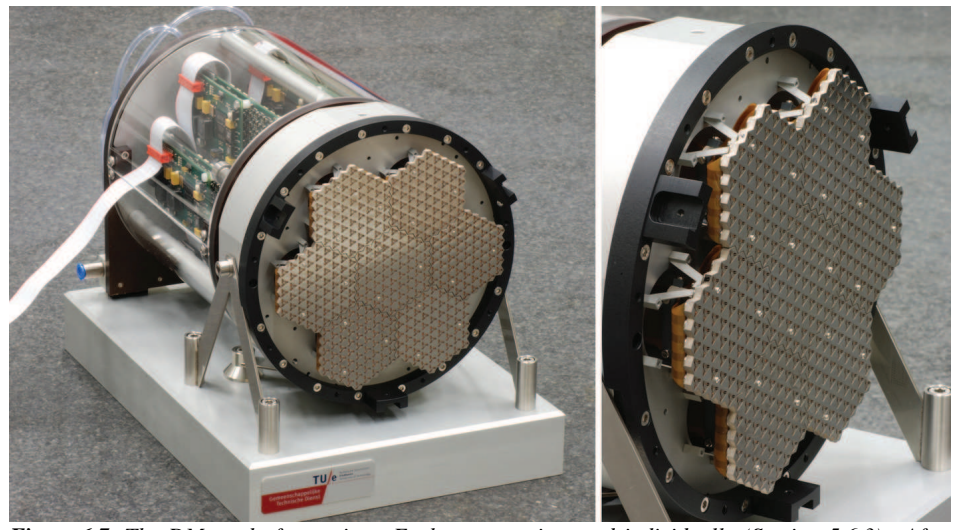


Figure 6.7: The DM ready for testing. Each actuator is tested individually (Section 5.6.3). After testing the facesheet is assembled.



Figure 6.8: CNC placement of the glue droplets on the actuator grids.



Figure 6.9: The mirror facesheet with connection struts is lowered on the actuator grids, while clamped on the air bearing.

porous air bearing. Figures 6.8 to 6.15 show pictures taken during this procedure. Figure 6.8 shows the CNC controlled placement of the droplets at the actuator side. The reference base with actuator grids is aligned on the machine bed prior to the droplet placement. When all droplets are placed, the mirror facesheet and the connection struts are lowered on the actuator grids. The tooling needed to align the connection struts with the droplets of glue is described in Section 3.6. Three V-grooves and balls are used to dock both parts of the assembly, whereas three micro spindles are used to lower the struts carefully into the droplets and to adjust for small angular alignment mismatches in φ and ψ . After curing of the glue, the vacuum is removed from the air bearing. The air bearing and its housing can now be removed. Figure 6.11 shows the mirror facesheet mounted on 427 struts on the actuator grids. Finally, the folded leafsprings needed to constrain the in-plane DOFs are placed



Figure 6.10: Placement of the mirror facesheet with struts suspended by the reference air bearing (upper part) on the reference base with the actuator grids.

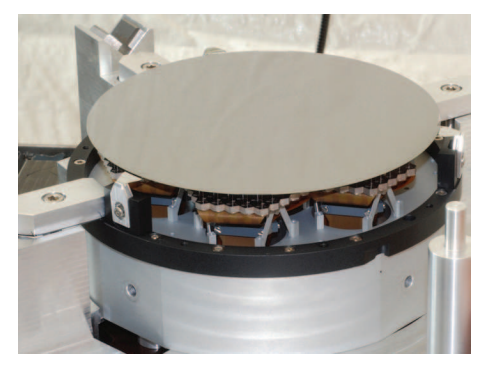
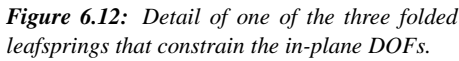


Figure 6.11: After removal of the air bearing and its aluminium housing, the mirror facesheet becomes visible, placed on the actuator grid.





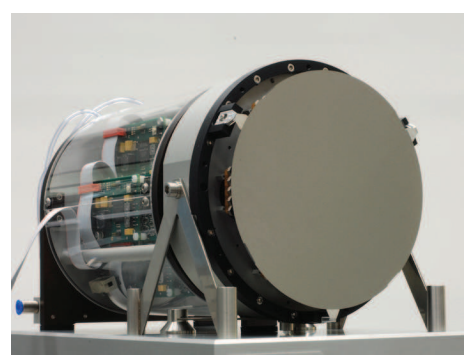


Figure 6.13: The assembled DM with 427 actuators.

(Figure 6.12) and the flex foils are connected to the electronics (Figure 6.13). The mirror is now fully assembled, except for the protective cover ring. Unfortunately, while placing the cover ring the mirror got damaged before any measurements could be obtained from the completed DM system. The results presented in the sequel of this thesis originate from the single actuator module prototype shown in Figure 6.3.

6.3 Static system validation

In this section, the static behavior of the DM is modeled, providing a description for the actuator influence functions. This involves modeling of the mirror facesheet and combining this with the static model of the actuator system from Chapter 5. The actual influence

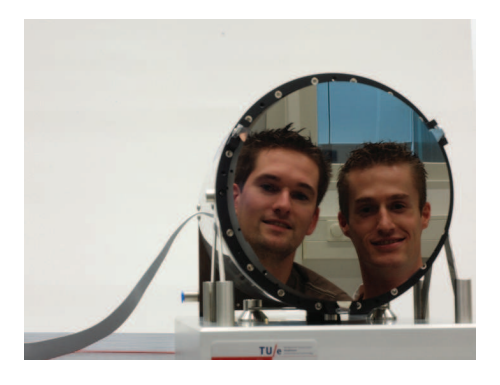


Figure 6.14: The author of this thesis and Dave Bax, the instrument maker who manufactured and assembled most of the DMs.

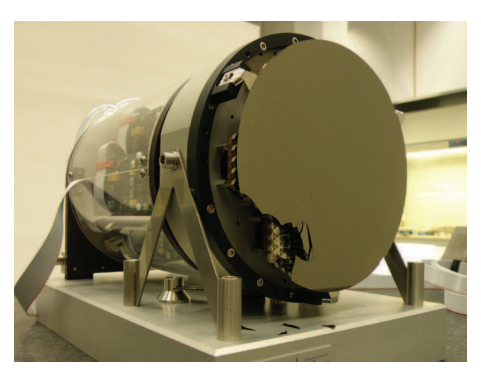


Figure 6.15: The broken DM.

functions of the DM system are measured using a Wyko interferometer to which the modeled influence functions are compared. This was done for all 61 actuators in the Ø50mm DM. Further, the influence matrix derived from the measurements is used to form the mirror facesheet into the first 28 Zernike mode-shapes including the piston term that represents the best flattened mirror [88, 89]. The measured shapes are compared to the perfect Zernike modes and to the least square fit based on the DC model derived.

No measurement results could be obtained from the \emptyset 150mm DM since it was broken. Only a best theoretical flatness for the \emptyset 150mm Pyrex dummy mirror, used in the glue experiment in Section 3.7, is computed using the static model. This results in actuator forces, stroke and power dissipation needed to obtain the best flat mirror.

6.3.1 Modeling

First a model for the reflective facesheet is derived, leading to an expression for the influence function matrix. Finally, this matrix is used in an algorithm to calculate the actuator commands that provide a facesheet that best approximates a certain Zernike shape in a least squares or absolute-error sense.

Facesheet modeling

The mirror facesheet is modeled as a circular plate with free edges, subjected to point forces. Although the facesheet has a large diameter to thickness ratio, the facesheet is still a plate with significant bending stiffness, particularly on the spatial scale of the actuator pitch. In contrast to a true membrane, there is no pre-tension from which it derives its stiffness and resonance frequency. Since the connection struts are only 100 µm thick – which is small in comparison to the pitch – the forces exerted on the reflective facesheet are considered to be point-forces. The in-plane stiffness is provided at the circumference by three folded leaf springs at 120° intervals. The out-of-plane stiffness that these springs contribute is negligible in comparison to the facesheet and can therefore be neglected (Section 3.3.2). The edge of the facesheet is thus considered to be free.

Let $r_{(i)}$ and $\rho_{(j)}$ for $i=1\ldots N_r$ and $j=1\ldots N_a$ be complex values corresponding to coordinates in the complex plane. The deflection $z_f(r_{(i)})$ at coordinate $r_{(i)}$ of a circular, thin plate of Hookean material, with radius r_f and free edge conditions due to a point force $F_{(j)}$ located at $\rho_{(j)}$ can be derived from the biharmonic plate equation [185] in terms of the Laplacian operator ∇^2 and the plate's flexural rigidity D_f as:

$$\nabla^4 z_f(r) = \frac{F_{(j)} r_f^2}{D_f},$$
 where
$$\nabla^2(r) = \frac{\delta^2}{\delta \mathbf{R} \mathbf{e}^2(r)} + \frac{\delta^2}{\delta \mathbf{I} \mathbf{m}^2(r)}, \qquad \text{and} \qquad D_f = \frac{E_f t_f^3}{12(1 - \nu_f^2)}.$$

Further, $\mathbf{Re}(r)$ and $\mathbf{Im}(r)$ denote the real and imaginary parts of r respectively, E_f is the plate material's Young's modulus, ν_f its Poisson ratio and t_f its thickness. The deflection

Table 6.1: Dimensions and material properties of the reflective facesheets of the 61 and 427 actuator DM prototypes.

Parameter	Value	Unit
r_f for the 61 actuator DM	25.4	mm
r_f for the 427 actuator DM	76.2	mm
E_f	64	GPa
$ ho_f$	2230	kg/m^3
t_f	100	μm
$ u_f$	0.2	-

 $Z(r_{(i)})$ can be expressed analytically in terms of $F_{(j)}$ as [125]:

$$Z(r_{(i)}) = \frac{F_{(j)}r_f^2}{16\pi D_f}W(r_{(i)}, \rho_{(j)}) + w_p + w_x \mathbf{Re}(r_{(i)}) + w_y \mathbf{Im}(r_{(i)}),$$

where w_p , w_x and w_y denote the rigid body motions in the out-of-plane direction and around the x- and y axes respectively. The function $W(r_{(i)}, \rho_{(j)})$ is defined as:

$$W(r_{(i)}, \rho_{(j)}) = \varrho_{(i,j)} \varrho_{(i,j)}^* \left\{ \ln(\varrho_{(i,j)}) + \ln(\varrho_{(i,j)}^*) + \frac{1-\nu_f}{3+\nu_f} \left[\ln(1-r_{(i)}\rho_{(j)}^*) + \ln(1-r_{(i)}^*\rho_{(j)}) \right] \right\}$$

$$+ \frac{(1-\nu_f)^2}{(1+\nu_f)(3+\nu_f)} r_{(i)} r_{(i)}^* \rho_{(j)} \rho_{(j)}^* + \frac{8(1+\nu_f)}{(1-\nu_f)(3+\nu_f)} \left\{ (1-r_{(i)}\rho_{(j)}^*) \ln(1-r_{(i)}\rho_{(j)}^*) + k(r_{(i)}\rho_{(j)}^*) + (1-r_{(i)}^*\rho_{(j)}) \ln(1-r_{(i)}^*\rho_{(j)}) + k(r_{(i)}^*\rho_{(j)}) \right\},$$

where the superscript * denotes the complex conjugate and

$$\varrho_{(i,j)} = r_{(i)} - \rho_{(j)} \qquad \text{and} \qquad k(x) = \int\limits_0^x \frac{\ln(1-\varsigma)}{\varsigma} d\varsigma = -\mathrm{dilog}(1-x).$$

This analytic expression allows the spatial grids to be discretized without loss of accuracy. The values of the geometric and material parameters for the 61 and 427 actuator DM prototypes can be found in Table 6.1.

Influence function modeling

The shape of the influence functions depend on the stiffness of the facesheet and actuators and the lay-out of the actuator grid. Linearity is assumed to allow linear superposition of multiple point forces. For convenience, matrix-vector notation is used, where matrices are set in a bold typeface.

Let $\mathbf{z}_{f,(i)} = Z(r_{(i)})$, $\mathbf{z}_{a,(i)} = Z(\rho_{(i)})$ and $\mathbf{F}_{\rho,(j)} = F_{(j)}$ be elements of the vectors \mathbf{z}_f , \mathbf{z}_a and \mathbf{F}_{ρ} respectively. Similarly, the coordinates $r_{(i)}$ and $\rho_{(j)}$ form the i^{th} and j^{th} elements of the vectors \mathbf{r} and $\boldsymbol{\rho}$ and $\boldsymbol{\Omega}_{r\rho,(i,j)} = w(r_{(i)},\rho_{(j)})$ the elements of the matrix $\boldsymbol{\Omega}_{r\rho}$. The

facesheet deflection \mathbf{z}_f can then be expressed as:

$$\mathbf{z}_f = \mathbf{\Omega}_{r\rho} \mathbf{F}_{\rho} + \mathbf{U}_r \mathbf{w}_{pxy},\tag{6.1}$$

where $\mathbf{U}_r = [\mathbf{1}^{N_r \times 1} \, \mathbf{Re}(\mathbf{r}) \, \mathbf{Im}(\mathbf{r})]$ and $\mathbf{w}_{pxy} = [w_p \, w_x \, w_y]^T$. The reflective facesheet is supported by actuators with effective mechanical stiffnesses that exert forces denoted by the vector \mathbf{F}_a . Since these stiffnesses can be considered linear (Section 5.6.4 on page 139), the following force equilibrium must be satisfied at the actuator locations in the vector $\boldsymbol{\rho}$:

$$\mathbf{F}_a - \mathbf{C}_a \mathbf{z}_a - \mathbf{F}_\rho = 0, \tag{6.2}$$

where C_a is a diagonal matrix whose i^{th} diagonal element is the stiffness c_a of actuator i and it is assumed that the facesheet deflection at the actuator locations is equal to the actuator deflection z_a .

Since the rigid body modes are not constrained by the free edge condition of the plate, the moments due to the net plate forces \mathbf{F}_{ρ} around the x and y axes and the net force in the out-of-plane direction should be zero. This leads to the extra condition $\mathbf{U}_{\rho}^T\mathbf{F}_{\rho}=0$, where \mathbf{U}_{ρ} is defined similar to \mathbf{U}_r as $\mathbf{U}_{\rho}=[\mathbf{1}^{N_r\times 1}\,\mathbf{Re}(\rho)\,\mathbf{Im}(\rho)]$. When Equation (6.1) is evaluated only on the actuator grid – i.e. $\mathbf{r}=\rho$ – it can be expressed as $\mathbf{z}_a=\Omega_{\rho\rho}\mathbf{F}_{\rho}+\mathbf{U}_{\rho}\mathbf{w}_{pxy}$, where $\Omega_{\rho\rho}=\Omega_{r\rho}|_{\mathbf{r}=\rho}$. Together with the rigid body constraint this can be written in matrix form as:

$$\begin{bmatrix} \mathbf{z}_a \\ 0 \end{bmatrix} = \begin{bmatrix} \mathbf{\Omega}_{\rho\rho} & \mathbf{U}_{\rho} \\ \mathbf{U}_{\rho}^T & 0 \end{bmatrix} \begin{bmatrix} \mathbf{F}_{\rho} \\ \mathbf{w}_{pxy} \end{bmatrix},$$

which can be inverted to:

$$\begin{bmatrix} \mathbf{F}_{\rho} \\ \mathbf{w}_{pxy} \end{bmatrix} = \begin{bmatrix} \mathbf{\Omega}_{\rho\rho} & \mathbf{U}_{\rho} \\ \mathbf{U}_{\rho}^{T} & 0 \end{bmatrix}^{-1} \begin{bmatrix} \mathbf{z}_{a} \\ 0 \end{bmatrix} = \begin{bmatrix} \mathbf{K}_{m} \\ \mathbf{K}_{z} \end{bmatrix} \mathbf{z}_{a}, \tag{6.3}$$

in which the matrices \mathbf{K}_m and \mathbf{K}_z are implicitly defined. Substitution of this result for \mathbf{F}_ρ into the force equilibrium in Equation (6.2) then yields:

$$\mathbf{F}_a - \mathbf{C}_a \mathbf{z}_a - \mathbf{K}_m \mathbf{z}_a = 0$$

and thus the facesheet deflection \mathbf{z}_a at the actuator positions is related to the actuator forces \mathbf{F}_a as

$$\mathbf{z}_a = (\mathbf{K}_m + \mathbf{C}_a)^{-1} \mathbf{F}_a, \tag{6.4}$$

The static force F_a of a certain actuator due to a supplied PWM voltage V_{PWM} can be expressed as the quotient of the motor constant K_a and the total electric resistance: $F_a = K_a/(R_a + R_a' + R_l + R_l')V_{PWM}$. This can be written in vector notation for all actuators as:

$$\mathbf{F}_a = \mathbf{K}_a (\mathbf{R}_a + \mathbf{R}'_a + \mathbf{R}_l + \mathbf{R}'_l)^{-1} \mathbf{V}_{PWM}, \tag{6.5}$$

where the i^{th} diagonal elements of the diagonal matrices \mathbf{K}_a , \mathbf{R}_a , \mathbf{R}'_a , \mathbf{R}_l and \mathbf{R}'_l are the values of the corresponding (regularly typefaced) symbols for all actuators $i=1\ldots N_a$. Further, the vector \mathbf{V}_{PWM} stacks the PWM voltages V_{PWM} of all actuators. Substitution of Equation (6.5) into Equation (6.4) then leads to:

$$\mathbf{z}_{a} = \underbrace{\left(\mathbf{K}_{m} + \mathbf{C}_{a}\right)^{-1} \mathbf{K}_{a} (\mathbf{R}_{a} + \mathbf{R}_{a}' + \mathbf{R}_{l} + \mathbf{R}_{l}')^{-1}}_{\mathbf{B}_{a}} \mathbf{V}_{PWM}, \tag{6.6}$$

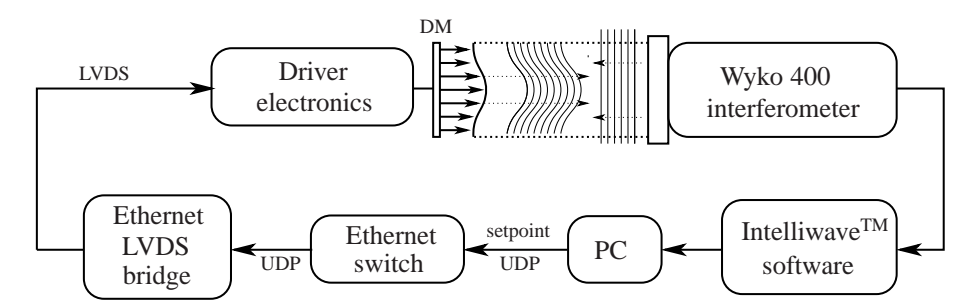


Figure 6.16: The measurement setup which is used to measure the influence functions of the DM.

where \mathbf{B}_{ρ} is the influence matrix that links PWM voltages to facesheet deflection at the actuator locations. The plate deflections due to point forces at positions $\overline{\rho}$ can also be evaluated over the arbitrary grid with complex coordinate vector \mathbf{r} . The results from Equation (6.3) can be substituted into the plate equation in Equation (6.1) together with Equation (6.4), yielding:

$$\mathbf{z}_{f} = (\mathbf{\Omega}_{r\rho}\mathbf{K}_{m} + \mathbf{U}_{r}\mathbf{K}_{z})\mathbf{F}_{a}$$

$$= (\mathbf{\Omega}_{r\rho}\mathbf{K}_{m} + \mathbf{U}_{r}\mathbf{K}_{z})\mathbf{B}_{\rho} \mathbf{V}_{PWM}, \tag{6.7}$$

where \mathbf{B}_f is the influence matrix that links PWM voltages to deflections at an arbitrary grid of points on the facesheet.

6.3.2 Measurements and results

This section describes the setup and procedure used to measure the mirrors influence functions and low order Zernike modes.

Interferometric measurement setup

The verification of the static behavior of the DM system is done using an interferometer setup. A Wyko 400 interferometer available at TNO Science and Industry measures the surface shape of the DM. IntelliwaveTM software is used to perform the reconstruction of the actual wavefront from the measured fringe patterns. Figure 6.16 shows the schematic of the measurement setup, where a PC sends desired setpoint commands \mathbf{V}_{PWM} via the ethernet/LVDS communication link to the DM. All shapes and measurements in the coming sections are considered w.r.t. an arbitrary grid as determined by the interferometer's CCD camera. Since the interferometer cannot observe the piston mode corresponding to a nonzero average deflection, it is assumed that all measurements $\hat{\mathbf{z}}$ are piston-free. When considering the zero-mean, white measurement noise \mathbf{n} , this allows the measurements $\hat{\mathbf{z}}_f \in \mathbb{R}^{N_w}$

to be expressed as:

$$\hat{\mathbf{z}}_f = \mathbf{P}\mathbf{z}_f + \mathbf{P}\mathbf{n},\tag{6.8}$$

where the rank deficient matrix $\mathbf{P} = \mathbf{I} - \mathbf{p}\mathbf{p}^T$ projects out the piston term denoted by the vector \mathbf{p} whose elements are all equal to $1/\sqrt{N_w}$ s.t. $\mathbf{p}^T\mathbf{p} = 1$.

Assuming the static response of the DM to be linear, let the shape \mathbf{z}_f of the DM facesheet be expressed as:

$$\mathbf{z}_f = \mathbf{B}_{f,w} \mathbf{V}_{PWM} + \mathbf{z}_{f,0},$$

where $\mathbf{z}_{f,(0)}$ is the initial unactuated shape of the DM facesheet and the matrix $\mathbf{B}_{f,w}$ is the influence matrix \mathbf{B}_f w.r.t. the measurement grid of the Wyko interferometer. Substitution of this expression for \mathbf{z}_f into Equation (6.8) then yields the measurement corresponding to a certain actuator command \mathbf{V}_{PWM} as:

$$\hat{\mathbf{z}}_f = \mathbf{P}\mathbf{B}_{f,w}\mathbf{V}_{PWM} + \mathbf{P}\mathbf{z}_{f,0} + \mathbf{P}\mathbf{n}$$
(6.9)

This measurement equation will be used in the following two subsections to estimate the influence function matrix $\mathbf{B}_{f,w}$ and fit the DM facesheet to a desired set of shapes.

Influence function measurements

As described in Section 6.3.1, the influence functions are the static responses of the DM to actuator commands. Analytically they are expressed over the actuator grid by the matrix \mathbf{B}_{ρ} in Equation (6.6) and over an arbitrary grid as \mathbf{B}_{f} in Equation (6.7). In this section the method is described that is used to measure the influence functions of the DM prototypes. The most obvious method to determine the influence functions is to individually poke each actuator, measure the response and then compute the influence function. Multiple measurements must be used per actuator to reduce the measurement noise and at least two different command values are required to determine the influence function as a linear relation between command and deflection. More command values and measurements can be used to distinguish any nonlinear behavior. Each Wyko measurement takes approximately 8 seconds including data processing. When several commands are used for each actuator and the number of actuators is large (e.g. 427) the measurements would take several hours to complete. And even then, each influence function has to be estimated from only a few measurements, still leading to a high sensitivity to measurement noise. Better and more efficient methods can be used. For instance, in [94, 115] columns of scaled Hadamard matrices [17] are used as the actuator command vectors. This setpoint choice will minimize the mean standard deviation of the estimation error of the influence matrix due to measurement noise and thus requires fewer measurements.

All elements of a Hadamard matrix $\mathbf{Q}_n \in \mathbb{R}^{n \times n}$ are either 1 or -1 and the matrix is orthogonal s.t. $\mathbf{Q}_n \mathbf{Q}_n^T = n\mathbf{I}$. Although it is yet unknown whether Hadamard matrices exist for all $n \in \mathbb{N}^+$, algorithms are available for specific dimensions. When an algorithm is unavailable for $n = N_a$, it is argued in [115] that virtual actuators can be added that do not influence the DM shape, but allow the use of a larger Hadamard matrix of size $N_{av} > N_a$ that does exist at the cost of additional measurements.

Accordingly, for the 61 actuator DM prototype a 64×64 Hadamard matrix is used that is generated by Matlab's hadamard function. For the 427 actuator DM, the 428×428

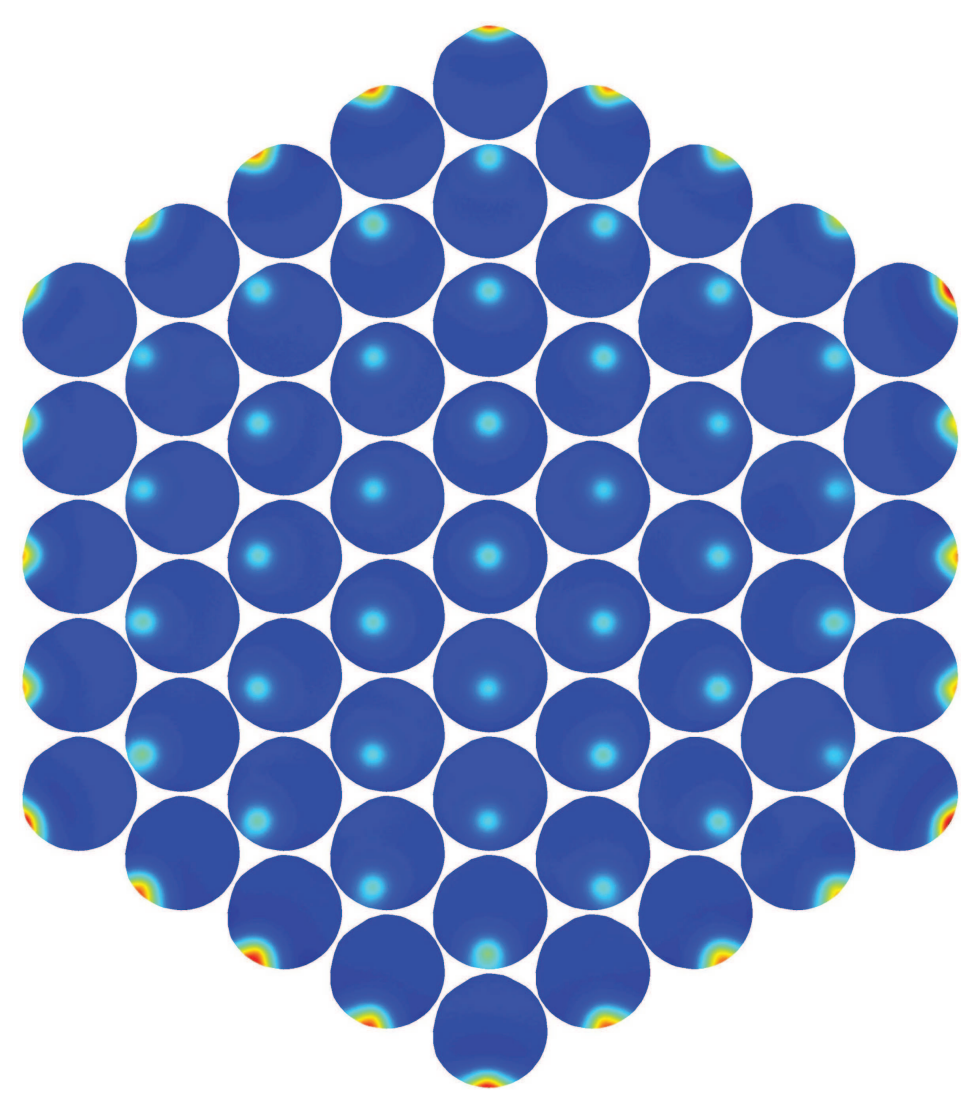


Figure 6.17: The 61 influence functions of the DM prototype shown in Figure 6.3. Each influence function is downsized and placed on the location of the corresponding actuator in the grid.

Hadamard matrix derived in [116] can be used. In the procedure described below, the influence matrix $\hat{\mathbf{B}}_r$ is estimated that includes influence functions of both the real and virtual actuators. After estimation, the columns corresponding to the virtual actuators are ignored. By individual scaling of the rows of the Hadamard command matrix it is possible to compensate for the lower stiffness at the edges of the DM that would lead to a larger deflection than at the center. This is done for optimal use of the measurement range of the interferom-

eter and avoid large deflections that would exceed the measurement range.

Let measurements be expressed as in Equation (6.9) using actuator setpoints V_{PWM} taken as the columns of the matrix V that consist of the vectors $\mathbf{v}_{(i)}$ s.t.

$$\mathbf{V} = [\mathbf{v}_{(0)} \ \mathbf{v}_{(1)} \ \dots \ \mathbf{v}_{(N_{av})}] \in \mathcal{R}^{N_{av} \times N_{av} + 1}.$$

Here $\mathbf{v}_{(0)}=0$ is a zero voltage command vector that is included to allow direct estimation of the unactuated shape $\mathbf{z}_{(0)}$. Further, $\mathbf{v}_{(i)}=\mathbf{\Lambda}\mathbf{q}_{(i)}$ for $i=1\ldots N_{av}$ are the command vectors based on the Hadamard matrix $\mathbf{Q}_{N_{av}}$, where $\mathbf{Q}_{N_{av}}=[\mathbf{q}_{(1)}\ldots\mathbf{q}_{(N_{av})}]$. The diagonal matrix $\mathbf{\Lambda}$ scales the rows of the Hadamard matrix $\mathbf{Q}_{N_{av}}$ and provides the mentioned individual setpoint gains for all actuators. This matrix will be derived from the DM system model. For the influence functions identification, Equation (6.9) becomes:

$$\hat{\mathbf{z}}_{f,(i)} = \mathbf{P}\mathbf{z}_{f,(0)} + \tilde{\mathbf{B}}_{f,w}\mathbf{v}_{(i)} + \mathbf{P}\mathbf{n}_{(i)},$$

where $\tilde{\mathbf{B}}_{f,w} = \mathbf{P}\mathbf{B}_{f,w}$. Before stating the estimation problem, let all measurements be expressed in matrix form as:

$$\hat{\mathbf{Z}}_f = \tilde{\mathbf{B}}_{f,w}\mathbf{V} + \mathbf{P}\mathbf{z}_{f,(0)}\mathbf{1}^T + \tilde{\mathbf{N}} = \underbrace{\begin{bmatrix} \tilde{\mathbf{B}}_{f,w} & \mathbf{P}\mathbf{z}_{f,(0)} \\ 1 & 1^T \end{bmatrix}}_{\mathbf{X}} \underbrace{\begin{bmatrix} \mathbf{0} & \Lambda \mathbf{Q}_{N_{av}} \\ 1 & 1^T \end{bmatrix}}_{\mathbf{Y}} + \tilde{\mathbf{N}},$$

where
$$\hat{\mathbf{Z}}_f = [\hat{\mathbf{z}}_{f,(0)} \ \hat{\mathbf{z}}_1 \dots \hat{\mathbf{z}}_{N_{av}}],$$
 $\tilde{\mathbf{N}} = \mathbf{P}[\mathbf{n}_{(0)} \ \mathbf{n}_{(1)} \ \dots \ \mathbf{n}_{(N_{av})}],$

and all elements of the column vectors $\mathbf{1}$ and $\mathbf{0}$ are equal to 1 and 0 respectively. The matrix \mathbf{X} of unknowns is estimated as:

$$\begin{split} \hat{\mathbf{X}} &= \arg\min_{\mathbf{X}} \operatorname{Tr} \left(\left(\hat{\mathbf{Z}}_f - \mathbf{X} \mathbf{\Upsilon} \right) \left(\hat{\mathbf{Z}}_f^T - \mathbf{\Upsilon}^T \mathbf{X}^T \right) \right), \\ &= \hat{\mathbf{Z}}_f \mathbf{\Upsilon}^T \left(\mathbf{\Upsilon} \mathbf{\Upsilon}^T \right)^{-1}, \\ &= \hat{\mathbf{Z}}_f \begin{bmatrix} -\frac{1}{N_{av}} \mathbf{1}^T \mathbf{Q}_{N_{av}}^T \mathbf{\Lambda}^{-1} & 1 \\ \frac{1}{N_{av}} \mathbf{Q}_{N_{av}}^T \mathbf{\Lambda}^{-1} & \mathbf{0} \end{bmatrix}, \end{split}$$

where the second step follows from a completion of squares argument and the last follows from the orthogonality of the Hadamard matrix $\mathbf{Q}_{N_{av}}$. The sought estimate of the influence matrix forms the first N_a columns of $\hat{\mathbf{X}}$ and that of the unactuated shape $\mathbf{Pz}_{f,(0)}$ the last column.

Although the Hadamard matrix approach has minimal sensitivity to measurement noise, it assumes linearity of the DM system and does not lead to an overdetermined set of equations from which to estimate the influence matrix. As a result, neither the quality of the estimate nor the linearity of the DM can be verified using criteria such as the Variance Accounted For (VAF). Such information can be obtained by extending the set of measurements, e.g. by repeating the measurements using scaled versions of the actuator setpoints.

Finally, it should be noted that the same procedure can be used to determine the influence functions from measurements of a Shack-Hartmann sensor.

Influence function results

The above described procedure is used on the 61 actuator DM prototype, where the command vector scaling matrix Λ was obtained as:

$$\mathbf{\Lambda} = \begin{bmatrix} \gamma_w \mathrm{diag}(\mathbf{B}_\rho)^{-1} & \mathbf{0} \\ \mathbf{0} & \mathbf{I} \end{bmatrix},$$

Here, the bottom-right identity matrix corresponds to the three virtual actuators and is of size 3×3 . The scalar γ_w determines the range of the facesheet deflections and thus the measurement range of the interferometer. A value $\gamma_w = 2\mu m$ has been used. The matrix \mathbf{B}_ρ was computed for this DM from Equation (6.6) by substitution of the relevant parameter values in Tables 4.1, 5.2 and 6.1. Further, $\operatorname{diag}(\cdot)$ denotes the diagonal operator that sets all elements of the matrix between brackets to zero except for the diagonal entries.

The estimated influence functions are shown in Figures 6.17, 6.18 and 6.19. Figure 6.17 shows the 61 influence functions downsized and placed on the location of the corresponding actuator. The facesheet deflection due to a unit voltage increases for actuators near the edge of the facesheet, which is the result of the decreased stiffness due to the facesheet boundary and the smaller number of surrounding actuators. As can be expected from a hexagonal actuator layout, a 60° symmetry is observed.

Figures 6.18 and 6.19 show the cross sections over two indicated axes of the measured and modeled influence functions. From the right figure the actuator coupling η can be well observed as the ratio between the the deflection value at a radius of 6mm (a single actuator spacing) from the maximum and the maximum deflection value. For the central actuator this leads to $\eta \approx 0.52$, whereas for the edge actuators this reduces to $\eta \approx 0.3$ due to the reduced facesheet stiffness at the edge. The in Section 3.4 estimated value for the actuator coupling was 0.65, which is slightly higher than was measured. This is attributed to the fact that only the six surrounding actuators were considered in the former analysis,

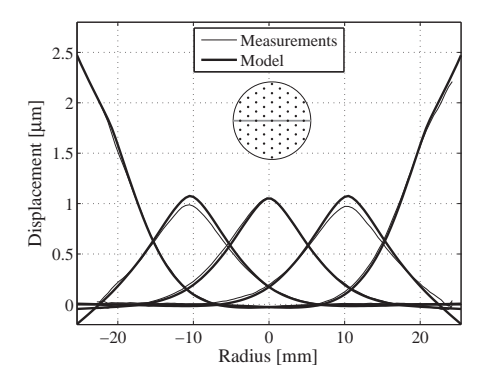


Figure 6.18: The cross-section of the five influence functions of Figure 6.17 along the x-axis. The thick lines represent the functions as derived with the model.

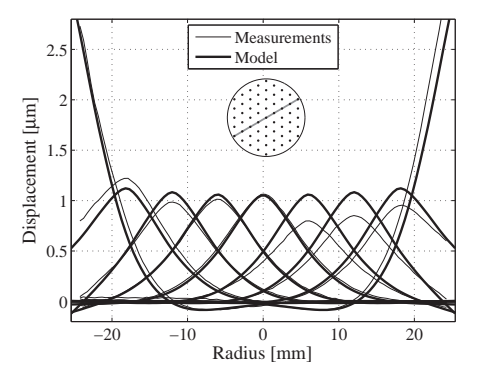


Figure 6.19: The cross-section of nine influence functions in Figure 6.17 along the axis rotated 30-degree counter-clockwise. The thick lines represent the functions as derived with the model.

which is an underestimation of the stiffness present and thus leads to an over-estimation of the coupling η . Although the influence function measured for the center actuator matches almost perfectly to the one derived from the model, the errors vary per actuator. This is attributed to the measured variation between actuators in properties that determine its DC-gain, i.e. motor constant K_a , stiffness c_a and the total electrical resistance $R_a + R'_a + R_l + R'_l$.

Zernike mode measurements and results

With superposition of the influence functions, the DM facesheet can be fit to a desired shape. This shape may be entirely flat, in which case the actuators must compensate for the initial unflatness of the DM. Here it is only possible to correct for spatial frequencies up to the Nyquist frequency, which is determined by the actuator spacing. Higher order deformations, e.g. caused by the shrinkage of the glue that connects the actuator struts to the reflective facesheet, or initial waviness in the polished facesheet, cannot be corrected.

The flat surface shape corresponds to the first Zernike mode: piston. With the influence function superposition also higher order Zernike modes are fit. The shape errors can be minimized for both the PTV and RMS norms, corresponding to the ℓ_1 and ℓ_2 norms respectively.

Let a shape measurement be denoted by the vector $\hat{\mathbf{z}}_f$ as defined in Equation (6.9) and subject to white measurement noise. Let the command vector $\hat{\mathbf{V}}_\ell$ for which the difference between the measured facesheet shape $\hat{\mathbf{z}}_f$ and the desired shape \mathbf{z}_d is minimized w.r.t. an arbitrary norm ℓ :

$$\begin{split} \hat{\mathbf{V}}_{\ell} &= \arg\min_{\mathbf{V}_{PWM}} \|\hat{\mathbf{z}}_f - \mathbf{z}_d\|_{\ell} \\ &= \arg\min_{\mathbf{V}_{PWM}} \left\| \mathbf{P} \mathbf{B}_f \mathbf{V}_{PWM} + \mathbf{P} \mathbf{z}_{f,(0)} + \mathbf{P} \mathbf{n} - \mathbf{z}_d \right\|_{\ell}. \end{split}$$

In practise the PWM voltage is limited to $V_{max}=3.3V$, leading to the constrained optimization problem:

$$\hat{\mathbf{V}}_{\ell} = \arg\min_{\mathbf{V}_{PWM}} \ \left\| \mathbf{P} \mathbf{B}_f \mathbf{V}_{PWM} + \mathbf{P} \mathbf{z}_{f,(0)} + \mathbf{P} \mathbf{n} - \mathbf{z}_d \right\|_{\ell}$$
subject to $-V_{max} \leq \mathbf{V}_{PWM} \leq V_{max}$.

The effects of the measurement noise \mathbf{n} can be reduced by taking $\hat{\mathbf{z}}_{f,(0)}$ as the average of several measurements. Since the actual influence matrix \mathbf{B}_f is not known, the product $\mathbf{P}\mathbf{B}_f$ shall be replaced by the piston removed estimate $\hat{\mathbf{B}}_f$.

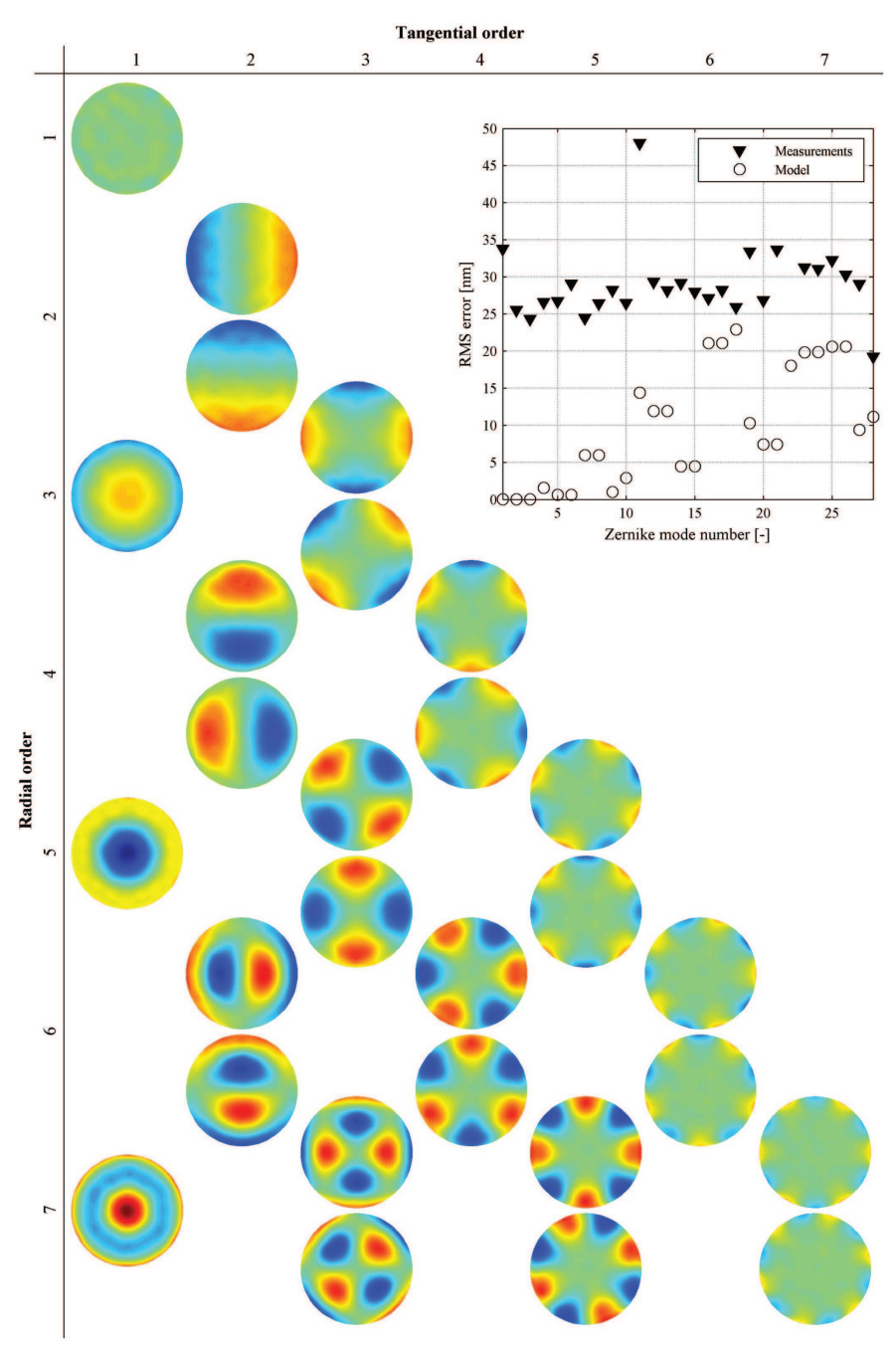


Figure 6.20: The first 28 Zernike modes made with the DM from Figure 6.3. The inset shows the RMS fitting errors w.r.t. the desired shape for the model and the measurements.

For the ℓ_1 norm (i.e. minimization of the PTV value), the optimization problem becomes a linear programming problem:

$$\hat{V}_{\ell_1} = \arg\min_{\mathbf{V}_{PWM}, \gamma} \gamma$$
 subject to

$$-\gamma \leq (\hat{\mathbf{B}}_f \mathbf{V}_{PWM} + \mathbf{P} \mathbf{z}_{f,(0)} + \mathbf{P} \mathbf{n} - \mathbf{z}_d) \leq \gamma \text{ and } -V_{max} \leq \mathbf{V}_{PWM} \leq V_{max}$$

For the ℓ_2 norm, the optimization problem becomes a quadratic programming problem:

$$\hat{V}_{\ell_2} = \arg\min_{\mathbf{V}_{PWM}} \ \left\| \hat{\mathbf{B}}_f \mathbf{V}_{PWM} + \mathbf{P} \mathbf{z}_{f,(0)} + \mathbf{P} \mathbf{n} - \mathbf{z}_d \right\|_{\ell_2}$$
subject to $-V_{max} \leq \mathbf{V}_{PWM} \leq V_{max}$.

However, due to e.g measurement noise \mathbf{n} and nonlinear behavior of the DM prototypes, the DM model in Equation (6.9) with \mathbf{PB}_f replaced by $\hat{\mathbf{B}}_f$ will not be correct. The estimated command vectors \hat{V}_{ℓ_1} and \hat{V}_{ℓ_2} will thus neither minimize $\|\mathbf{PB}_f\mathbf{V}_{PWM}+\mathbf{Pz}_{f,(0)}-\mathbf{z}_d\|_{\ell}$ for the ℓ_1 norm, nor for the ℓ_2 norm. Therefore, an iterative process with iteration index m is used to derive the vector $\hat{\mathbf{V}}_{\ell}^{(m)}$:

$$\hat{\mathbf{V}}_{\ell}^{(m+1)} = \hat{\mathbf{V}}_{\ell}^{(m)} + \arg\min_{\Delta\mathbf{V}_{PWM}} \left\| \hat{\mathbf{B}}_{f} \Delta\mathbf{V}_{PWM} + \hat{\mathbf{z}}_{f}^{(m)} - \mathbf{z}_{d} \right\|_{\ell},$$

where the minimization is subject to $-V_{max} - \hat{\mathbf{V}}_{\ell}^{(m)} \leq \Delta \mathbf{V}_{PWM} \leq V_{max} - \hat{\mathbf{V}}_{\ell}^{(m)}$. Each new setpoint yields the measurement:

$$\hat{\mathbf{z}}_f^{(m)} = \mathbf{P}\mathbf{B}_f \hat{V}_{\ell}^{(m)} + \mathbf{P}\mathbf{z}_{f,(0)} + \mathbf{P}\mathbf{n}^{(m)}.$$

Here again the effect of measurement noise can be reduced by taking $\hat{\mathbf{z}}_f^{(m)}$ as the average of several measurements.

The above procedure has been applied for the 61 actuator DM prototype, using an \emptyset 44mm circular aperture area that corresponds the inscribed circle of the hexagonal actuator grid. The results for the first 28 Zernike modes with an RMS amplitude of 400nm are shown in Figure 6.20. Since the DM has only a limited number of regularly spaced actuators, there will be a fitting error. The inset in Figure 6.20 shows the RMS errors w.r.t. a perfect Zernike mode together with the numerically evaluated fitting error of the derived static model.

Since the latter is not subject to measurement noise, nonlinearities or initial unflatness, this forms the error contribution only due the limited number of actuators. From the piston, tip and tilt mode it becomes clear that the higher order unflatness is $\approx 25 \text{nm RMS}$. This unflattness can not be compensated by the (limited) number of actuators. For the higher order Zernike modes this unflattness can result in better or in worse fitting.

Flattening of the $\varnothing 150mm$ dummy mirror

Since the 427 actuator DM prototype was broken during the last assembly step, it was not possible to measure its initial unflatness, static or dynamic behavior. Also the effect of

combining multiple actuator modules into a DM system with a single continuous facesheet could not be analyzed. However, a dummy mirror (Figure 3.35) was assembled from an identical facesheet and 427 struts glued using the same procedure as used for the broken DM prototype. The shape of this mirror, measured with the Wyko 400 interferometer is depicted in Figure 3.38 on the left and shows a PTV unflatness of approximately 4.5 μ m. Since the results of the above influence function measurements for the 61 actuator DM indicate that the influence functions are well predicted by the model, it is inferred that the same is true for the 427 actuator DM. With the influence matrix \mathbf{B}_f evaluated with the parameters from Tables 4.1, 5.2 and 6.1, the dummy mirror is flattened fictitiously. The flattening procedure, described in the previous section, is here not applicable, since the facesheet is here supported by 427 struts and a rigid reference plate instead of soft actuators. The shape of interest is the initial unflatness of the facesheet, when it would have been glued to soft actuators instead of to a stiff base. The soft actuators will deflect due to stresses in the facesheet, whereas the stiff base does not. Therefore, the flattening must thus be performed after 'replacing' the stiff base with soft actuators.

This is analyzed as follows. Let the vector $\hat{\mathbf{z}}_{f,b}$ contain the deflections measured at the strut positions and $\hat{\mathbf{z}}_{f,a}$ the deflections after placing the facesheet on the soft actuators. The force \mathbf{F}_a that the actuators must exert on the facesheet to keep the shape $\hat{\mathbf{z}}_{f,b}$ is obtained using Equation (6.3) as $\mathbf{F}_a = \mathbf{K}_m \hat{\mathbf{z}}_{f,a}$. This force is generated by deflection of the actuators from their measured $\hat{\mathbf{z}}_{f,b}$ positions via the effective actuator stiffness as $\mathbf{F}_a = \mathbf{C}_a(\hat{\mathbf{z}}_{f,b} - \hat{\mathbf{z}}_{f,a})$. Combination of both equations yields:

$$\hat{\mathbf{z}}_{f,a} = \underbrace{(\mathbf{K}_m + \mathbf{C}_a)^{-1}}_{\mathbf{T}} \mathbf{C}_a \hat{\mathbf{z}}_{f,b}.$$
 (6.10)

Observe that \mathbf{T} is the influence matrix that links force to deflection and \mathbf{C}_a is a diagonal matrix with the actuator stiffnesses. Since application of the first part to a vector has a low-pass filter effect and the latter part is only a linear scaling, the transformation from $\hat{\mathbf{z}}_{f,b}$ to $\hat{\mathbf{z}}_{f,a}$ is a smoothing operation. The strength of this smoothing effect depends on the widths of the influence functions and thus on the facesheet and actuator stiffnesses.

At this point the fictitious DM with initial unflatness $\hat{\mathbf{z}}_{f,a}$ is flattened w.r.t. an RMS criterion by applying a set of suitable fictitious actuator forces \mathbf{F}_a^f . The forces \mathbf{F}_a^f that minimize the unflatness w.r.t. the weighting function $\|\hat{\mathbf{z}}_{f,a} - \mathbf{T}\mathbf{F}_a\|_F^2$ are found using a completion of

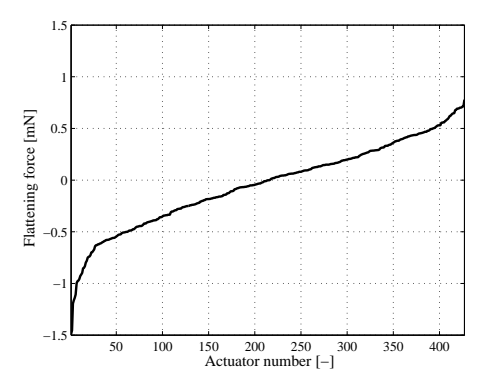


Figure 6.21: Forces required to obtain the flattened shape of the 427 struts glue experiment in Figure 3.38. Actuators are sorted on value for insight into the spread.

squares argument as:

$$\mathbf{F}_a^f = (\mathbf{T}^T \mathbf{T})^{-1} \mathbf{T}^T \hat{\mathbf{z}}_{f,a} = \mathbf{C}_a \hat{\mathbf{z}}_{f,b},$$

where the second step uses the definition of \mathbf{T} in Equation (6.10). The resulting forces \mathbf{F}_a^f are plotted in Figure 6.21. Note that these forces are independent of the influence functions and just overcome the actuator spring forces corresponding to the deflection $\hat{\mathbf{z}}_{f,b}$. Figure 3.38 shows the hypothetical unflatness that remains when fictitious, soft actuators exert the force \mathbf{F}_a^f . For this dummy mirror the residual RMS unflatness is approximately 20nm, requiring an RMS actuator force of 0.4mN. With the average values of the actuator properties K_a , R_a , R_l as measured in the previous chapter, the latter corresponds to an RMS actuator voltage of 0.17V which is approximately 5% of the available maximum voltage. In Section 3.6 this fraction was budgetted smaller then 10%.

6.3.3 Power dissipation

Based on the measured influence functions and flattening commands, the expected average power dissipation to correct atmospheric wavefront distortions, is estimated. For realistic results, a trade-off is made between power dissipation and performance in terms of fitting error. The RMS power \mathbf{P}_a , dissipated by the actuators, can be expressed in terms of the actuator voltage setpoint and the total resistance $\mathbf{R}_a + \mathbf{R}'_a + \mathbf{R}_l + \mathbf{R}'_l$ estimated in Sections 5.6.2 and 5.6.3 as:

$$\mathbf{P}_{a} = \left(\mathbf{R}_{a} + \mathbf{R}'_{a} + \mathbf{R}_{l} + \mathbf{R}'_{l}\right)^{-1} \left\langle \mathbf{V}_{PWM}^{2}(t) \right\rangle, \tag{6.11}$$

where $(\cdot)^2$ denotes the element-wise square and t the time. The actuator voltages consists of the static voltages \mathbf{V}_f required for the initial flattening of the DM and the dynamic voltages $\mathbf{V}_d(t)$ required to correct atmospheric wavefront disturbances. The value $\langle \mathbf{V}_{PWM}^2(t) \rangle$ in Equation (6.11) can be expressed accordingly as $\langle (\mathbf{V}_d(t) + V_f)^2 \rangle$. This reduces to $\langle \mathbf{V}_d^2(t) \rangle + \mathbf{V}_f^2$ when the atmospheric wavefront distortion and thus \mathbf{V}_d is a zero-mean signal that is therefore not correlated with the constant signal \mathbf{V}_f . Application of these simplifications to Equation (6.11) yields:

$$\mathbf{P}_{a} = \left(\mathbf{R}_{a} + \mathbf{R}'_{a} + \mathbf{R}_{l} + \mathbf{R}'_{l}\right)^{-1} \left(\left\langle \mathbf{V}_{d}^{2}(t)\right\rangle + \mathbf{V}_{f}^{2}\right). \tag{6.12}$$

An estimate for the vector \mathbf{V}_f with flattening voltages is obtained from the measurements described above. To quantify $\langle \mathbf{V}_d^2(t) \rangle$, consider the atmospheric wavefront disturbance to have a Von Karmann spatial spectrum (Section 2.1.2) with covariance matrix $\mathbf{C}_{\phi} = \langle \phi(t) \phi^T(t) \rangle$. Here the vector $\phi(t)$ denotes the wavefront distortion over a fine grid over the telescope aperture in radians. The matrix \mathbf{C}_{ϕ} is numerically approximated using the approach described in [96] with the modification that the Kolmogorov structure function has been replaced by the Von Karmann structure function [98] corresponding to the power spectrum given in Equation (2.5) on page 18:

$$D_{\phi}^{vk}(r) = 6.88 \left(\frac{r}{r_0}\right)^{\frac{5}{3}} \left[1 - 1.485 \left(\frac{r}{L_0}\right)^{1/3} + 5.383 \left(\frac{r}{L_0}\right)^2 - 6.381 \left(\frac{r}{L_0}\right)^{7/3}\right].$$

The resulting covariance matrix is an approximation, since the continuous spatial integrals are replaced by numerical sums over a discrete grid of points within the telescope aperture.

The incoming wavefront is corrected by reflection on the DM. Let the DM shape $\mathbf{z}_f(t)$ be expressed by Equation (6.6), based on the estimated influence matrix $\hat{\mathbf{B}}_f$. Although inertial forces are neglected, the static model accurately describes the DM facesheet deflections, since its first resonance frequency lies far above the control bandwidth. A fine grid is used to model the wavefront distortions and the DM influence functions. Hereby a realistic estimate of the fitting error and power dissipation is made. When considering the open loop controlled case, let the actuator voltages be chosen as the minimizing argument of a quadratic cost function that weights both fitting error and control effort. Let the fitting error, in meters, be expressed as:

$$\mathbf{e}_{fit}(t) = \frac{\lambda}{2\pi} \phi(t) - \hat{\mathbf{B}}_f \mathbf{V}_{PWM}(t)$$

where λ is the wavelength of the incoming light. The optimal actuator command vector $\mathbf{V}_d(t)$ is chosen as:

$$\mathbf{V}_{d}(t) = \arg\min_{\mathbf{V}_{PWM}(t)} \left\langle \left\| \mathbf{e}_{fit}(t)^{T} \mathbf{e}_{fit}(t) \right\|_{F}^{2} \right\rangle + \gamma \left\| \left\langle \left\| \mathbf{V}_{d}^{T}(t) \right\|_{F}^{2} \right\rangle$$

$$= \frac{\lambda}{2\pi} \hat{\mathbf{B}}_{f}^{+} \phi(t), \tag{6.13}$$

where $\hat{\mathbf{B}}_f^+ = (\hat{\mathbf{B}}_f^T \hat{\mathbf{B}}_f + \gamma^2 \mathbf{I}) \hat{\mathbf{B}}_f^T$ is a regularized pseudo inverse of $\hat{\mathbf{B}}_f$ and γ is a weighting factor for the control effort. For this command vector the fitting error $\mathbf{e}_{fit}(t)$ becomes:

$$\mathbf{e}_{fit} = \underbrace{\left(\mathbf{I} - \hat{\mathbf{B}}_f \hat{\mathbf{B}}_f^+\right)}_{\hat{\mathbf{B}}_f^-} \boldsymbol{\phi}(t) \tag{6.14}$$

and the command signal covariance matrix $C_{\mathbf{V}_d}$ can be expressed as:

$$\mathbf{C}_{\mathbf{V}_d} = \left\langle \mathbf{V}_d(t) \mathbf{V}_d^T(t) \right\rangle = \left(\frac{\lambda}{2\pi}\right)^2 \hat{\mathbf{B}}_f^+ \mathbf{C}_\phi \left(\hat{\mathbf{B}}_f^+\right)^T,$$

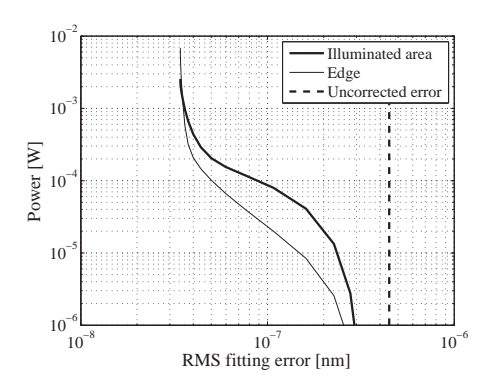
where the second step follows after substitution of Equation (6.13). The diagonal elements of the covariance matrix $\mathbf{C}_{\mathbf{V}_d}$ now form the vector $\langle \mathbf{V}_d^2 \rangle$. Similarly, using Equation (6.14) the fitting error covariance matrix \mathbf{C}_{fit} can be expressed as:

$$\mathbf{C}_{fit} = \left\langle \mathbf{e}_{fit}(t)\mathbf{e}_{fit}^{T}(t) \right\rangle = \left(\frac{\lambda}{2\pi}\right)^{2} \hat{\mathbf{B}}_{f}^{-} \mathbf{C}_{\phi} \left(\hat{\mathbf{B}}_{f}^{-}\right)^{T},$$

from which the RMS fitting error $\sigma_{fit,d}$ can be derived as:

$$\sigma_{fit,d} = \sqrt{\frac{\text{Tr}(\mathbf{C}_{fit})}{n_f}},$$

where n_f is the number of grid points used. To provide insight in the power dissipation, based on measurements on a 61 actuator prototype, several parameters must be scaled. Firstly, in Chapter 2 the number of actuators for an 8 meter telescope is 5000, which implies that for the same actuator density, the 61 actuator DM prototype should be used on a 0.9m telescope. Secondly, a continuous facesheet type DM can only prescribe the slope of the facesheet at the aperture edge if there is at least one ring of actuators outside



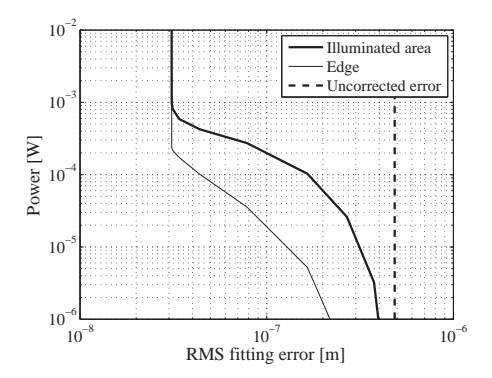


Figure 6.22: Relation between the fitting error $\sigma_{fit,d}$ and the average power dissipation per actuator based on the measured influence matrix of the 61 actuator DM prototype. Power dissipation is differentiated between actuators in- and outside the \varnothing 32mm illuminated area (λ =550nm).

Figure 6.23: Relation between the fitting error $\sigma_{fit,d}$ and the average power dissipation per actuator based on the modeled influence matrix of a 427 actuator DM. Power dissipation is differentiated between actuators in- and outside the $\varnothing 102mm$ illuminated area (λ =550nm).

Table 6.2: The expected average power dissipation in mW per actuator based on the influence function measurements for a 0.9m telescope using a $\varnothing 32$ mm illuminated area on the DM and a Von Karmann spectrum with a Fried parameter r_0 =0.16m (λ =550nm) and an outer scale L_0 =100m.

	Atmospheric	Flattening	Total
	turbulence		
Edge	1.5	23.8	25.3
Illuminated area	1.4	5.5	6.9
Full area average	1.4	14.5	15.9

the illuminated aperture. Therefore, an illuminated diameter of 32mm will be considered over which the Von Karmann spectrum is to be corrected. Actuators outside this area are only used for flattening and for prescribing the boundary conditions. By varying the control effort weighting factor γ and assuming a wavelength $\lambda=550$ nm, evaluation of Equation (6.12) yields the relation between fitting error and power dissipation shown in Figure 6.22. When a fitting error of 35nm is taken, which is 2.5% above the best achievable value, the corresponding average power dissipation of the actuators is listed in Table 6.2. A distinction is made between actuators in the illuminated area and those at the edges. Also the two causes for the dissipation – i.e. the correction of wavefront errors due to atmospheric turbulence and the correction of the initial DM unflatness – are stated separately. The dissipation for actuators in the illuminated area required for atmospheric wavefront correction is approximately 1.4mW. Although this is less than the 3.2mW estimated in Section 5.7, it depends on the chosen regularization factor γ . Further, the dissipation required for flattening is larger than the functional dissipation, due to significant

Table 6.3: The expected average power dissipation in mW per actuator based on the influence function measurements for a 2.3m telescope using a $\varnothing 102$ mm illuminated area on the DM and a Von Karmann spectrum with a Fried parameter r_0 =0.16m (λ =550nm) and an outer scale L_0 =100m.

	Atmospheric turbulence	Flattening	Total
Edge	0.2	0.4	0.6
Illuminated area	0.6	0.2	0.8
Full area average	0.4	0.2	0.6

initial unflatness of the DM, especially at the edge of the DM.

For the \emptyset 150mm dummy DM a similar table is derived based on an illuminated area of \emptyset 102mm. This corresponds to the largest diameter, which is fully filled with actuators, as can be observed in Figure 6.26. With the same actuator density as the 5000 actuator DM proposed for an 8m class telescope, this DM is suitable for a 2.3m wavefront. The forces as derived in Section 6.3.2 are assumed to be indicative of the forces required to compensate the initial unflatness of the \emptyset 150mm facesheet. Figure 6.23 shows the trade-off between performance and effort for this DM and Table 6.3 shows the estimated power dissipation for the same fitting error $\sigma_{fit,d}$ of 35nm as used for the 61 actuator DM. The table shows that both the power dissipated to correct the initial unflatness as well as the power dissipated to correct the atmospheric wavefront distortions with a Von Karman spectrum is smaller than for the 61 actuator DM. However, this only holds true for the regularization factor chosen.

6.4 Dynamic system validation

In Section 6.3 the static behavior of the DM system was validated. In this section the dynamic behavior will be added to the DM facesheet model and combined with the actuator models. The resonance frequencies, mode shapes, modal damping and transfer functions from this model will then be compared to a black-box model, identified from measurement data, using the PO-MOESP subspace identification algorithm.

6.4.1 Dynamic modeling

There is no known analytic solution available for the biharmonic plate equation for a circular plate including inertia and viscous damping terms subjected to multiple point forces. The dynamic behavior can be modeled using a FEM approach, but here it will be done by combining the derived models for the actuators and the facesheet and extending this with lumped masses and dampers.

Let the force equilibrium in Equation (6.2) be extended accordingly to:

$$\mathbf{F}_a - \mathbf{F}_\rho - \mathbf{C}_a \mathbf{z}_a - \mathbf{B}_a \dot{\mathbf{z}}_a - \mathbf{M}_{af} \ddot{\mathbf{z}}_a = 0, \tag{6.15}$$

where each (i,i) element of the diagonal matrices \mathbf{B}_a and \mathbf{M}_{af} are the viscous actuator damping b_a and the sum of the lumped facesheet mass and the moving actuator mass at coordinate ρ_i respectively. Note that for simplicity it is assumed that the actuator and lumped mass/damper locations coincide, but this can be generalized by using an arbitrary grid and appropriately attributing mass, stiffness and damping values. The mass distribution chosen leads to adequate approximations of the mode shapes with spatial frequencies significantly below the Nyquist frequency of the actuator grid, which corresponds to the lower eigenfrequencies. These are the most relevant for the achievable correction quality, since they pose the tightest limit on the achievable control bandwidth. Moreover, the stiffness matrix used corresponds to the solution of the biharmonic plate equation under the assumption of pure bending. For high spatial frequencies, shear forces become dominant and this assumption loses its validity.

When the result in Equation (6.3) for \mathbf{F}_{ρ} is substituted into Equation (6.15) and transformed to the Laplace domain this yields the dynamic system:

$$\left(\mathbf{C}_{af} + \mathbf{B}_{a}s + \mathbf{M}_{af}s^{2}\right)\mathbf{z}_{a} = \mathbf{F}_{a},\tag{6.16}$$

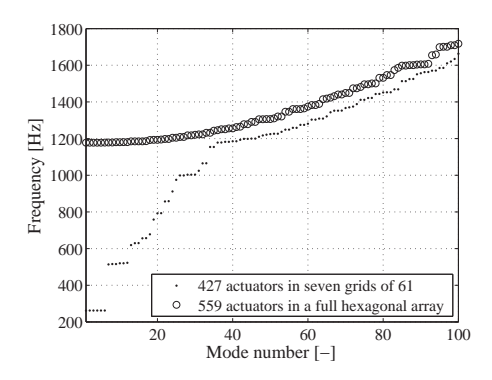
where $\mathbf{C}_{af} = \mathbf{K}_m + \mathbf{C}_a$. The undamped mechanical eigenfrequencies $f_{e,(i)}$ and mode shapes $\mathbf{x}_{(i)}$ for $i = 1 \dots N_a$ can be obtained by solving the generalized eigenvalue problem:

$$\left(\mathbf{C}_{af} - \lambda_{(i)}\mathbf{M}_{af}\right)\mathbf{x}_{(i)} = 0,$$

where
$$f_{e,(i)} = \sqrt{\lambda_{(i)}}/2/\pi$$
.

This procedure has been performed for two different cases. Firstly for a DM with regularly placed actuators with 6mm pitch in a hexagonal pattern. Equal lumped masses were added at all actuator grid points and all actuator and facesheet properties were used as given in Tables 4.1, 5.2 and 6.1. The first 100 resonance frequencies for this model are plotted as circles in Figure 6.24 and the first twelve resonance modes are shown in Figure 6.25. From Figure 6.24 it is clear that the first resonance modes occur in a small frequency band and from Figure 6.25 it is clear that the modal shapes correspond very well to the Zernike polynomials [141]. Traditionally, these polynomials are used to describe both the aberrations in the optical domain as well as the dynamic modes of the wavefront corrector in the mechanical domain.

However, the resonance frequencies and corresponding modal shapes are influenced by the edge conditions of the reflective facesheet. When considering the 427 actuator DM prototype that consists of seven hexagonal actuator modules, observe that the gaps between the hexagons at the outside have no actuators that support the mirror facesheet. In the dynamic model in Equation (6.16) leads to 'zero' elements on the diagonals of the matrices C_a and B_a and to lower values of the corresponding diagonal elements in M_{af} due to the absence of moving actuator masses. The lack of support stiffness in the edge areas leads to lower resonance frequencies with local mode shapes. To properly attribute lumped mass fractions of the facesheet to grid points in edge areas, its mass is distributed based on the Voronoi diagram of the grid points (Figure 6.26). The Voronoi diagram is the dual of the Delaunay grid triangulation [131, 168] that is frequently used to draw a surface defined at arbitrary grid of points. The Voronoi diagram creates a polygon area around each grid point in which all points are closest to that particular grid point. For most grid points this yields a closed polygon, but for edge points this is open towards the edge. The polygon area determines the



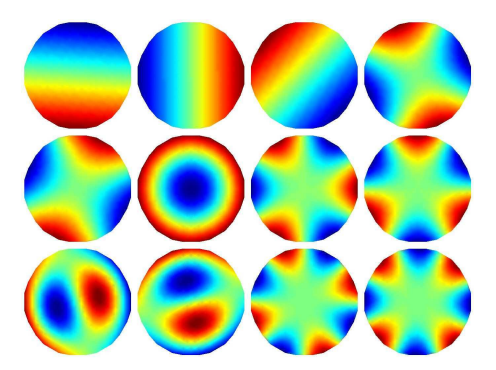


Figure 6.24: The lowest 100 undamped mechanical resonance frequencies.

Figure 6.25: The lowest 12 undamped mechanical resonance modes corresponding to the frequencies plotted as circles in Figure 6.24.

lumped fraction of the facesheet mass and can for closed polygons be computed using Matlab's polyarea function [131]. The open edge polygons are first extended with two points on the circular facesheet edge by which the polygon is closed. The total area is then the sum of the area of the artificially closed polygon and the area between these two points and the circle, which follows from the distance between the two additional edge points. Since all areas can be calculated analytically, no approximations are made and the summed area for all grid points exactly equals πr_f^2 . For the 427 actuator DM prototype the result is plotted in Figure 6.26.

The lowest 100 eigenfrequencies for this case are plotted in Figure 6.24 as the solid dots. The first resonance frequencies are lower than in the homogenously supported case and the corresponding modal shapes are local bending modes of the unsupported edge areas. Clearly, the actuator layout of future DMs should be chosen such that the facesheet edges are uniformly supported.

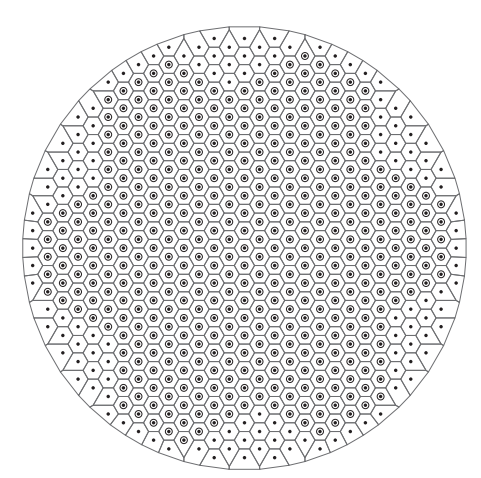
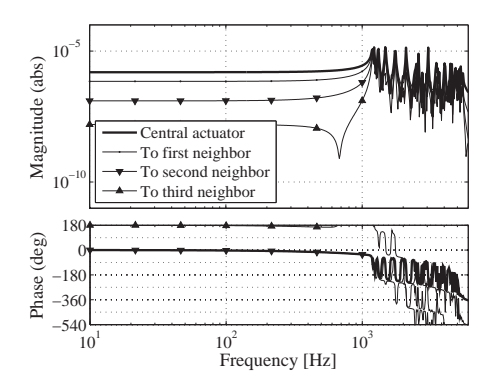


Figure 6.26: Voronoi diagram for the hexagonally arranged grid points marked with a small dot. The actuator grid of the 427 actuator DM prototype is marked with "o".



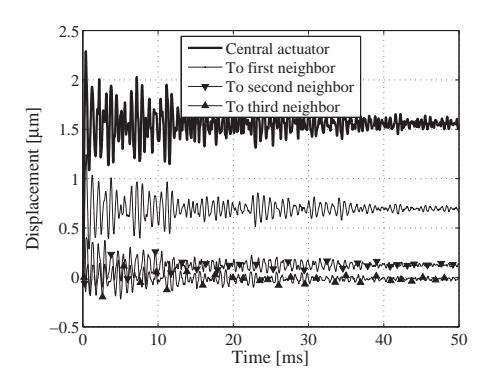


Figure 6.27: Bode plots from the PWM voltage of the central actuator to the position of itself and three neighbors.

Figure 6.28: Step response from the PWM voltage of the central actuator to the position of itself and three neighbors.

Although the mechanics largely determine the behavior of the DM in terms of resonance frequencies, the electronics influence the damping, response time, gain, etc. Therefore, the state-space description for the single actuator behavior in Equation (5.4) on page 131 is extended to describe the behavior of multiple actuators and combined with the mechanical equations of motion in Equation (6.15). The scalar states I_{R_l} , I_a , V_{C_l} , z_a and \dot{z}_a become the vectors \mathbf{I}_{R_l} , \mathbf{I}_a , \mathbf{V}_{C_l} , \mathbf{z}_a and $\dot{\mathbf{z}}_a$ whose i^{th} elements contain the corresponding states of the i^{th} actuator. Similarly, the scalar parameters K_a , R_a , R_l , L_a , L_l and C_l for each actuator i become the (i,i) diagonal elements of the square diagonal matrices \mathbf{K}_a , \mathbf{R}_a , \mathbf{R}_l , \mathbf{L}_a , \mathbf{L}_l and \mathbf{C}_l respectively. Further, instead of the mechanical equation of motion for the single, uncoupled actuator in Equation (4.25), the dynamic equation in Equation (6.16) will be used, leading to:

$$\begin{bmatrix} \mathbf{I}_{a} \\ \dot{\mathbf{z}}_{f} \\ \dot{\mathbf{z}}_{f} \\ \dot{\mathbf{V}}_{a} \\ \dot{\mathbf{I}}_{R_{l}} \end{bmatrix} = \underbrace{\begin{bmatrix} -\mathbf{L}_{a}^{-1}\mathbf{R}_{a} & \mathbf{0} & -\mathbf{L}_{a}^{-1}\mathbf{K}_{a} & \mathbf{L}_{a}^{-1} & \mathbf{0} \\ \mathbf{0} & \mathbf{0} & \mathbf{I} & \mathbf{0} & \mathbf{0} \\ \mathbf{M}_{af}^{-1}\mathbf{K}_{a} - \mathbf{M}_{af}^{-1}\mathbf{C}_{af} - \mathbf{M}_{af}^{-1}\mathbf{B}_{a} & \mathbf{0} & \mathbf{0} \\ -\mathbf{C}_{l}^{-1} & \mathbf{0} & \mathbf{0} & \mathbf{0} & \mathbf{C}_{l}^{-1} \\ \mathbf{0} & \mathbf{0} & \mathbf{0} - \mathbf{L}_{l}^{-1} - \mathbf{L}_{l}^{-1}\mathbf{R}_{l} \end{bmatrix} \underbrace{\begin{bmatrix} \mathbf{I}_{a} \\ \mathbf{z}_{f} \\ \dot{\mathbf{z}}_{f} \\ \mathbf{V}_{a} \\ \mathbf{I}_{R_{l}} \end{bmatrix}}_{\mathbf{B}_{fm}} + \underbrace{\begin{bmatrix} \mathbf{0} \\ \mathbf{0} \\ \mathbf{0} \\ \mathbf{L}_{l}^{-1} \end{bmatrix}}_{\mathbf{B}_{fm}} \mathbf{V}_{PWM}$$

$$(6.17)$$

The transfer matrix $\mathbf{H}(s)$ between the PWM voltage \mathbf{V}_{PWM} and the facesheet deflection \mathbf{z}_f can be expressed accordingly as:

$$\mathbf{H}(s) = \begin{bmatrix} \mathbf{0} & \mathbf{I} & \mathbf{0} & \mathbf{0} & \mathbf{0} \end{bmatrix} (s\mathbf{I} - \mathbf{A}_{fm})^{-1} \mathbf{B}_{fm}^T.$$

The DC-gain of this transfer matrix is equal to Equation (6.6) and can be derived by evaluating $\mathbf{H}(s)$ for s=0:

$$\mathbf{H}(0) = -\begin{bmatrix} \mathbf{0} & \mathbf{I} & \mathbf{0} & \mathbf{0} \end{bmatrix} \mathbf{A}_{fm}^{-1} \mathbf{B}_{fm}^{T} = \mathbf{C}_{af}^{-1} \mathbf{K}_{t} (\mathbf{R}_{a} + \mathbf{R}_{l})^{-1} = \mathbf{B}_{\rho},$$
 (6.18)

where A_{fm} and B_{fm} are defined in Equation (6.17) and the final expression follows from the definition of B_{ρ} in Equation (6.6).

The model in Equation (6.17) has been generated numerically for a $\varnothing 150$ mm reflective facesheet that is regularly supported by 6mm spaced actuators over its entire area. The actuator, electronics and facesheet properties used are given in Tables 4.1, 5.2 and 6.1. In Figure 6.27 Bode plots are shown of the entries of the transfer matrix corresponding to the PWM voltage of the central actuator and the position of itself and three neighbors at 6, 12 and 18mm distance. It shows that the static DC response to neighboring actuator positions indeed decays rapidly with the spatial distance, but that the global shapes of the lightly damped, lowest dynamic modes (Figure 6.25) lead to a strong coupling between the actuators at high frequencies. To illustrate this low damping, Figure 6.28 shows the step response of the same actuators due to a step input at the PWM voltage of the central actuator. In practise the damping will be higher due to the presence of air above the facesheet, intrinsic damping of the facesheet and strut materials, deformation of the glue between the struts and the facesheet, etc. To quantify this effect, the relative damping of the resonant modes of this model will be compared to the damping derived from a modal analysis in Section 6.4.3.

6.4.2 System identification

Modal (or structural) analysis is frequently performed using the Eigensystem Realization Algorithms (ERAs) [9, 63] and its variants [120]. The ERAs are a subspace based identification methods that estimate a state space by taking the Singular Value Decomposition (SVD) of a Hankel matrix of the system's impulse response function. This impulse response function is either measured directly from impulse excitation or estimated from more generic input-output data. For open loop measurement data of MIMO systems the MOESP algorithm [191] and its variants [194] are very suitable. For closed loop identifications the Predictor Based Subspace IDentification (PBSID) identification algorithm [35, 37] can be used, which has been applied for the identification of a DM with 60 actuators and 104 sensors of the MAD (Multi-conjugate Adaptive-optics Demonstrator) system in [36]. However, the DM can here be identified in open loop, making the added complexity of the PBSID algorithm superfluous. Besides subspace based identification algorithms that use state-space parameterizations, other algorithms can be used for MIMO system identifications with other parameterizations. For instance, in [177] a MIMO Transfer Function (TF) parametrization is shown to be very efficient in both the number of parameters and the required computational effort, when compared to subspace algorithms. The identification algorithm used for modal analysis of the DM prototype is chosen based on several requirements. It must be able to deal with 61 simultaneous inputs and at least as many outputs. Since the sampling frequency of the setup used is limited to 10kHz, the dynamics of the electronics that become dominant above 5kHz will not be well observable from the measurement data. Although the DM facesheet dynamics are of infinite order, the low frequent resonance modes can be adequately described using a limited number of lumped masses. This means that the system order required for identification is at least twice the number of lumped masses, which in this case is in the order of hundreds. It also means that the model parametrization used must allow the large number of poles and zeros to be independent to properly describe the numerous resonance modes of the DM facesheet. The poles will be used after the identification step to compute the resonance frequencies, their relative damping and the modal shapes.

Since for identification of a state-space model a high state dimension and large numbers of in- and outputs are required, the identification algorithm used must be efficient w.r.t. both memory and computation steps. Moreover, the method must be suitable for the available measurement setup, which is the same as used previously to identify the behavior of single actuators and depicted in Figure 5.11. In this setup, the deflection of the DM facesheet can be measured only at a single point at a time with a Polytec laservibrometer. The obtained measurement data is thus expected to be significantly corrupted both by measurement and process noise, since the measurements are performed in a noisy environment without vibration isolation facilities. The identification algorithm must be robust for these types of noise. On the other hand, since all quantization is performed in the control PC in an open loop setting there is no quantization noise.

Identification using the MOESP algorithm

The MOESP algorithm is a subspace identification algorithm that uses a QR decomposition [76] of the input-output data matrix to compress the data and thus improve the computational efficiency. The algorithm and its variants are found in literature [192–194] and Matlab implementations are readily available. Since the identification is subject to both measurement and process noise, the PO-MOESP algorithm will be used, which uses past inputs and outputs as instrumental variables to provide unbiased estimates w.r.t. measurement and process noise. Since in literature this variant of the algorithm is generally intended when referring to MOESP, the prefix PO- will here also be neglected.

Details on the theory and implementation of the MOESP identification method used on this DM are found in [183].

The quality of the obtained system is evaluated by applying the estimated system realization to a validation data sequence and computing the VAF, defined as:

$$extit{VAF} = \left[1 - rac{\left\langle \left(\hat{\mathbf{z}}_f(t) - ilde{\mathbf{z}}_f(t)
ight)^T \left(\hat{\mathbf{z}}_f(t) - ilde{\mathbf{z}}_m(t)
ight)
ight
angle_{t_0}^N}{\left\langle \hat{\mathbf{z}}_f^T(t)\hat{\mathbf{z}}_f(t)
ight
angle_{t_0}^N}
ight] \cdot 100\%,$$

where $\tilde{\mathbf{z}}_f(t)$ is obtained by simulating the identified model for the known excitation signal $\mathbf{V}_{PWM}(t)$ and $\hat{\mathbf{z}}_f(t)$ is the vector of facesheet deflections measured by the laser vibrometer. The VAF represents the fraction of the signal variance that is accounted for by the model and should be close to 100%.

6.4.3 Modal analysis

The modal analysis of the identified system begins with a modal decomposition of its A-matrix. This decomposition is such that $\Lambda \hat{A} = M \hat{A}$, where the diagonal matrix Λ contains the (complex) eigenvalues of \hat{A} and the columns of M contain the (complex) eigenvectors. The matrix M forms a state transform matrix that diagonalizes the system and yields a state-space description with state $\mathbf{x}(t)$ whose state transition matrix is equal to Λ :

$$\begin{cases} \tilde{\mathbf{x}}(t+1) &= \mathbf{\Lambda}\tilde{\mathbf{x}}(t) + \mathbf{M}^{-1}\mathbf{B}\mathbf{u}(t), \\ \mathbf{z}_f(t) &= \mathbf{C}\mathbf{M}\tilde{\mathbf{x}}(t), \end{cases}$$

where the influence of process and measurement noise is neglected. For the discrete time system, each eigenvalue $\lambda_{(i)}$ on the diagonal of Λ is related to the resonance frequency $\omega_{n,(i)}$ and relative damping $\zeta_{(i)}$ of mode i as [64]:

$$\lambda_{(i)} = e^{T_s \left(-\zeta_{(i)}\omega_{n,(i)} \pm j\omega_{n,(i)} \sqrt{1-\zeta_{(i)}^2}\right)} = |\lambda_{(i)}| \cdot \angle \lambda_{(i)},$$

where T_s is the sampling frequency and

$$|\lambda| = e^{-T_s \zeta_{(i)} \omega_{n,(i)}}, \qquad \qquad \angle \lambda = e^{\pm T_s j \omega_{n,(i)} \sqrt{1 - \zeta_{(i)}^2}}.$$

Inversely, the resonance frequencies $\omega_{n,(i)}$ and damping ratio's $\zeta_{(i)}$ can be computed as:

$$\omega_{n,(i)} = \frac{\ln \angle \lambda - \ln |\lambda|}{T_s} \qquad \text{and} \qquad \zeta_{(i)} = -\frac{\ln |\lambda|}{\ln |\lambda| - \ln \angle \lambda}.$$

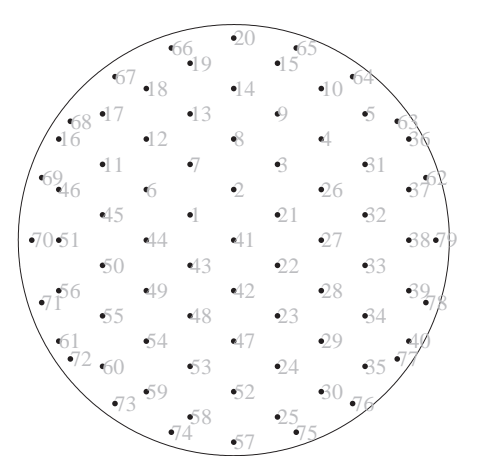
Further, the vectors of the matrix CM form the facesheet shapes corresponding to the system's eigenfrequencies. Since complex poles occur in conjugate pairs (a, b) with the same modal frequency $\omega_{n,a} = \omega_{n,b}$, the matrix's complex part and columns corresponding to complex conjugate eigenvalues will for the modal analysis be ignored.

Results

For the 61 actuator DM prototype, the facesheet response is measured on the 79 points shown in Figure 6.29. These are the 61 actuator locations and 18 points on the facesheet along its edge. The signal acquisition and DM setpoint update rate is chosen as high as possible to minimize the effects of sampling and aliasing. The 10kHz sampling frequency used, is close to the upper limit of the serial communication chain but still significantly lower than the PWM actuator voltage base frequency. The laser vibrometer is pointed at each grid location for 10 seconds, producing 100.000 measurements. A zero-mean, bandlimited, white noise sequence $\mathbf{V}_{PWM}(t) \in \mathcal{N}(\mathbf{0}, \sigma_e^2 \mathbf{I})$ is generated with $\sigma_e = 0.13\mathbf{V}$ and $t = 0...10\mathbf{s}$ and applied on each location. Except for small variations in initial conditions and timing (i.e. jitter), the obtained data is equal to the data that would have been obtained when the response of all points is measured simultaneously.

The obtained measurement data set is split into an identification set of 85.000 samples and

Figure 6.29: The grid of points at which the response of the 61 actuator DM prototype was measured. Points 1...61 correspond to the actuator locations.



a validation set of 15.000. The MOESP system identification method is applied to the first part of this input-output data and the VAF value is computed after simulation on the second part. The VAF found is 95%. Figures 6.30 and 6.31 show the first 12 resonance frequencies and the corresponding modal shapes derived from the analytic model in Equation (6.17) and the black-box model identified with the MOESP algorithm. For the modal analysis of the analytic model, the average measured actuator properties listed in Table 5.3 are used. When all actuators have equal properties, the modal shapes show a high degree of symmetry (Figure 6.30). In practice the actuator properties vary, leading to the asymmetric mode shapes in Figure 6.31. The lowest resonance mode of the system lies at ~725Hz and corresponds to a motion of the lower-left edge area of the facesheet.

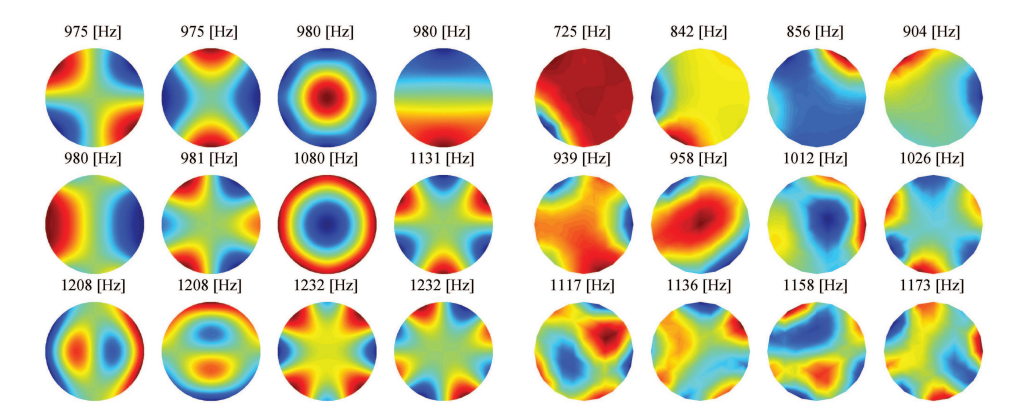
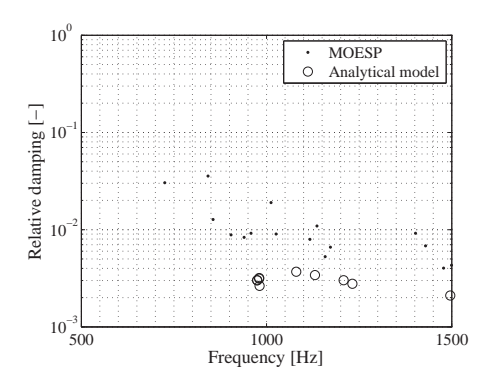


Figure 6.30: The first 12 modal shapes derived from the analytic model in Equation (6.17) using the average actuator properties listed in Table 5.3 and the facesheet properties listed in Table 6.1.

Figure 6.31: The first 12 modal shapes derived with the MOESP system identification method.



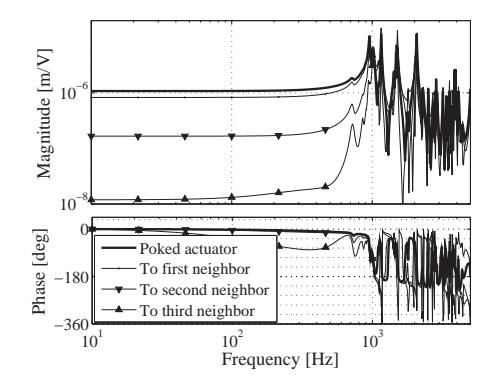


Figure 6.32: Relative damping ζ corresponding to the eigenfrequencies of the models identified with the MOESP algorithm and of the analytical model from Equation (6.17).

Figure 6.33: Bode plot of the model identified with the MOESP algorithm between the command voltage at actuator 2 and its first, second and third neighboring actuators 41, 42 and 47 respectively.

This frequency is lower than expected. Since the edges are supported by a few actuators, the low resonance may be caused by a lower stiffness c_a of only a few actuators. The relative damping ζ identified with the MOESP algorithm and in the analytical model from Equation (6.17), based on the average actuator properties listed in Table 5.3, are shown in Figure 6.32. The relative damping in the analytical model is significantly lower than in the black-box model, which means that the damping observed in the DM system is not entirely due to the actuators. This suggests the presence of other dissipative processes such as material damping, damping in the glue used or damping due to the movement of air above the facesheet. The latter is a likely explanation, since the facesheet vibrations due to the noise excitations used were clearly audible.

A Bode plot of the identified model is shown in Figure 6.33 for the transfer functions

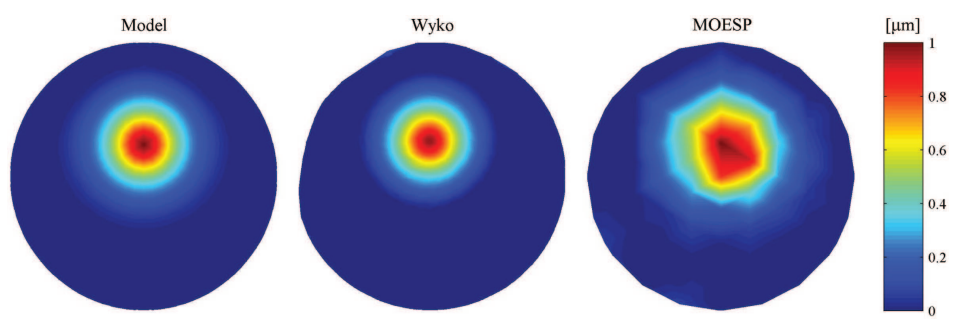
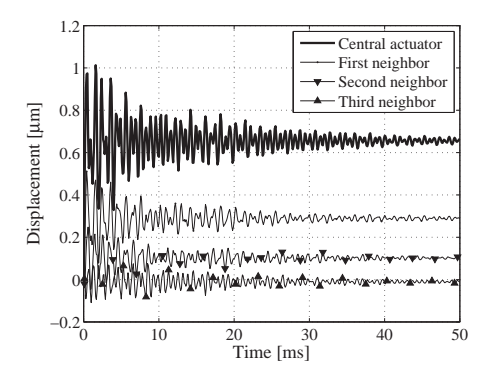
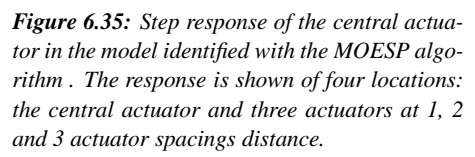


Figure 6.34: The influence function of actuator 2 (Figure 6.29) as derived from the analytical model (left), from the Wyko measurements of Section 6.3.2 (middle) and from the model identified using MOESP (right).





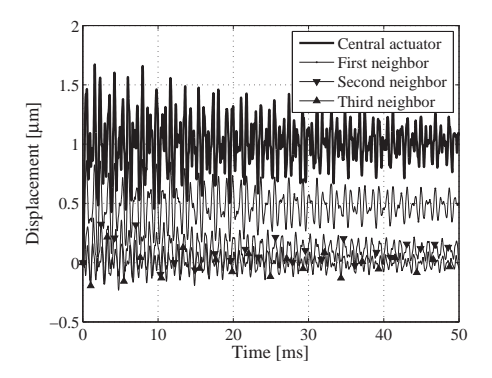


Figure 6.36: Step response of the central actuator of the analytical model in Equation (6.17), using the average actuator parameters listed in Table 5.3. The response is shown of four locations: the central actuator and three actuators at 1, 2 and 3 actuator spacings distance.

from the actuator voltage at actuator 2 to the displacement at its first, second and third neighboring actuators 41, 42 and 47. This shows the high peaks in the magnitude response as a result of the low relative damping. However, where the magnitude of the peaks does not decrease with frequency in the Bode plot of the analytical model in Figure 6.27, they do in the model as identified, which suggests the presence of additional dissipative processes at high frequencies.

Further, the influence functions have been derived from the model identified by computing the DC gain matrix of the system according to Equation (6.18) as $\hat{\mathbf{C}}(\mathbf{I}-\hat{\mathbf{A}})^{-1}\hat{\mathbf{B}}$ whose columns contain the influence functions. The influence function of actuator 2 is shown in Figure 6.34 together with the influence functions of the same actuator derived from the analytic model and the Wyko measurements of Section 6.3.2. The shape and magnitude match qualitatively, but some quantitative error can be observed.

This is partly due to the poor alignment accuracy of the laser vibrometer spot.

Finally, the step response functions derived from the model from the central actuator voltage setpoint to the displacement of four points on the reflective surface are shown in Figure 6.35. The four points are the location of the actuator itself and that of three neighbors with 1, 2 and 3 actuator spacings distance. In Figure 6.36, the corresponding step response derived from the analytical model is shown for the same actuators. A comparison with Figure 6.35 confirms that in the analytical model of the 61 actuator DM damping is underestimated.

6.5 Conclusions 179

6.5 Conclusions

The assembly of two DMs prototypes is shown: a \emptyset 50mm DM with 61 actuators and a \emptyset 150mm DM with 427 actuators. In the first prototype a single actuator grid is used, whereas for the second prototype modularity is shown by the assembly of seven identical grids on a common base. The seven actuator grids, with accompanying dedicated driver boards, are attached to a single, continuous, facesheet.

The actuator model derived in the Chapter 5 is extended with a linear model of the continuous facesheet, based on an analytic solution of the biharmonic plate equation and point forces. Lumped masses are added to obtain the dynamic behavior. Both static and dynamic performance is validated on the Ø50mm DM using measurements. Scaled Hadamard matrices for the actuator voltage command vectors are used to measure the 61 influence functions in front of a Wyko interferometer. This approach minimizes the variance estimation errors of the influence matrix due to measurement noise.

The measured actuator coupling of the central actuators is 52% and close to the 65% from the estimate in Section 3.4 and the predicted value from the static model in Section 6.3.2. In the estimate, only the six surrounding actuators were included, thereby neglecting the stiffness contribution of other actuators and leading to an over-estimation of the coupling. In the static model from Section 6.3.2 these were included and the prediction close to the measurements.

The measured shape and amplitude of the influence functions agree with the prediction with the static model (Figures 6.18 and 6.19). This includes the increased static gain (m/V) of the actuators at the edge of the DM due to the reduced facesheet stiffness from the mirror's free-edge boundary condition. The variation in the static gain is observed and attributed to variation in motor constant, actuator stiffness and electrical resistance and driver circuits.

The influence matrix derived from the measurements is used to shape the mirror facesheet into the first 28 Zernike modes, which includes the piston term that represents the best flat mirror. The interferometrically measured shapes are compared to the perfect Zernike modes and to the Zernike modes as made with the limited number of regularly spaced actuators in the actuator grid. The total RMS error is \approx 25nm for all modes, whereas the inevitable fitting error varies between 0 and 23nm depending on the mode.

The power dissipation in each actuator of the $\varnothing 50 \mathrm{mm}$ mirror to correct the Von Karman turbulence spectrum ($D/r_0=5.4$, $L_0=100 \mathrm{m}$) is estimated. Actuators outside the illuminated area are distinguished from those inside this area. Furthermore, the estimated power dissipation is split into turbulence correction and mirror flattening. For the turbulence correction, 1.5mW for the outer and 1.4mW for the inner actuators, is dissipated. For static flattening these values are 23.8mW and 5.5mW respectively.

The 427 actuator DM prototype was broken during placement of its protective cover, therefor it was not possible to measure its unflatness, static or dynamic behavior. A dummy mirror (Figure 3.35) with similar facesheet specifications, which was used to test the assembly procedure of the 427 connection struts, was interferometrically measured instead. This mirror showed $\approx\!4.5\mu m$ PTV unflatness. This mirror was fictitiously flattened, with the use of the modeled influence matrix and requires 0.17V RMS actuator voltage, which corresponds to 5% of the available output voltage range and a power dissipation of 0.2mW per actuator.

The predicted dynamic behavior of the DM is validated by measurements. A laser vibrometer is used to measure the displacement of the mirror facesheet, while the actuators are driven by zero-mean, bandlimited, white noise voltage sequence. Using the MOESP system identification algorithm, high-order black-box models are identified with VAF values around 95%. This identified model is compared with the derived analytical model. The latter uses the average actuator properties as measured in Chapter 5. The first resonance frequency identified is 725Hz, and lower than the 974Hz expected from the analytical model. This is attributed to the variations in actuator properties, such as actuator stiffness.

The relative modal damping of the model identified is an order of magnitude higher than the damping in the analytical model, where only actuator damping is considered. The difference is attributed to the presence air damping and damping in the glue used for the connection struts.

Chapter seven

Conclusions

In the previous chapters the design, realization and test of the adaptive deformable mirror based on electromagnetic actuators is shown. This chapter will summarize the main conclusions from these chapters and outline the subjects of future work. 182 7 Conclusions

7.1 Conclusions

Refractive index variations in the earth's atmosphere limit the resolution in ground based telescopes. Existing large and future even larger telescopes can only be utilized fully, when they are equipped with AO systems that enhance optical resolution. The development of DM technology that meets the requirements for these future AO systems is essential.

The requirements for the adaptive deformable mirror and control system are derived from typical atmospheric conditions (r_0 =0.166 (λ =550nm) and f_G =25Hz). The spatial and temporal properties of the atmosphere are hereby covered by the spatial and temporal spectra of Kolmogorov turbulence and the frozen flow assumption. The fitting error, caused by a limited number of actuators and the temporal error, caused by a limited control bandwidth, are the most important for the DM design. \approx 5000 actuators and 200Hz bandwidth form a balanced choice for the number of actuators and the control bandwidth and can correct an 8m wavefront in the visible to nearly diffraction limited. An actuator stroke of \approx 5.6 μ m and \approx 0.36 μ m inter actuator stroke is needed. Together with the nm's resolution, low power dissipation, no hysteresis and drift, form these the main actuator requirements.

The design, realization and tests of a new DM that meets these requirements and is extendable and scalable in mechanics, electronics and control is presented.

The DM design

In the DM design a few layers are distinguished: the mirror facesheet, the actuator grid and the base frame. The first layer is the thin reflective facesheet, which is the deformable element. The facesheet is continuous and stretches over the full aperture. In the underlying layer - the actuator grid - low voltage electro-magnetic push-pull actuators are located. The actuator grid consists of a number of identical actuator modules, each with 61 actuators. Each actuator is connected via a strut to the mirror facesheet. The mirror facesheet, the mirror-actuator connection and the actuator modules form a thin structure with low out-of-plane stiffness, so a third layer is added, the base frame, to provide a stable and stiff reference plane for the actuators.

The mirror facesheet

A thin facesheet is needed for low actuator forces and power dissipation, whereby its lower limit is set by the inter actuator deflection. This deflection is determined by gravity or, if present, by wind pressure. For both situations the scaling laws for the total actuator force F and power dissipation P are derived, depending on the size of the uncompressed wavefront D_t , the compression factor c_D , which is the ratio between the uncompressed wavefront and the DM that performs the correction, the number of actuators and the thickness of the facesheet. If no significant wind pressure is present (v<1m/s), and the telescope's optical design and desired optical quality is fixed, the power dissipation is minimized by selecting a facesheet material with high $\frac{E_f}{\rho_f^2}$. When significant wind pressure p_w is present, the total

actuator force is $F \propto \left(\frac{D_t}{c_D}\right)^2 p_w$. F and P are then independent of the facesheet material

7.1 Conclusions 183

properties and the number of actuators.

Here only gravity induced deflection is taken into account. Minimum power dissipation is achieved when beryllium is used for the mirror facesheet. With 35 μ m facesheet thickness and an actuator grid with 6mm pitch, 1nm RMS inter actuator deflection is present. Since thin beryllium facesheets are expensive and several are needed for the prototype developments, Pyrex facesheets with 100 μ m thickness are chosen as a best practical, alternative. Struts connect the facesheet to the actuators. The connection struts allow the mirror facesheet to form a smooth surface over the imposed heights. The diameter and length of the struts are determined by taken into account its bending stiffness, axial stiffness, resonance frequency and buckling load. A round stainless steel strut with \emptyset 0.1×8mm is selected. During assembly, the facesheet is supported by a porous graphite air bearing. First the struts are glued to the facesheet, hereby supported by a tool. In the second step, the facesheet with struts is placed in droplets of glue at the actuator side. The flatness of a \emptyset 150mm facesheet with 427 struts attached, is measured and 4μ m PTV, which is in the same order of the unflattness of the air bearing reference surface. Interferometric measurements show a local 3nm RMS surface unflattness around the glued attachment.

The stiffnesses of the actuators form the out-of-plane constraints for the mirror facesheet and determine the mirrors first resonance frequency f_e . When the actuator stiffness c_a is smaller than the bending stiffness of the facesheet between two actuators, f_e is well approximated with $=\frac{1}{2\pi}\sqrt{\frac{c_a}{m_{a_f}}}$, where m_{a_f} is the total mass of the facesheet divided by the number of actuators carrying the facesheet. The first resonance is then independent of the mirror diameter and the mode shape is a global bending of the mirror. When c_a is further increased, local modes appear and higher stiffness will not increase the resonance frequency.

Actuators

The application of electromagnetic actuators for adaptive deformable mirrors has several advantages. Electromagnetic actuators can be designed with a limited stiffness, such that failure of an actuator will not cause a hard point in the reflective surface and thus a small optical degradation compared to e.g. stiff piezo-electric elements exists. Other advantages are the low costs, low driving voltages and negligible hysteresis and drift. Reluctance type actuators are chosen because of their high efficiency and low moving mass. The actuators consist of a closed magnetic circuit in which a PM provides static magnetic force on a ferromagnetic core, which is suspended in a membrane. This attraction force is influenced by a current through a coil, which is situated around the PM to provide movement of the core. With the direction of the current the attractive force of the PM is either increased or decreased, allowing movement in both directions. The actuators are free from mechanical hysteresis, friction and play and therefore have a high positioning resolution with high reproducibility. The stiffness of the actuator is determined by the membrane suspension and the magnetic circuit. There exists a large design freedom for both. Actuators are realized in modules of 61 actuators, hexagonally arranged with 6mm pitch. The hexagonal actuator layout is chosen since this gives the highest actuator areal density. The grids are design in layers. This reduces the number of parts and the complexity of assembly and improves the uniformity of the actuator properties. The grids are given a hexagonal contour to accommodate the assembly of large DMs from many actuator modules.

184 7 Conclusions

Electronics

The electronics consist of two parts: the communication electronics that supply the setpoints as computed by the control system and the driver electronics that generate the corresponding actuator voltages. Since the L_a/R_a time of the actuator is short: 75 μ s, the advantage of current control over voltage control is limited. The motor constant K_a , stiffness c_a and – in the case of a voltage source – the resistance R of the actuator circuit, will vary from actuator to actuator and vary with temperature, causing slow gain variations. A current source will compensate for variations in the resistance R, but variations of K_a and c_a must still be compensated by the AO control system. PWM based voltage drivers are chosen because of their high efficiency and capability to be implemented in large numbers with only a few electronic components. A LVDS based serial communication is chosen for its low power consumption (15mW/transceiver), high bandwidth (up to 655Mb/s) and consequently low latency, low communication overhead and extensive possibilities for customization. The driver electronics for 61 actuators are located on a single, multi-layer PCB and consist of FPGAs to generate the PWM signals, FETs for the H-bridge switches and coil/capacitor pairs that form 2^{nd} order low-pass filters. A flat-cable connects up to 32 electronics modules to a custom designed communications bridge, which translates ethernet packages into LVDS packages and vice versa. The ethernet side of the communications bridge is connected to the control computer at a speed of 100Mbit/s and uses the UDP protocol to minimize overhead and latency.

Results

Two DMs prototypes were successfully assembled: a \emptyset 50mm DM with 61 actuators and a \emptyset 150mm DM with 427 actuators. In the first prototype a single actuator grid is used, whereas for the second prototype modularity is shown by the assembly of seven identical modules on a common base. All actuators are attached to a single, continuous, facesheet.

Actuator and electronics performance

The dynamic performance of each actuator is measured, including its dedicated driver and communication electronics. All actuators were found to be functional, indicating that the manufacturing and assembly process is reliable. A nonlinear model of the actuator was derived describing both its static and dynamic behavior based on equations from the magnetic, mechanic and electric domains. The nonlinear spring force characteristic of the membrane suspension was modeled and verified via measurements in a dedicated measurement setup. The communication is modeled as a pure delay and the driver electronics as a voltage source with an analog 2^{nd} order low-pass filter. The actuator model was linearized, leading to expressions for the actuator transfer function and linear electromechanical properties such as motor constant, coil inductance, actuator stiffness and resonance frequency. The actuator model including its communication and driver electronics was validated by measurements. The measurements include communication tests, static and dynamic response measurements and power dissipation measurements. It is shown that the commu-

7.1 Conclusions 185

nication latency is well represented by $\tau_c=89.7\cdot 10^{-6}+39\cdot 10^{-6}N_m$, where N_m is the number of the actuator module. With the frequency response measurements, actuator properties as stiffness ($c_a=473\pm46\mathrm{N/m}$), motor constant ($K_a=0.11\pm0.02\mathrm{N/A}$), damping ($b_a=0.30\pm0.11\mathrm{mNs/m}$), inductance($L_a=3.0\pm0.2\mathrm{mH}$) and resonance frequency ($f_e=1.83\pm91\mathrm{Hz}$) are verified. These properties showed some variation between actuators, but this could not be attributed to the location of the actuator in the grid.

The time domain response of an actuator to a 4Hz sine voltage was used to determine hysteresis and semi-static nonlinear response of the actuator. This showed the first to be negligible and the second to remain below 5% for the intended $\pm 10 \mu m$ stroke.

Measurements also showed that in the expected operating range, the total power dissipation is dominated by indirect losses in the FPGAs. An alternative FPGA implementation is investigated. A reduction of 40% in the master FPGA and 29% in the slave FPGAs is thereby achieved.

Static DM performance

The actuator model is extended with a linear model of the continuous facesheet, based on an analytic solution of the biharmonic plate equation and point forces. The static performance is validated on the $\varnothing 50$ mm DM using interferometric measurements. Scaled Hadamard matrices for the actuator voltage command vectors are used to measure the 61 influence functions. This approach minimizes the variance estimation errors of the influence matrix due to measurement noise. The measured shape and amplitude of the influence functions agree with the prediction from the static model. This includes the increased static gain (m/V) of the actuators at the edge of the DM due to the reduced facesheet stiffness from the mirror's free-edge boundary condition. Other small variation in the static gain is observed and attributed to variation in motor constant, actuator stiffness, electrical resistance and driver circuits. The measured actuator coupling of the central actuators is 52% and close to the predicted value from the static model.

The influence matrix, derived from the measurements, is used to shape the mirror facesheet into the first 28 Zernike modes, which includes the piston term that represents the best flat mirror. The interferometrically measured shapes are compared to the perfect Zernike modes and to the Zernike modes as made with the limited number of regularly spaced actuators in the actuator module. The total RMS error is $\approx 25 \, \mathrm{nm}$ for all modes, whereas the inevitable fitting error varies between 0 and 23nm depending on the mode.

Dynamic DM performance

Lumped masses are added to the model to obtain the dynamic behavior. The predicted dynamic behavior of the DM is validated by measurements. A laser vibrometer is used to measure the displacement of the mirror facesheet, while the actuators are driven by a zero-mean, bandlimited, white noise voltage sequence. Using the MOESP system identification algorithm, high-order black-box models are identified with VAF values around 95%. This identified model is compared with the derived analytical model. The latter uses the average actuator properties as measured. The first resonance frequency identified is 725Hz, and lower than the 974Hz expected from the analytical model. This is attributed to the varia-

186 7 Conclusions

tions in actuator properties, such as actuator stiffness. The relative modal damping of the model identified is an order of magnitude higher than the damping in the analytical model, where only actuator damping is considered. The difference is attributed to the presence of air damping and damping in the glue used to attach the connection struts.

The power dissipation in each actuator of the $\varnothing 50$ mm mirror to correct the Von Karmann turbulence spectrum ($D/r_0=5.4, L_0=100$ m) is estimated. Actuators outside the illuminated area are distinguished from those inside this area. Furthermore, the estimated power dissipation is split into turbulence correction and mirror flattening. For the turbulence correction, ≈ 1.5 mW for the outer and ≈ 1.4 mW for the inner actuators, is dissipated. For static flattening these values are ≈ 23.8 mW and ≈ 5.5 mW respectively.

7.2 Recommendations

Recoatability

One of the drawbacks in the DM design as presented, is the limited possibility to recoat the facesheet. This is due to the fact that the facesheet with connection struts and actuators form one glued assembly. The (cheap) facesheet can not be replaced without replacement of the whole actuator grid. A possible solution would be to make an additional separation layer. In the current design, the connection struts are glued to the membrane suspension and moving core. This suspension is currently glued to the actuator baseplate. In future designs, this baseplate could be separated in two layers, where the upper part forms an assembly with the suspension and the moving core and the lower part forms the assembly with the PMs and coils. For recoating the upper part could be separated from the lower part and replaced together with the facesheet.

Actuator performance

To further improve the actuator properties it is recommended to lower the reluctance of the radial airgap. In a sensitivity analysis of the actuator model, this showed to be of strong influence on the motor constant and actuator stiffness. A factor of two in reluctance reduction will increase the motor constant to 0.37N/A and increase the actuator stiffness to 750N/m. This can be realized by a smaller gap width or by a larger gap area. Besides the higher motor constant, increased electronic damping of the mechanical resonance frequency is then observed and will become less limiting for the controller performance without adding complexity to the actuator or electronics design.

Assembly

Dust, trapped between the facesheet and the porous airbearing, proved difficult to avoid and made the placement of the facesheet onto the air bearing one of the most difficult steps in the assembly. This could be simplified by the addition of small grooves in the air bearing. The chance that a dust particle causes a bump in the mirror surface, is thereby reduced.

Measurement of the magnetic properties of PMs

A Helmholtz test setup is realized to measure the magnetic properties of the PMs. The purpose of the setup is to verify the magnetic properties, especially the 2nd quadrant of the B-H curve, as provided by the PM manufacturer and to select a subset of PMs for which the magnetic properties show only small variations to obtain uniformity in the resulting electromagnetic actuators characteristics.

The Helmholtz coil set

A Helmholtz coil test setup is chosen because it is made relatively easy at low costs, measurements can be made in a short time and the PMs are not exposed to external magnetic fields that could affect its magnetization. Figure A.1 shows a Helmholtz coil in schematic. The Helmholtz coil consists of a pair of identical circular coils on a common axis. If the coils are connected in series and current flows through the coils in the same direction, a uniform magnetic field is produced at the center. With the Biot-Savart law, the magnetic field produced by a current loop can be calculated. The magnetic field from the two coils of the Helmholtz coil arrangement can be obtained by superimposing the two constituent fields. The primary component of the uniform magnetic field is parallel to the axes of the two coils. The uniform field is the result of the addition of the two field components parallel to the axes of the two coils and the difference between the components perpendicular to the axes. For a given coil radius, the optimal coil separation can be calculated needed for the largest uniform central field. This separation is equal to the radius of the coils. Furthermore,

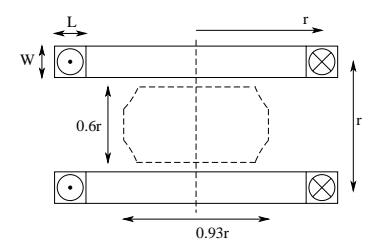


Figure A.1: Schematic of a Helmholtz coil. The region within the dashed lines holds an uniform magnetic field when a current is applied through both coils.

190 7 Conclusions

to get a homogeneous field for coils with finite dimensions, the coil's cross-section should be according to [132]:

 $\frac{W}{L} = \sqrt{\frac{31}{36}}$

The resulting area with a uniform field (<1% variation) is also shown in Figure A.1 and expressed as fraction of the coil mean radius. A Helmholtz coil can not only be used to produce a uniform magnetic field, but also, if coupled to an integrating volt meter or flux meter, to measure the magnetic dipole moment of a PM placed in that region [40].

With a Helmholtz coil, the magnetic dipole moment at the actual operating point of the PM is measured. The measured magnetic dipole moment depends on the magnet volume, shape and its relative permeability. The magnetic moment represents the product of the pole strength and magnetic length of the sample. The pole strength is a measure of total flux at the pole. The magnetic length is not the same as physical length of the PM and varies from 0.7 times the physical length in long and/or low coercivity PMs to nearly the physical length in short and/or high coercivity PMs and varies with the level of magnetization [176]. By reciprocity, the coil flux caused by the dipole will not depend on the position in the area of uniform field as described above. If the PM is placed closer to one coil, that coil is cut by more flux and the other coil by less, but the total flux seen by the two coils remains constant. By Faraday's law it follows that the voltage generated is proportional with the rate of the change of the flux in the loop. Magnetic flux is hereby defined as the product of the magnitude of the magnetic field and the area of the loop. By inserting or extracting a PM, the voltage induced can be integrated as a measure for the dipole moment. If the inserted PM is rotated over 180 degrees over an axis perpendicular to the coil axis, the magnetic dipole moment as measured is doubled. A turn at the center of the cross section of each of the two coils will enclose a specific flux when a magnetic dipole, with m_z as a dipole moment is inserted in the center of the coil. This flux is given by [40]:

$$\phi = \frac{\mu_0 m_z N}{r} \frac{2}{5} \sqrt{\frac{4}{5}}$$

For a coil with N turns and a finite cross section the coupled flux is [40]:

$$\phi = \frac{\mu_0 m_z N}{r} \frac{2}{5} \sqrt{\frac{4}{5}} \left(1 - \frac{1}{60} \left(\frac{w}{r} \right)^2 \right) = k_H m_z$$

The constant k_H is linked to the Helmholtz coil geometry.

Reconstructing the 2nd quadrant of the B-H curve

Because the PMs used in the actuators can be stacked, it is possible to reconstruct a significant part of the B-H curve with the Helmholtz coil test setup [40].

The 2nd quadrant of the B-H curve can for linear permanent magnetic materials be described by:

$$B = \mu_0 H + \mu_0 M(H)$$

= \(\mu_0 \mu_r H + B_r\) (A.1)

Where B is the magnetic induction in T, B_r is the magnetic remanence in T, μ_0 is the permeability in vacuum, equivalent to $4\pi\cdot 10^{-7}$ Tm/A, μ_r is the relative permeability and H is the magnetic field intensity in A/m and M(H) is the average magnetization in A/m. The average magnetization M(H) per unit volume of the measured (stack) PMs can be calculated by:

$$M(H) = \frac{m_z(H)}{V_m}$$

where V_m is the volume of the PMs. The measured value is lower than the value of M_0 because M(H) is dependent on the internal field in the PM:

$$M = \frac{M_0}{\mu_0} - \frac{\mu_r - 1}{\mu_0 \mu_r} B$$

The average value of B inside the PM in air depends only on the PM shape. The internal B-value increases with the relative length in the magnetization direction. To obtain the value of B in Equation (A.1) the value for H and M(H) is needed. It is possible to obtain the value of B by the introduction of the demagnetization factor N_d .

$$H = -N_d M (A.2)$$

The value of N_d is between 0 and 1 and depends only on the shape of the PM [34]. The process to get from the measurements with the Helmholtz coil to a reconstructed B-H curve is:

- 1. Measuring the magnetic dipole moment m_z of stacks of the PMs (e.g. 1,2,3,..., 16 PMs).
- 2. Calculate the average value of M(H) per unit volume.
- 3. Determining the demagnetization factor for each of the stacks, depending on the diameter and height.
- 4. Calculate the value of the magnetic field intensity H with Equation (A.2).
- 5. Calculate the average value of the flux density B from Equation (A.1).

The found values for B and H are plotted to form the linear part of the 2nd quadrant of the B-H curve.

Measurements with the Helmholtz coil test setup

A dedicated Helmholtz coil test setup is fabricated to measure the small PMs used in the actuators ($\emptyset 1.0 \times 0.3$ mm). The mean diameter of the coils is 15mm. Each coil has 580 windings with 50 μ m copper wire. The coil constant for the conversion between measured flux and magnetization is 6.87e-2. The Helmholtz coil setup has a rotation table into which the PMs can be inserted and two stops to rotate the table over 180 degrees, see Figure A.2. The setup can be connected to a commercially available flux meter. The realized test

192 7 Conclusions



Figure A.2: Photo of the realized Helmholtz test setup



Figure A.3: The rotation table within the \emptyset 15mm coils with its end stops is visible.

setup is shown in Figure A.2 and Figure A.3. A set of 200 SmCo $_5$ PMs with dimensions $\varnothing 1.0 \times 0.3$ mm were measured. The histogram of the flux measurements with the designed Helmholtz coil and commercial flux meter is given in Figure A.4. The figure shows that one of the PMs is probably not well magnetized. All other PMs show small differences: the mean value for the integrated voltage is 9.6Vs and the variance is $0.05 \text{ V}^2\text{s}^2$.

A set of PMs with the mean measured value is taken for the reconstruction of the 2^{nd} quadrant of the B-H curve. The steps as described in Section A to get from the flux measurements with the Helmholtz coil to a reconstructed B-H curve are taken. The result is shown in Figure A.5 together with the data from the PM supplier: H_{c_m} =676±40 kA/m and B_r =1.05±0.05T are plotted. Differences might be caused by the size of the PMs. In the small PMs the surface area is rather large in comparison to its volume. Damage of the surface caused by grinding has a relatively big influence. An increase of the magnet thickness will compensate for lower measured dipole moment. The reluctance in the actuator will hereby also increase.

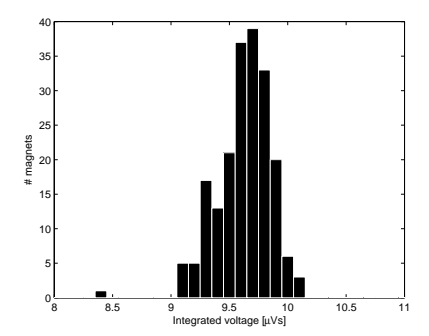


Figure A.4: Histogram of the flux measurements

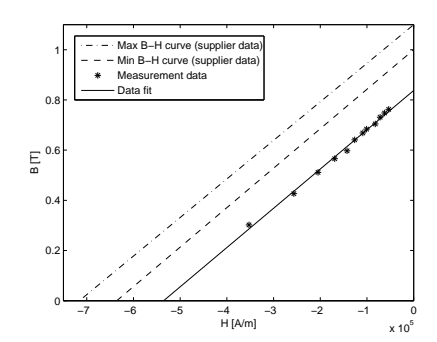


Figure A.5: Reconstruction of the 2nd quadrant of the B-H curve of the PM material.

Setup to measure the nonlinear stiffness of the membrane suspensions

A measurement setup is designed and built to measure both the nonlinear stiffness of membrane suspensions as used in the different actuator designs (Section 4.3) and the dynamic behavior of single actuators [126].

Measurements of the nonlinear stiffness of the membrane suspension

Figure B.1 shows the schematic lay-out of the measurement device. In the set up the out-ofplane displacement of the membrane suspension is coupled to the force exerted. In the set up, the force is measured piezo-electrically and the displacement optically, by a Philtec D21 sensor. Each of the sensors is placed in a separate, monolithic block on an elastic parallel guiding mechanism, driven via a lever by a micro spindle.

The spindle, which is connected to the force sensor's parallel guiding mechanism is used to

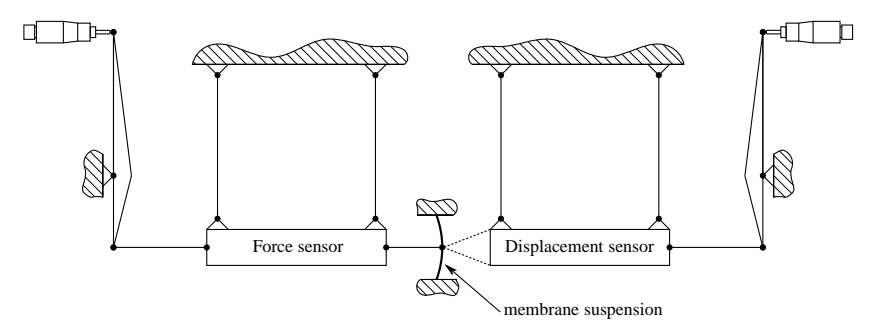


Figure B.1: Schematic of the measurement setup to measure the nonlinear stiffness of a membrane suspension.

194 7 Conclusions

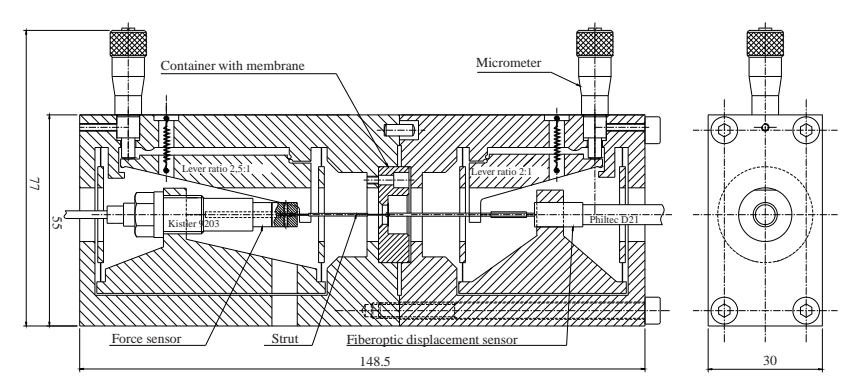


Figure B.2: The CAD drawing of the cross section of the setup to test the nonlinear stiffness of the membrane suspension in the variable reluctance actuator.

enforce a displacement in the membrane suspension. The force sensor is connected to the membrane suspension by means of a strut to decouples all DOFs, except the axial displacement.

The optical sensor is placed co-axial with the force sensor and brought into range by means of its micro spindle, lever and guiding mechanism. The suspension is placed in a container $(\emptyset 25x8mm)$ to be more handy and placed between the two blocks. Force can thus be measured as function of the displacement.

Figure Figure B.2 shows a cross section of the setup in detail, including its main dimensions. The test setup as realized is shown in Figure B.3. The containers with the different membranes are shown in Figure B.4 and Figure B.5.

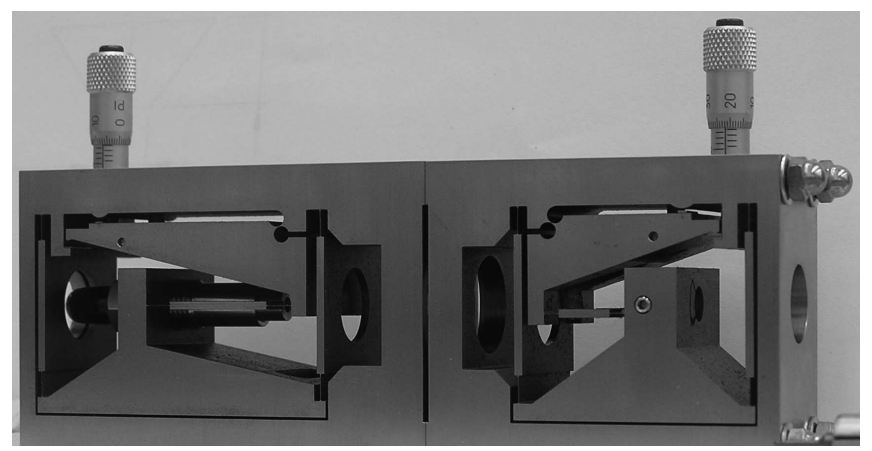


Figure B.3: Photo of the manufactured test setup.



Figure B.4: Photo of the container with membrane suspension.

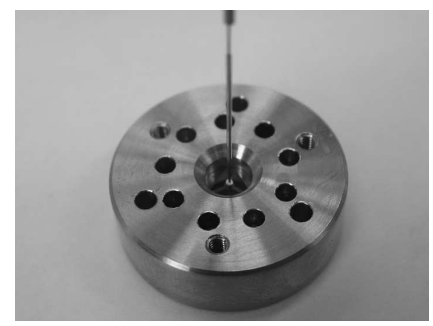


Figure B.5: The strut that connects the membrane suspension to the force sensor is clearly visible.

Dynamic measurements of single actuators

With the same optical sensor and the use of a SiglabTM[43] system, the dynamic characteristic of single actuators can be measured. The block with the force sensor is thereby replaced by a block that holds the container with a fully assembled actuator. This is shown in Figure B.6 and Figure B.7. The SiglabTM system can be used to generate an excitation signal which can be fed to a current amplifier and to the coil wires. By measurement of the Siglab's generated signal and the displacement of the optical sensor FRFs are constructed.



Figure B.6: The actuator placed in the container

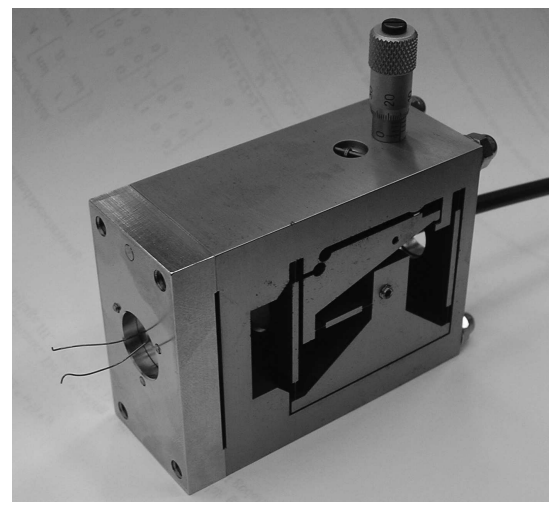


Figure B.7: The block with the fully assembled actuator connected to the block that holds the optical displacements sensor.

Fourier series of a PWM signal

A PWM signal is a periodic signal with period T_{PWM} that switches between a high value and a low value depending on a duty cycle $r_{PWM} \in \{0,1\}$. For the BD modulation principle used in Section 5.2.2, the high value is equal to the clamp voltage V_{cc} and the low value equal to zero. Let the PWM signal y(t) be defined as a function of time t as:

$$y(t) = \begin{cases} V_{cc}, & \text{for } -T_{PWM}r_{PWM}/2 + kT_{PWM} \le t \le T_{PWM}r_{PWM}/2 + kT_{PWM}, \\ 0, & \text{otherwise,} \end{cases}$$
 (C.1)

where $k \in \mathbb{Z}$.

According to Fourier theory, any periodic signal can be written as a sum of sines and cosines. Since this signal is symmetric in t=0, it can be expressed in cosines only as:

$$y(t) = a_0 + \sum_{n=1}^{\infty} a_n \cos(2\pi n f_{PWM} t),$$
 (C.2)

where $f_{PWM} = 1/T_{PWM}$. The Fourier coefficients a_n for $n \ge 1$ can be determined by integrating the product of y(t) with a single cosine over one full period. Let this integral I_n be defined as:

$$\begin{split} I_n &= \int\limits_{-T_{PWM}/2}^{T_{PWM}/2} y(t) \cos(2\pi f_{PWM} n t) dt, \\ &= \int\limits_{-T_{PMW}/2}^{T_{PWM}/2} \left[a_0 + \sum_{m=1}^{\infty} a_m \cos(2\pi m f_{PWM} t) \right] \cos(2\pi f_{PWM} n t) dt, \end{split}$$

where the second step follows from substitution of Equation (C.2). This can be further simplified to $I_n=a_nT_{PWM}/2$ for $n\geq 1$ and to $I_0=a_0T_{PWM}$ for n=0 using the following goniometric identities:

$$\int\limits_{-T_{PWM}/2}^{T_{PWM}/2}\cos(2\pi fmt)\cos(2\pi fnt) = \begin{cases} 0 & \text{for } n\neq m,\\ T_{PWM} & \text{for } n=m=0,\\ T_{PWM}/2 & \text{for } n=m\geq 1. \end{cases}$$

198 7 Conclusions

Conversely, the coefficients a_n for $n \ge 1$ can be calculated as:

$$a_{n} = \frac{2I_{n}}{T_{PWM}}$$

$$= \frac{2}{T_{PWM}} \int_{-T_{PWM}/2}^{T_{PWM}/2} y(t) \cos(2\pi f_{PWM}nt) dt,$$

$$= \frac{2}{T_{PWM}} \int_{-\tau/2}^{\tau/2} V_{cc} \cos(2\pi f_{PWM}nt) dt,$$

$$= \frac{2V_{cc} \sin(2\pi f_{PWM}nt)}{2\pi f_{PWM}nT_{PWM}} \Big]_{-\tau/2}^{\tau/2},$$

$$= V_{cc} \frac{\sin(\pi f_{PWM}n\tau)}{\pi n},$$

$$= V_{cc} \frac{\sin(\pi n\tau_{PWM}n\tau)}{\pi n}.$$
(C.4)

where $\tau = T_{PWM}r_{PWM}$. In Equation (C.3), the signal y(t) from Equation (C.1) is substituted and the remaining steps use $T_{PWM}f_{PWM}=1$ and other common algebra identities to simplify the result.

The derived result is not valid for n = 0, but a_0 can be obtained directly as $a_0 = I_0/T_{PWM}$, which reduces to:

$$a_0 = \frac{1}{T_{PWM}} \int_{-T_{PWM}/2}^{T_{PWM}/2} y(t)dt = \frac{V_{cc}t}{T_{PWM}} \bigg]_{-\tau/2}^{\tau/2} = V_{cc}r_{PWM}.$$

Summarizing, the PWM signal y(t) as defined in Equation (C.1) can be expressed as an infinite series of cosines by substituting this a_0 and a_n from Equation (C.4) into Equation (C.2), yielding:

$$y(t) = V_{cc} \left(r_{PWM} + \sum_{n=1}^{\infty} \frac{\sin(\pi n r_{PWM})}{\pi n} \cos(2\pi n f_{PWM} t) \right).$$

The LVDS protocol

The electronics modules communicate with the communication bridge over an LVDS connection. This communication method uses a current source to transmit information instead of a voltage source, which makes it much less sensitive to the cable length or resistance. The sign of the current defines the binary *high* and *low* values.

The LVDS connection does not use a clock signal to synchronize the communication. Each message is preceded by 18 *pause bits* on which a message pointer can be synchronized and one *start* and one *stop* bit on which the 16-bit data words can be synchronized. A start bit is high and the pause and stop bits are low. No *parity bits* are used.

Each message consists of four parts: 18 pause bits, a header, the data and a checksum. The header consists of one 16-bit word of which the lower eight bits are formed by the module identifier and the upper eight by the message identifier:

byte index	number of bits	description
0	8	module identifier
1	8	message identifier
2	depends on message type	command data
?	16	checksum

The sum of all data words – including the checksum itself – equals zero, which makes the checksum the 2's complement of the sum of the preceding words. The data structure depends on the message identifier, which can be one of the following.

Burst write (1)

A burst-write message contains setpoints for all 61 actuators on the specified module. The message identifier for this message is 1 and the command data field is defined as:

byte index	number of bits	description
0	16	setpoint for actuator 1
2	16	setpoint for actuator 2
:	:	:
120	16	setpoint for actuator 61

200 7 Conclusions

Register write (2)

A *register write* message can be used to modify a specific register on one of the modules. The message identifier for this message is 2 and the command data field is defined as:

byte index	number of bits	description
0	16	register number
2	16	new register value

Register read (3)

A *register read* message can be used to read back a specific register on one of the modules. The message identifier for this message is 3 and the command data field consists only of a 16-bit register number.

The module will respond with a message with the format of a *register write* and the module and message identifiers set to the values used in the requesting *register read* message.

Registers

Each module contains the following registers:

index	description
0x000x1e	PWM setpoints for actuators 131
0x1f	not used
0x200x21	Enable PWM A bits for actuators 131
0x220x23	Enable PWM B bits for actuators 131
0x240x25	Enable PWM C bits for actuators 131
0x260x27	Coil integrity control bits for actuators 131 (read-only)
0x28	Global settings register for actuators 131
0x290x3f	not used
0x400x5d	PWM setpoints for actuators 3261
0x5e0x5f	not used
0x600x61	Enable PWM A bits for actuators 3261
0x620x63	Enable PWM B bits for actuators 3261
0x640x65	Enable PWM C bits for actuators 3261
0x660x67	Coil integrity control bits for actuators 3261 (read-only)
0x68	Global settings register for actuators 3261
0x690x7f	not used
0x800xff	reserved

Global settings registers

Each slave FPGA has a global, 16-bit settings register with which its global behavior can be controlled. Its bits have the following meaning:

Bit index	Description
03	Dead-time in 8ns steps (default = '0111')
46	Not used
7	Set global PWM B to high (used for <i>coil integrity check</i>)
8	Global PWM C enable
9	Global PWM B enable
10	Global PWM A enable
11	Testmode (used for <i>coil integrity check</i>)
12:15	Revision number (= '0001')

Coil integrity check

The FPGA slaves can be put into test-mode to perform the so-called *coil integrity check*. This can be used to determine whether the actuator coil conducts electricity or not.

First, the fine PWM C signal that is directly provided by the FPGA is set to high (figure 5.4) and the course PWM signals are disabled. If the actuator coil does not conduct (e.g. because of a broken wire), this will charge capacitor C_l (figure 5.3) and build up a capacitor voltage. Otherwise, the actuator coil will prevent this build-up and the voltage will quickly drop to zero when PWM C is disabled. This behavior can be checked by reversing the directionality of the FPGA pin corresponding to the PWM C signal and using it to measure the capacitor voltage. If the voltage is zero, the actuator coil is fine and if it's high, it does not conduct electricity.

These operations are controlled via specific bits of the global settings registers. The coil integrity check procedure should be as follows:

- 1. Enable bits 7 and 11 of the global settings registers. This enables the test mode for which the course PWM signals are disabled and the fine PWM signal is permanently high.
- 2. Wait at least four times the time constant R_aC_l of the system to allow charging of the capacitor.
- 3. Set bits 7 of the global settings registers to zero, causing the FPGA pins corresponding to PWM's C to go into tri-state and allowing them to measure the capacitor voltages.
- 4. Disable the test-mode by setting bits 11 of the global settings registers to zero. The results of the voltage measurements can now be found in the *coil integrity control* registers. These should be zero for conducting actuator coils and one for malfunctioning ones.

The UDP protocol

UDP is a very lean communication protocol, since no feedback is given whether the message is properly received. Each message is a stand-alone message and not part of a stream such as a Transmission Control Protocol (TCP)/IP message. Besides the required IP header, the message contains a small UDP header that contains the *source* and *destination* ports, the message *length* and a *checksum*:

byte index	number of bits	description
0	16	source port
2	16	destination port
4	16	message length
6	16	checksum
8	??	UDP data

The checksum value is ignored by the LVDS communications bridge to improve latency. The data of the UDP message comes after the checksum field and has a substructure that consists of the following parts: a module identifier (8 bits), a message identifier (8 bits) and the command data:

byte index	number of bits	description	
0	8	module identifier	
1	8	message identifier	
2	??	command data	

The module identifier byte specifies the module for which the message is intended and the message identifier specifies the type of message that follows. The command data specification depends on the type of message used. The message type can be one of the following.

Burst write

A burst-write message contains setpoints for all 61 actuators on the specified module. The message identifier for this message is 1 and the command data field is defined as:

204 7 Conclusions

byte index	number of bits	description
0	16	setpoint for actuator 1
2	16	setpoint for actuator 2
:	:	:
120	16	setpoint for actuator 61
122	16	Reserved
124	16	Sequence number (for diagnostics)

Together with the module and message identifier bytes, a burst write message is thus exactly 128 bytes in length. It is possible to include up to eight of such burst messages in one single UDP message. Since the UDP-to-LVDS communication bridge has a processing time of 85μ s per message, this significantly reduces the latency in case of many modules.

The communications bridge will recognize a combined UDP message by its size and splits it into multiple LVDS messages before transmitting them sequentially over the LVDS connection. The limit of eight burst messages per UDP message is due to the protocol limit of the UDP message size.

Register write

A *register write* message can be used to modify a specific register on one of the modules. The message identifier for this message is 2 and the command data field is defined as:

byte index	number of bits	description	
0	16	register number	
2	16	new register value	

Register read

A *register read* message can be used to read back a specific register on one of the modules. The message identifier for this message is 3 and the command data field consists only of a 16-bit register number.

The module will respond over the LVDS connection in the form specified in appendix D. This is wrapped into the standard UDP form by the communication bridge. The module and message identifiers will be identical to those bytes of the request message and the command data field is identical to that of a register write message.

Diagnostic messages

Finally, the communications bridge counts the number of burst messages that it has properly received since start-up. This 16-bit number can be read back by reading register 255 of module 255. This counter can also be set by writing to this same register.

Spatial variation of actuator properties

The two figures below illustrate that there is no obvious correlation between the values of the resonance frequency and motor constant of the actuators measured and their location in the grid.

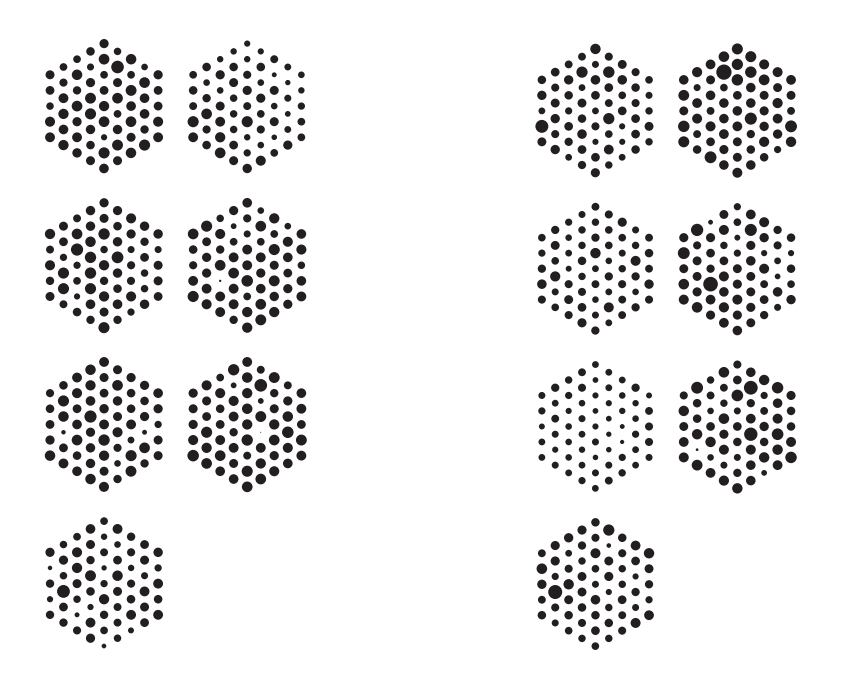


Figure F.1: The value of the resonance frequencies, represented proportionally by the size of the dots for the modules 1...7 from left to right and then top to bottom.

Figure F.2: The value for the motor constants, represented proportionally by the size of the dots for the modules 1...7 from left to right and then top to bottom

Quantization

In Chapter 5 a choice was made to use a 16 bit PWM voltage signal generator to drive the actuators, leading to sufficiently small quantization errors. At that point, the consideration was based on general design parameters of the system, which is here performed in more detail to validate the choice.

The RMS wavefront error σ_{quant} due to quantization errors has been specified in Chapter 2 as at most 5nm. Due to quantization, the actual command vector $\tilde{\mathbf{V}}_{PWM}$ will be the sum of the intended actuator voltage \mathbf{V}_{PWM} and quantization noise \mathbf{n} . Since wavefront correction is only possible for frequencies below the control bandwidth, which is generally below the first system resonance, the static DM system model from Equation (6.7) on page 157 with influence matrix \mathbf{B}_f will here be used:

$$\hat{\mathbf{z}}_f = \mathbf{B}_f \tilde{\mathbf{V}}_{PWM} = \mathbf{B}_f (\mathbf{V}_{PWM} + \mathbf{n}),$$

where $\hat{\mathbf{z}}_f$ denotes the actual facesheet deflection in contrast to the facesheet deflection for the intended command \mathbf{V}_{PWM} . According to the design requirements, the variance σ^2_{quant} of the quantization noise \mathbf{n} should be such that $\sigma_{quant} = \langle ||\mathbf{B}_f \mathbf{n}||_F \rangle \leq 5$ nm, where

$$\sigma_{quant}^{2} = \frac{1}{N_{q}} \operatorname{Tr} \left(\mathbf{B}_{f} \left\langle \mathbf{n} \mathbf{n}^{T} \right\rangle \mathbf{B}_{f}^{T} \right). \tag{G.1}$$

To derive the covariance matrix $\langle \mathbf{n} \mathbf{n}^T \rangle$, let the elements n_i of \mathbf{n} be uncorrelated stochastic values with a square probability density function $P_n(n_i)$:

$$P_n(n_i) = \begin{cases} q^{-1} & \text{for } |n_i| \le q/2, \\ 0 & \text{otherwise,} \end{cases}$$

where q is the command quantization step size in Volt. Each diagonal element of $\langle \mathbf{n}\mathbf{n}^T \rangle$ can thus be expressed as [136]:

$$\left\langle n_i^2 \right\rangle = \int\limits_{-\infty}^{\infty} n_i^2 P_n(n_i) dn_i = \int\limits_{-q/2}^{q/2} \frac{n_i^2}{q} dn_i = \frac{q^2}{12}$$

hence $\left<\mathbf{n}\mathbf{n}^T\right>=rac{q}{12}I.$ Using Equation (G.1) the q for which σ_{quant} is smaller than 5nm can

208 7 Conclusions

now be derived as:

$$\begin{split} \frac{1}{N_a} \mathrm{Tr} \left(\frac{q^2}{12} \mathbf{B}_f \mathbf{B}_f^T \right) &\leq (5 \cdot 10^{-9})^2, \\ \frac{q^2}{12} \mathrm{Tr} (\mathbf{B}_f \mathbf{B}_f^T) &\leq (5 \cdot 10^{-9})^2 N_a, \\ q &\leq \sqrt{\frac{12(5 \cdot 10^{-9})^2 N_a}{\mathrm{Tr} (\mathbf{B}_f \mathbf{B}_f^T)}}. \end{split}$$

Using the influence matrix identified in Section 6.3.2 for the 61 actuator DM system this yields $q\approx 190\mu\text{V}$, which is only slightly more than the $100\mu\text{V}$ accuracy provided by the realized 16 bit PWM voltage source with a supply voltage of 3.3V. The quantization value of the driver electronics was thus properly chosen.

Finally, note that incorporation of noise shaping techniques [77, 167, 170] into the controller design may enlarge the required quantization step. Such techniques could push the quantization effects to (high) temporal frequencies for which the wavefront disturbance has a low magnitude, so reducing the effect on the optical performance.

- [1] www.disco.co.jp/eg/solution/library/thin.html.
- [2] www.goodfellow.com.
- [3] www.vacuumschmelze.de.
- [4] C. A. Aerts. Optimizing and implementing leaf springs for the reluctance motor. Technical Report DCT 2005.94, Technische Universiteit Eindhoven, 2005.
- [5] R. Angel, J. Burge, K. Hege, M. Kenworthy, and N. Woolf. Stretched membrane with electrostatic curvature (SMEC): A new technology for ultra-lightweight space telescopes. In J. B. Breckinridge and P. Jakobsen, editors, *Proceedings of SPIE: UV, Optical, and IR Space Telescopes and Instruments*, volume 4013, Munich, 2000.
- [6] V. Apollonov, V. Borodin, A. Brynskikh, G. Vdovin, and S. Murav. Cooled adaptive mirror with magnetostrictive spring-type actuators. *Soviet Journal of Quantum Electronics*, 20(11):1403–1406, 1990.
- [7] R. Arsenault, R. Biasi, D. Gallieni, A. Riccardi, P. Lazzarini, N. Hubin, E. Fedrigo, R. Donaldson, S. Oberti, S. Stroebele, R. Conzelmann, and M. Duchateau. A deformable secondary mirror for the VLT. In *Proceedings of SPIE*, volume 6272, 2006.
- [8] H. Babcock. The possibility of compensating astronomical seeing. *Publications of the Astronomical Society of the Pacific*, 65(386):229–236, October 1953.
- [9] F. Bazán. Eigensystem realization algorithm (ERA): reformulation and system pole perturbation analysis. *Journal of Sound and Vibration*, 274:433–444, 2004.
- [10] A. Bejan. Heat transfer. John Wiley and Sons Ltd, 1990.
- [11] W. Belvin, H. Edighoffer, and C. Herstrom. Quasistatic shape adjustment of a 15-meter-diameter space antenna. *Journal of Spacecraft and Rockets*, 26:129–136, May 1989.
- [12] R. Biasi, M. Andrighettoni, D. Veronese, V. Biliotti, L. Fini, A. Riccardi, P. Mantegazza, and D. Gallieni. LBT adaptive secondary electronics. In P. L. Wizinowich and D. Bonaccini, editors, *Proceedings of SPIE: Astronomical Telescopes and Instrumentation*, volume 4839, pages 772–782, Waikoloa, Hawaii, USA, August 2002.
- [13] K. Birch and M. Downs. Correction to the updated Edlen equation for the refractive index of air. *Metrologia*, 31(4):315–316, 1994.
- [14] R. Blevins. Formulas for natural frequency and mode shape. Krieger Publishing Company, 1979.
- [15] M. Born and E. Wolf. *Principles of Optics: Electromagnetic Theory of Propagation, Interference, and Diffraction of Light*. Cambridge University Press, 7th edition, 1999.
- [16] A. H. Bouchez, R. G. Dekany, J. R. Angione, C. Barane, K. Bui, R. S. Burruss, J. R. Crepp, E. E. Croner, J. L. Cromer, S. R. Guiwits, D. D. Hale, J. R. Henning, D. Palmer, J. E. Roberts, M. Troy, T. N. Truong, and J. Zolkower. Status of the PALM-3000 high-order adaptive optics system. In N. Hubin, C. E. Max, and P. L.

Wizinowich, editors, *Proceedings of SPIE: Adaptive Optics Systems*, volume 7015, 2008.

- [17] J. Brenner and L. Cummings. The hadamard maximum determinant problem. *American Mathematics Montly*, 79(6):626–630, 1972.
- [18] G. Brusa, A. Riccardi, M. Accardo, V. Biliotti, M. Carbillet, C. del Vecchio, S. Esposito, B. Femenía, O. Feeney, L. Fini, S. Gennari, L. Miglietta, P. Salinari, and P. Stefanini. From adaptive secondary mirrors to extra-thin extra-large adaptive primairy mirrors. In ESO Conference Proceedings, 1999.
- [19] G. Brusa, A. Riccardi, V. Biliotti, C. D. Vecchio, P. Salinari, P. Stefanini, P. Mantegazza, R. Biasi, M. Andrighettoni, C. Franchini, and D. Gallieni. Adaptive secondary mirror for the 6.5m conversion of the Multiple Mirror Telescope: first laboratory testing results. In R. K. Tyson and R. Q. Fugate, editors, *Proceedings of SPIE: Adaptive Optics Systems and Technology*, volume 3762, September 1999.
- [20] G. Brusa-Zappellini, A. Riccardi, S. D. Ragland, S. Esposito, C. D. Vecchio, L. Fini, P. Stefanini, V. Biliotti, P. Ranfagni, P. Salinari, D. Gallieni, R. Biasi, P. Mantegazza, G. Sciocco, G. Noviello, and S. Invernizzi. Adaptive secondary P30 prototype: laboratory results. In D. Bonaccini and R. K. Tyson, editors, *Proceedings of SPIE: Adaptive Optical System Technologies*, volume 3353, pages 764–775, September 1998.
- [21] J. Burge, J. Angel, B. Cuerden, H. Martin, S. Miller, and D. Sandler. Lightweight mirror technology using a thin facesheet with active rigid support. In P. Y. Bely and J. B. Breckinridge, editors, *Proceedings of SPIE: Space Telescopes and Instruments V*, volume 3356, pages 690–701, 1998.
- [22] J. Burge, J. Angel, B. Cuerden, and N. Woolf. Glass Membrane Mirrors beyond NGST. In Conference proceedings of SPIE: Ultra Lightweight Space Optics Challenge Workshop, Napa, CA, March 1999.
- [23] J. Burge, S. DeRigne, R. Angel, B. Cuerden, S. Clapp, G. Rivlis, P. Woida, P. Gohman, S. Bell, and R. Kingston. NGST Mirror System Demonstrator from the University of Arizona. In *Proceedings of SPIE: Imaging Technology and Telescopes*, volume 4451, pages 105–113, 2001.
- [24] J. Burge, E. Sabatke, J. Angel, and N. Woolf. Optical Design of Giant Telescopes for Space. In J. M. Sasian, editor, *Proceedings of SPIE: Novel Optical Systems Design and Optimization III*, volume 4092, pages 82–93, 2000.
- [25] G. S. Burley, J. R. Stilburn, and G. A. H. Walker. Membrane mirror and bias electronics. *Applied Optics*, 37(21):4649–4655, 1998.
- [26] B. L. Burton. Amine-Blushing problems? No Sweat! In *Epoxy Resin Formulators Meeting of The Society of the Plastics Industry.*, 2001.
- [27] D. Buscher. A Thousand and One Nights of Seeing on Mt. Wilson. In J. B. Breckinridge, editor, *Proceedings of SPIE: Amplitude and Intensity Spatial Interferometry II*, volume 2200, pages 260–271, 1994.
- [28] O. Carlin. Lightweight mirror systems for spacecraft an overview of materials and manufacturing needs. In *IEEE Aerospace Conference Proceedings*, volume 4, pages 169–182, 2000.
- [29] R. A. Carreras, D. K. Marker, and J. M. Wilkes. Membrane mirror characteristics for used with real time holography. In J. D. Gonglewski and M. A. Vorontsov, editors, *Proceedings of SPIE: Artificial Turbulence for Imaging and Wave Propagation*, volume 3432, pages 120–128, 1999.

- [30] C. Cassapakis and M. Thomas. Inflatable Structures Technology Development Overview. *American Institute of Aeronautics and Astronautics*, 1995.
- [31] R. G. Castro, L. A. Jacobson, and P. W. Stanek. Beryllium processing technology review for applications in plasma-facing components. Technical Report LA–12545-MS, Los Alamos National Laboratory, July 1993.
- [32] R. Centamore and A. Wirth. High bias membrane mirror. In M. A. Ealey, editor, *Proceedings of SPIE: Active and Adaptive Optical Components*, volume 1543, pages 128–132, 1991.
- [33] R. Changhai and S. Lining. Hysteresis and creep compensation for piezoelectric actuator in open-loop operation. *Sensors and Actuators A*, 122:124–130, 2005.
- [34] D.-X. Chen, J. A. Brug, and R. Goldfarb. Demagnetizing Factors for Cylinders. *IEEE Transactions on magnetics*, 27:3601–3619, 1991.
- [35] A. Chiuso. The role of vector autoregressive modeling in predictor-based subspace identification. *Automatica*, 43:1034–1048, 2007.
- [36] A. Chiuso, R. Muradore, and E. Marchetti. Dynamic calibration of adaptive optics systems: a system identification approach. In *Proceedings of the Conference on Decision and Control*, 2008.
- [37] A. Chiuso and G. Picci. Consistency analysis of some closed loop subspace identification methods. *Automatica*, 41(3):377–391, 2005.
- [38] S. Chodimella, J. D. Moore, B. G. Patrick, B. DeBlonk, and D. K. Marker. Design, fabrication, and validation of an ultra-lightweight membrane mirror. In *Proceedings of SPIE: Advanced wavefront control*, volume 5894, 2005.
- [39] P. Ciddor. Refractive index of air: new equations for the visible and near infrared. *Applied Optics*, 35:1566–1573, 1996.
- [40] J. Compter and L. van der Veen. Magnetic analysis with a Helmholz coil set. *IEE Proceedings Science, Measurement and Technology*, 150:177–182, 2003.
- [41] J.-M. Conan, G. Rousset, and P.-Y. Madec. Wavefront temporal spectra in high-resolution imaging through turbulence. *Journal of the Optical Society of America A*, 12:1559–1570, July 1995.
- [42] R. Conan, R. Avila, and L. Sanchez. Wavefront outer scale and seeing measurements at San Pedro Martir Observatory. *Astronomy and Astrophysics*, 396:723–730, 2002.
- [43] D. T. Corporation. SigLab Users Guide, 1994.
- [44] A. Cox, editor. AllenŠs Astrophysical Quantities. AIP Press., 2000.
- [45] L. Cuellar, P. Johnson, and D. Sandlar. Performance tests of a 1500 degree-of-freedom adaptive optics system for atmspheric compensation. In *Proceedings of SPIE: Active and adaptive optical systems*, volume 1542, pages 468–476, 1991.
- [46] O. Cugat, S. Basrour, C. Divoux, P. Mounaix, and G. Reyne. Deformable magnetic mirror for adaptive optics: technological aspects. *Sensors and Actuators A: Physical*, 89:1–9, 2001.
- [47] O. Cugat, P. Mounaix, S. Basrour, C. Divoux, and G. Reyne. Deformable magnetic mirror for adaptive optics: first results. In *The* 13th Annual International Conference on Micro Electro Mechanical Systems, 2000.
- [48] J. Dainty, D. Hennings, and K. O'Donnel. Space-time correlation of stellar speckle patterns. *Journal of the Optical Society of America*, 71:490–492, April 1981.

[49] B. J. de Blonk. *Optical-Level Structural Modelling of Membrane Mirrors for Space-borne Telescopes*. PhD thesis, Massachusetts Institute of Technology, 2003.

- [50] B. J. de Blonk and D. W. Millery. Narrowing the design space of a large membrane mirror. In *Ultra Lightweight Space Optics Challenge Workshop*, 1999.
- [51] W. de Bruijn. Low power deformable mirror actuator controller. Master's thesis, Technische Universiteit Eindhoven (TU/e), Den Dolech 2, 5600MB, Eindhoven, The Netherlands, 2009.
- [52] P. Dierickx and R. Gilmozzi. Progress of the OWL 100-m Telescope Conceptual Design. In T. A. Sebring and T. Andersen, editors, *Proceedings of SPIE: Telescope Structures, Enclosures, Controls, Assembly/Integration/Validation, and Commissioning*, volume 4004, pages 290–299, Munich, March 2000.
- [53] T. Döhring, R. Jedamzik, P. Hartmann, H. Esemann, and C. Kunisch. Forming mandrels for X-ray telescopes made of modified Zerodur. In O. Citterio and S. L. O'Dell, editors, *Prococeedings of SPIE: Optics for EUV, X-Ray, and Gamma-Ray Astronomy*, volume 5168, pages 148–156, 2003.
- [54] M. Ealey. Deformable mirrors at Litton/Itek: A historical persepective. In D. Vukobratovich, editor, *Proceedings of SPIE: Precision Engineering and Optomechanics*, volume 1167, November 1989.
- [55] M. Ealey and J. Washeba. Continous facesheet low voltage deformable mirrors. *Optical Engineering*, 29:1191–1198, October 1990.
- [56] F. Eaton and G. Nastrom. Preliminary estimates of the vertical profiles of inner and outer scales from White Sands Missile Range. *Radio Science*, 33:895–903, 1998.
- [57] Edlén. The refractive index of Air. Metroligia, 2:71-80, 1966.
- [58] S. E. Egner. *Multi-Conjugate Adaptive Optics for LINC-NIRVANA*. PhD thesis, Max Planck Institute for Astronomy, University of Heidelberg, 2006.
- [59] B. Ellerbroek. Efficient computation of minimum-variance wave-front reconstructors with sparse matrix techniques. *Journal of the Optical Society of America A*, 19:1803–1816, September 2002.
- [60] S. Errico, R. Angel, B. Stamper, J. Burge, and T. Connors. Stretched Membrane with Electrostatic Curvature (SMEC) Mirrors: A new technology for large lightweight space telescopes. In *Proceedings of SPIE: Highly Innovative Space Telescope Con*cepts, volume 4849, pages 356–364, December 2002.
- [61] H. Fang, U. Quijano, K. Knarr, J. Huang, and R. Lovick. Experimental and Analytical Studies of a Large In-Space Deployable Dual-Band Membrane Reflectarray Antenna. Technical report, Jet Propulsion Laboratory, California Institute of Technology, 2007.
- [62] A. E. Fitzgerald, C. K. Jr., and S. D. Umans. *Electric Machinery*. McGraw-Hill, 6^th edition, 2003.
- [63] A. Florakis and S. Fassois. MIMO LMS-ARMAX identification of vibrating structures part II: a critical assessment. *Mechanical systems and signal processing*, 15, 2001.
- [64] G. F. Franklin, J. Powell, and A. Emami-Naeini. *Feedback control of dynamic systems*. Addison-Wesley, 3rd edition, 1994.
- [65] D. Fried. Statistics of a Geometric Representation of Wavefront Distortion. *Journal of the Optical Society of America*, 55:1427–1435, November 1965.

- [66] D. Fried. Time delay induced mean square error in adaptive optics. *Journal of the Optical Society of America A*, 7(7):1224–1225, 1990.
- [67] M. E. Furber and D. Jordan. Optimal design of wavefront sensors for adaptive optical systems: part 1, controllability and observability analysis. *Optical Engineering*, 36:1843–1855, July 1997.
- [68] M. E. Furber and D. Jordan. Optimal design of wavefront sensors for adaptive optical systems: part 2, optimization of sensor subaperture locations. *Optical Engineering*, 36:1856–1871, July 1997.
- [69] A. Fuschetto. Three-actuator deformable water-cooled mirror. *Journal of Optical Engineering*, 20(2):310–315, March/April 1981.
- [70] D. Gallieni, E. Anaclerio, P. Lazzarini, A. Ripamonti, R. Spairani, C. DelVecchio, P. Salinari, A. Riccardi, P. Stefanini, and R. Biasi. LBT adaptive secondary units final design and construction. In P. L. Wizinowich and D. Bonaccini, editors, *Proceedings* of SPIE: Adaptive Optical System Technologies II, volume 4839, pages 765–771, 2003.
- [71] C. Garner and M. Leipold. Developments and Activities in Solar Sail Propulsion. *American Institute of Aeronautics and Astronautics*, 2003.
- [72] A. Gelb. Applied optimal estimation. The MIT press, 15th edition, 1999.
- [73] L. Gilles. Order-N sparse minimum-variance open-loop reconstructor for extreme adaptiveoptics. *Optics Letters*, 28(20):1927–1929, October 2003.
- [74] R. Gilmozzi and J. Spyromilio. The European Extremely Large Telescope. The Messenger (Telescopes and Instrumentation) 127, European Southern Observatory, March 2007.
- [75] A. Glecker, D. Markason, and G. Ames. PAMELA; Control of a segmented mirror via wavefront tilt and segment piston sensing. In M. A. Ealey, editor, *Proceedings op SPIE: Active and Adaptive Optical Components*, volume 1543, pages 176–189, January 1991.
- [76] G. H. Golub and C. F. V. Loan. *Matrix computations*. Johns Hopkins University Press, Baltimore, MD, USA, 3rd edition, 1996.
- [77] G. Goodwin, D. Quevedo, and D. McGrath. Moving-horizon optimal quantizer for audio signals. *Journal of the Audio Engineering Society*, 51(3):138–149, 2003.
- [78] D. Greenwood. Bandwidth specification for adaptive optics systems. *Journal of the Optical Society of America*, 67:390, 1977.
- [79] G. Greschik, C. V. White, and M. A. Salama. On the precisely uniform and uniaxial tensioning of a film sheet via integrated catenary. In *44th AIAA/ASME/ASCE/AHS Structures, Structural Dynamics, and Materials Conference*, 2003.
- [80] G. Grossman and G. Williams. Inflatable concentrators for solar propulsion and dynamic space power. *Journal of Solar Energy Engineering*, 112:229–236, November 1990.
- [81] R. Grosso and M. Yellin. The membrane mirror as an adaptive optical element. *Journal of the Optical Society of America*, 67:399–406, 1977.
- [82] C. J. Hailey, S. Abdali, F. E. Christensen, W. W. Craig, T. R. Decker, F. A. Harrison, and M. A. Jimenez-Garate. Investigation of substrates and mounting techniques for the High Energy Focusing Telescope (HEFT). In R. B. Hoover and A. B. Walker, editors, *Proceedings of SPIE: EUV, X-ray and Gamma-ray instrumentation for Astronomy VIII*, volume 3114, 1997.

[83] R. Hamelinck. Ontwerp van een adaptieve deformeerbare spiegel voor het corrigeren van atmosferische turbulentie. Master's thesis, Technische Universiteit Eindhoven, Den Dolech 2, 5600MB, Eindhoven, The Netherlands, 2003.

- [84] R. Hamelinck, R. Ellenbroek, N. Rosielle, M. Steinbuch, M. Verhaegen, and N. Doelman. Validation of a new adaptive deformable mirror concept. In N. Hubin, C. E. Max, and P. L. Wizinowich, editors, *Proceedings of SPIE: Astronomical telescopes and instrumentation*, volume 7015, Marseille, France, June 2008.
- [85] R. Hamelinck, N. Rosielle, and N. Doelman. Large adaptive deformable membrane mirror with high actuator density: design and first actuator tests. In *Proceedings of the 5th Workshop on Adaptive Optics for Industry and Medicine*, August 2005.
- [86] R. Hamelinck, N. Rosielle, and N. Doelman. Large adaptive deformable mirror: design and first prototypes. In M. T. Gruneisen, J. D. Gonglewski, and M. K. Giles, editors, *Proceedings of SPIE: Advanced Wavefront Control: Methods, Devices, and Applications III*, volume 5894, San Diego, August 2005.
- [87] R. Hamelinck, N. Rosielle, J. Kappelhof, B. Snijders, and M. Steinbuch. Large adaptive deformable membrane mirror with high actuator density. In D. B. Calia, B. L. Ellerbroek, and R. Ragazzoni, editors, *Proceedings of the SPIE: Astronomical Telescopes and Instrumentation*, volume 5490, pages 1482–1492, Glasgow, UK, June 2004.
- [88] R. Hamelinck, N. Rosielle, and M. Steinbuch. Modular adaptive deformable mirror technology based on electromagnetic actuators. In 8th International Workshop on Adaptive Optics for Industry and Medicine, Shatura, Russia, 2009.
- [89] R. Hamelinck, N. Rosielle, M. Steinbuch, and N. Doelman. Electromagnetic dm technology meets future ao demands. In *AO4ELT*, Paris, France, 2009.
- [90] R. Hamelinck, N. Rosielle, M. Steinbuch, N. Doelman, R. Ellenbroek, and M. Verhaegen. Actuator grid design for an adaptive deformable mirror. In *Proceedings of the 7th EUSPEN International Conference*, Bremen, Germany, May 2007.
- [91] R. Hamelinck, N. Rosielle, M. Steinbuch, R. Ellenbroek, M. Verhaegen, and N. Doelman. Actuator tests for a large deformable membrane mirror. In B. L. Ellerbroek and D. C. B. Calia, editors, *Proceedings of SPIE: Astronomical telescopes and instrumentation Advances in Adaptive Optics*, volume 6272, May 2006.
- [92] R. Hamelinck, N. Rosielle, M. Steinbuch, R. Ellenbroek, M. Verhaegen, and N. Doelman. Deformable membrane mirror with high actuator density and distributed control. In 6th International Workshop on Adaptive Optics for Industry and Medicine, Galway, Ireland, June 2007.
- [93] R. Hamelinck, N. Rosielle, M. Steinbuch, R. Ellenbroek, M. Verhaegen, and N. Doelman. Test results of an adaptive deformable mirror for future large telescopes. In *Proceedings of the 8th EUSPEN International Conference*, 2008.
- [94] P. J. Hampton, R. Conan, O. Keskin, C. Bradley, and P. Agathoklis. Self-characterization of linear and nonlinear adaptive optics systems. *Applied Optics*, 47(2):126–134, Januari 2008.
- [95] Handshake Solutions. Haste-Programming Language Manual, 2007.
- [96] C. M. Harding, R. A. Johnston, and R. G. Lane. Fast simulation of a Kolmogorov phase screen. *Applied Optics*, 38(11):2161–2170, April 1999.

- [97] J. Hardy. Instrumental limitations in adaptive optics for astronomy. In *Proceedings of SPIE: Active telescope systems*, volume 1114, pages 2–13, November 1989.
- [98] J. Hardy. *Adaptive optics for Astronomical Telescopes*. Oxford University Press, New York, 1998.
- [99] N. Hartman, D. Li, and J. Corlett. Thin Beryllium Windows Analysis and Design Status. Technical Report 180, 2002.
- [100] Hecht, editor. Optics. Addison Wesley, 2002.
- [101] R. Heilmann, G. Monnelly, O. Mongrard, N. Butler, C. Chen, L. Cohen, C. Cook, L. Goldman, P. Konkola, M. McGuirk, G. Ricker, and M. Schattenburg. Novel methods for shaping thin-foil optics for x-ray astronomy. In R. B. Hoover and A. B. Walker, editors, *Proceedings of SPIE: X-ray Optics, Instruments, and Missions*, 2001.
- [102] M. Helmbrecht, M. He, and C. Kempf. Scaling of the Iris AO segmented MEMS DM to larger arrays. In S. S. Olivier, T. G. Bifano, and J. A. Kubby, editors, *Proceedings of SPIE: MEMS Adaptive Optics III*, volume 7209, February 2009.
- [103] G. Hickey, S. Lih, and T. Barbee. Development of nanolaminate thin shell mirrors. In H. A. MacEwen, editor, *Conferences of SPIE: Highly Innovative Space Telescope Concepts*, volume 4849, pages 63–76, August 2002.
- [104] K. J. Hinnen. Data-Driven Optimal Control for Adaptive Optics. Phd dissertation, Delft University of Technology, January 2007. ISBN 978-90-9021188-6.
- [105] P. Hinz, M. Kenworthy, D. Miller, V. Vaitheeswaran, G. Brusa, and G. Zappellini. Riding the hub: characterization of the MMT adaptive secondary performance. In B. L. Ellerbroek and D. C. B. Calia, editors, *Proceedings of SPIE: Astronomical telescopes and instrumentation*, volume 6272, 2006.
- [106] W. F. Hoffmann, P. M. Woida, J. H. Burge, and B. Catanzaro. Active Composite Membrane Mirrors. In *Ultra Lightweight Space Optics Challenge Workshop*, 1999.
- [107] N. Hubin. Technical specification for the Conceptual Design, Prototyping, Preliminary Design of the M4 adaptive unit for the E-ELT. Technical Report E-ESO-SPE-106-0037 1.0, European Southern Observatory, 2007.
- [108] B. Hulburd and D. Sandler. Segmented mirrors for atmospheric compensation. *Optical Engineering*, 29(10):1186, 1990.
- [109] R. Irwan. *Wavefront estimation in astronomical imaging*. PhD thesis, Department of electrical engineering, University of Canterbury, March 1999.
- [110] R. Irwan and R. G. Lane. Analysis of optimal centroid estimation applied to Shack-Hartmann sensing. *Applied Optics*, 38:6737–6743, November 1999.
- [111] C. Jenkins. Gossamer Spacecraft: Membrane and Inflatable Structures Technology for Space Applications. *American Institute of Aeronautics and Astronautics*, 191, 2001.
- [112] C. Jenkins, R. Freeland, J. Bishop, and W. Sadeh. An up-to-date review of inflatables structures technology for space-based applications. In R. Galloway and S. Lokaj, editors, *Proceedings of the 6th International Conference and Exposition of Engineering, Construction, and Operations in Space*, pages 66–73, 1998.
- [113] M. Johns, R. Angel, S. Shectman, R. Bernstein, D. Fabricant, P. McCarthy, and M. Phillips. Status of the Giant Magellan Telescope (GMT) Project. In *Proceedings of SPIE*, volume 4007, 2000.

[114] F. Jones. The refractivity of air. *Journal of Research of the National Bureau of Standards*, 86:27–32, 1981.

- [115] M. Kasper, E. Fedrigo, D. P. Looze, H. Bonnet, L. Ivanescu, and S. Oberti. Fast calibration of high-order adaptive optics systems. *Journal of the Optical Society of America A*, 2:1004–1008, 2004.
- [116] H. Kharaghani and B. Tayfeh-Rezaie. A hadamard matrix of order 428. *Journal of Combinatorial Designs*, 13:435–440, 2005.
- [117] A. Kolmogorov. *Dissipation of energy in a locally isotropic turbulence*, volume 3 of *Turbulence*, *Classic Papers on Statistical Theory*. Wiley-Interscience, New York, October 1961.
- [118] M. Langlois, R. Angel, M. Lloyd-Hart, F. W. G. Love, and A. Naumov. High Order Reconstructor-Free Adaptive Optics for 6-8 meter class Telescopes. In *ESO Conference & Workshop Proceedings, Beyond Conventional Adaptive Optics*, volume 58, pages 113–120, Venice, Italy, 2001.
- [119] W. Langlois. Isothermal squeeze films. *Quarterly applied mathematics*, XX:131–150, 1962.
- [120] J.-S. Lew, J.-N. Juang, and R. Longman. Comparison of several system identification methods for flexible structures. *Journal of Sound and Vibration*, 167(3):461–480, November 1993.
- [121] D. Li, A. Ladran, D. Lozano, and R. Rimmer. Mechanical and thermal analysis of beryllium windows for RF cavities in a muon cooling channel. Technical Report DE2002-799628, 2002.
- [122] P. M. Livingston. Proposed method for inner scale measurements in a turbulent atmosphere. *Applied Optics*, 11(3):684–687, 1972.
- [123] M. Lloyd-Hart, F. Wildi, H. Martin, P. McGuire, M. Kenworthy, R. Johnson, B. Fitz-Patrick, G. Angeli, S. Miller, and R. Angel. Adaptive optics for the 6.5m MMT. In P. L. Wizinowich, editor, *Proceedings of SPIE: Adaptive Optical Systems Technology*, volume 4007, pages 167–174, 2000.
- [124] M. Loktev. *Modal wavefront correctors based on nematic liquid crystals*. PhD thesis, Delft University of Technology, 2005.
- [125] M. Loktev, D. W. D. L. Monteiro, and G. Vdovin. Comparison study of the performance of piston, thin plate and membrane mirrors for correction of turbulenceinduced phase distortions. *Optics Communications*, 192:91–99, May 2001.
- [126] E. Manders. Design of a device to measure the out-of-plane, nonlinear stiffness of circular membranes. Technical report, Technische Universiteit Eindhoven, 2004.
- [127] D. Marker and R. Carreras. On the system identification for an optical quality membrane mirrors. In *IEEE International Conference on Systems, Man and Cybernetics*, volume 3, pages 2899–2904, 2005.
- [128] D. K. Marker and C. H. Jenkins. Surface precision of optical membranes with curvature. *Optics Express*, 1(11), 1997.
- [129] H. Martin, J. Burge, C. D. Vecchio, L. Dettmann, S. Miller, B. Smith, and F. Wildi. Optical fabrication of the MMT adaptive secondary mirror. In P. L. Wizinowich, editor, *Proceedings of SPIE: Adaptive Optical Systems Technology*, volume 4007, pages 502–507, 2000.

- [130] P. Massioni and M. Verhaegen. Distributed Control for Identical Dynamically Coupled Systems: a Decomposition Approach. Submitted paper.
- [131] T. Mathworks. Scientific computing software, 2009. http://www.mathworks.com.
- [132] J. Maxwell. *A treatise on electricity & magnetism*, volume 2. Dover Publications, 3rd edition, 1954.
- [133] Mentor Graphics Corporation. ModelSim User's Manual, 2007.
- [134] D. Mihora and P. Redmond. Electrostatically formed antennas. *Journal of Spacecraft and Rockets*, 17(5):465–473, September 1980.
- [135] O. Mongrard. High-Accuracy Foil Optics for X-ray Astronomy. Master's thesis, Massachusetts Institute of Technology, 2001.
- [136] D. C. Montgomery and G. C. Runger. Applied statistics and probability for engineers. John Wiley and Sons, Inc., New York, 2^{nd} edition, 1999.
- [137] A. Moussessian, L. D. Castillo, J. Huang, G. Sadowy, J. Hoffman, P. Smith, T. Hatake, C. Derksen, and B. Lopez. Membrane Array Using T/R Membranes. In *Earth Science Technology Conference*, 2005.
- [138] R. M. Myers, A. J. Longmore, C. R. Benn, D. F. Buscher, P. Clark, N. A. Dipper, N. Doble, A. P. Doel, C. N. Dunlop, X. Gao, T. Gregory, R. A. Humphreys, D. Ives, R. Østensen, P. Peacocke, R. G.M.Rutten, C. J. Tierney, A. J. Vik, M. R. Wells, R. W. Wilson, S. P. Worswick, and A. Zadrozny. The NAOMI Adaptive Optics System for the 4.2m William Herschel Telescope. In P. L. Wizinowich and D. Bonaccini, editors, *Proceedings of SPIE: Adaptive Optical System Technologies II*, volume 4839, pages 647–658, 2003.
- [139] I. Newton. Opticks. based on 4th edition, 1979 (1730).
- [140] M. Nicolle, T. Fusco, G. Rousset, and V. Michau. Improvement of Shack-Hartmann wave-front sensor measurement for extreme adaptive optics. *Optics Letters*, 29(23):2743–2745, 2004.
- [141] R. Noll. Zernike polynomials and atmospheric turbulence. *Journal of the Optical Society of America*, 66:207–211, March 1976.
- [142] J. Owens. Optical refractive index of air: dependence on pressure, temperature and composition. *Applied Optics*, 6:51–59, 1967.
- [143] S. Oya, A. Bouvier, O. Guyon, M. Watanabe, Y. Hayano, H. Takami, M. Iye, M. Hattori, Y. Saito, M. Itoh, S. Colley, M. Dinkins, M. Eldred, and T. Golota. Performance of deformable mirror for Subaru LGSAO system. In B. L. Ellerbroek and D. C. B. Calia, editors, *Proceedings of SPIE: Astronomical telescopes and instrumentation Advances in Adaptive Optics*, volume 6272, 2006.
- [144] A. Papavasiliou, S. Olivier, T. Barbee, R. Miles, and K. Chang. Large-Scale Nanolaminate Deformable Mirror. In S. S. Olivier, S. A. Tadigadapa, and A. K. Henning, editors, *Proceedings of SPIE: MEMS/MOEMS Components and Their Applications III*, volume 6113, pages 200–209, 2006.
- [145] A. Papavasiliou, S. Olivier, T. Barbee, R. Miles, C. Walton, M. Cohn, and K. Chang. Nanolaminate Deformable Mirrors. In *IEEE/LEOS International Conference on Optical MEMS and Their Applications*, pages 158–159, 2006.
- [146] A. Papavasiliou, S. Olivier, T. Barbee, C. Walton, and M. Cohn. MEMS Actuated Deformable Mirror. In S. S. Olivier, S. A. Tadigadapa, and A. K. Henning, editors, *Proceedings of SPIE: MEMS/MOEMS Components and Their Applications III*, volume 6113, pages 190–199, 2006.

[147] I. Paul, B. Majeed, K. M. Razeeb, and J. Barton. Characterizing stress in ultrathin silicon wafers. *Applied Physics Letters*, 89, 2006.

- [148] E. Peck and K. Reeder. Dispersion of air. *Journal of the Optical Society of America*, 62:958–962, 1972.
- [149] J. Perreault, P. Bierden, M. Horenstein, and T. Bifano. Manufacturing of an optical-quality mirror system for adaptive optics. In J. Gonglewski, M. Vorontsov, and M. Gruneisen, editors, *Proceedings of SPIE: X-ray Optics, Instruments, and Missions*, volume 4493, pages 13–20, February 2002.
- [150] R. Ragazzoni. Pupil plane wavefront sensing with an oscillating prism. *Journal of Modern Optics*, 43(2):289–293, 1996.
- [151] F. Rasmussen, J. Ravnkilde, P. Tang, O. Hansen, and S. Bouwstra. Electroplating and characterization of CoNiFe and NiFe for magnetic microsystems applications. In *Eurosensors XIV*, pages 505–508, 2000.
- [152] J. Rehder, L. H. Andersen, P. Rombach, and O. Hansen. Magnetic reluctance change actuator for loudspeaker application. In *Proceedings of Eurosensors XVI*, 2002.
- [153] J. Rehder, P. Rombach, and O. Hansen. Balanced membrane micromachined loudspeaker for hearing instrument application. *Journal of Micromechanics and Micro*engineering, 11:334–338, 2001.
- [154] J. M. Renno. *Dynamics and Control of Membrane Mirrors for Adaptive Optic Applications*. PhD thesis, Virginia Polytechnic Institute and State University, 2008.
- [155] F. Roddier. Curvature sensing and compensation: a new concept in adaptive optics. *Applied Optics*, 27(7):1223–1225, 1988.
- [156] F. Roddier. Adaptive optics in astronomy. Cambridge University Press, 1999.
- [157] R. C. Romeo and P. C. Chen. Ultra Lightweight Composite Replica Mirror Technology. In *Ultra Lightweight Space Optics Challenge Workshop*, 1999.
- [158] E. J. Ruggiero. *Modeling and Control of SPIDER Satellite Components*. PhD thesis, Virginia Polytechnic Institute and State University, 2005.
- [159] T. Ruppel, M. Lloyd-Hart, D. Zanotti, and O. Sawodny. Modal Trajectory Generation for Adaptive Secondary Mirrors in Astronomical Adaptive Optics. *IEEE International Conference on Automation Science and Engineering*, pages 430–435, 2007.
- [160] D. Saint-Jacques and J. E. Baldwin. Taylor's hypothesis: good for nuts. In P. J. Lena and A. Quirrenbach, editors, *Proceedings of SPIE: Interferometry in Optical Astronomy*, volume 4006, pages 951–962, 2000.
- [161] T. Sakai and H. Kawamoto. Improvement in Time-Dependent Displacement Degradation of Piezoelectrc Ceramics by Manganese/Indium Addition 1427. *Journal of the American Ceramic Society*, 83:1423–1427, 2000.
- [162] P. Salinari, C. D. Vecchio, and V. Biliotti. A study of an adaptive secondary mirror. In F. Merkle, editor, *ICO-16 Satellite conference on Active and Adaptive Optics*, 1993.
- [163] P. Salzenstein, O. Dupuis, M. Helal, E. Lheurette, O. Vanbésien, P. Mounaix, and D. Lippens. Coplanar waveguides on dielectric membranes micromachined on a GaSa substrate. *Electronics Letters*, 32(9):821–822, September 1996.
- [164] V. Samarkin, A. Aleksandrov, and V. Dubikovsky. Water-cooled wavefront correctors. *Advanced Optoelectronics and Lasers*, 1:119, 2005.

- [165] J. Sass, K. Mazur, B. Surma, F. Eichhorn, D. Litwin, J. Galas, and S. Sitarek. X-ray studies of ultra-thin si wafers for mirror application. *Nuclear instruments & methods in physics research. Section B, Beam interactions with materials and atoms*, 253:236–240, 2006.
- [166] J. Sauvage, T. Fusco, G. Rousset, and C. Petit. Calibration and precompensation of noncommon path aberrations for extreme adaptive optics. *Journal of the Optical Society of America A*, 24:2334–2346, 2007.
- [167] R. Schreier and G. Temes. *Delta-Sigma data converters: theory, design and simulation*. IEEE Press, 1997.
- [168] T. N. Science and T. R. C. for Computation and Visualization of Geometric Structures. Qhull software, 2009. http://www.qhull.org.
- [169] R. V. Shack and B. C. Platt. Production and use of a lenticular hartmann screen. *Journal of the Optical Society of America*, 61:656, 1971.
- [170] E. Silva, G. Goodwin, D. Quevedo, and M. Derpich. Optimal Noise Shaping for Networked Control Systems. In *Proceedings of the European Control Conference*, Kos, Greece, 2007.
- [171] J. Sinquin, J. Lurçon, and C. Guillemard. Deformable mirrors technologies for astronomy at CILAS. In N. Hubin, C. E. Max, and P. L. Wizinowich, editors, *Proceedings of SPIE: Adaptive Optics Systems*, volume 7015, 2008.
- [172] H. Song, R. Fraanje, M. Verhaegen, and G. Vdovin. Hysteresis compensation for piezo deformable mirror. In Proceedings of the 6th International Workshop on Adaptive Optics for Industry and Medicine, 2007.
- [173] H. P. Stahl. Ares V Launch Capability Enables Future Space Telescopes. In H. A. MacEwen and J. B. Breckinridge, editors, *Proceedings of SPIE: UV/Optical/IR Space Telescopes: Innovative Technologies and Concepts III*, volume 6687, 2007.
- [174] T. Stalcup and K. Powell. Image motion correction using accelerometers at the MMT observatory,. In *Proceedings of SPIE*, volume 7018, 2008.
- [175] B. Stamper, R. Angel, J. Burge, and N. Woolf. Flat Membrane Mirrors for Space Telescopes. In J. W. Bilbro, J. B. Breckinridge, R. A. Carreras, S. R. Czyzak, M. J. Eckart, R. D. Fiete, and P. S. Idell, editors, *Proceedings of SPIE: Imaging Technology and Telescopes*, volume 4091, pages 126–136, 2001.
- [176] R. E. Stelter. Low Cost Method For Magnet Testing. Brochure, June 1993.
- [177] P. Stoica and M. Jansson. MIMO system identification: state-space and subspace approximations versus transfer function and instrumental variables. *IEEE Transactions on Signal Processing*, 48:3087–3099, 2000.
- [178] K. Szeto, S. Roberts, S. Sun, L. Stepp, J. Nelson, M. Gedig, N. Loewen, and D. Tsang. TMT telescope structure system design and development. In L. M. Stepp, editor, *Proceedings of SPIE: Ground-based and airborne telescopes*, volume 6267, May 2006.
- [179] H. Takami, S. Colley, M. Dinkins, M. Eldred, O. Guyon, T. Golot, M. Hattori, Y. Hayano, M. Ito, M. Iye, S. Oya, Y. Saito, and M. Watanabe. Status of Subaru Laser Guide Star AO System. In B. L. Ellerbroek and D. C. B. Calia, editors, Proceedings of SPIE: Astronomical telescopes and instrumentation - Advances in Adaptive Optics, volume 6272, 2006.

[180] H. Takami and M. Iye. Membrane deformable mirror for SUBARU adaptive optics. In M. A. Ealey and F. Merkle, editors, *Proceedings of SPIE: Adaptive Optics in Astronomy*, volume 2201, page 762Ű767, 1994.

- [181] C. Talley, W. Clayton, P. Gierow, J. McGee, and J. Moore. Advanced membrane materials for improved solar sail capabilities. *American Institute of Aeronautics and Astronautics*, 2002.
- [182] V. Tatarski. Wavefront Propagation in a Turbulent Medium. McGraw-Hill, 1961.
- [183] R.M.L. Ellenbroek. *Adaptive deformable mirror feasibility of modularly distributed control*. PhD thesis, Delft university of technology, 2010. ISBN 123-456-789-0.
- [184] S. Thomas. Optimized centroid computing in a Shack-Hartmann sensor. In D. B. Calia, B. L. Ellerbroek, and R. Ragazzoni, editors, *Proceedings of SPIE: Advance-ments in Adaptive Optics.*, volume 5490, pages 1238–1246, 2004.
- [185] S. Timoshenko and S. Woinowsky-Krieger. *Theory of plates and shells*. McGraw-Hill, Auckland, second edition edition, 1989.
- [186] A. A. Tokovinin, B. Gregory, H. E. Schwarz, V. Terebizh, and S. Thomas. A visible-light AO system for the 4.2-m SOAR telescope. In P. L. Wizinowich and D. Bonaccini, editors, *Proceedings of SPIE: Adaptive Optical System Technologies II*, volume 4839, pages 673–680, 2003.
- [187] R. K. Tyson. Principles of adaptive optics. Academic Press, 1998.
- [188] G. Vdovin and P. Sarro. Flexible mirror micro-machined in silicon. *Applied Optics*, 34(16):2968–2972, 1995.
- [189] C. D. Vecchio. Aluminium reference plate, heat sink, and actuator design for an adaptive secondary mirror. In D. Bonaccini and R. K. Tyson, editors, *Proceedings of SPIE: Adaptive Optical System Technologies*, volume 3353, pages 839–849, 1998.
- [190] C. D. Vecchio, W. Gallieni, P. Salinari, and P. Gray. Preliminary mechanical design of an adaptive secondary unit for the MMT-conversion telescope. In M. Cullum, editor, *Proceedings of ESO*, volume 54, page 243, 1996.
- [191] M. Verhaegen. Subspace model identification part 3. analysis of the ordinary outputerror state-space model identification algorithm. *International Journal of Control*, 56:555–586, 1993.
- [192] M. Verhaegen. Identification of the deterministic part of state-space models in innovations form from input-output data. *Automatica*, 30(1):61–74, 1994.
- [193] M. Verhaegen and P. Dewilde. Subspace model identification part I The outputerror state-space model identification class of algorithms. *International Journal of Control*, 56(5):1187–1210, 1992.
- [194] M. Verhaegen and V. Verdult. Filtering and system identification. Cambridge university press, New York, 1st edition, 2007.
- [195] C. Vogel. Sparse matrix methods for wavefront reconstruction revisited. In B. L. Ellerbroek and R. Ragazzoni, editors, *Proceedings of SPIE: Advancements in Adaptive Optics*, volume 5490, pages 1327–1335, 2004.
- [196] C. R. Vogel and Q. Yang. Fast optimal wavefront reconstruction for multi-conjugate adaptive optics using the fourier domain preconditioned conjugate gradient algorithm. *Optics Express*, 14:7487–7498, 2006.

- [197] M. Vorontsov, G. Izakson, A. Kudryashov, G. Kosheleva, S. Nazarkin, Y. F. Suslov, and V. I. Shmalgauzen. Adaptive cooled mirror for the resonator of an industrial laser. *Soviet Journal of Quantum Electronics*, 15(7):888, 1985.
- [198] B. Wada and M. Lou. Pre-flight validation of gossamer structures. *American Institute of Aeronautics and Astronautics*, 2002.
- [199] F. Wildi, G. Brusa, A. Riccardi, R. Allen, M. Lloyd-Hart, D. Miller, B. Martin, R. Biasi, and D. Gallieni. Progress of the MMT adaptive optics program. In R. K. Tyson, D. Bonaccini, and M. C. Roggemann, editors, *Proceedings of SPIE*, volume 4494, pages 11–18, 2001.
- [200] F. Wildi, G. Brusa, A. Riccardi, M. Lloyd-Hart, M. Martin, and L. Close. Towards 1st light of the 6.5m MMT adaptive optics system with deformable secondary mirror. In P. L. Wizinowich and D. Bonaccini, editors, *Proceedings of SPIE: Adaptive Optical System Technologies II*, volume 4839, pages 155–163, 2002.
- [201] J. M. Wilkes and D. K. Marker. A review of membrane optics research. Technical Report A924634z, Air Force Research Laboratory, 2005.
- [202] C. Wilson and P. Beck. Fracture testing of bulk silicon microcantilever beams subjected to a side load. *Journal of microelectromechanical Systems*, 5:142–150, 1996.
- [203] P. Wizinowich. Adaptive optics at the keck oservatory. *IEEE Instrumentation and measurement magazine*, 2005.
- [204] P. Woida and W. Hoffmann. Enhancing CFRP panels with silicon monoxide to improve as-replicated figure accuracy. In R. B. Hoover and A. B. C. Walker, editors, *Proceedings of SPIE: Grazing Incidence and Multilayer X-Ray Optical Systems*, volume 3113, pages 494–499, 1997.
- [205] Y. Wong and S. Pellegrino. *Textile Composites and inflateble structures*, volume 3, chapter Amplitude of wrinkles in thin membranes, pages 109–122. Springer Netherlands, 2003.
- [206] Y. Wong, S. Pellegrino, and K. Park. Prediction of Wrinkle Amplitudes in Square Solar Sails. *American Institute of Aeronautics and Astronautics*, 2003.
- [207] Xilinx Inc. Xilinx ISE 9.1i Software Manuals and Help.
- [208] E.-H. Yang and D. V. Wiberg. A Wafer-Scale Membrane Transfer Process for the Fabrication of Optical Quality, Large Continuous Membranes. *Journal of Micro-ElectroMechanical Systems*, 12(6):804 – 815, 2003.
- [209] T. Young. An Essay on the Cohesion of Fluids. *Philosophical Transactions of the Royal Society*, 95:65–87, 1805.
- [210] A. Zadrozny, M. Chang, D. Buscher, R. Myers, A. Doel, C. Dunlop, R. Sharples, and R. Arnold. First Atmospheric Compensation With a Linearised High Order Adaptive Mirror -ELECTRA. In E. D. Bonaccini, editor, ESO Conference Workshop Proceedings, number 56, pages 459–468. ESO, 1999.

Samenvatting

Brekingsindex variaties in de atmosfeer veroorzaken golffrontverstoringen en limiteren daarmee de resolutie in aardse telescopen. Met adaptieve optiek kunnen de golffrontverstoringen in realtime worden gecorrigeerd. Meestal bestaat een adaptief systeem uit een golffrontsensor, een deformeerbare spiegel en een regeling.

De huidige grootste telescopen hebben een 10m primaire spiegel. Voor de toekomst zijn telescopen met een grotere apertuur en een betere resolutie gewenst. Op dit moment worden ELTs ontworpen met diameters tot 42m. AO systemen voor deze telescopen zijn een grote uitdaging. Dit proefschrift richt zich op de uitdagingen voor de deformeerbare spiegel.

Een 8 meter telescoop, op een representatieve locatie, dient hierbij als startpunt. De atmosfeer wordt daarbij voorgesteld met Kolmogorov turbulentie en frozen flow wordt aangenomen. De golffrontfitfout, veroorzaakt door een beperkt aantal actuatoren en de temporele fout, veroorzaakt door een beperkte regelbandbreedte, vormen de belangrijkste opwerpparameters voor de deformeerbare spiegel. Voor een 8 meter telescoop vormt de combinatie van 5000 actuatoren en 200Hz bandbreedte een goede balans tussen beide foutenbronnen en levert bijna diffractiebegrensde kwaliteit voor zichtbaar licht. Een actuatorslag van $\approx 5.6 \mu m$ en $\approx 0.36 \mu m$ interactuatorslag zijn nodig. Vrij van hysterese en drift, met nm resolutie en de lage warmteontwikkeling vormen daarbij de belangrijkste eisen.

In dit proefschrift worden het ontwerp, de realisatie en de testresultaten van een deformeerbare spiegel die hieraan voldoet gepresenteerd. Het ontwerp is uitbreidbaar in mechanica, elektronica en regeltechniek en daarmee ook geschikt voor de toekomstige grotere telescopen. Het spiegelontwerp is opgebouwd uit lagen: de facesheet, de actuatorgrid en de steunstructuur. Onder de facesheet bevinden zich de elektromagnetische actuatoren die zowel kunnen duwen als trekken aan de facesheet. Identieke actuatormodules met in elk 61 actuatoren, in een hexagonale lay-out op een 6mm steek, kunnen worden samengevoegd tot grote grids. De steunstructuur dient hierbij als stijve en stabiele referentie.

Om de actuatorkrachten en warmteontwikkeling laag te houden is een dunne facesheet vereist. De ondergrens wordt daarbij bepaald door de doorbuiging van de facesheet tussen de actuatoren onder invloed van zwaartekracht of winddruk. Voor beide situaties zijn de schaalwetten voor actuatorkracht en warmteontwikkeling afgeleid. Deze warmteontwikkeling is minimaal door gebruik te maken van beryllium als facesheet materiaal. Vanuit praktisch oogpunt worden echter voor de prototypes goed verkrijgbare $100\,\mu m$ dikke Pyrex facesheets gebruikt. Door de toepassing van sprieten ($\emptyset 0.1 \times 8 mm$) als verbinding tussen de facesheet en de actuatoren wordt een glooiend spiegeloppervlak verkregen en is laterale beweging tussen de facesheet en de actuatoren mogelijk. Metingen tonen aan dat de lokale onvlakheid veroorzaakt door de gebruikte lijmverbinding 3nm RMS is. De actuatoren leggen de vrijheidsgraden uit het vlak van de facesheet vast en bepalen daarmee de eerste eigenfrequentie van de spiegel. De actuatorstijfheid is zo ontworpen dat de eigenfrequentie hoog

224 Samenvatting

genoeg is voor de beoogde regelbandbreedte, maar niet hoger dan noodzakelijk om daarmee overbodige warmte ontwikkeling in de actuatoren te voorkomen. Tevens wordt hiermee voorkomen dat een kapotte actuator een punt in het spiegeloppervlak fixeert. De elektromagnetische variabele reluctantie actuatoren zijn efficiënt en hebben een lage bewegende massa. Andere voordelen zijn de prijs, de lage aanstuurspanning en de verwaarloosbare hysterese en drift. De actuatoren bestaan uit een magneetcircuit, waarin een permanente magneet een ferromagnetische kern voorspant in zijn membraanophanging. Deze kracht wordt met een spoel vergroot of verkleind. De actuatoren bewegen daarbij wrijvingsloos, zonder mechanische hysterese en vrij van speling. De actuatormodules zijn opgebouwd uit lagen om het aantal onderdelen te verminderen, de assemblage te vereenvoudigen en tevens uniforme actuator eigenschappen te verkrijgen.

Communicatie- en besturingselektronica is ontwikkeld. In FPGAs geïmplementeerde, PWMs spanningversterkers zijn toegepast vanwege de hoge efficiëntie en mogelijkheid deze in grote aantallen te realiseren met een beperkt aantal componenten. Een multidrop LVDS seriëële communicatie is gekozen vanwege de hoge bandbreedte en lage latency en lage overhead. Aan de flat cable kunnen maximaal 32 elektronica modules wordt verbonden, ieder goed voor de aansturing van 1 actuatorgrid met 61 actuatoren. De flatcable is verbonden met een communicatie box die Ethernet pakketten van de control PC vertaald in LVDS. Twee deformeerbare spiegels zijn succesvol geassembleerd. Een Ø50mm deformeerbare spiegel met 61 actuatoren en een Ø150mm spiegel met 427 actuatoren. Met het laatste prototype is de modulariteit aangetoond door het gebruik van 7 identieke grids die zijn geplaatst op een gemeenschappelijk basis. De dynamische eigenschappen van iedere actuator, inclusief de communicatie en aansturingelektronica, zijn gemeten. Alle actuatoren zijn functioneel, hetgeen betrouwbaarheid van het productie en assemblage proces aantoont. Een niet lineair model van de actuator is afgeleid, dat zowel de statische als dynamische eigenschappen in het magnetische, mechanische en elektrische domein beschrijft. Met linearisatie is de overdrachtsfunctie van de spanning naar actuatorpositie en zijn eigenschappen zoals motorcontante, spoelinductie, actuatorstijfheid en eigenfrequentie afgeleid. Frequentie responsie metingen tonen kleine afwijkingen in deze eigenschappen ten opzichte van het model en tevens dat de spreiding over alle actuatoren gering is. De gemiddelde actuatorstijfheid en eigenfrequentie is respectievelijk 0.47kN/m en 1.8kHz en ligt dicht bij de ontwerpwaarde van 0.5kN/m en 1.9kHz. Met een 4Hz sinusvormige spanning is de hysterese en de semi-statische non-lineaire responsie van de actuator gemeten. De hysterese blijkt verwaarloosbaar en de niet lineariteit minder dan 5% over de $\pm 10 \mu m$ slag. Metingen tonen dat de warmteontwikkeling wordt gedomineerd door verliezen in de FPGAs.

De statische performance is gevalideerd voor een interferometer. De gemeten influence matix is gebruikt om 28 Zernike modes in de spiegel te maken, inclusief de piston term, die de best mogelijke vlakke spiegel voorstelt. De fout ten opzichte van de perfecte Zernike mode is ≈ 25 nm voor alle modes. Het dynamische gedrag is gevalideerd door metingen met een laser vibrometer. Hiermee is de verplaatsing van het spiegeloppervlak gekoppeld aan een witte ruis input spanningssignaal. Identificatie van de spiegel is uitgevoerd met het MOESP systeem identificatie algoritme. The VAF waarden zijn hierbij $\approx 95\%$. De gemeten eerste eigenfrequentie is 725Hz en lager dan de verwachtte 974Hz. Dit te wijten aan variaties in de actuator eigenschappen, zoals actuatorstijfheid. De energie dissipatie in warmte in een actuator in de $\varnothing 50$ nm spiegel tijdens de correctie van een typisch Von Karmann turbulentie spectrum is ≈ 1.5 mW.

Het is even geleden dat er hardware binnen deze promotie gereed kwam. Hier is nu het laatste stuk; de gedrukte letters. De promotie was voor mij een prachtkans om een eigen idee van papier om te zetten in werkende hardware... en vervolgens weer in papier.

Tijdens mijn promotie heb ik veel kunnen leren, waarvoor ik dankbaar ben. Een aantal mensen is hierbij onmisbaar geweest en wil ik hier bedanken.

Beste Nick, vanaf september 2001 heb ik in het lab tijdens mijn stage, afstuderen en promotie plezier gevonden in dit vak. Jouw kennis, inzicht en creativiteit hebben mij geïnspireerd, keer op keer. Ik heb veel van je mogen leren. Het plezier daarvan ervaar ik dagelijks. Dank voor alles en ik wens in de toekomst nog veel met je samen te werken.

Beste Maarten, ondanks je vele studenten, promovendi en andere werkzaamheden heb je altijd wel even ergens tijd. Ook nog tussen het maandelijkse overleg door. Ik wil je bedanken voor het luisterend oor, de ruimte die je biedt voor ontwikkeling, het aanstekelijke enthousiasme en de hulp waar nodig. De mogelijkheden die je bood om naar conferenties te gaan om daar te presenteren en andere vakgenoten te ontmoeten waren ongekend.

Beste Rogier, je was al een goede vriend voordat we aan onze promotie begonnen. Dat is gedurende deze jaren alleen maar versterkt. Je kwaliteit, inzet en betrouwbaarheid waardeer ik enorm. Het was prettig samenwerken! Niet alleen doordeweeks, maar ook in de weekenden. Nog even en jouw promotie zit er ook op!

Beste Dave, je bent een goede instrumentmaker en daarbij ook prettig om mee samen te werken. Zonder jouw toewijding en constante kwaliteit was het niet mogelijk zoveel onderdelen betrouwbaar te realiseren en te assembleren. In belangrijke mate heb jij het succes van deze promotie mede mogelijk gemaakt. Bedankt!

Beste Pieter en Jacob Jan, vanaf het begin zijn jullie vanuit het toenmalig TNO TPD bij dit onderwerp betrokken. Tijdens mijn afstuderen en als mede-initiatiefnemers van het IOP project. Hartelijk dank voor jullie inzet en de mogelijkheden die jullie mij geboden hebben.

Erik, Corné en William wil ik bedanken voor hun stage- en afstudeerbijdragen. Ik heb met plezier met jullie samengewerkt. Jullie bijdrage was waardevol en jullie begeleiding voor mij een leerzame ervaring.

226 Dankwoord

Een bedankje is op zijn plaats voor de mensen bij het toenmalige TNO TPD en latere TNO Industrie en Techniek voor de samenwerking en ondersteuning en in het bijzonder Paul Keijzer voor zijn bijdrage aan de elektronica. Daarnaast is er nog de expertise van de mensen van de Sterrewacht Leiden met Rudolf in het bijzonder. Jouw enthousiasme gecombineerd met kennis van zaken werkt aanstekelijk!

Dit project was niet mogelijk geweest zonder het IOP Precisie Technologie. Lou, Eddy en Casper wil ik hiervoor bedanken, evenals het projectteam en de leden van de begeleidingscommissie. De halfjaarlijkse bijeenkomsten met de feedback gaven een frisse blik van buitenaf en een stimulans om door te gaan.

A special thanks to prof.dr. Andreas Quirrenbach (Universität Heidelberg), prof.ir. Rob Munnig Schmidt (TU Delft) and prof.dr. Elena Lomonova (TU/e) for their effort to read my thesis and their useful comments.

Verder was mijn verblijf aan de TU/e lang niet zo plezierig geweest zonder de labgenoten en collega's bij DCT. In het bijzonder wil ik daarvoor Rens en Chris bedanken. Het was erg prettig om met jullie vele jaren te delen!

Verder wil ik ook mijn 'oude' vrienden bedanken voor alle ontspanning die jullie al jaren bieden.

Beste pa en ma, dankzij de ruimte en mogelijkheden die jullie me boden heb ik me kunnen ontwikkelen. Kon ik worden wie ik nu ben en kan ik met plezier en een goed gevoel terugkijken. Bedankt voor alles!

Ook wil ik Ranko bedanken. Ik kan me geen betere broer wensen.

Niet op de minste plaats ben ik veel dank verschuldigd aan Annemarie. Voor de ruimte die je me geeft en het begrip dat je hebt opgebracht voor al die avonden en weekenden die ik achter mijn laptop doorbracht.

Bedankt dat je me laat zien dat er veel meer is dan werk en promotie alleen!

Roger Breda, mei 2010

Curriculum Vitae

Roger Hamelinck was born on May 6, 1979 in Dongen, the Netherlands. After finishing Atheneum in 1997 at the 'Cambreurcollege' in Dongen, he studied Mechanical Engineering at the Technische Universiteit Eindhoven. In 2003 he graduated within the Constructions & Mechanisms Group on the design of an adaptive deformable mirror, carried out at TNO TPD in Delft. This work was granted with a KIVI-award for best Mechanical Engineering master thesis of the year at the Technical University of Eindhoven. From 2004 to 2009 he continued the design and realization of the deformable mirror in a PhD project, of which the results are presented in this thesis. Since October 2007 he is employed by the Precision Motion Systems department of TNO Science and Industry.

